CENOZOIC TECTONO-THERMAL HISTORY OF THE SOUTHERN TALKEETNA MOUNTAINS, ALASKA: MULTIPLE TOPOGRAPHIC DEVELOPMENT DRIVERS THROUGH TIME

By

Patrick J. Terhune, B.S.

A Thesis Submitted in Partial Fulfillment of the Requirements

for the Degree of

Master of Science

in

Geoscience

August 2018

APPROVED:

Dr. Jeffrey Benowitz, Committee Chair
Dr. Jeffrey Freymueller, Committee Co-Chair
Robert Gillis, Committee Member
Dr. Paul McCarthy, Chair
Department of Geosciences
Dr. Anupma Prakash, Interim Dean
College of Natural Science and Mathematics
Dr. Michael Castellini
Dean of the Graduate School

Abstract

Intraplate mountain ranges can have polyphase topographic development histories reflecting diverse plate boundary conditions. We apply $^{40}Ar/^{39}Ar$, apatite fission track (AFT) and apatite (U-Th)/He (AHe) geochronology-thermochronology to plutonic and volcanic rocks in the southern Talkeetna Mountains of Alaska to document regional magmatism, rock cooling and inferred exhumation patterns as proxies for the deformation history of this long-lived intraplate mountain range. High-temperature $^{40}Ar/^{39}Ar$ geochronology on muscovite, biotite and K-feldspar from Jurassic granitoids indicates post-emplacement (~158-125 Ma) cooling and Paleocene (~61 Ma) thermal resetting. $^{40}Ar/^{39}Ar$ whole rock volcanic ages and AFT cooling ages in the southern Talkeetna Mountains are predominantly Paleocene-Eocene, suggesting that the Range is partially paleotopography that formed during an earlier tectonic setting. Miocene AHe cooling ages within ~10 km of the Castle Mountain Fault suggest ~2-3 km of vertical displacement that also contributed to mountain building, likely in response to the inboard progression of the subducted Yakutat microplate. Paleocene-Eocene volcanic and exhumation ages across interior southern Alaska north of the Border Ranges Fault System are similar and show no N-S or W-E progressions, suggesting a broadly synchronous and widespread volcanic and exhumation event that conflicts with the proposed diachronous subduction of an active west-east sweeping spreading ridge beneath south-central Alaska. To reconcile this, we propose a new model for the Cenozoic tectonic evolution of southern Alaska. We infer that slab breakoff sub-parallel to the trench and subsequent mantle upwelling drove magmatism, exhumation and rock cooling synchronously across south-central Alaska and played a primary role in the development of the southern Talkeetna Mountains.

Acknowledgements

I would like to sincerely thank my advisor, Dr. Jeffrey Benowitz, for his years of mentorship in geochronology, field work techniques and the geologic history of southern Alaska. His constant guidance and support at the UAF Geochronology Facility has been invaluable towards the development of this research project and my personal growth as a scientist. I would also like to thank my committee members, Dr. Jeffrey Freymueller and Robert Gillis for their feedback and advice throughout my Master's work. I would like to extend appreciation to Dr. Jeffrey Trop at Bucknell University who's sample contributions and feedback greatly improved the quality of my work. Thanks to the University of Alaska Fairbanks Department of Geosciences for the teaching assistantships and funding opportunities that have allowed me to complete my graduate studies. Finally, I would like to thank all the organizations that provided the funding that made my thesis work possible, including URSA (Undergraduate Research and Scholarly Activity), the Geological Society of America, the Alaska Geological Society and the American Association of Petroleum Geologists.

General Introduction

After more than 80 years of detailed geologic research in southern Alaska, the history of orogenesis in the region is still poorly understood. Previous research has made clear that the uplift and exhumation of the numerous mountain ranges extending across southern Alaska did not happen contemporaneously, but rather at different times over a period of 65 million years or more, through a series of tectonic and geologic processes. Numerous research methods have been employed to reconstruct the topographic development history of southern Alaska mountain ranges, including geologic mapping, structural and basin analysis, and geochronology, but many questions remain unanswered.

The Talkeetna Mountains of south-central Alaska are a broad topographic high that sit between two relatively well studied mountain ranges: the Alaska Range and Chugach Mountains. However, the timing and causation of topographic development in the Talkeetna Mountains remains unclear. Given this, I apply geochronology and thermochronology, tools that act as both a geologic clock and thermometer, to rocks I collected across a vast portion of the southern Talkeetna Mountains to answer three broad research questions: 1) How old are the southern Talkeetna Mountains? 2) Are there local structural controls on topographic development or evidence for rock uplift driven by a thermal event? And 3) how do my results align with the current models for the Cenozoic tectonic evolution of southern Alaska? I achieve this by integrating my newly established dataset with previously published geochronology-thermochronology constraints to elucidate rock cooling patterns and create a topographic development history of the region.

The new geochronology-thermochronology ages produced by this study elucidate the prolonged and complex topographic development history of the Talkeetna Mountains and

provide insight into the Cenozoic tectonic evolution history of southern Alaska. The new ages from this study will greatly benefit the southern Alaska tectonics community and geologic researchers in their pursuit of understanding the natural processes that have shaped the many mountain ranges that span across the region..

This thesis has been submitted to the journal *Geosphere* for publication. Although this project was a collaborative effort, I served as the primary conductor of this research, which included sample collection, sample analysis at the UAF Geochronology Facility, sample preparation for analysis at other labs, and data analysis and interpretation. I was also the primary author of this manuscript. This work benefitted greatly from the input, constructive criticism and guidance I received from my co-authors: Jeffrey A. Benowtiz, Jeffrey M. Trop, Paul B. O'Sullivan, Robert J. Gillis, and Jeffrey T. Freymueller.

Table of Contents

Page

List of Figures

Page

List of Tables

Page

List of Appendices

Page

Cenozoic tectono-thermal history of the southern Talkeetna Mountains, Alaska: Multiple topographic development drivers through time[1]

INTRODUCTION

Intraplate mountain belts are common topographic features located at considerable distances from plate boundaries, for example in central Asia (Mongolian Altai, Cunningham, 2005), Australia (Flinders Ranges, Dyksterhuis and Müller, 2008) and western North America (Rocky Mountains, Kluth and Coney, 1981). Rock samples from intraplate orogens can preserve a record of a region's thermal regime, which is often driven by far-field plate boundary processes.

Highly-coupled flat-slab subduction can drive intraplate orogenesis and the removal of the mantle wedge during flat-slab subduction can cool the regional geothermal gradient (<20° C/km) (e.g. Andean foreland, Dávila and Carter, 2013). The subduction of a buoyant slab that acts as an upward force on the overriding plate can also lead to deformation and the lowering of the region's geothermal gradient far inboard from the subduction trench (e.g. Nazca, Gutscher et al., 2000). Thermal effects from slab windows (e.g. Baja, Michaud et al., 2006), the subduction of active spreading ridges (e.g. Antarctica, Guenthner et al., 2010) and hotspots (Vogl et al., 2014) can produce topography inboard from the trench that is often domal in shape and linked with high (>50° C/km) geothermal gradients (Sakaguchi, 1996).

The distribution of intraplate deformation can be controlled by conditions in the upper-plate, such as continental-scale strike-slip faults that accommodate strain transferred inboard from subduction zones, resulting in complex topographic development histories through time (e.g. Andes, Cunningham, 1993). Discrete regions with significant vertical displacement are also common along strike-slip faults, if the obliquity of the applied stress is high (e.g. Big Bend of the

[1] This thesis has been submitted to the journal *Geosphere* for publication. Co-authors include Jeffrey A. Benowitz, Jeffrey M. Trop, Paul B. O'Sullivan, Robert J. Gillis, and Jeffrey T. Freymueller.

Alpine Fault, New Zealand, Sagar et al., 2016). In these transpressional settings, horizontal motion forces uplift and acts as a fundamental driver of the creation of near-fault topography (Sylvester, 1988).

Plate convergence can be partitioned onto pre-existing inboard structures via linkages between transform and intraplate strike-slip faults (Bowman et al., 2003). Oblique plate motion can also be partitioned onto pre-existing and rheologically weak intraplate faults resulting in significant amounts of horizontal and vertical displacement (Storti et al., 2003). These structures are often lithospheric heterogeneities separating crustal blocks of differing strength and hence with a differing resistance to deformation (Fitzgerald et al., 2014). Given the polyphase slip histories of many continental strike-slip faults (Betka et al., 2017) and the long-lived and complex histories of convergent margins (Z. Li et al., 2012), inboard mountain ranges may record prolonged mountain building under changing convergent margin processes. Hence, more case studies are needed of intraplate mountain ranges that ostensibly formed during modern plate configurations to understand if there is a paleotopographic component and a potentially inherited thermal regime from a previous tectonic event.

The Talkeetna Mountains of south-central Alaska are positioned more than 350 km inboard from the Pacific-North American plate boundary (Fig. 1). Today the Talkeetna Mountains completely overlay the subducted portion of the Yakutat microplate, a buoyant oceanic plateau that has been undergoing flat-slab subduction with southern Alaska since Late Oligocene time (Figs. 1 and 2) (Benowitz et al., 2011; 2014; Lease et al., 2016). The range is also believed to have experienced Eocene slab window magmatism (Cole et al., 2006). The active transpressive Castle Mountain Fault (CMF), which is thought to have formed as early as the Late Cretaceous (Bunds, 2001), defines the southern border of the Talkeetna Mountains (Fig.

1) (Parry et al., 2001; Haeussler et al., 2002). This spatial relationship suggests that vertical tectonics along the CMF may have contributed to the development of the Range (Fuchs, 1980; Clardy, 1974; Trop et al., 2003). For these reasons, the Talkeetna Mountains are an excellent location to study how long-lived and diverse convergent margin processes drove intraplate orogenesis in a region with pre-existing structures (Trop and Ridgway, 2007).

In order to better understand the tectonic history of this region, we have applied $^{40}Ar/^{39}Ar$ (whole rock, hornblende, muscovite, biotite and K-feldspar), apatite fission track, and apatite (U-Th)/He thermochronology to bedrock samples collected from transects along and across the strike of the CMF and along vertical profiles throughout the glaciated high peak region of the southern Talkeetna Mountains. The specific objectives of this study are to: 1) determine if the Talkeetna Mountains are primarily a paleotopographic expression of an earlier phase of tectonism and if the production of topography was driven by a Paleocene-Eocene plate boundary event prior to the current Late Oligocene to present Yakutat flat-slab plate configuration, or conversely, 2) determine if Late Oligocene to present subduction of the Yakutat microplate primarily drove topographic development in the Range, 3) test the model of a west-east time-transgressive sweep of Paleocene-Eocene volcanism driven by spreading ridge subduction, similar to that expressed in the accretionary prism (described below) and 4) better understand the role of the CMF in the construction of the Talkeetna Mountains.

Our $^{40}Ar/^{39}Ar$ and fission track results suggest that the Talkeetna Mountains are in part residual topography that formed in response to a Paleocene-Eocene thermal event, as proposed for the western Alaska Range (Fig. 1) (Benowitz et al., 2012a). A compilation of new and regional thermochronology and dating of volcanics shows no west-east progression in the timing of initiation of Paleocene-Eocene exhumation or magmatism, which is inconsistent with the

current diachronous spreading ridge subduction model. Finally, (U-Th)/He thermochronology suggests there has been ~2-3 km of vertical displacement along the CMF since Miocene time in response to flat-slab subduction of the Yakutat microplate which has also contributed to the creation of topography.

Southern Alaska and Talkeetna Mountains Tectonic Framework

Mesozoic Plate Boundary History

Southern Alaska's plate boundary (Fig. 1) has been dominated by convergent margin tectonics since at least the Triassic (Amato et al., 2007), including accretion of numerous allochthonous terranes during Jurassic-Cretaceous time (Plafker and Berg, 1994; Nokleberg and Richter, 2007; Trop and Ridgway, 2007) and subduction of an oceanic spreading ridge during Cretaceous time (~125 Ma, Amato et al., 2010).

Paleomagnetism studies of rocks from the Wrangellia Composite Terrane (WCT) of southern Alaska, located south of the Denali Fault and north of the Border Ranges Fault system (Fig. 1), suggest that during the Late Cretaceous (~80 Ma), the region was positioned at a paleolatitude ~15° to the south of its current location (Stamatakos et al., 2001). Northward displacement of the WCT is inferred to have occurred along structures such as the Denali Fault and Tintina Fault systems, which accommodated at least ~1,000 km of combined dextral slip based on offset geologic features (Denali Fault: Lowey, 1998, Benowitz et al., 2012b; Tintina Fault: Tempelman-Kluit and Wanless, 1975; Gabrielse, 1985). The WCT was near its present-day latitude by ~40-54 Ma judging from paleomagnetic constraints from southern Talkeetna Mountain Eocene lava flows (Panuska et al., 1990).

Kula-Resurrection Spreading Ridge Subduction Hypothesis

The Early Cenozoic history of southern Alaska is unclear. It has been proposed that during Late Paleocene-Eocene time, southern Alaska experienced diachronous subduction of the active Kula-Resurrection oceanic spreading ridge (Fig. 2A) (Bradley et al., 1992; 2007; Haeussler et al., 2003). The Kula-Resurrection ridge is interpreted to have subducted at an oblique angle and along an eastward sweeping trajectory in a sub-parallel motion with respect to the paleo-trench (Farris and Paterson, 2009). This model stems chiefly from a ~2,000 km-long string of near-trench plutons, the Sanak-Baranof belt, in the accretionary prism (Figs. 1 and 2A) that show an eastward progression in the timing of magmatism from ~63 Ma to ~47 Ma. Many other datasets also document a regional ~63-47 Ma "near-trench" thermal event within the prism, including high-temperature/low-pressure metamorphism, mafic underplating, extensive fluid circulation, and rapid exhumation/erosion (e.g., Haeussler et al., 1995; Kusky et al., 1997; Lytwyn et al., 2000, Pavlis and Sisson, 2003; Clendenen et al., 2003; Kusky et al., 2003; Roeske et al., 2003; Sisson et al., 2003; Farris et al., 2006; Farris and Paterson, 2009; Scharman et al., 2012; Gasser et al., 2011).

However, the Sanak-Baranof near-trench magmatic belt may have been positioned ~1,000 km to the south along the western margin of North America ~63 Ma to ~47 Ma and subsequently translated to its current location by the Late Eocene along orogeny-parallel faults such as the Border Ranges Fault System (BRFS) (Cowan, 2003; Garver and Davidson, 2015; Davidson and Garver, 2017). This competing model is based in part on a paleomagnetism study by Bol et al. (1992) and detrital zircon studies by Garver and Davidson (2015) and Davidson and Garver (2017). If this is the case, then a relatively stationary Paleocene-Eocene slab window or

other thermal perturbation (hot spot?) that led to the Sanak-Baranof belt formation occurred ~1,500 km to the south as the overlying plate was translated to the north (Cowan, 2003).

Similarly, the WCT was translated northward, but likely to a lesser extent, along the Tintina and Denali Fault systems during this time interval before reaching its present latitude by ~54-40 Ma (Gabrielse, 1985; Stamatakos et al., 2001; Panuska et al., 1990). Thus, the WCT presently located in interior south-central Alaska north of the BRFS may or may not have been impacted by the inferred sweeping Resurrection-Kula spreading ridge responsible for the ~63-47 Ma Sanak-Baranof belt (Haeussler et al., 2003; Davidson and Garver et al., 2017).

There is compelling evidence for a widespread Paleocene-Eocene thermal event that drove rapid rock cooling (e.g. Yukon-Tanana, Dusel-Bacon and Murphy, 2001; western Alaska Range, Benowitz et al., 2012a; Saint Elias Range, Enkelmann et al., 2017), thermal resetting (Finzel et al., 2016), basin subsidence and inversion (Ridgway et al., 2012; Kortyna et al., 2013) and widespread volcanism (Cole et al., 1999; 2006; 2007). The competing hypotheses for Paleocene-Eocene spreading ridge subduction and associated diachronous slab window evolution beneath southern Alaska and conversely variable large strike-slip translation of terranes during this time-period predict different thermal regimes for the upper plate in southern Alaska north of the BRFS. For the case of ridge subduction with minimal strike-slip displacement (<500 km) between the accretionary prism and region north of the BRFS since ~63-47 Ma, there should be a rock record of west to east and south to north progressions of the initiation of thermal events. A lack of any west to east or south to north patterns would favor a tectonic model in which interior Alaska was not impacted by a hypothesized spreading ridge that emplaced near-trench plutons in the prism and may be offset from the adjacent prism by significant dextral displacement (>500 km). The understudied Talkeetna Mountains are situated in the upper plate north of the BRFS

within the region where many previous studies have been conducted, therefore we can integrate previously published geochronology-thermochronology constraints to test these competing hypotheses.

Flat-Slab Subduction of the Yakutat Microplate

Since the Late Oligocene, the primary driver of orogenic processes in southern Alaska has been the ongoing highly-coupled flat-slab subduction of the Yakutat microplate, a ~15 to ~30 km thick, buoyant oceanic plateau (Fig. 2B) (Worthington et al., 2012). The Yakutat flat-slab extends ~350 km inboard before the dip angle increases (Eberhart-Phillips et al., 2006) and this has been suggested to cause the almost complete gap in magmatism between the Aleutian and Wrangell Arcs (Finzel et al., 2011; Trop et al., 2012). Active transpressional fault systems across southern Alaska accommodate the oblique convergence of the Yakutat flat-slab, resulting in numerous regions of deformation far inboard from the trench interface (Haeussler, 2008; e.g. Denali Fault, Benowitz et al., 2014).

It has been proposed that the topographic development of the Talkeetna Mountains coincided with the flat-slab subduction of the Yakutat microplate (Figs. 1 and 2B) (Hoffman and Armstrong, 2006; Finzel et al., 2011). This is primarily based on the modern position of the Range over the subducted portion of the flat-slab and Miocene Talkeetna Mountain AHe bedrock cooling ages (e.g. Arkle et al., 2013) and enhanced sediment accumulation rates and sediment delivery from bedrock sources exhumed above the flat-slab region (Cook Inlet and Tanana basins; Ridgway et al., 2007; Finzel et al., 2011; 2016).

Jadamec et al. (2013) used three-dimensional numerical models to test if the deformational patterns across southern Alaska can be explained by the modern plate configuration (Fig. 3A). The models produce results that match most of Alaska's modern

topography. However, in the Talkeetna Mountains region they do not predict a topographic high, but rather a basin (Figs. 3A and B). The models suggest that basins correlate to where the slab dip-angle increases and separates from the overriding plate, dynamically pulling down the overlying crust (Fig. 3B). The existence of the Talkeetna Mountains contradicts the models of Jadamec et al. (2013) unless most of the topographic relief pre-dates the modern configuration, which would suggest that the modern plate configuration is not the dominant control of topography in the range.

The Jadamec et al. (2013) modeling includes a rheologically weak zone where the Denali Fault is and correctly predicts topographic construction in the Alaska Range along this strike-slip structure. Conversely, this model does not account for the existence of the CMF and its potential for focusing deformation and vertical displacement, which may explain its failure to predict the Talkeetna Mountains. Therefore, the possibility of topographic development due to vertical tectonics along the CMF is not eliminated by these models, if the CMF is also a rheologically weak zone, as argued by Bunds (2001).

A cross section of seismicity from the Aleutian trench to interior Alaska displays the flat-slab subduction of the Yakutat microplate under the North American plate (Fig. 4A) and highlights the significant active structural elements such as the Denali Fault, which is clearly shown as a crustal scale feature (Fig. 4B). The Yakutat slab dips sub-horizontally until it reaches the Talkeetna Mountains region, where the dip angle dramatically increases to ~55°. Beneath the Talkeetna Mountains, seismicity appears to be diffuse and the CMF does not appear to display significant seismicity compared to the area immediately to the north. The limited shallow seismicity and the imaged depth of the down going Yakutat slab suggests that the interacting plates are not highly coupled and that the buoyant slab is not acting as an upward force on the

crust of the Talkeetna Mountains. Given this framework, we can use thermochronology to test if the Talkeetna Mountains reflect a paleotopographic contribution that formed during a previous tectonic event and the role, if any, of the CMF in the region's topographic development history.

The Castle Mountain Fault

The sub-vertical CMF extends ~250 km along the southern border of the Talkeetna Mountains without any obvious restraining or releasing bends and ends in a horsetail splay at the eastern end of the range (Figs. 1 and 5). The CMF separates denser rocks to the south from less dense rocks to north (Mankhemthong et al., 2013) and these strength heterogeneities may play a role in where deformation is focused along the fault zone. This fault zone is also rheologically weaker than the crust surrounding it and accommodates strain transferred inboard from the plate margin (Bunds, 2001). Approximately 130 km of Cenozoic horizontal displacement has been suggested along the CMF (Trop et al., 2005; Pavlis and Roeske, 2007). Willis et al. (2007) provide a commonly referenced Holocene horizontal slip-rate estimate along the western portion of the CMF at ~2-3 mm/yr based on an offset postglacial outwash channel, although this slip-rate may decrease significantly to the east where slip is likely being partitioned into an oblique component. Fuchs (1980) suggested a post-Eocene slip-rate of ~0.5 mm/yr based on field mapping observations and finite-element models by Kalbas et al. (2008) suggested a Holocene rate of ~1 mm/yr. Conversely, lidar-based geomorphic studies along the western segment of the CMF suggest a much diminished Holocene dextral slip rate (<0.3 mm/yr) and vertical motion at a rate of ~0.5 mm/yr (Koehler et al., 2012). The vertical displacement history along the CMF is not well constrained; regional mapping studies document up to 3 km of Neogene vertical slip based on offset Jurassic to Paleogene strata (Grantz, 1966) but detailed cross-sections have not been reported. South of our study area, the structure dips steeply to the north and accommodated

north-side up vertical displacement, which may contribute to the topographic break between the Talkeetna Mountains to the north and the Matansuka Valley to the south. We apply thermochronology to rocks collected from transects along and across the CMF to document rock cooling patterns and the role of this structure in regional deformation patterns.

Geology of the Talkeetna Mountains

The Talkeetna Mountains are bordered to the west by a Cenozoic intraplate and forearc composite basin (Susitna Basin) and to the east and south by remnant Cenozoic forearc basins (Copper River Basin and Matanuska Valley Basin respectively) (Fig. 2B) (Trop and Ridgway, 2007; Stanley et al., 2014). The sub-vertical Talkeetna Fault bisects the Range and acts as a lithospheric terrane boundary between the WCT and the Alaska Range Suture Zone (ARSZ) (Fig. 1) (Brennan et al., 2011). North of the Talkeetna Fault, the ARSZ primarily consist of a ~3 to ~5 km thick package of Kahiltna Basin marine meta-sedimentary strata that were subaerially uplifted during the Mesozoic WCT collision (Ridgway et al., 2002; Hampton et al., 2010). South of the Talkeetna Fault, the region of focus for this study, large batholiths intruding the WCT represent the Late Triassic-Early Jurassic Talkeetna Arc, which was emplaced in this region from ~183-153 Ma (Hacker et al., 2011). A series of Late Jurassic trondhjemite plutons intrude the interior Talkeetna Mountains and constitute Mount Sovereign, the highest peak in the Range (~2,700 m) (Fig. 5) (Rioux et al., 2007). The erosion-resistant nature of these plutonic bodies and the mafic crust of the WCT relative to the Kahiltna Basin rocks may explain the difference in relief between the northern and southern regions of the Range; further research in the northern Talkeetna Mountains is planned in part to test this hypothesis.

Overall, the structural configuration of the southern Talkeetna Mountains is not well constrained. Approximately NW-SE striking extensional fault systems bisect the region of the

Caribou Creek volcanic field and Willow Creek mining district in the Hatcher Pass region (Fig. 5) (Cole et al., 2006; Harlan et al., 2017). These extensional faults are thought to have been active during a period of Paleocene-Eocene volcanism in the Caribou Creek volcanic field and regional Paleocene-Eocene crustal extension (Cole et al., 2006). Faults also appear to partially bound the the high peak region of the southern Talkeetna Mountains, established by the Jurassic trondhjemite pluton (Fig. 5), suggesting that the region may have exhumed as an independent crustal block. A series of meso-scale folds and reverse faults deform Paleocene-Eocene strata exposed within ~10 km of the CMF, recording post ~50 Ma shortening along the CMF (Bartsch-Winkler and Schmoll, 1992; Kassab et al., 2009; Robertson, 2015).

Cenozoic Thermal History of Southern Alaska

Southern Alaska has experienced a complex thermal history that has not been well constrained. The varied convergent margin configurations the region has undergone suggests that the thermal regime of southern Alaska has changed throughout the Cenozoic (Riccio et al., 2014; Lease et al., 2016). Thermochronology in the western Alaska Range (Fig. 1) shows evidence for a higher than normal geothermal gradient (>50 °C/km) (Benowitz et al., 2012a) during Eocene times, suggesting that high heat flow and the injection of magma into the upper crust, contributed to regional mountain building. Finzel et al. (2016) also infer a possible high geothermal gradient (>100 °C) across southern Alaska during the Paleocene-Eocene based on reset detrital zircon fission track ages from Cretaceous-Cenozoic strata. This anomalously high geothermal gradient event likely extended across southern Alaska and persisted for ~20 million years (O'Sullivan et al., 1996; Cole and Stewart, 2009). However, it is not known when the modern thermal regime was emplaced.

The southern Talkeetna Mountains are thought to occupy a region that was subjected to elevated heat flow above a migrating slab window to the asthenosphere and was subsequently cooled from flat-slab subduction of the Yakutat microplate (Cole et al., 2006; Finzel et al. 2011). Therefore, the regional rock record should register a marked shift in its thermal structure through time and space. The basis for this inference is a package of Eocene volcanic rocks which have been linked to a Paleocene-Eocene spreading ridge subduction event (Fig. 5) (Cole et al., 2006; Bradley et al., 2007; Cole and Stewart, 2009), and the current position of the range over the subducted portion of the Yakutat microplate (Fig. 1). The Talkeetna Mountains Jurassic trondhjemite plutons have been intruded by mafic dikes and K-feldspar rich fluids (Fig. 6 P1, P2 and P3) (see results section), providing additional evidence for a regional thermal event. Currently there are no active hot spring systems in the region, however there are abundant outcrops displaying hydrothermal alteration, especially within the trondhjemite plutons (Fig. 6 P3). Spatially the Talkeetna Mountains are located ~300 km from presently active arcs (Fig. 1) so the region's thermal history has not been overprinted by modern volcanism. The juxtaposition of mafic volcanic and granitoid rocks makes the setting optimal for thermochronological analyses on multiple minerals in both plutonic rocks (e.g. hornblende, muscovite, biotite, K-feldspar; AFT, AHe) and volcanic rocks (whole rock) and alteration minerals (e.g. sericite) allowing for exploration of the region's thermal evolution from ~450°C to 0°C (modern annual surface temperature) (Reiners and Brandon, 2006).

Previously published low-temperature thermochronology data in the region, which has generally been focused in the southernmost region of the Talkeetna Mountains near the CMF (Little and Naeser, 1989; Parry et al., 2001; Hoffman and Armstrong, 2006; Hacker et al., 2011; Bleick et al., 2012), indicate temporal-spatial variability in the timing of Talkeetna Mountains

rock cooling and exhumation. AFT ages in the Hatcher Pass Region (Figs. 5 and 7) record Paleocene-Eocene structural and erosional exhumation (Bleick et al., 2012). Miocene AHe ages near the CMF are indicative of a more recent rock cooling and exhumation event in the southern Talkeetna Mountains (Hoffman and Armstrong, 2006). Younger (~16-22 Ma) AFT ages south of the CMF suggest exhumation coincided with the highly-coupled flat slab subduction of the Yakutat microplate (Little and Naeser, 1989; Hoffman and Armstrong, 2006). However, little low-temperature thermochronology data is available in the high peak region of the Talkeetna Mountains and previously published ages were not collected in a way that could elucidate age-elevation relationships, thermal resetting, or a CMF structural control on cooling age patterns.

Overall, this study utilizes a multi-thermochronometer and geochronological approach applied to bedrock samples collected between the Talkeetna Fault and the CMF and one sample south of the CMF, combined with previously published results (Hacker et al., 2011; Bleick et al., 2012; Arkle et al., 2013), to constrain rock cooling histories. Our results provide insight into the Cenozoic topographic development history of the southern Talkeetna Mountains, Cenozoic evolution of the region's thermal regime and how strain is partitioned onto pre-existing structures during multiple convergent margin configurations. Our results also have broader implications for the tectono-thermal evolution of southern Alaska.

METHODS

Sampling Strategy

We use a range of geochronology ($^{40}Ar/^{39}Ar$ on whole rock volcanics) and thermochronology techniques ($^{40}Ar/^{39}Ar$: hornblende, muscovite, K-feldspar, biotite, apatite fission track (AFT) and apatite (U-Th)/He) (AHe)) to constrain regional patterns of volcanism and time-temperature histories for rock samples in our study area (Fig. 7). In order to discern

regional cooling age patterns with respect to the CMF and with elevation, our sampling strategy included bedrock sampling transects along and across strike of the CMF and over a substantial portion of the high peak region of the Talkeetna Mountains (Fig. 7) (Spotila, 2005). We also conducted two vertical profiles collecting bedrock samples every ~100 m over a ~1,300 m vertical distance: One vertical profile along Mount Sovereign (~2,700 m) and one along a peak off the Sheep Glacier (~2,250 m), referred to herein as Sheep Mountain (Fig. 5). The bulk of our samples were collected within a large Jurassic trondhjemite pluton and a Jurassic granite pluton (Fig. 5). Sample 01Chic is a meta-basalt collected in the CMF zone (Fig. 7). One tonalite sample was collected south of the CMF (05King). We collected samples at different distances from Eocene volcanic intrusions on the outskirts of the Jurassic trondhjemite pluton (Fig. 6 P5 and P6) to test for thermal resetting. We also sampled volcanic rocks representing 5 different phases of magmatism at a minimum distance of ~5 m from sample 01Sov (Figs. 6 and 7) to further test for thermal resetting. We integrated our ages with existing thermochronology (Silberman and Grantz, 1984; Little and Naeser, 1989; Parry et al., 2001; Cole et al., 2006; Hoffman and Armstrong, 2006; Hacker et al., 2011; Bleick et al., 2012; Arkle et al., 2013) to constrain the Cenozoic exhumation and magmatic history of the range.

Geochronology-Thermochronology Techniques: $^{40}Ar/^{39}Ar$

$^{40}Ar/^{39}Ar$ geochronology-thermochronology was performed at the University of Alaska Fairbanks Geochronology Facility on hornblende (05King), muscovite (01Sov, 03Sov, 13Sov), sericite (01Red), biotite (13Sov), K-feldspar (01Sov, 03Sov) and whole-rock volcanics (samples 01Sov, 02Sov, 14Sov). Samples were crushed, sieved for the 250-1000 μm grain size, washed and underwent heavy liquids, magnetic and hand picking mineral separation techniques. Samples were analyzed on a VG-3600 mass spectrometer using laser step heating techniques described in

Benowitz et al. (2014). Dating multiple minerals in the same sample provides information about a rocks thermal history from ~150-450°C. Whole rock volcanic ages provide information about the timing of magmatism and diking.

The monitor mineral MMhb-1 (Samson and Alexander, 1987) with an age of 523.5 Ma (Renne 1994) was used to monitor neutron flux (and calculate the irradiation parameter, J). The 45 mineral separates and standards were wrapped in aluminum foil and loaded into aluminum cans of 2.5 cm diameter and 6 cm height. The samples were irradiated in position 5c of the uranium enriched research reactor of McMaster University in Hamilton, Ontario, Canada for 20 megawatt-hours.

Upon their return from the reactor, the sample and monitors were loaded into 2 mm diameter holes in a copper tray that was then loaded into an ultra-high vacuum extraction line. The monitors were fused, and samples heated, using a 6-watt argon-ion laser following the technique described in York et al. (1981), Layer et al. (1987) and Layer (2000). Argon purification was achieved using a liquid nitrogen cold trap and a SAES Zr-Al getter at 400C. The samples were analyzed in a VG-3600 mass spectrometer at the Geophysical Institute, University of Alaska Fairbanks. The argon isotopes measured were corrected for system blank and mass discrimination, as well as calcium, potassium and chlorine interference reactions following procedures outlined in McDougall and Harrison (1999). Typical full-system 8 min laser blank values (in moles) were generally 2×10^{-16} mol ^{40}Ar, 3×10^{-18} mol ^{39}Ar, 9×10^{-18} mol ^{38}Ar and 2×10^{-18} mol ^{36}Ar, which are 10–50 times smaller than the sample/standard volume fractions. Correction factors for nucleogenic interferences during irradiation were determined from irradiated CaF_2 and K_2SO_4 as follows: $(^{39}Ar/^{37}Ar)Ca = 7.06 \times 10^{-4}$, $(^{36}Ar/^{37}Ar)Ca = 2.79 \times 10^{-4}$ and $(^{40}Ar/^{39}Ar)K = 0.0297$. Mass discrimination was monitored by running calibrated air

shots. The mass discrimination during these experiments was 1.3 % per mass unit. While doing our experiments, calibration measurements were made on a weekly to monthly basis to check for changes in mass discrimination with no significant variation seen during these intervals.

A summary of all the $^{40}Ar/^{39}Ar$ results is given in Table 1, with all ages quoted to the ± 1 sigma level and calculated using the constants of Renne et al. (2010) and detailed isotopic tables and in figures in Appendix A and Appendix B. The integrated age is the age given by the total gas measured and is equivalent to a potassium-argon (K-Ar) age. The spectrum provides a plateau age if three or more consecutive gas fractions represent at least 50% of the total gas release and are within two standard deviations of each other (Mean Square Weighted Deviation less than or equal to 2.5).

The K-feldspar age spectra for samples 01Sov and 03Sov (Fig. 8) are interpreted using multidomain diffusion modelling (Lovera et al., 2002) to understand their thermal histories. Instead of performing diffusion experiments, we look at the timing of closure of the high temperature (~350°C) and low temperature (~150°C) domains for K-feldspar (Benowitz et al., 2012a; Löbens et al., 2017).

Thermochronology Techniques: Apatite Fission Track

Under typical continental geothermal gradients, AFT thermochronology provides information about the thermal history of a rock sample in the upper ~3-5 km of the crust (Dodson, 1973). This technique involves analysis of the damage tracks formed by the spontaneous fission of ^{238}U (Tagami and O'Sullivan, 2005). Depending on the apatite grain composition and cooling rate, fission tracks will partially anneal at temperatures >60°C and completely anneal at temperatures >120°C. This temperature window is referred to as the partial annealing zone (PAZ). The temperature sensitivity of fission tracks allows for analysis of a rock

sample's thermal history by measuring track lengths; shorter tracks indicate a longer residence time in the PAZ (60-120°C) and a relatively slower cooling rate (Donelick et al., 2005). Track length distributions that include both long and partially annealed tracks indicate more complex thermal histories. For this study, AFT analyses were performed on 20 samples. Age and track length information is reported in Table 2 and AFT analytical data is reported in Table 3.

Apatite separates for all samples were obtained from crushed and separated material using standard gravimetric and magnetic mineral separation techniques. Apatite grain mounts were prepared by Paul O'Sullivan at the GeoSep Services (GSS) facilities in Moscow, Idaho. Spontaneous track counts and confined track length measurements were performed by Paul O'Sullivan using nonpolarized light at 2000x magnification. Laser ablation–inductively coupled plasma–mass spectrometer (LA-ICP-MS) analyses of samples used in age determinations were performed using the Element2 mass spectrometer located at the Washington State University School of Earth and Environmental Sciences GeoAnalytical Laboratory in Pullman, Washington.

A general discussion of the methods undertaken to process and analyze samples by GSS is presented below; see Donelick et al. (2005) for a complete and detailed discussion of these methods and their justification. For each sample subjected to apatite fission-track analysis (AFT), at least one $1cm^2$ grain mount, consisting of apatite grains immersed in epoxy resin, was prepared, cured at 90°C for 1 hour, and polished to expose internal surfaces of the apatite grains. After polishing, mounts were immersed in 5.5N HNO_3 for 20.0 seconds (± 0.5 seconds) at 21°C (± 1°C) to reveal all natural fission tracks that intersected the polished grain surfaces.

The feasibility of measurement of apatite fission-track grain ages and track lengths was assessed by scanning the polished and etched grain mount to determine if any dateable apatite

grains were present. Measurement of fission-track parameters was considered feasible if more than one dateable grain was observed.

Representative kinetic parameters (*D*par—the maximum diameter of fission track etch pits at their intersection with the polished and etched, c-axis-parallel apatite surface, which is used as a proxy for the solubility of fission tracks in their host apatite grains) were measured and spontaneous (natural) fission-track densities were counted for each grain considered suitable for dating. Between one and four etch pit diameters were measured and an arithmetic mean *D*par value was calculated for each datable grain.

LA-ICP-MS U, Th, Sm Analysis

Grains were then revisited using the LA-ICP-MS to make spot analyses to determine U, Th, and Sm concentrations of each grain for which natural fission-track densities had been previously determined. A single stationary spot of 16 μm diameter was used for each grain, centered in the approximate center of the area where tracks had been counted. Note that if optical examination suggested that natural track densities were even moderately inconsistent within a grain, which is evidence of U zoning, that grain was not dated.

For apatite, the fundamental assumption is made that Ca occurs in stoichiometric amounts in all grains analyzed. The isotope ^{43}Ca is used as the indicator of the volume of apatite ablated. Samples were ablated in a helium atmosphere to reduce condensation and elemental fractionation. A total of 30 scans for ^{238}U, ^{232}Th, ^{147}Sm, and ^{43}Ca were performed for each spot analyzed. Of these scans, approximately 10 were performed while the laser was warming up and blocked from contacting the grain surface, during which time background counts were collected. Once the laser was permitted to hit the grain surface, a cylindrical pit was excavated to a depth beyond which uranium did not contribute fission tracks to the etched grain surface. Between 15

and 20 scans performed during pit excavation were required to reach this depth. The depths of a representative number of laser pits were measured and the $^{238}U/^{43}Ca$ value for each pit as a whole was determined based on the weighted mean of the $^{238}U/^{43}Ca$ value for individual scans relative to the depths from which the ablated material was derived (see Hasebe et al. 2004; Donelick et al. 2005).

Fission Track Age Measurement

Fission-track ages and errors were calculated using: (a) the ratio of the density of natural fission tracks present in the grain to the amount of ^{238}U present and (b) a modified version of the radioactive decay equation that includes a LA-ICP-MS zeta calibration factor (see equations 1b for age equation and 2b for error calculation in Donelick et al. 2005). The zeta calibration factor is determined for each sample analyzed during each LA-ICP-MS session by analyzing the U:Ca ratio of apatite calibration standards with known ages at the beginning and end of each LA-ICP-MS session. The standard used was Durango apatite, 30.6 ± 0.3 Ma.

Calculation of a single pooled AFT age for each sample takes into account the distribution of all of the individual grain ages and their uncertainties, which are a function of the number of spontaneous tracks counted over a known area, the U content determined by LA-ICP-MS, and thermal history. Only pooled ages are reported as these incorporate original track counts and isotopic values for each grain, and therefore are most representative of the original data generated for each sample, even when multiple grain-age populations might be present as suggested by the Chi^2 value.

Apatite Fission Track Length Measurement

In order to enhance the number of confined tracks available for length measurement (e.g., Donelick and Miller 1991; Donelick et al. 2005), subsequent to fission-track age determination

the grain mounts were irradiated with approximately 10^7 tracks/cm^2 fission fragments from a ^{252}Cf source in a vacuum chamber. Donelick and Miller (1991) demonstrated that irradiating apatite grains with ^{252}Cf-derived fission fragments could yield a 20-fold increase in the number of available fission tracks for length measurement. The ^{252}Cf-irradiated apatite mounts were re-etched using the same formula as before in order to reveal horizontal, confined fission tracks within the apatite grains. Only natural, horizontal, confined fission tracks in apatite with clearly visible ends were considered candidates for length measurement. The length and crystallographic orientation of each fission track were determined using a digitizing tablet interfaced with a personal computer. The precision of each track length is estimated to be ±0.20 μm; the precision of each track angle to the crystallographic c-axis is estimated to be ±2 degrees.

Thermochronology Techniques: Apatite (U-Th)/He

(U-Th)/He thermochronology involves the analysis of alpha particles (^{4}He) accumulated in a mineral due to the radioactive decay of Uranium and Thorium (Reiners and Brandon, 2006). With a nominal closure temperature of 55-80°C, apatite (U-Th)/He thermochronology (AHe) provides information about the thermal history of a rock sample in the upper ~2-4 km of the crust (Farley, 2002). The closure temperature of an apatite grain varies depending on the grain size, cooling rate and radiation damage accumulated in the crystal lattice (Reiners and Farley, 2001). In addition, ^{4}He particles travel ~20 microns from their parent atoms during radioactive decay, resulting in the ejection of ^{4}He produced near the edge of a grain, requiring corrections (Ketcham, 2007).

(U-Th)/He analyses were performed by the University of Colorado Thermochronology Research and Instrumentation Lab (CU TRaIL). Individual mineral grains were handpicked using a Leica M165 binocular microscope equipped with a calibrated digital camera and capable

of both reflected and transmitted, polarized light. The grains were screened for quality, including crystal size, shape, and the presence of inclusions. After characterization, grains were placed into small Nb tubes that are then crimped on both ends. This Nb packet was then loaded into an ASI Alphachron He extraction and measurement line. The packet is placed in the UHV extraction line (~3 X 10^{-8} torr) and heated with a 50W diode laser to ~800-1100°C for 5 to 10 minutes to extract the radiogenic ^{4}He. The degassed ^{4}He was then spiked with approximately 13 ncc of pure ^{3}He, cleaned via interaction with two SAES getters, and analyzed on a Balzers PrismaPlus QME 220 quadrupole mass spectrometer. This procedure was repeated at least once to ensure complete mineral degassing. Degassed grains were then removed from the line and taken to a Class 10 clean lab for dissolution. Apatite grains, still enclosed in the Nb tubes, were placed in 1.5 mL Cetac vials, spiked with a ^{235}U - ^{230}Th – ^{145}Nd tracer in HNO_3, capped, and baked in a lab oven at 80°C for 2 hours. Once the minerals were dissolved, regardless of the dissolution process, they were diluted with 1 to 3 mL of doubly-deionized water, and taken to the ICP-MS lab for analysis. Sample solutions, along with normal solutions and blanks, were analyzed for U, Th, and Sm content using an Agilent 7900 Quadrupole inductively-coupled plasma mass spectrometer equipped with an inert sample introduction system. Once the U, Th, and Sm contents had been measured, He dates and all associated data were calculated on a custom spreadsheet made by CU TRaIL staff using the methods described in Ketcham et al. (2011). Every batch of samples includes standards run sporadically throughout the process to monitor procedures and maintain consistency from run to run.

12 AHe ages were determined for this study on 4-7 grains for each rock sample. Ft corrections were applied to raw ages to correct for alpha particle ejection effects (Farley, 2002). Single grain outliers, which were significantly older or younger than the mean age of grains in a

that sample, were found in 3 analyses. In general, this was due to low concentrations of Uranium or ^{4}He in that particular grain. We excluded these outliers from our pooled age calculations and it did not affect our results or interpretations. Given the natural dispersion for intra-sample single grains in (U-Th)/He ages, we calculated the standard deviation for each sample grain set and applied this as the best approximation of the geologic error for the analysis (Spotila and Berger, 2010). Pooled ages, errors and analytical data are reported in Table 4.

HeFTy Thermal Modelling

Inverse thermal models were created for each of our samples using the program HeFTy (Ketcham, 2007). Using an estimate of the present-day surface temperature and higher-temperature (^{40}Ar/^{39}Ar) thermochronology data as constraints, HeFTy models the time-temperature cooling history of a sample. The program evaluates "best fit" cooling paths and slopes based on input age and AFT track length constraints. We present Monte Carlo method inverse models showing 50,000 acceptable and good cooling paths constrained in envelopes and weighted mean T-t paths. Input constraints for the models include ^{40}Ar/^{39}Ar hornblende (~400-600°C), muscovite (~400-425°C), biotite (~250-350°C) and K-feldspar (~180-350°C) ages, AFT data (~60-120°C) (single grain ages, Dpar, track lengths, angle of tracks to the c-axis) and pooled AHe ages (~40-80°C). HeFTy also generates annealing models and AFT track length histograms. These models are supplemented with AFT age-elevation profiles, where distinct slope inflection points are interpreted to mark changing exhumation/rock cooling rates (e.g. Fitzgerald et al., 1993). We evaluate these thermal histories with respect to possible resetting due to dike emplacement at a minimum distance of ~5 m from these samples and potential closure to post emplacement thermal relaxation, exhumation and resetting due to a regional thermal event.

RESULTS AND INTERPRETATIONS

Field Observations

The northeast edge of the Jurassic trondhjemite pluton is characterized by a contact with Paleocene-Eocene volcanic rocks and numerous exhumed lithified volcanic bodies and magma conduits and mafic dikes that intrude into the trondhjemite pluton for ~3 km (Figs. 5 and 6 P1 and P2). The mafic dikes intrude along exfoliation joints in the trondhjemite pluton and are evidence for some degree of unroofing prior to dike emplacement. Approximately 60-50 Ma sedimentary strata locally overlie these Jurassic plutons and volcanic rocks along a prominent nonconformity (Sunderlin et al., 2014; Wilson et al., 2015) requiring significant unroofing prior to emplacement of Eocene dikes. The concentration of dikes significantly decreases moving southwest from sample 03Sov. There are rare dikes diffusely dispersed across the interior trondhjemite pluton such as samples 14Sov and 12Talk (Figs. 5 and 7).

We did not observe any faults in the region of our vertical profiles (Fig. 5), although there are mapped structures that appear to partially bound the edges of the trondhjemite pluton (Fig. 5) (Wilson et al., 2015). Between samples 13Talk and 14Talk there is a distinct ~N-S-striking shear zone consisting of exhumed amphibolite with extensive mineralization and a mapped ~NW-SE striking fault (Figs. 5 and 7). Throughout the trondhjemite pluton, outcrop faces show evidence for fluid infiltration, hydrothermal alteration and subsequent mineralization (Fig. 6 P3 and P4). This is most apparent along the Sheep Mountain profile where sample 01Red was collected (Fig. 7). Here a portion of the trondhjemite pluton has been metasomatized to K-feldspar and sericite-rich rocks (Fig. 6 P4). We observed a mining claim staked in this area, which speaks to the likely extent of the mineralization.

Samples collected for this study outside of the Jurassic trondhjemite pluton (Fig. 5) were rushed spot samples collected via helicopter. Hence, this study does not document any field

relationships outside of the trondhjemite pluton and the region immediately surrounding it. Samples collected outside of the trondhjemite pluton were generally granitoids (01King, 02King, 03King, 05King), but also included a metabasalt collected in the CMF zone (01Chic).

$^{40}Ar/^{39}Ar$ Geochronology and Thermochronology Results

15 $^{40}Ar/^{39}Ar$ ages were produced for this study and are presented below organized by mineral type. Ages are reported at ± 1σ (Table 1). Age spectra are shown for each sample in Figures 8 and 9 (also see Appendix A) and in general are flat, suggesting minimal argon loss. Isochron ages were calculated when possible and are shown in Appendix A and isotopic analytical data is reported in Appendix B.

Hornblende Age

A homogeneous hornblende separate from sample 05King, a tonalite collected from hypabyssal intrusions south of the CMF (unit Jktm on Fig. 5), was analyzed (Fig. 8 and Table 1). The integrated age (59.9 ± 13.5 Ma) and the plateau age (47.6 ± 11.9 Ma.) are within error. We prefer the plateau age of 47.6 ± 11.9 Ma for sample 05King because of the higher atmospheric content of the lower temperature-step heat release. The large uncertainty is likely due to the low K concentration of the hornblende separate.

Mica Ages

Homogeneous muscovite separates from samples 01Sov, 03Sov and 13Sov, trondhjemite samples from unit Jtr (Fig. 5) were analyzed (Figs. 8 and 9 and Table 1). For Sample 01Sov, the integrated age (149.8 ± 0.7 Ma) and the plateau age (149.9 ± 0.6 Ma) are within error. For sample 03Sov, the integrated age (157.7 ± 0.9 Ma) and the plateau age (157.9 ± 0.9 Ma) are within error. For sample 13Sov, the integrated age (148.9 ± 1.2 Ma) and the plateau age (150.2 ± 1.2 Ma) are within error. We prefer the plateau ages of 149.9 ± 0.6 Ma (01Sov), 157.9 ± 0.9 Ma

(03Sov) and 150.2 ± 1.2 Ma (13Sov) because of the high atmospheric content of the low temperature step heats.

A homogeneous biotite separate from sample 13Sov was analyzed (Figs. 8 and 9 and Table 1). The integrated age (148.2 ± 0.6 Ma) and the plateau age (148.7 ± 0.6 Ma) are within error. We prefer the plateau age of 148.7 ± 0.6 Ma because of the high atmospheric ^{40}Ar content of the low temperature step heat. The time between closure of the muscovite and biotite mineral systems in sample 13Sov is ~1.5 Ma (Fig. 9).

A homogeneous sericite separate from sample 01Red, collected in unit Jtr (Fig. 5), was analyzed (Fig. 8, Table 1). The integrated age (102.8 ± 1.2 Ma) and the plateau age (99.1 ± 0.9 Ma) are not within error. We prefer the plateau age of 99.1 ± 0.9 Ma because of the anomalously older age for the lowest temperature step heat.

K-feldspar Ages

Homogenous K-feldspar separates from samples 01Sov and 03Sov were analyzed (Figs. 8 and 9 and Table 1). For sample 01Sov the age spectrum is bimodal, suggesting a more complex thermal history. The age spectrum did not meet the criteria for a plateau age (3 consecutive steps) so therefore weighted average ages are reported. The integrated age (163.6 ± 4.4 Ma), maximum weighted average age (86.5 ± 2.5 Ma) and minimum weighted average age (61.0 ± 3.1 Ma) are not within error. We prefer a maximum weighted average age ($KFAT_{max}$) of 86.5 ± 2.5 Ma and a minimum weighted average age ($KFAT_{min}$) of 61.0 ± 3.1 Ma for sample 01Sov. The duration of time between closure of the ~350°C and ~150°C nominal temperature domains for K-feldspar is ~26.5 Ma. The duration of time between closure of the muscovite and the high temperature K-feldspar mineral phases in sample 01Sov is ~63.4 Ma. The age spectrum for sample 03Sov is simpler and suggests a less complex thermal history (Fig. 8). The integrated age

(133.3 ± 2.3 Ma) and the plateau age (124.9 ± 1.8 Ma) are not within error. We prefer the plateau age of 124.9 ± 1.8 Ma for sample 03Sov because of the anomalously older age for the lowest temperature step heat. An isochron age of 129.1 ± 3.2 Ma was determined and is within error of the plateau age. The duration of time between closure of the muscovite and K-feldspar mineral phases in sample 03Sov is ~33 Ma (Figs. 8 and 9).

Whole Rock Ages

Homogenous, phenocryst free whole-rock separates from samples 01Sov (5 different phases of magmatism near to each other), 02Sov and 14Sov, which are mafic dikes intruding the trondhjemite pluton (unit Jtr in Fig. 5), were analyzed (Fig, 8, Table 1). Samples 01Sov and 02Sov are located at the northeast edge of the trondhjemite pluton and while sample 14Sov is located towards its interior (Figs. 5 and 7). The 5 different magmatic phases of sample 01Sov (located at the contact of units Tepv and Jtr in Fig. 5) have plateau ages from ~42.3 Ma to ~46.5 Ma (Fig. 8). 4 of the 5 different magmatic phases have isochron ages of 42.2 ± 0.2, 42.7 ± 1.0, 44.6 ± 0.6 and 44.5 ± 0.5 (See Appendix A). We prefer plateau ages for these samples because of the higher atmospheric content of the lower temperature-step heat releases. For sample 02Sov, the integrated age (46.5 ± 0.5 Ma), plateau age (46.3 ± 0.4 Ma) and isochron age (46.3 ± 0.4 Ma) are all within error. We prefer the plateau age of 46.3 ± 0.4 Ma because of its higher precision. For sample 14Sov, the integrated age (52.6 ± 2.5 Ma), plateau age (52.4 ± 2.5 Ma) and isochron age (49.6 ± 5.8 Ma) are all within error. We prefer the plateau age of 52.4 ± 2.5 Ma because of the anomalously high age of the highest temperature step heat.

Apatite Fission Track Thermochronology Results

20 AFT cooling ages were produced for this study on intrusive rocks (Fig. 7 and Table 2) and are compiled with previously existing AFT cooling ages in the region (Little and Naeser,

1989; Parry et al., 2001; Bleick et al., 2012). We report pooled ages with calculated errors representing the ± 95% confidence interval (2σ) (Table 2). Dpar was measured in most dated grains and average sample Dpar values range from ~1.7-2.7 μm (Table 3). There is no correlation between Dpar values and age (Fig. 10A) or track lengths (Fig. 10B), suggesting similar annealing kinetics for all samples. Confined track length distributions are reported in Appendix C.

North of CMF

17 samples north of the CMF (Fig. 7) have Paleocene-Eocene cooling ages ranging from ~42.6 Ma to ~63.0 Ma (Fig. 11A). The highest elevation sample (13Sov) has a Cretaceous cooling age of ~74.2 Ma (Fig. 11A). Sample 03King was collected within ~5 m of the granite-metamorphic rock contact between units Jgr and PSm (Fig. 5) and has an Oligocene cooling age of ~34.2 Ma. These results agree with other AFT cooling ages north of the CMF from Bleick et al (2012), which are predominantly Paleocene-Eocene. Mean track lengths from our sample set range from 12.9 μm to 14.4 μm (Table 2).

AFT cooling ages in the southern Talkeetna Mountains have two separate cooling domains divided by elevation. Samples located outside of the trondhjemite pluton at lower elevations (less than about 1,500 m) and near the CMF do not have an age-elevation relationship (Fig. 11A). AFT cooling ages from samples collected along vertical profiles of Mount Sovereign and Sheep Mountain have an age-elevation relationship with an inflection point at ~59 Ma that suggests more rapid exhumation after that at a maximum rate of ~188 m/my (Fig. 11B). Samples 06Sov, 10Sov and 12Sov have AFT ages of ~42.6 Ma, ~45.0 and ~51.9 Ma respectively and are distinct outliers from the age-elevation relationship (Fig, 11B). This is likely due to thermal resetting from the injection of hydrothermal fluids during Middle Eocene magmatism based on

field observations of hydrothermal alteration (Fig. 6 P3), new whole rock $^{40}Ar/^{39}Ar$ constraints on Mount Sovereign Eocene magmatism (Fig. 7) and the apparently elevation invariant AHe cooling ages along the same vertical profile (Fig. 11B). This inference of sample variant resetting due to injection of hydrothermal fluids is further discussed below.

Sample 04King has an age of ~44.0 Ma and is not within error of the vertical profile. This sample is located away from the main vertical profile sample cluster (Fig. 7) and across a mapped fault that may be affecting its age (Fig. 5). Sample 03King, the closest sample to 04King, also has a regionally young AFT age of ~34.2 Ma adding credence to the possibility of an unmapped structure in the region. Alternatively, the young age of sample 03King may be due to fluid flow along the unit contact with the metamorphic rocks (Fig. 5).

Conversely, proximity and differential unroofing towards the CMF might be controlling these AFT age-elevation patterns. To test this, we collected 8 samples along a N-S transect approaching the CMF. Their AFT cooling ages (Figs. 7 and 11C) have an apparent pattern of getting younger towards the fault. However, these samples also decrease in elevation moving towards the CMF and the correlation between age and elevation along the same transect is slightly stronger (Fig. 11D), making it more likely that block exhumation along a vertical trajectory (reflected in age-elevation relationships) is the primary control on these cooling age patterns, rather than the proximity to the CMF.

South of CMF

Sample 05King has an AFT cooling age of 31.2 Ma (Figs. 7 and 11A). This result is consistent with regional AFT cooling ages from Little and Naeser (1989) and Parry et al. (2001) who document distinctly younger cooling ages (~21-32 Ma) within and south of the CMF. From this AFT cooling age pattern, we infer that the north side of the CMF did not have a significant

vertical component during the Eocene-Early Oligocene. This is consistent with mapping studies that infer chiefly Neogene vertical displacement across the fault (Grantz, 1966; Fuchs, 1980; Trop et al., 2003).

Apatite (U-Th)/He Thermochronology Results

12 AHe cooling ages were produced for this study on intrusive rock samples collected north of the CMF. Pooled ages and 1σ errors are reported (Table 4) and were calculated following the techniques outlined in the methods section. Sample 05Talk yielded a large spread of individual apatite grain cooling ages (Table 4) that did not meet the parameters to calculate a pooled age and is therefore excluded from our interpretations. AHe cooling ages range from ~10.5 Ma to ~45.3 Ma. These new AHe results were compiled with published ages from Hoffman and Armstrong (2006) and Hacker et al. (2011) and combined show a distinct pattern of ages getting younger approaching the CMF (Fig. 12A). Sample 01King, located directly north of the continuous strand of the CMF is ~42.4 Ma (Fig. 7 and 12C). Sample 02King located north of a splay off of the CMF is ~12.1 Ma. There is no relationship between AHe cooling age and elevation (Fig. 12B). 8 samples along a N-S transect approaching the CMF show a distinct pattern of getting younger towards the Fault (Fig. 12C) and young cooling ages near the CMF suggests there has been exhumation along this structure since at least the Miocene. There is a weak relationship between age and elevation along the same transect (Fig. 12D) adding support to the notion that vertical displacement along the CMF is controlling AHe cooling age patterns.

Cooling Patterns in Time and Space

All the published whole rock $^{40}Ar/^{39}Ar$, AFT and AHe cooling ages, confined to north of the CMF and south of the Talkeetna Fault, were compiled into a normalized probability density plot (Fig. 13) (Silberman and Grantz, 1984; Parry et al., 2001; Cole et al., 2006; Hoffman and

Armstrong, 2006; Oswald, 2006; Hacker et al., 2011; Bleick et al., 2012; Arkle et al., 2013). This plot demonstrates that volcanic ages and intrusive rock cooling ages from these radiometric systems are predominantly Paleocene-Eocene. AHe cooling ages vary from Eocene to Miocene, but have a higher frequency of Miocene ages.

When plotted versus latitude and longitude, whole rock $^{40}Ar/^{39}Ar$ in the southern Talkeetna Mountains show no N-S or W-E age progressions (Fig. 14A and B). When plotted versus latitude and longitude, AFT cooling ages in the southern Talkeetna Mountains show no N-S or W-E age progressions (Fig. 14A and B). There is also no clear evidence of regional resetting of AFT or AHe cooling age due to Eocene volcanism (Figs. 13 and 14).

Similarly, region-wide Paleocene-Eocene exhumation related cooling ages and volcanic ages from southwest Alaska (O'Sullivan et al, 2010), the Revelation Mountains region (Reed and Lanphere, 1972), the Tordrillo Mountains (Haeussler et al., 2008; Benowitz et al., 2012a), the Kichatna Mountains (Ward, 2010), the Kenai Mountains (Valentino et al., 2016), the Foraker Glacier region (Reed and Lanphere, 1972; Cole and Layer, 1984), the Susitna Basin (Stanley et al., 2014) the Cantwell Volcanics (Cole et al., 1999), the Jack River Volcanics (Cole et al., 2007), the Talkeetna Mountains (Silberman and Grantz., 1984; Parry et al., 2001; Cole et al., 2006; Hoffman and Armstrong, 2006; Oswald, 2006; Cole et al., 2007; Bleick et al., 2012; Hacker et al., 2011) the St. Elias Mountains (Enkelmann et al., 2017) and three sites in the Yukon-Tanana Terrane (Tempelman-Kluit and Wanless, 1975; Dusel-Bacon and Murphy, 2001; Enkelmann et al., 2017) have no apparent N-S or W-E age progressions (Fig. 15).

HeFTy Thermal Models

To construct a detailed thermal history of the region, inverse thermal models were produced for all our samples using all available U-Pb zircon, $^{40}Ar/^{39}Ar$, AFT and AHe age

constraints. A representative group of thermal models are shown in figures 16 and 17 (for all thermal models see Appendix C). The thermal models display some spatial and elevation controlled variations, but in general record three main rock cooling events: The highest elevation sample from the Mount Sovereign vertical profile (13Sov) records relatively slow rock cooling from the Cretaceous to Present (~1-4°C/My) (Figs. 16 and 17). Thermal models of lower elevation samples (01Sov, 03Sov) show relatively slow, but not well constrained cooling until ~60 Ma (~1-4°C/My), when the cooling rate significantly increases for a period of ~20 My (>16°C/My). This is followed by slow cooling and relative tectonic quiescence from ~45 Ma to present (~1°C/My). 3 samples near the CMF (01Trop, 02King, 04King) show a second relatively rapid cooling event (~4°C/My) that initiated in the Miocene (Fig. 16), although the exact timing of onset is not well constrained by our current cooling age data set. Additional analyses are planned.

DISCUSSION

Mechanisms for Rock Cooling in the Southern Talkeetna Mountains

Thermochronology can be used to delineate the time-temperature history of a rock (Reiners and Brandon, 2006). Cooling ages can reflect monotonic rock cooling or thermal resetting and supporting evidence is required to determine if cooling ages are related to exhumation, burial, magmatic events or the compression and/or relaxation of isotherms (e.g. Benowitz et al., 2012a).

Dike swarms, predominantly mafic, intrude into the northeastern edge of the southern Talkeetna Mountains trondhjemite pluton and in general do not intrude past the location of sample 03Sov (~1,500 m), which was collected immediately outside the area effected by diking. There is at least one mafic dike intruding the interior trondhjemite pluton (e.g. sample 14Sov)

(Figs. 5 and 7). To test for thermal resetting due to diking, AFT analyses were performed on samples 01Sov and 02Sov (Fig. 7 and Table 2), which are trondhjemite rocks collected at a minimum distance of ~5 m from Eocene volcanic intrusions at the northeastern edge of the pluton (Fig. 6 P5 and P6). The AFT cooling ages of samples 01Sov and 02Sov (~49 Ma and ~48 Ma respectively) are older than the volcanic ages of the proximal dikes (~42 Ma to ~46 Ma) (Fig. 7 and Table 1), providing evidence that the rocks of the trondhjemite pluton were not thermally reset during dike emplacement.

Throughout the trondhjemite pluton, outcrops show variable evidence for alteration from hydrothermal fluids (Fig. 6 P3) that were likely injected during the period of peak Eocene magmatism (Cole et al., 2006). Previous studies have demonstrated that the heat effects from hydrothermal fluids can result in the thermal resetting of the AFT system (Roden and Miller, 1989). Samples 06Sov, 10Sov and 12Sov have AFT cooling ages of ~42 Ma, ~45 Ma and ~51 Ma respectively and are distinct outliers from the Mount Sovereign-Sheep Mountain AFT age-elevation relationship (Fig. 11B), suggesting they have been thermally reset. HeFTy thermal models of these three outlier samples show more rapid Paleocene-Eocene rock cooling rates (up to ~30°C/My) compared to the other samples in the AFT age-elevation profile (~16°C/My) (see Appendix C), indicating the two sample sets have experienced different thermal histories. AHe cooling ages are invariant with elevation along the Mount Sovereign-Sheep Mountain vertical profile with ages generally around ~45 Ma adding support to this being a period of peak hydrothermal fluid injection and thermal resetting. We test this with HeFTy thermal modelling and find that the thermal models provide better fits if reheating is allowed (Appendix C).

We have already established that the rocks of the trondhjemite pluton were not thermally reset during Eocene dike emplacement. Therefore, we infer that samples 06Sov, 10Sov and

12Sov were thermally reset from the injection of hydrothermal fluids during peak Eocene magmatism (Fig. 11B). Alternatively, there may be unidentified structures within the trondhjemite pluton that became active after ~42 Ma. We did not observe any evidence of structures within the trondhjemite pluton where we collected samples, nor dikes near these samples. Hence, given the available information on coeval magmatism during this time period, we prefer a model of thermal resetting by injection of hydrothermal fluids to explain these outlier cooling ages.

Sample 04King is also an outlier from the Mount Sovereign-Sheep Mountain AFT age-elevation relationship (Fig. 11B). This sample was included in the AFT age-elevation relationship based on its position at a higher elevation within the trondhjemite pluton. However, sample 04King was collected at a considerable distance from the main sample cluster of our Mount Sovereign-Sheep Mountain vertical profile (Fig. 7) and there is a mapped fault between the two sites that may be affecting its age (Fig. 5) (Wilson et al., 2015). We did not observe any field evidence for hydrothermal fluid alteration at the collection site for sample 04King, but it was a rushed helicopter spot sampling station, so it is possible we missed observing any.

Sample 03King was collected within ~5 m of a granite-metamorphic rock contact and has a regionally young AFT age of ~34 Ma (Fig. 7 and Table 2). The possibility of an unmapped structure between the main sample cluster and sample 03King may explain the younger age (Fig. 5). Alternatively, the younger age could be due to fluid flow along the unit contact with metamorphic rocks. No dikes were observed near sample 03King.

Figure 13 is a normalized probability density plot of southern Talkeetna Mountains cooling ages and volcanic ages confined to north of the CMF and south of the Talkeetna Fault (Fig. 7) for the whole rock $^{40}Ar/^{39}Ar$, AFT and AHe radiometric systems. AFT cooling ages that

we interpret to be thermally reset or reflecting displacement along unmapped structures (06Sov, 10Sov, 12Sov, 03King) are excluded. This plot shows that AFT cooling ages are predominantly Paleocene-Eocene and has a distinct peak that reflects a period of heightened regional rapid rock cooling. The whole rock volcanic peak is younger than the AFT peak, suggesting that AFT cooling ages represent exhumation and not thermal resetting. Our interpretation that AFT cooling ages are exhumation related is consistent with field observations and geochronology constraints from the Matanuska Valley region that document rapid accumulation of a >2 km thick succession of ~56-60 Ma fluvial strata unconformably upon ~70 Ma and older granitoid plutons (Figs. 5 and 18) (Arkose Ridge Formation, Kortyna et al., 2013; Sunderlin et al., 2014; Trop et al., 2015).

The compilation of AHe cooling ages (Fig. 13) indicates parts of the southern Talkeetna Mountains cooled below the ~80°C isotherm during the Eocene. Samples 01Sov, 06Sov and 13Sov have AHe cooling ages that may reflect thermal resetting from hydrothermal fluids during Eocene magmatism (Fig. 11B) based on their invariant with elevation age relationship and regional evidence of hydrothermal fluid injection at the time. Overall, the AHe data supports a southern Talkeetna Mountains rock cooling event in Oligocene-Miocene time. Support for this interpretation includes deposition of Miocene fluvial strata in the footwall of the CMF in the southern Talkeetna Mountains (Bristol et al., 2017). This is consistent with our interpretation that exhumation was driven by vertical displacement along the CMF. The relationship between these ages and the displacement history of the CMF is further discussed below.

In summary, in the context of regional basin analysis and the magmatic record, a compilation of the geochronology-thermochronology data from the southern Talkeetna Mountains supports Paleocene-Eocene and Oligocene-Miocene exhumation events with evidence

of spatially limited thermal resetting related to hydrothermal fluid injection. The occurrence of spatially variable resetting should be taken into account by future thermochronology studies in this region, detrital studies in particular, because of the difficulty in distinguishing monotonic cooling ages from thermally reset ages without field evidence of outcrop alteration from hydrothermal fluids, age-elevation relationships and structural control.

Southern Talkeetna Mountains Paleogeothermal Gradient

Geothermal gradient constraints must be known to quantify the total amount of exhumation. We have no quantitative measurement of paleogeothermal gradients for the Talkeetna Mountains. Therefore, we use our exhumation and cooling rate calculations (discussed below), along with petrological observations and other regional geothermal gradient constraints, to assess qualitative variations in the geothermal gradient through time, allowing us to make inferences about the amount of southern Talkeetna Mountains exhumation.

We also test for an anomalously high Paleocene-Eocene southern Talkeetna Mountains geothermal gradient regime, which has been proposed to have existed in the western Alaska Range and across interior southern Alaska (Fig. 1) (Benowitz et al., 2012a; Finzel et al., 2016). Overall, documenting variations in the geothermal gradient through time allows us to make interpretations about how the southern Alaska thermal regime evolved throughout a sequence of Cenozoic plate configurations. This is integral to understanding the Cenozoic tectonic evolution of southern Alaska.

Southern Talkeetna Mountains Geochronology and Thermochronology Details

$^{40}Ar/^{39}Ar$ Mica Ages

Muscovite from three samples collected along the Mount Sovereign vertical profile (13Sov, 03Sov, 01Sov) have $^{40}Ar/^{39}Ar$ cooling ages of 150.2 ± 1.2 Ma, 157.9 ± 0.9 Ma and

149.9 ± 0.6 Ma respectively (Figs. 7, 8 and 15 and Table 1). Biotite from sample 13Sov has a cooling age of 148.7 ± 0.6 Ma. These ages are similar to the U-Pb zircon crystallization age of the trondhjemite pluton (Figs. 7 and 17) (~157 Ma, Rioux et al., 2007) and are likely related to thermal relaxation after pluton emplacement. The duration of time between closure of the muscovite and biotite mineral phases (~100°C) is geologically instantaneous (~1.5 My) (Figs. 9 and 17). This suggests rapid rock cooling (~67°C/My) following the Late Jurassic emplacement of the trondhjemite pluton (Fig. 19), which may have been protracted (Hacker et al., 2011).

$^{40}Ar/^{39}Ar$ K-feldspar Ages

$^{40}Ar/^{39}Ar$ K-feldspar thermochronology on sample 03Sov (Fig. 7) yields a plateau age of 124.9 ± 1.8 Ma (Table 1) with a flat age spectrum indicative of rapid cooling (Figs. 8, 9 and 17). Sample 03Sov records relatively slow Cretaceous rock cooling between the muscovite and rapid closure K-feldspar temperature domains (~5°C/My) (Figs. 9 and 17). The entirety of our geochronology-thermochronology data set points to a complex Cretaceous thermal history for the Talkeetna mountains, which is beyond the scope of our research, but is deserving of further study.

Conversely, $^{40}Ar/^{39}Ar$ K-feldspar thermochronology on sample 01Sov, located ~200 meters below sample 03Sov, (Fig. 7) has a bimodal age spectrum that we infer demonstrates thermal resetting at ~61 Ma and subsequent rock cooling (Figs. 8, 9 and 13 and Table 1), indicating a more complex cooling history. The partial thermal resetting of K-feldspar in sample 01Sov (~61 Ma) happened prior to the main episode of regional dike emplacement at ~40-50 Ma (Fig. 7 and 19). One ~60 Ma whole rock age indicates that minor dike emplacement began earlier, but the ~60 Ma sample (SG5 in Fig. 7) is located far south of sample 01Sov and therefore these similar ages are not spatially linked.

Sample 01Sov records relatively slow Cretaceous rock cooling between the muscovite and high temperature K-feldspar domains (~2°C/My) (Figs. 9 and 17). We interpret sample 01Sov's K-feldspar age spectrum to show thermal resetting of the low temperature domain at ~61 Ma (Figs. 8 and 9). We attribute the thermal resetting of K-feldspar in sample 01Sov to an elevated geothermal gradient induced by high heat flow through a slab window beneath the Talkeetna Mountains, as proposed by Cole et al. (2006) and subsequent rock cooling related to exhumation (Fig. 19). This time-period (~61 Ma) also overlaps with a period of thermal resetting constrained by detrital zircon fission track analysis on Cook Inlet (Fig. 2) Cretaceous strata (Finzel et al., 2016) and this inference is consistent with regional evidence for an elevated geothermal gradient (Benowitz et al., 2012a) and is further discussed below.

$^{40}Ar/^{39}Ar$ Whole Rock Volcanic Ages

7 whole rock $^{40}Ar/^{39}Ar$ volcanic ages produced for this study range from ~42 Ma to ~52 Ma (Figs. 7 and 8 and Table 1). When integrated with 19 previously published whole rock $^{40}Ar/^{39}Ar$ ages in the Talkeetna Mountains (north of the CMF and south of the Talkeetna Fault), ages range from ~31 to ~60 Ma (Figs. 7 and 13) (Silberman and Grantz, 1984; Cole et al., 2006; Oswald, 2006; Cole et al., 2007). Our ages support the interpretation by Cole et al. (2006) of a period of volcanism that persisted for millions of years during the Paleocene-Eocene.

Apatite Fission Track Cooling Age-Elevation Relationships

We utilize age-elevation relationships to calculate variations in the rate of exhumation through time (Fig. 11); we interpret breaks in slope as reflecting a change in the exhumation rate (Fitzgerald et al., 1993). Rock cooling rates and estimated exhumation rates are also calculated using the HeFTy thermal modelling program (Ketcham, 2007).

17 samples north of the CMF have Paleocene-Eocene AFT cooling ages (~44 Ma to ~63 Ma) (Figs. 7 and 11A and Tables 2 and 3). When these ages are compiled with previously published AFT cooling ages in the region (Parry et al., 2001; Bleick et al., 2012), there is a complex age-elevation relationship that can be divided into two different cooling domains (Fig. 11A). Samples at lower elevations (<1,500 m) do not have an age-elevation relationship (Fig. 11A).

AFT cooling ages at higher elevations (>1,500 m) that are within the trondhjemite pluton along the Mount Sovereign-Sheep Mountain vertical profile do have an age-elevation relationship (Fig, 11B) and show no evidence to suggest the shape of isotherms varied significantly over the short horizontal distance of our Mount Sovereign-Sheep Mountain vertical profile (~20 km). As discussed above, a few of the samples along the AFT vertical profile show evidence for spatially variable thermal resetting that we infer is related to hydrothermal fluid injection. The Mount Sovereign-Sheep Mountain AFT vertical profile shows three distinct periods of exhumation: **1)** Relatively slow Late Cretaceous-Early Paleocene (~74 to ~60 Ma) exhumation at a rate of ~15 m/My, **2)** a break in slope at ~58-60 Ma indicating relatively rapid exhumation at a maximum rate of ~188 m/My and **3)** a second break in slope at ~56 Ma indicating a less rapid exhumation rate of ~65 m/My. Alternatively, the AFT cooling ages have large error bars that allow there to be only one inflection point at ~58-60 Ma with a more moderate exhumation rate. We do not favor this interpretation because it is not supported by the HeFTy thermal models, which show a significant increase in rock cooling rates at ~60 Ma and an inferred increase in exhumation rates at this time (Fig. 16). These results suggest that rapid exhumation began immediately after the thermal resetting and subsequent cooling of K-feldspar

in sample 01Sov (~61 Ma), coeval with the initiation of minor dike emplacement at ~60 Ma and continued during the main episode of dike emplacement from ~40-50 Ma (Figs. 7 and 13).

As stated above, AFT cooling ages from samples at lower elevations (<1,500 m) and closer to the CMF do not have an age-elevation relationship (Fig. 11A). The two most likely explanations for the lack of an AFT age-elevation relationship at lower elevations are potential differential erosion after the closure of the AFT system, possibly related to Cenozoic deformation or Late Cenozoic glaciation (Williams et al., 1989) and the perturbation of isotherms at lower elevations around the trondhjemite pluton by the Paleocene-Eocene volcanism, resulting in possible erratic rock cooling profiles (Reiners, 2007).

AFT cooling ages south of the CMF are distinctly younger than those to the north (Arkle et al., 2013), which is counter to what is expected if the CMF experienced significant Eocene-Oligocene north-side up displacement and is the primary control on Cenozoic AFT cooling age patterns. There are only 4 AFT cooling ages available in the Talkeetna Mountains region south of the CMF (Fig. 7), including sample 05King from this study (~31 Ma), one sample located in the fault zone from Parry et al. (2001) (~31 Ma) and two samples from Little and Naeser (1989) (~21 Ma and ~24 Ma). The lack of data makes it difficult to draw interpretations from these cooling ages. However, Arkle et al. (2013) attribute these regionally younger ages to exhumation in the Chugach syntaxis driven predominantly by underplating from the Yakutat flat-slab since the Oligocene. According to their model, the exhumation effects driven by underplating die out north of the CMF, which may explain why ages south of the fault are younger than ages north of the CMF. The AFT ages south of the CMF are also located near the BRFS and one sample is located south of a BRFS strand. Therefore, it is possible that the ages were affected by the Neogene contractional reactivation of the BRFS (Little and Naeser, 1989).

Apatite (U-Th)/He Cooling Ages

11 AHe cooling ages analyzed for this study range from ~10 Ma to ~45 Ma (Table 4). When integrated with previously published cooling ages (Hoffman and Armstrong, 2006; Hacker et al., 2011), samples range from Cretaceous to Miocene (~73 Ma to ~10 Ma) (Fig. 12A). All integrated AHe ages show a clear pattern of getting younger approaching the CMF (Fig. 12A), indicating that vertical displacement along the CMF is structurally controlling cooling age patterns.

The AHe age from sample 01King, located directly north of the continuous strand of the CMF, is ~42 Ma (Fig. 7). The AHe age from sample 02King, located north of the northern splay of the fault, is ~12 Ma. This recognizably younger age is evidence that the northern splay has been the active strand of the CMF since at least the Miocene.

HeFTy Thermal Modelling

Rock cooling paths were constructed for all our samples using the HeFTy thermal modelling program (Ketcham, 2007) and all available thermochronology constraints. These time-temperature paths highlight the approximate timing and duration of multiple rock cooling events. A representative group of HeFTy models are shown in Figure 16. HeFTy models for all samples can be found in Appendix C.

Rock cooling paths for samples 13Sov, 03Sov and 01Sov show cooling patterns that vary with elevation (Figs. 16 and 17). The highest elevation sample (13Sov) has a much slower cooling rate relative to the lower elevation samples. Sample 03Sov shows a cooling rate that significantly increases after ~60 Ma. Sample 01Sov also shows a similarly increased cooling rate after the low temperature K-feldspar domain is thermally reset and subsequently cooled at ~61 Ma (Figs. 8 and 9).

All our HeFTy models show distinct rock cooling patterns that vary spatially and with elevation. To highlight these variations, we divided the thermal models into three groups with similar cooling histories (Fig. 20): **1)** The two highest elevation samples collected from the summits of Mount Sovereign and Sheep Mountain (13Sov, 07Talk) (Fig. 7), **2)** 7 samples from the interior Talkeetna Mountains along the two vertical profiles (01Sov, 02Sov, 03Sov, 08Sov, 11Sov, 05Talk, 13Talk), and **3)** 3 samples near the CMF (01Trop, 02King, 04King).

The thermal models suggest four distinct rock cooling events in the southern Talkeetna Mountains topographic development history: **1)** The highest elevation samples record relatively slow rock cooling from Cretaceous to Present (~1-3°C/My) (Fig. 20). Mapping studies in the southern Talkeetna Mountains document Cretaceous crustal shortening (Csejtey et al., 1978; Fuchs, 1980), suggesting that rock cooling was related to exhumation. **2)** The interior Talkeetna Mountains/vertical profile samples and near CMF samples both record a rapid rock cooling event (>16°C/My) initiating at ~60 Ma (Fig. 20). The models suggest that this elevated cooling rate persisted for ~20 million years. This is consistent with the inferred timing of a prolonged period of Paleocene-Eocene volcanism (Cole et al., 2006) and our constrained onset of rapid exhumation at ~58-60 Ma (Fig. 11B) following the thermal resetting of K-feldspar in sample 01Sov at ~61 Ma (Figs. 8 and 9). **3)** The rapid rock cooling event is followed by a period of relative Middle Eocene-Miocene tectonic quiescence with a rock cooling rate of ~1°C/My. More thermochronology data is needed to determine the exact duration of this rock cooling event, which is unclear from our dataset. **4)** The group of samples near the CMF record a second, more rapid rock cooling event (~4°C/My) during the Miocene, likely in response to vertical displacement and exhumation along the CMF. More low temperature thermochronology data is needed near the CMF to define the timing of initiation of this rock cooling event.

Our AFT age-elevation relationship suggests a maximum exhumation rate of 0.2 km/My (Fig. 11B). When the maximum sustained cooling rate from our HeFTy thermal models (~16°C/My) is converted to an exhumation rate (0.8 km/My) using a normal continental geothermal gradient of 20°C/km, the two individual calculations disagree. Alternatively, when the ~16°C/My cooling rate is converted to an exhumation rate using a much higher geothermal gradient of ~80°C/km, the two exhumation calculations agree well (0.2 km/My). When geothermal gradients are obtained from the time-averaged cooling rates between ~60 Ma and ~45 Ma from 5 individual HeFTy thermal models, the geothermal gradient is ~55°C/km on average, indicating a non-steady state geothermal gradient during this time-period. This is not unexpected given the dynamic nature of slab windows and associated upwelling of the asthenosphere (Thorkelson, 1996). Hence, thermochronology results from this study provide independent evidence for an anomalously high geothermal gradient during Paleocene-Eocene times, which aligns with previous southern Alaska paleogeothermal gradient interpretations (e.g. Benowitz et al., 2012a; Finzel et al., 2016).

We acknowledge that the age-elevation profile does not provide a unique rock cooling scenario, given the large uncertainty associated with our AFT ages (Fig. 11). It is also possible that large amounts of tilting could explain the disconnect between exhumation rate calculated from our AFT age-elevation relationship and the exhumation rate calculated from our HeFTy thermal models. However, as discussed earlier, vertical lithified volcanic bodies and magma conduits cross cut the mafic dikes that appear to intrude along exfoliation joints (Fig. 6 P1 and P2), suggesting there has not been significant tilting since the Eocene. Given this and the regional evidence for a high Paleocene-Eocene geothermal gradient across southern Alaska (O'Sullivan and Currie, 1996; Dusel-Bacon and Murphy., 2001; e.g. Benowitz et al., 2012a;

Riccio et al., 2014; Finzel et al., 2016), we favor the interpretation of an elevated Paleocene-Eocene southern Talkeetna Mountains geothermal gradient averaging ~55°C/km.

Cole et al. (2006) proposed that Paleocene-Eocene volcanic rocks in the southern Talkeetna Mountains (Fig. 5) were emplaced due to extensional faulting driven by the hypothesized oroclinal bending of southern Alaska (Hillhouse et al., 1994) and/or derived from depleted basaltic magmas and emplaced through a slab window beneath southern Alaska during the Late Paleocene. Our results suggest that high heat flow and upwelling of asthenospheric mantle through this slab window is the most likely mechanism for producing the elevated (~55°C/km on average) geothermal gradient inferred from our thermochronology results and HeFTy models. This interpretation is consistent with regional evidence for an elevated geothermal gradient as previously discussed above. We infer that the elevated geothermal gradient is responsible for the thermal resetting of the K-feldspar system in sample 01Sov at ~61 Ma (Figs. 8, 9 and 17). This was followed by rapid rock cooling, as shown in our HeFTy models (Fig. 20), and an increase in the exhumation rate at ~58-60 Ma recorded by our AFT age-elevation relationship (Fig. 11B). Minor dike emplacement began at ~60 Ma and diking was at a maximum between ~40 Ma and ~50 Ma (Figs. 7 and 17).

Topographic Development Summary for the Southern Talkeetna Mountains

Paleocene-Eocene Paleotopography

Geophysical models of southern Alaska from Jadamec et al. (2013) predict that the modern plate configuration would develop a basin in the region of the Talkeetna Mountains rather than high topography (see introduction and Fig. 3). Volcanic ages and cooling ages from the whole rock $^{40}Ar/^{39}Ar$ and AFT radiometric systems are predominantly Paleocene-Eocene (Fig. 13). These results in part reconcile the models from Jadamec et al. (2013) by suggesting

that the southern Talkeetna Mountains have a significant component of paleotopography that formed prior to the modern Yakutat flat-slab plate configuration (Fig. 2B).

Adding support to this interpretation, Eocene dikes intrude sub-horizontally into the Mount Sovereign trondhjemite pluton along exfoliation joints (Fig. 18) and are cross-cut by vertical dikes and lithified volcanic bodies and magma conduits which display a visible lack of tilting (Fig. 6 P1 and P2). This suggests that southern Talkeetna Mountains unroofing initiated before dike emplacement, consistent with previous studies in the region (e.g. Trop, 2008) and the region was uplifted as a uniform crustal block. We speculate that the prolonged episode of dike emplacement, along with possible magmatic underplating during slab window magmatism (C. Li et al., 2012), could have thickened the crust and may in part explain the sustained high topography into modern times. We interpret these overall findings to suggest that Paleocene-Eocene topographic development across the southern Talkeetna Mountains is related to the creation and persistence of a Paleocene-Eocene slab window (Cole et al., 2006; Benowitz et al., 2012a).

Structural Control on the Topographic Development of the Southern Talkeetna Mountains

The structures involved in accommodating southern Talkeetna Mountains exhumation related to an inferred Paleocene-Eocene slab window are not well constrained (Fig. 5). Faults appear to partially bound the edges of the trondhjemite pluton (Fig. 5) (Wilson et al., 2015). Our AFT age-elevation relationship suggests that there are two separate rock cooling domains defined by elevation (Fig. 11A), based on the relatively well-defined age-elevation relationship within the trondhjemite pluton. Sample 04King is located across a fault on the western edge of the pluton (Fig. 5) away from the Mount Sovereign vertical profile sample cluster (Fig. 5) and is an outlier from our AFT age-elevation relationship (Fig. 11B). Similarly, samples 13Talk and

14Talk are located near a mapped fault (Fig. 5) and their AFT cooling ages fall in the cooling domain that does not display an age-elevation relationship (Fig. 11A). This is evidence that at least the structure on the western boundary of the trondhjemite pluton was active in the Paleocene-Eocene and supports the notion that the high peak region, established by the trondhjemite pluton, exhumed as an independent crustal block along these structures.

There are also numerous mapped NW-SE trending normal faults to the east of our study area. It is unclear whether these NW trending normal faults were created and reactivated to allow for volcanism and exhumation driven solely by mantle processes (i.e. a slab window) (Trop et al., 2003; Cole et al., 2006), or conversely if crustal extension and the creation and reactivation of structures were influenced by the hypothesized counterclockwise rotation and oroclinal bending of southern Alaska (discussed below) (Hillhouse et al., 1994) in the presence or absence of a slab window. The orientation of these structures is also consistent with transtension linked to dextral slip along the CMF (Cole et al., 2006).

Physiographically, the southern Talkeetna Mountains are bounded by the Castle Mountain Fault to the south and the Talkeetna Fault to the north (Fig. 7). Additionally, the western edge of the Talkeetna Mountains is a prominent lineament separating high topography from the Susitna Basin and the eastern edge of the Talkeetna Mountains is a prominent lineament separating high topography from the Copper River Basin (Fig. 7). Further research may illuminate the existence of range bounding faults (as suggested for the Susitna Basin by Saltus et al., 2016) and the role these inferred structures may play in regional uplift and subsidence.

Based on the documented evidence for an elevated Paleocene-Eocene southern Alaska geothermal gradient (Benowitz et al., 2012a) and widespread slab window magmatism (Cole et al., 2006; Madsen et al., 2006), we favor a similar interpretation that normal faulting and

exhumation were primarily driven by the thermal effects from a slab window beneath southern Alaska on the upper plate (Trop et al., 2003; Cole et al., 2006). However, there is not enough evidence to equivocally dismiss the oroclinal bending model (Hillhouse et al., 1994) which deserves further study. Paleocene-Eocene regional extension may have additionally been driven by concurrent transform margin tectonics (see transform discussion below).

Overall, comparisons can be made between the Paleocene-Eocene southern Talkeetna Mountains and the Pioneer-Boulder Mountains (Yellowstone region) where Vogl et al. (2014) document Miocene topographic construction over the Yellowstone hotspot (a different tectonic environment, but with similar heat input as a slab window) in a region with pre-existing normal faults. They conclude that exhumation was largely driven by thermal effects from the hotspot and that normal faulting was not the primary control on exhumation.

The Castle Mountain Fault

The geophysical models by Jadamec et al. (2013) do not account for the existence of the CMF, which may in part explain the disconnect between the model results and actual topography (Fig. 3). To test how southern Alaska structures control patterns of deformation, we compiled the youngest AFT cooling ages along a ~N-S transect across southern Alaska (Figs. 1 and 21A), including published data (Kveton, 1989; Parry et al., 2001; Bleick et al., 2012; Arkle et al., 2013; Frohman, 2014) and ages from this study. This compilation shows a pattern of ages abruptly changing across major faults, supporting the notion that Cenozoic deformation has been focused along these structures. However, the ages do not change as distinctly across the CMF, suggesting it has experienced less vertical displacement. AFT ages directly to the north of the CMF are ~44 Ma to ~63 Ma (Table 2), suggesting there has been less than ~3-5 km of vertical displacement and unroofing along the CMF since the Eocene and possibly even less considering the evidence

for an elevated geothermal gradient. This is consistent with previous estimates of ~ 3 km of Neogene vertical slip based on mapping studies (Grantz, 1966; Fuchs, 1980).

To test the premise that vertical displacement along the CMF controlled Paleocene-Eocene cooling age patterns, we graphed 8 AFT cooling ages (samples 13Sov, 13Talk, 07Talk, 05Talk, 04King, 03King, 02King, 01King) along a ~N-S transect approaching the CMF (Figs. 7 and 11C). The AFT cooling ages along this transect show an apparent trend of younging towards the CMF (Fig, 11C), indicating a possible structural control. However, a compilation of all AFT cooling ages in the range do not show a pattern of younging towards the CMF (Fig. 14), discounting the notion of the CMF controlling AFT cooling age patterns. The locations of the 8 transect samples also decrease in elevation towards the fault so it is possible that these samples reflect an age-elevation relationship. Adding support to elevation being the primary control on the transect age patterns is the slightly stronger correlation between AFT cooling age and elevation (Fig. 11D) versus the correlation between AFT cooling age and distance from CMF (Fig. 11C). An age-elevation relationship is what we would expect from a coherent crustal block moving upwards through stationary isotherms given the lack of evidence for tilting (Fig. 6).

However, if sample 03King, which has a distinctly younger age (Fig 7), is excluded from this test, the correlations between AFT ages approaching the CMF and AFT ages and elevation are similar. Conversely, the younger sample 03King may reflect differential erosion in the region, which exposed this younger rock. Therefore, this test does not provide definitive evidence for vertical displacement along the CMF during the Paleocene-Eocene. There is some regional evidence for Eocene displacement along the CMF. Wishbone Formation strata south of the CMF are deformed by footwall synclines that are consistent with syndepositional rotation and displacement (Trop et al., 2003; 2015). ~48-50 Ma lavas capping Castle Mountain and

Puddingstone Hill located south of the CMF, unconformably overlie deformed conglomerates with ~52-55 Ma detrital zircons, indicating some footwall tilting, folding and erosion prior to ~48-50 Ma (Trop et al., 2015). However, the amount of Eocene displacement is unclear.

Miocene AHe cooling ages near the CMF are the youngest in the southern Talkeetna Mountains (Fig. 7 and Table 4). The youngest available AHe cooling ages compiled along an ~N-S transect across southern Alaska (Figs. 1 and 21B) (Arkle et al., 2013; Riccio et al., 2014) show a pattern of cooling ages abruptly changing across major faults, similar to that of the AFT cooling age transect discussed above (Fig. 21A). However, the change in AHe cooling ages across the CMF (Fig. 21B) is more pronounced than the change in AFT cooling ages (Fig. 21A).

To test the premise that AHe cooling age patterns have been controlled by vertical displacement along the CMF, we graphed 7 AHe cooling ages (samples 13Sov, 06Sov, 01Sov, 04King, 03King, 02King, 01King) along a ~N-S transect approaching the CMF. The AHe cooling ages show a clear trend of getting younger towards the CMF (Fig. 12C). There is no relationship between AHe cooling age and elevation along the same transect (Fig. 12D). This is strong evidence for CMF vertical displacement control on AHe cooling pattern since the Miocene as rocks near the CMF are being cooled more rapidly (Fig. 20).

This interpretation is consistent with HeFTy thermal models which indicate a rapid rock cooling event initiating by the Miocene (Fig. 20) and a study by Bristol et al. (2017; personal communication 2017) that documents the juxtaposition of Miocene fluvial strata against Cretaceous granitoids along the CMF. When the Miocene rock cooling rate from our HeFTy models (~4°C/My) is converted into an exhumation rate using a continental geothermal gradient of 20°C/My, which is expected due to cooling from the removal of the mantle wedge during the flat-slab subduction of the Yakutat microplate (Christenson et al., 2010), as reflected in the gross

modern geothermal gradient along a ~N-S transect across southern Alaska (Figs. 1 and 21B), the approximate exhumation rate is 0.2 mm/yr. These overall findings suggest that vertical displacement along the CMF has played a role in the exhumation of the southern Talkeetna Mountains since the Miocene, with slip on the CMF likely in response to the flat-slab subduction of the Yakutat microplate (Haeussler, 2008).

Cenozoic Tectonic Reconstruction of Southern Alaska

Paleocene-Eocene Slab Breakoff

A ~2,000 km long string of eastward-younging Paleocene-Eocene near-trench plutons in the accretionary prism of southern Alaska (Figs. 1 and 2A) provides the basis for the proposed subduction of an active spreading ridge and an associated slab window sweeping eastward across southern Alaska (Haeussler et al., 2003; Farris and Paterson, 2009). The timing and proposed slab window mechanism for Paleocene-Eocene topographic development of the southern Talkeetna Mountains coincides with this inferred ridge subduction event (Cole et al., 2006). The ridge subduction model is also the presumed mechanism for the Eocene creation of topography and an elevated geothermal gradient (>~50°C/km) in the western Alaska Range (Fig. 1) (Benowitz et al., 2012a), an elevated geothermal gradient of ~45°C/km in the Yukon-Tanana Uplands (Dusel-Bacon and Murphey, 2001), rapid rock cooling in the St. Elias Range (Fig. 15) (Enkelmann et al., 2017) and the intrusion of dike swarms and mafic volcanic rocks throughout southern Alaska.

Given the model of a Paleocene-Eocene eastward sweeping spreading ridge, there are geologic tests to this hypothesis. Specifically, a west to east and south to north progression in the timing of volcanism and exhumation across southern Alaska inboard from the BRFS would be expected. To examine this hypothesis, we applied whole rock $^{40}Ar/^{39}Ar$ geochronology to

volcanic rocks in the Talkeetna Mountains (Table 1) and compiled our results with previously published regional Paleocene-Eocene volcanic ages to test this prediction. We also applied AFT thermochronology to plutonic rocks in the Talkeetna Mountains (Table 2) and compiled our results with previously published regional Cenozoic cooling ages to test this hypothesis.

Whole rock $^{40}Ar/^{39}Ar$ ages in the southern Talkeetna Mountains show no overall N-S or W-E relationships, suggesting no local spatial progressions in the timing of volcanism (Fig. 14). AFT cooling ages in the southern Talkeetna Mountains also show no overall N-S or W-E relationships, suggesting no local spatial progressions in the timing of exhumation (Fig. 14). More importantly, region-wide Paleocene-Eocene exhumation related cooling ages and volcanic ages from southwest Alaska (O'Sullivan et al, 2010), the Revelation Mountains region (Reed and Lanphere, 1972), the Tordrillo Mountains (Haeussler et al., 2008; Benowitz et al., 2012a), the Kichatna Mountains (Ward, 2010), the Kenai Mountains (Valentino et al., 2016), the Foraker Glacier region (Reed and Lanphere, 1972; Cole and Layer, 1984), the Susitna Basin (Stanley et al., 2014) the Cantwell Volcanics (Cole et al., 1999), the Jack River Volcanics (Cole et al., 2007), the Talkeetna Mountains (Silberman and Grantz., 1984; Parry et al., 2001; Cole et al., 2006; Hoffman and Armstrong, 2006; Oswald, 2006; Cole et al., 2007; Bleick et al., 2012; Hacker et al., 2011), the St. Elias Mountains (Enkelmann et al., 2017) and three sites in the Yukon-Tanana Terrane (Tempelman-Kluit and Wanless, 1975; Dusel-Bacon and Murphy, 2001; Enkelmann et al., 2017) have no apparent N-S or W-E relationships (Fig. 15).

The Paleocene-Eocene cooling and volcanic ages across southern Alaska are all broadly similar, suggesting a synchronous exhumation and volcanic event that was widespread across interior southern Alaska and persisted for millions of years. The apparent lack of any N-S or W-E progressions in the timing of Paleocene-Eocene volcanism and exhumation across interior

southern Alaska north of the BRFS conflicts with the proposed model of an eastward sweeping active spreading ridge impacting the region. The lack of any spatial age patterns like those observed in the prism suggests interior southern Alaska was likely not influenced by diachronous ridge subduction or thermal perturbation as evidenced by the age varying near-trench Sanak-Baranof belt plutons in the Chugach accretionary prism to the south (Fig. 1). Oblique ridge-trench convergence does prompt to an unzipping pattern, whereby slab window geometry is triangular and the opening widens progressively as the ridge descends into the mantle; thus, spatial patterns may be more diffuse farther inboard of the trench (Dickinson and Snyder, 1979; Thorkelson, 1996; Breitsprecher and Thorkelson, 2009). However, the absence of any age progression, regardless of rate, across a >800 km wide swath of interior southern Alaska makes it difficult to link diachronous ridge subduction to the region. Therefore, a different mechanism is required to explain the regional synchronous and long-lived slab window event recorded in interior southern Alaska.

To reconcile this, we propose a new model for the Paleocene-Eocene tectonic configuration of southern Alaska. We suggest that a Paleocene-Eocene slab window formed sub-parallel to the trench (Fig. 22) and drove exhumation and volcanism synchronously across interior southern Alaska while also significantly increasing the regional geothermal gradient. The cause of this Paleocene-Eocene slab window event is unclear, but in Baja, California, a similarly proposed tectonic setting (Michaud et al., 2006), a Miocene slab window event has been attributed to the subduction of a spreading ridge parallel to the trench that led to slab detachment and the opening of a slab window sub-parallel to the trench. Another possible mechanism for the opening of a Palecene-Eocene slab window across southern Alaska includes the subduction of a

bathymetric high (e.g. aseismic ridge or seamount chain) that was part of the Kula plate, leading to slab breakoff.

This model of the subduction of a bathymetric high and shutting off of subduction is consistent with the lack of evidence for subduction-related magmatism in interior southern Alaska during Late Paleocene-Early Eocene time (Cole et al., 2006) and stratigraphic/detrital geochronologic evidence for subaerial uplift and exhumation of the formerly marine forearc region followed by subsidence and nonmarine sedimentation (e.g. Trop, 2008; Ridgway et al., 2012; Kortyna et al., 2013; Finzel et al., 2015).

In our new model, interior southern Alaska (WCT) was located distal from the Chugach accretionary prism during Late Paleocene-Early Eocene time while the ~63 to ~47 Ma near-trench plutons were emplaced in this prism. The Paleocene-early Eocene margin outboard of interior southern Alaska was likely a transform setting characterized by dextral slip along the BRFS. Both regions were subsequently shuffled laterally by dextral displacement along orogen-parallel strike-slip faults, consistent with paleomagnetic data indicating that interior southern Alaska (WCT) and the Chugach accretionary prism were positioned hundreds of kilometers south of their current position during Latest Cretaceous-Paleocene time, but still distal from each other (Bol et al., 1992; Stamatakos et al., 2001; Garver and Davidson, 2015; Garver 2017).

Large-scale translation of the Chugach accretionary prism was likely accommodated along the BRFS and other orogen-parallel fault systems (Fig. 23). The slip history of the BRFS is prolonged and complex, with multiple episodes of displacement suggested during the Late Cretaceous-Paleogene and reactivation during the Neogene (Pavlis and Roeske, 2007). Roeske et al. (2003) proposed at least ~600-1000 km of Late Cretaceous-Eocene BRFS slip and geologic relationships allow for post-Eocene displacement (Cowen, 2003; Garver and Davidson, 2017).

Slip may have been partitioned onto other structures across southern Alaska (Fig. 1) such as the Castle Mountain Fault, which has been suggested to accommodate ~130 km of dextral slip (Pavlis and Roeske, 2007), the Denali Fault which has an inferred ~400 km of post-Early Cretaceous dextral displacement (Lowey, 1998, Benowitz et al., 2012b), or faults within the Chugach accretionary prism with poorly understood slip histories such as the Eagle River Fault (Kochelek et al., 2011) or Glacier Creek Fault (Little, 1990). Rocks making up our study area in interior southern Alaska were positioned at a paleolatitude ~15° to the south of their current location at ~80 Ma (Stamatakos et al., 2001) and were translated to near their current latitude by ~54-40 Ma judging from paleomagnetic data (Panuska et al., 1990), consistent with significant northward translation during Late Paleocene-Early Eocene time.

Eocene Oroclinal Bending

Paleo-vectors of Pacific plate motion relative to the North American plate do not favor large translation along the North American plate boundary, driven by Pacific plate motion, given the modern geographic configuration of North America (Fig. 24) (Doubrovine and Tarduno, 2008). However, if the southern Alaska orocline was unbent during the Paleocene-Middle Eocene (Fig. 24), the paleo-vectors are more compatible with the northward translation of the near-trench plutons along the western margin of North America (Garver and Davidson, 2015). Paleomagnetic declinations of Late Cretaceous-Paleocene rocks support ~30-50° counterclockwise rotation of southern Alaska by the Late Eocene (Fig. 22) (Hillhouse et al., 1994). This oft cited, but loosely constrained model explains the curvature of regional structures and mountain ranges (e.g. Denali Fault, Alaska Range) and is known as the southern Alaska orocline (e.g. Cole et al., 2007).

Given the heating of the southern Alaska thermal regime during the inferred slab window event (Figs. 22 and 23), it is possible that oroclinal bending may have been facilitated in part due to the thermally induced weakening of the crust, making it less elastic and more deformable. A similar mechanism for oroclinal bending due to thermal weakening has been suggested for the Pamir Mountains of Central Asia (Yin et al., 2001). As southern Alaska was rotated, the angle of convergence between the plate boundary and the Pacific Plate would increase, allowing for normal subduction to resume by the Late Eocene (Fig. 23) (Jicha et al., 2006; Stern and Gerya, 2017). The re-initiation of normal subduction by the Late Eocene is also supported by a study of the Hawaii-Emperor Chain Bend documenting a major change in Pacific Plate motion by ~47 Ma (Torsvik et al., 2017), which would change the convergence angle of the incoming plate along the southern Alaska plate boundary. Our results and interpretations align with the proposed Middle-Late Eocene oroclinal bending of southern Alaska. However, the loosely constrained orocline model would benefit from higher-resolution, integrated paleomagnetic-geochronologic studies across southern Alaska.

The unbending of the southern Alaska orocline may not be necessary for a Paleocene-Eocene plate boundary configuration that favored a transform margin. As stated above, paleomagnetism of Eocene volcanic rocks in the southern Talkeetna Mountains (Panuska et al., 1990; Stamatakos et al., 2001) suggests the sampled rocks (and the underlying WCT north of the BRFS) were not in their current location, but rather were positioned at lower latitudes at the time of our proposed Paleocene-Eocene slab breakoff event. The southern Talkeetna Mountains are thought to have then been translated northward along structures such as the Denali Fault and Tintina Fault systems, which are believed to have accommodated at least ~1,000 km of combined displacement since the Cretaceous (Denali Fault: Lowey, 1998, Benowitz et al.,

2012b; Tintina Fault: Tempelman-Kluit and Wanless, 1975; Gabrielse, 1985). This paleo-position would favor transform margin tectonics given known constraints on the incoming plate convergence angle with North America (Fig. 24). Hence, if the Talkeetna Mountains were located ~1,000 km to the southeast of its present location at the time of our proposed slab breakoff event, their position along western North America would still favor transform margin tectonics with or without Cenozoic oroclinal bending of southern Alaska.

Summary

Our proposed Cenozoic tectonic evolution of southern Alaska is summarized in Figure 23 and can be divided into four separate plate configurations: **1)** the Late Cretaceous-Early Paleocene plate configuration was characterized by normal subduction and the approach of what we infer to be a trench-parallel bathymetric high (e.g. aseismic ridge or seamount chain) (Fig. 23A). **2)** The Middle Paleocene-Middle Eocene plate configuration was characterized by a slab window event beneath interior southern Alaska, region-wide volcanism and exhumation, the heating of the thermal regime (Fig. 23B) and synorogenic sedimentation. We infer that at this time the BRFS was a transform boundary, allowing for the northward translation of the near-trench intrusions within the prism along the western margin of North America. The rotation and oroclinal bending of southern Alaska, possibly due in part to the thermally induced weakening of the crust, initiated by the Middle Eocene. **3)** The Late Eocene-Oligocene plate configuration was characterized by the resumption of normal subduction (Fig. 23C) and a period of relative tectonic quiescence (Fig. 19). **4)** The Miocene-Present plate configuration is characterized by the flat-slab subduction of the Yakutat microplate, displacement and mountain building along southern Alaska structures and the cooling of the thermal regime due to the removal of the mantle wedge during flat-slab subduction (Fig. 23D).

CONCLUSION

$^{40}Ar/^{39}Ar$ (hornblende, muscovite, biotite, K-feldspar and whole rock), AFT and AHe thermochronology data indicate that the southern Talkeetna Mountains have a polyphase topographic development history that can be divided into four distinct rock cooling events (Fig. 20): **1)** slow rock cooling (~1-3°C/My) and exhumation from the Late Cretaceous-Early Paleocene (~74 Ma to ~60 Ma), **2)** rapid rock cooling (>16°C/My) and exhumation initiating by the Middle Paleocene (~60 Ma) and persisting for ~20 million years, **3)** a period of slow rock cooling (~1°C/My) and relative tectonic quiescence during the Late Eocene-Oligocene (starting by ~45 Ma with Oligocene constraints not well defined by our results) and **4)** more rapid rock cooling (~4°C/My) and exhumation focused along the CMF that initiated by the Miocene (~12 Ma). $^{40}Ar/^{39}Ar$ whole rock volcanic ages and AFT cooling ages in the southern Talkeetna Mountains are predominantly Paleocene-Eocene (Fig. 13), suggesting that the Range has a component of paleotopography that formed prior to the current Yakutat flat-slab plate configuration. Our thermochronology dataset also provides evidence for an elevated Paleocene-Eocene geothermal gradient (~55°C/km on average) and suggests that the thermal effects of a slab window beneath southern Alaska drove exhumation. Miocene AHe cooling ages near the CMF (Fig. 7) suggest ~2-3 km of vertical displacement that also contributed to topographic development, consistent with vertical offset of Paleocene-Eocene strata across the CMF. Miocene-recent vertical slip along the the CMF was likely driven by the highly coupled flat-slab subduction of the Yakutat microplate (Fig. 23D).

Paleocene-Eocene volcanic ages and cooling ages across southern Alaska north of the BRFS are generally similar and show no apparent N-S or W-E relationships (Figs. 14 and 15), suggesting a synchronous and widespread volcanic and exhumation event. To reconcile this, we

propose a new model for the Paleocene-Eocene tectonic configuration of southern Alaska. We suggest that region-wide Paleocene-Eocene volcanism and exhumation was driven by a trench-parallel slab window event beneath southern Alaska (Fig. 22) and that at this time the BRFS was a transform boundary, allowing for the northward translation of the near-trench plutons and the prism to their current position (Fig. 23). We infer that normal subduction resumed following a major change in the direction of Pacific Plate motion during the Middle-Late Eocene and the possible oroclinal bending of southern Alaska. Finally, the Oligocene-Present flat-slab subduction of the Yakutat microplate developed the modern tectono-thermal regime of southern Alaska.

General Conclusion

For this study, I produced a new geochronology-thermochronology dataset consisting of 46 new ages for rocks I collected across a vast portion of the southern Talkeetna Mountains. These new ages elucidate the temporal-spatial variability and complexity in the topographic development history of the Range. My results also provide insight into the amount of Cenozoic vertical displacement along the CMF, a structure whose slip history is not well constrained.

The objectives for this study included answering three broad research questions about the Talkeetna Mountains: 1) How old are the southern Talkeetna Mountains? 2) Are there local structural controls on topographic development or evidence for rock uplift driven by a thermal event? And 3) how do my results align with the current models for the Cenozoic tectonic evolution of southern Alaska? The geochronology-thermochronology dataset produced for this study suggests that 1) The southern Talkeetna Mountains have both a component of Paleocene-Eocene paleotopography that formed prior to the modern plate configuration, and a component of topography that has formed since the Miocene during the modern plate configuration. 2)

Topographic development in the southern Talkeetna Mountains was driven in part by a Paleocene-Eocene thermal event and Miocene to Recent vertical displacement along the CMF. And 3) when the geochronology-thermochronology results from this study are integrated with previously published ages from across southern Alaska, the age progressions conflict with the current model for the Cenozoic tectonic evolution of southern Alaska. To reconcile this, this study proposes a new model for the Paleocene-Eocene tectonic configuration of southern Alaska.

The results from this study do not provide any information about the topographic development history of the Talkeetna Mountains region located between Mount Sovereign and the Talkeetna Fault. Our understanding of the production of topography in the Talkeetna Mountains would benefit greatly from a similar geochronology-thermochronology study between the high peak region and the Talkeetna Fault. Along with possibly providing information about the poorly understood slip history of the Talkeetna Fault, a geochronology-thermochronology study in this region would help to develop a more complete tectono-thermal history of the entire Talkeetna Mountains region. Understanding this region is a pivotal component in developing a complete and accurate model for the Cenozoic tectonic evolution of southern Alaska.

REFERENCES

Amato, J.M., Bogar, M.J., Gehrels, G.E., Farmer, G.L., and Mcintosh, W.C., 2007, The Tlikakila complex in southern Alaska: A suprasubduction-zone ophiolite between the Wrangellia Composite terrane and North America: Tectonic Growth of a Collisional Continen- tal Margin: Crustal Evolution of Southern Alaska: Geological Society of America Special Paper 431, v. 2431, p. 227–252, doi: 10.1130/2007.2431(10).

Amato, J.M., and Pavlis, T.L., 2010, Detrital zircon ages from the Chugach terrane, southern Alaska, reveal multiple episodes of accretion and erosion in a subduction complex: Geology, v. 38, p. 459–462, doi: 10.1130/G30719.1.

Arkle, J.C., Armstrong, P.A., Haeussler, P.J., Prior, M.G., Hartman, S., Sendziak, K.L., and Brush, J.A., 2013, Focused exhumation in the syntaxis of the western chugach mountains and prince william sound, alaska: Bulletin of the Geological Society of America, v. 125, p. 776–793, doi: 10.1130/B30738.1.

Bartsch-Winkler, S., and Schmoll, H.R., 1992, Utility of radiocarbon-dated stratigraphy in determining late Holocene earthquake recurrence intervals, upper Cook Inlet region, Alaska: Geological Society of America Bulletin, v. 104, p. 684–694, doi: 10.1130/0016-7606(1992)104<0684:UORDSI>2.3.CO;2.

Benowitz, J.A., Haeussler, P.J., Layer, P.W., O'Sullivan, P.B., Wallace, W.K., and Gillis, R.J., 2012a, Cenozoic tectono-thermal history of the Tordrillo Mountains, Alaska: Paleocene-Eocene ridge subduction, decreasing relief, and late Neogene faulting: Geochemistry, Geophysics, Geosystems, v. 13, doi: 10.1029/2011GC003951.

Benowitz, J., Vansant, G., Roeske, S., Layer, P.W., Hults, C.P., and O'Sullivan, P., 2012b, Geochronological constraints on the Eocene to present slip rate history of the eastern Denali Fault system: Abstracts with Programs - Geological Society of America, v. 44, p. 634.

Benowitz, J.A., Layer, P.W., Armstrong, P., Perry, S.E., Haeussler, P.J., Fitzgerald, P.G., and VanLaningham, S., 2011, Spatial variations in focused exhumation along a continental-scale strike-slip fault: The Denali fault of the eastern Alaska Range: Geosphere, v. 7, p. 455–467, doi: 10.1130/GES00589.1.

Benowitz, J.A., Layer, P.W., and Vanlaningham, S., 2014, Persistent long-term (*c.* 24 Ma) exhumation in the Eastern Alaska Range constrained by stacked thermochronology: Geological Society, London, Special Publications, v. 378, p. 225–243, doi: 10.1144/SP378.12.

Betka, P.M., Gillis, R.J., and Benowitz, J.A., 2017, Cenozoic sinistral transpression and polyphase slip within the Bruin Bay fault system, Iniskin-Tuxedni region, Cook Inlet, Alaska: Geosphere, v. 13, p. 1806–1833, doi: 10.1130/GES01464.1.

Bleick, H.A., Till, A.B., Bradley, D.C., O'Sullivan, P.B., Wooden, J.L., Bradley, D.B., Taylor, T.A., Friedman, S.B., and Hults, C.P., 2012, Early Tertiary exhumation of the flank of a forearc basin, southwest Talkeetna Mountains, Alaska: US Geological Survey Open-File Report, no. 2012-1232.

Breitsprecher, K., and Thorkelson, D.J., 2009, Neogene kinematic history of Nazca–Antarctic–Phoenix slab windows beneath Patagonia and the Antarctic Peninsula: Tectonophysics, v. 464, p. 10-20.

Bol, A.J., Coe, R.S., Groomé, C.S., and Hillhouse, J.W., 1992, Paleomagnetism of the Resurrection Peninsula, Alaska: Implications for the tectonics of southern Alaska and the Kula-Farallon ridge: Journal of Geophysical Research: Solid Earth, v. 97, p. 17213-17232.

Bowman, D., King, G., and Tapponnier, P., 2003, Slip partitioning by elastoplastic propagation of oblique slip at depth: Science, v. 300, p. 1121–1123, doi: 10.1126/science.1082180.

Bradley, D.C., Haeussler, P.J., and Kusky, T.M., 1992, Timing of early Tertiary ridge subduction in southern Alaska: Geologic studies in Alaska by the US Geological Survey, p. 163–177,

Bradley, D.C., McClelland, W.C., Wooden, J.L., Till, A.B., Roeske, S.M., Miller, M.L., and Glen, J.M.G., 2007, Detrital zircon geochronology of some Neoproterozoic to Triassic rocks in interior Alaska: Geological Society of America Special Papers, v. 431, p. 155-190.

Brennan, P.R.K., Gilbert, H., and Ridgway, K.D., 2011, Crustal structure across the central Alaska Range: Anatomy of a Mesozoic collisional zone: Geochemistry, Geophysics, Geosystems, v. 12, doi: 10.1029/2011GC003519.

Bristol, I., Trop, J., Benowitz, J., and Davis, K., 2017, Major Miocene paleodrainage in south-central Alaska: Sedimentology, depositional age and provenance of strata exposedin the southwestern Talkeetna Mountains: Geological Society of America Abstracts with Programs, v. 49, no. 4, doi:10.1130/abs/2017CD-292545.

Bunds, M.P., 2001, Fault strength and transpressional tectonics along the Castle Mountain strike-slip fault, Southern Alaska: Bulletin of the Geological Society of America, v. 113, p. 908–919, doi: 10.1130/0016-7606(2001)113<0908:FSATTA>2.0.CO;2.

Christeson, G.L., Gulick, S.P.S., van Avendonk, H.J.A., Worthington, L.L., Reece, R.S., and Pavlis, T.L., 2010, The Yakutat terrane: Dramatic change in crustal thickness across the transition fault, Alaska: Geology, v. 38, p. 895–898, doi: 10.1130/G31170.1.

Clardy, B.I., 1974, Origin of the Lower and Middle Tertiary Wishbone and Tsadaka formations, Matanuska Valley, Alaska: [M.S. thesis]: Fairbanks, Alaska, University of Alaska, 50 p.

Clendenen, W.S., Fisher, D. and Byrne, T., 2003, Cooling and exhumation history of the Kodiak accretionary prism, southwest Alaska: Geological Society of America Special Papers, p.71-88.

Cole, R.B., and Layer, P.W., 1984, Stratigraphy, age and geochemistry of Tertiary volcanic rocks and associated synorogenic deposits, Mount McKinley quadrangle, Alaska: US Geological Survey Professional Paper, v. 1662, p. 19.

Cole, R.B., Layer, P.W., Hooks, B., Cyr, A., and Turner, J., 2007, Magmatism and deformation in a terrane suture zone south of the Denali fault, northern Talkeetna Mountains, Alaska: The Geological Society of America Paper 431, v. 2431, p. 477–506, doi: 10.1130/2007.2431(19).

Cole, R.B., Nelson, S.W., Layer, P.W., and Oswald, P.J., 2006, Eocene volcanism above a depleted mantle slab window in southern Alaska: Bulletin of the Geological Society of America, v. 118, p. 140–158, doi: 10.1130/B25658.1.

Cole, R.B., Ridgway, K.D., Layer, P.W., and Drake, J., 1999, Kinematics of basin development during the transition from terrane accretion to strike-slip tectonics, Late Cretaceous-early Tertiary Cantwell Formation, south central Alaska: Tectonics, v. 18, p. 1224–1244, doi: 10.1029/1999TC900033.

Cole, R.B., and Stewart, B.W., 2009, Continental margin volcanism at sites of spreading ridge subduction: Examples from southern Alaska and western California: Tectonophysics, v. 464, p. 118–136, doi: 10.1016/j.tecto.2007.12.005.

Cowan, D.S., 2003, Revisiting the Baranof-Leech River hypothesis for early Tertiary coastwise transport of the Chugach-Prince William terrane: Earth and Planetary Science Letters, v. 213, p. 463–475, doi: 10.1016/S0012-821X(03)00300-5.

Csejtey, B., Nelson, W.H., Jones, D.L., Silberling, N.J., Dean, R.M., Morris, M.S., Lanphere, M.A., Smith, J.G., and Silberman, M.L., 1978, Reconnaissance geologic map and geochronology, Talkeetna Mountains quadrangle, northern part of Anchorage Quadrangle and southwest corner of Healy quadrangle, Alaska: US Geological Survey, no. 78-558 A.

Cunningham, D., 2005, Active intracontinental transpressional mountain building in the Mongolian Altai: Defining a new class of orogen: Earth and Planetary Science Letters, v. 240, p. 436–444, doi: 10.1016/j.epsl.2005.09.013.

Cunningham, W.D., 1993, Strike-slip faults in the southernmost andes and the development of the Patagonian orocline: Tectonics, v. 12, p. 169–186, doi: 10.1029/92TC01790.

Davidson, C. and Garver, J.I., 2017, Age and origin of the resurrection ophiolite and associated turbidites of the Chugach–Prince William Terrane, Kenai Peninsula, Alaska: The Journal of Geology, v. 125, p.681-700.

Dávila, F.M., and Carter, A., 2013, Exhumation history of the andean broken foreland revisited: Geology, v. 41, p. 443–446, doi: 10.1130/G33960.1.

Dickinson, W.R., and Snyder, W.S., 1979, Geometry of subducted slabs related to the San Andreas transform: Journal of Geology, v. 87, p. 609627.

Dodson, M.H., 1973, Closure temperature in cooling geochronological and petrological systems: Contributions to Mineralogy and Petrology, v. 40, p. 259–274, doi: 10.1007/BF00373790.

Donelick, R.A., O'Sullivan, P.B., and Ketcham, R.A., 2005, Apatite Fission-Track Analysis: Reviews in Mineralogy and Geochemistry, v. 58, p. 49–94, doi: 10.2138/rmg.2005.58.3.

Donelick, R.A., and Miller, D.S., 1991, Enhanced tint fission track densities in low spontaneous track density apatites using 252Cf-derived fission fragment tracks: A model and experimental observations: International Journal of Radiation Applications and Instrumentation. Part, v. 18, p. 301–307, doi: 10.1016/1359-0189(91)90022-A.

Doubrovine, P. V., and Tarduno, J.A., 2008, A revised kinematic model for the relative motion between Pacific oceanic plates and North America since the Late Cretaceous: Journal of Geophysical Research: Solid Earth, v. 113, doi: 10.1029/2008JB005585.

Dusel-Bacon, C., and Murphy, J.M., 2001, Apatite fission-track evidence of widespread Eocene heating and exhumation in the Yukon-Tanana Upland, interior Alaska: Canadian Journal of Earth Sciences, v. 38, p. 1191–1204, doi: 10.1139/cjes-38-8-1191.

Dyksterhuis, S., and Müller, R.D., 2008, Cause and evolution of intraplate orogeny in Australia: Geology, v. 36, p. 495–498, doi: 10.1130/G24536A.1.

Eberhart-Phillips, D., Christensen, D.H., Brocher, T.M., Hansen, R., Ruppert, N.A., Haeussler, P.J., and Abers, G.A., 2006, Imaging the transition from Aleutian subduction to Yakutat collision in central Alaska, with local earthquakes and active source data: Journal of Geophysical Research: Solid Earth, v. 111, doi: 10.1029/2005JB004240.

Enkelmann, E., Piestrzeniewicz, A., Falkowski, S., Stübner, K., and Ehlers, T.A., 2017, Thermochronology in southeast Alaska and southwest Yukon: Implications for North American Plate response to terrane accretion: Earth and Planetary Science Letters, v. 457, p. 348–358, doi: 10.1016/j.epsl.2016.10.032.

Farley, K.A., 2002, (U-Th)/He dating: Techniques, calibrations, and applications: Reviews in Mineralogy and Geochemistry, v. 47, p. 819-844.

Farris, D.W., Haeussler, P., Friedman, R., Paterson, S.R., Saltus, R.W. and Ayuso, R., 2006, Emplacement of the Kodiak batholith and slab-window migration: Geological Society of America Bulletin, v. 118, p.1360-1376.

Farris, D.W., and Paterson, S.R., 2009, Subduction of a segmented ridge along a curved continental margin: Variations between the western and eastern Sanak-Baranof belt, southern Alaska: Tectonophysics, v. 464, p. 100–117, doi: 10.1016/j.tecto.2007.10.008.

Finzel, E.S., Enkelmann, E., Falkowski, S., and Hedeen, T., 2016, Long-term fore-arc basin evolution in response to changing subduction styles in southern Alaska: Tectonics, v. 35, p. 1735–1759, doi: 10.1002/2016TC004171.

Finzel, E.S., Flesch, L.M., Ridgway, K.D., Holt, W.E., and Ghosh, A., 2015, Surface motions and intraplate continental deformation in Alaska driven by mantle flow: Geophysical Research Letters, v. 42, p. 4350–4358, doi: 10.1002/2015GL063987.

Finzel, E.S., Trop, J.M., Ridgway, K.D., and Enkelmann, E., 2011, Upper plate proxies for flat-slab subduction processes in southern Alaska: Earth and Planetary Science Letters, v. 303, p. 348–360, doi: 10.1016/j.epsl.2011.01.014.

Fitzgerald, P.G., Roeske, S.M., Benowitz, J.A., Riccio, S.J., Perry, S.E., and Armstrong, P.A., 2014, Alternating asymmetric topography of the Alaska range along the strike-slip Denali fault: Strain partitioning and lithospheric control across a terrane suture zone: Tectonics, v. 33, p. 1519–1533, doi: 10.1002/2013TC003432.

Fitzgerald, P.G., Stump, E., and Redfield, T.F., 1993, Late cenozoic uplift of denali and its relation to relative plate motion and fault morphology: Science (New York, N.Y.), v. 259, p. 497–499, doi: 10.1126/science.259.5094.497.

Frohman, R.A., 2014, Identification and evolution of tectonic faults in the greater Fairbanks Area, Alaska [M.S. Thesis], Fairbanks, Alaska, University of Alaska, Fairbanks.

Fuchs, W.A., 1980, Tertiary tectonic history of the Castle Mountain fault system in the Talkeetna Mountains: [Ph. D. dissertation]: Salt Lake City, University of Utah, p. 152.

Gabrielse, H., 1985, Major dextral transcurrent displacements along the Northern Rocky Mountain Trench and related lineaments in north-central British Columbia: Geological Society of America Bulletin, v. 96, no. 1, p. 1–14, doi: 10.1130/0016-7606(1985)962.0.CO;2.

Garver, J.I., 2017, Accretion and translation of the Chugach, Prince William and Yakutat Terranes in Aalaska: Geological Society of America Abstracts with Programs, v. 49, No. 6, doi: 10.1130/abs/2017 AM-302956.

Garver, J.I., and Davidson, C.M., 2015, Southwestern Laurentian zircons in Upper Cretaceous flysch of the Chugach-Prince William terrane in Alaska: American Journal of Science, v. 315, p. 537–556, doi: 10.2475/06.2015.02.

Gasser, D., Bruand, E., Stüwe, K., Foster, D.A., Schuster, R., Fügenschuh, B. and Pavlis, T., 2011, Formation of a metamorphic complex along an obliquely convergent margin: Structural and thermochronological evolution of the Chugach Metamorphic Complex, southern Alaska. Tectonics, v. 30.

Grantz, A., 1966, Strike-slip faults in Alaska: US Geological Survey Report, No. 66-53.

Guenthner, W.R., Barbeau, D.L., Reiners, P.W., and Thomson, S.N., 2010, Slab window migration and terrane accretion preserved by low-temperature thermochronology of a magmatic arc, northern Antarctic Peninsula: Geochemistry, Geophysics, Geosystems, v. 11, doi: 10.1029/2009GC002765.

Gutscher, M.A., Spakman, W., Bijwaard, H., and Engdahl, E.R., 2000, Geodynamics of flat subduction: Seismicity and tomographic constraints from the Andean margin: Tectonics, v. 19, p. 814–833, doi: 10.1029/1999TC001152.

Hacker, B.R., Kelemen, P.B., Rioux, M., McWilliams, M.O., Gans, P.B., Reiners, P.W., Layer, P.W., Söderlund, U., and Vervoort, J.D., 2011, Thermochronology of the Talkeetna intraoceanic arc of Alaska: Ar/Ar, U-Th/He, Sm-Nd, and Lu-Hf dating: Tectonics, v. 30, doi: 10.1029/2010TC002798.

Haeussler, P.J., Freymueller, J.T., and Wesson, R.L., 2008, An Overview of the Neotectonics of Interior Alaska : Far-F ield Deformation From the Yakutat Microplate Colli sion: Active Tectonics and Seismic Potential of Alaska, p. 83–108.

Haeussler, P.J., Best, T.C., and Waythomas, C.F., 2002, Paleoseismology at high latitudes: Seismic disturbance of upper Quaternary deposits along the Castle Mountain fault near Houston, Alaska: Bulletin of the Geological Society of America, v. 114, p. 1296–1310, doi: 10.1130/0016-7606(2002)114<1296:PAHLSD>2.0.CO;2.

Haeussler, P.J., Bradley, D., Goldfarb, R., Snee, L. and Taylor, C., 1995, Link between ridge subduction and gold mineralization in southern Alaska: Geology, v. 23, p.995-998.

Haeussler, P.J., Bradley, D.C., Wells, R.E., and Miller, M.L., 2003, Life and death of the resurrection plate: Evidence for its existence and subduction in the northeastern Pacific in Paleocene-Eocene time: Bulletin of the Geological Society of America, v. 115, p. 867–880, doi: 10.1130/0016-7606(2003)115<0867:LADOTR>2.0.CO;2.

Hampton, B. A., Ridgway, K. D., & Gehrels, G. E., 2010, A detrital record of Mesozoic island arc accretion and exhumation in the North American Cordillera: U-Pb geochronology of the Kahiltna basin, southern Alaska: Tectonics, v. 29.

Harlan, S.S., Vielreicher, R.M., Mortensen, J.M., Bradley, D.C., Goldfarb, R.J., Snee, L.W., and Till, A.B., 2017, Geology and timing of ore formation in the Willow Creek Gold District, Talkeetna Mountains, Southern Alaska: Economic Geology, v. 112, p. 1177–1204, doi: 10.5382/econgeo.2017.4506.

Hasebe, N., Barbarand, J., Jarvis, K., Carter, A., and Hurford, A.J., 2004, Apatite fission-track chronometry using laser ablation ICP-MS: Chemical Geology, v. 207, p. 135–145, doi: 10.1016/j.chemgeo.2004.01.007.

Hillhouse, J.W., Coe, R.S., Plafker, G., and Berg, H.C., 1994, Paleomagnetic data from Alaska, eds. The geology of Alaska: Boulder, Colorado: Geological Society of America, Geology of North America, v. G-1, p. 797-812.

Hoffman, M.D., and Armstrong, P.A., 2006, Miocene exhumation of the southern Talkeetna Mountains, south-central Alaska, based on apatite (U-Th)/He thermochronology: Geological Society of America Abstracts with Programs, v. 38, no. 5, p. 9.

Jadamec, M.A., Billen, M.I., and Roeske, S.M., 2013, Three-dimensional numerical models of flat slab subduction and the Denali fault driving deformation in south-central Alaska: Earth and Planetary Science Letters, v. 376, doi: 10.1016/j.epsl.2013.06.009.

Jicha, B.R., Scholl, D.W., Singer, B.S., Yogodzinski, G.M., and Kay, S.M., 2006, Revised age of Aleutian Island Arc formation implies high rate of magma production: Geology, v. 34, p. 661–664, doi: 10.1130/G22433.1.

Kalbas, J.L., Freed, A.M., and Ridgway, K.D., 2008, Contemporary fault mechanics in southern Alaska, *in* Geophysical Monograph Series, v. 179, p. 321–336, doi: 10.1029/179GM18.

Kassab, C.M., Kortyna, C.D., Ridgway, K.D., and Trop, J.M., 2009, Sedimentology, structural framework, and basin analysis of the eastern Arkose Ridge Formation, Talkeetna Mountains, Alaska: Geological Society of America Abstracts with Programs, v. 41, no. 7, p. 304.

Ketcham, R.A., 2007, Apatite to Zircon. Inc: 2007b, HeFTy software version 1.4.

Ketcham, R.A., Gautheron, C., and Tassan-Got, L., 2011, Accounting for long alpha-particle stopping distances in (U-Th-Sm)/He geochronology: Refinement of the baseline case: Geochemica et Cosmochimica Acta, v. 75, p. 7779-7791.

Kluth, C.F., and Coney, P.J., 1981, Plate tectonics of the Ancestral Rocky Mountains: Geology, v. 9, p. 10–15, doi: 10.1130/0091-7613(1981)9<10:PTOTAR>2.0.CO;2.

Kochelek, E.J., Amato, J.M., Pavlis, T.L., and Clift, P.D., 2011, Flysch deposition and preservation of coherent bedding in an accretionary complex: Detrital zircon ages from the Upper Cretaceous Valdez Group, Chugach terrane, Alaska: Lithosphere, v. 3, p. 265–274, doi: 10.1130/L131.1.

Koehler III, R.D., Reger, R.D., Carver, G.A., Spangler, E., and Gould, A., 2014, Castle Mountain Fault southcentral Alaska: Observations on slip partitioning from lidar and paleoseismic trenching: Geological Society of America Abstracts with Programs, v. 46, no. 6, p. 661.

Kortyna, C., Donaghy, E., Trop, J.M., and Idleman, B., 2013, Integrated provenance record of a forearc basin modified by slab-window magmatism: Detrital- zircon geochronology and sandstone compositions of the Paleogene Arkose Ridge Formation, south-central Alaska: Basin Research, v. 26, p. 436–460, doi: 10.1111/bre.12033.

Kusky, T.M., Bradley, D.C. and Haeussler, P., 1997, Progressive deformation of the Chugach accretionary complex, Alaska, during a Paleogene ridge-trench encounter: Journal of Structural Geology, v. 19, p.139-157.

Kusky, T., Haeussler, P., Coldfarb, R., Miller, M. and Dumoulin, J., 2003, Geologic signature of early Tertiary ridge subduction in Alaska: Geology of a transpressional orogen developed during ridge-trench interaction along the North Pacific margin, v. 371, p.19.

Kveton, K., 1989, Structure, thermochronology, provenance and tectonic history of the Orca Group in southwestern Prince William south Alaska [P.h D. dissertation], Seattle, Washington, University of Washington.

Layer, P.W., Hall, C.M., and York, D., 1987, The derivation of $^{40}Ar/^{39}Ar$ age spectra of single grains of hornblende and biotite by laser step-heating: Geophysical Research Letters, v. 14, p. 757-760.

Layer, P.W., 2000, Argon-40/Argon-39 age of El'gygytgyn impact event, Chukotka, Russia: Meteoritics and Planetary Science, v. 35, p. 591-599.

Lease, R.O., Haeussler, P.J., and O'Sullivan, P., 2016, Changing exhumation patterns during Cenozoic growth and glaciation of the Alaska Range: Insights from detrital thermochronology and geochronology: Tectonics, v. 35, p. 934–955, doi: 10.1002/2015TC004067.

Li, Z.X., Li, X.H., Chung, S.L., Lo, C.H., Xu, X., and Li, W.X., 2012, Magmatic switch-on and switch-off along the South China continental margin since the Permian: Transition from an Andean-type to a Western Pacific-type plate boundary: Tectonophysics, v. 532–535, p. 271–290, doi: 10.1016/j.tecto.2012.02.011.

Li, ., Zhang, M., Fu, P., Qian, Z., Hu, P. and Ripley, E.M., 2012, The Kalatongke magmatic Ni–Cu deposits in the Central Asian Orogenic Belt, NW China: product of slab window magmatism?: Mineralium Deposita, v. 47, p.51-67.

Little, T.A., 1990, Kinematics of wrench and divergent-wrench deformation along a central part of the Border Ranges Fault System, Northern Chugach Mountains, Alaska: Tectonics, v. 9, p. 585–611, doi: 10.1029/TC009i004p00585.

Little, T.A., and Naeser, C.W., 1989, Tertiary tectonics of the Border Ranges fault system, Chugach Mountains, Alaska: Deformation and uplift in a forearc setting: Journal of Geophysical Research: Solid Earth, v. 94, p. 4333-4359.

Löbens, S., Oriolo, S., Benowitz, J., Wemmer, K., Layer, P., and Siegesmund, S., 2017, Late Paleozoic deformation and exhumation in the Sierras Pampeanas (Argentina): 40Ar/39Ar-feldspar dating constraints: International Journal of Earth Sciences, v. 106, p. 1991–2003, doi: 10.1007/s00531-016-1403-3.

Lovera, O.M., Grove, M., and Harrison, T.M., 2002, Systematic analysis of K-feldspar $^{40}Ar/^{39}Ar$ step heating results II: Relevance of laboratory argon diffusion properties to nature: Geochemica et Cosmochimica Acta, v. 66, p. 1237-1255.

Lowey, G.W., 1998, A new estimate of the amount of displacement on the Denali Fault system based on the occurrence of carbonate megaboulders in the Dezadeash Formation (Jura-Cretaceous), Yukon, and the Nutzotin Mountains sequence (Jura-Cretaceous), Alaska: Bulletin of Canadian Petroleum Geology, v. 46, p. 379–386.

Lytwyn, J., Lockhart, S., Casey, J. and Kusky, T., 2000, Geochemistry of near-trench intrusives associated with ridge subduction, Seldovia quadrangle, southern Alaska: Journal of Geophysical Research: Solid Earth, v. 105, p.27957-27978.

Madsen, J.K., Thorkelson, D.J., Friedman, R.M., and Marshall, D.D., 2006, Cenozoic to recent plate configurations in the Pacific Basin: Ridge subduction and slab window magmatism in Western North America: Geosphere, v. 2, p. 11–34, doi: 10.1130/GES00020.1.

Mankhemthong, N., Doser, D.I., and Pavlis, T.L., 2013, Interpretation of gravity and magnetic data and development of two-dimensional cross-sectional models for the border ranges fault system, south-central alaska: Geosphere, v. 9, p. 242–259, doi: 10.1130/GES00833.1.

McDougall, I., and Harrison, T.M., 1999, Geochronology and thermochronology by the $^{40}Ar/^{39}Ar$ method: Oxford Univ. Press, New York, p.269.

Michaud, F., Royer, J.Y., Bourgois, J., Dyment, J., Calmus, T., Bandy, W., Sosson, M., Mortera-Gutiérrez, C., Sichler, B., Rebolledo-Viera, M., and Pontoise, B., 2006, Oceanic-ridge subduction vs. slab break off: Plate tectonic evolution along the Baja California Sur continental margin since 15 Ma: Geology, v. 34, p. 13–16, doi: 10.1130/g22050.1.

Nokleberg, W.J., and Richter, D.H., 2007, Origin of narrow terranes and adjacent major terranes occurring along the Denali fault in the Eastern and Central Alaska Range, Alaska: Geological Society of America Special Papers, v. 431, p. 129–154, doi: 10.1130/2007.2431(06).

O'Sullivan, P.B., and Currie, L.D., 1996, Thermotectonic history of Mt Logan, Yukon Territory, Canada: implications of multiple episodes of middle to late Cenozoic denudation: Earth and Planetary Science Letters, v. 144, p. 251–261, doi: 10.1016/0012-821X(96)00161-6.

O'Sullivan, P., Donelick, M., and Donelick, R., 2010, Apatite fission-track resultsfrom the regionof the Pebble Deposit, southwest Alaska: Apatite to Zircon Inc., Report no. 950, minerals.usgs.gov/mrerp/reports/O'Sullivan-08HQGR0061.pdf.

Oswald, P.J., 2006, Eocene volcanic rocks of the southern Talkeetna Mountains, Alaska: Anomalous forearc volcanism in an extensional setting: [Ph. D. dissertation], University of Idaho.

Panuska, B. C., Stone, D.B., and Turner, D.L., 1990, Paleomagnetism of Eocene volcanic rocks, Talkeetna Mountains, Alaska: Journal of Geophysical Research: Solid Earth, v. 95 no. B5, pp. 6737-6750.

Parry, W.T., Bunds, M.P., Bruhn, R.L., Hall, C.M., and Murphy, J.M., 2001, Mineralogy,40Ar39dating and apatite fission track dating of rocks along the Castle Mountain fault, Alaska: Tectonophysics, v. 337, p. 149–172, doi: 10.1016/S0040-1951(01)00117-2.

Pavlis, T.L., and Roeske, S.M., 2007, The Border Ranges fault system, southern Alaska: Geological Society of America Special Paper 431, p. 95–127, doi: doi:10.1130/2007.2431(05).

Pavlis, T.L. and Sisson, V.B., 2003, Development of a subhorizontal decoupling horizon in a transpressional system, Chugach metamorphic complex, Alaska: Evidence for rheological stratification of the crust. Special paper-Geological Society of America, v. 371, p.191-216.

Plafker, G., and Berg, H.C.,1994, Overview of the geology and tectonic evolution of Alaska. In: *The Geology of Alaska* (Ed. by G. Plafker and H.C. Berg), The Geology of North America Geological Society of America, v. G-1, 989–1021.

Reed, B.L., and Lanphere, M.A., 1972, Generalized geologic map of the Alaska-Aleutian Range batholith showing potassium-argon ages of the plutonic rocks: US Geological Survey Field Study Map, no. 372.

Reiners, P.W., 2007, Thermochronologic Approaches to Paleotopography: Reviews in Mineralogy and Geochemistry, v. 66, p. 243–267, doi: 10.2138/rmg.2007.66.10.

Reiners, P.W., and Brandon, M.T., 2006, USING THERMOCHRONOLOGY TO UNDERSTAND OROGENIC EROSION: Annual Review of Earth and Planetary Sciences, v. 34, p. 419–466, doi: 10.1146/annurev.earth.34.031405.125202.

Reiners, P.W., and Farley, K.A., 2001, Influence of crystal size on apatite (U-Th)/He thermochronology: An example from the Bighorn Mountains, Wyoming: Earth and Planetary Science Letters, v. 188, p. 413–420, doi: 10.1016/S0012-821X(01)00341-7.

Renne, P.R., 1994, Intercalibration of astronomical and radioisotopic time: Geology, v. 22, p. 783–786, doi: 10.1130/0091-7613(1994)022<0783:IOAART>2.3.CO.

Renne, P.R., Mundil, R., Balco, G., Min, K., and Ludwig, K.R., 2010, Joint determination of 40K decay constants and 40Ar*/40K for the Fish Canyon sanidine standard, and improved accuracy for 40Ar/39Ar geochronology: Geochimica et Cosmochimica Acta, v. 74, p. 5349–5367, doi: 10.1016/j.gca.2010.06.017.

Riccio, S.J., Fitzgerald, P.G., Benowitz, J.A., and Roeske, S.M., 2014, The role of thrust faulting in the formation of the eastern Alaska Range: Thermochronological constraints from the Susitna Glacier Thrust Fault region of the intracontinental strike-slip Denali Fault system: Tectonics, v. 33, p. 2195–2217, doi: 10.1002/2014TC003646.

Ridgway, K.D., Finzel, E.S., and Trop, J.M., 2012, Modification of Continental Forearc Basins by Flat-Slab Subduction Processes: A Case Study from Southern Alaska, in Tectonics of Sedimentary Basins: Recent Advances, p. 327–346, doi: 10.1002/9781444347166.ch16.

Ridgway, K.D., Thoms, E.E., Layer, P.W., Lesh, M.E., White, J.M. and Smith, S.V., 2007. Neogene transpressional foreland basin development on the north side of the central Alaska Range, Usibelli Group and Nenana Gravel, Tanana basin: Special Paper of the Geological Society of America, v. 431, p.507-547.

Ridgway, K.D., Trop, J.M., Nokleberg, W.J., Davidson, C.M. and Eastham, K.R., 2002. Mesozoic and Cenozoic tectonics of the eastern and central Alaska Range: Progressive basin development and deformation in a suture zone. Geological Society of America Bulletin, 114(12), pp.1480-1504.

Rioux, M., Hacker, B., Mattinson, J., Kelemen, P., Blusztajn, J., and Gehrels, G., 2007, Magmatic development of an intra-oceanic arc: High-precision U-Pb zircon and whole-rock isotopic analyses from the accreted Talkeetna arc, south-central Alaska: Bulletin of the Geological Society of America, v. 119, p. 1168–1184, doi: 10.1130/B25964.1.

Robertson, P.B., 2015, Structural configuration of a modified Mesozoic to Cenozoic forearc basin system, south-central Alaska: [M.S. Thesis], Purdue University.

Roden, M.K., and Miller, D.S., 1989, Apatite fission-track thermochronology of the Pennsylvania Appalachian Basin: Geomorphology, v. 2, p. 39–51, doi: 10.1016/0169-555X(89)90005-6.

Roeske, S.M., Snee, L.W., and Pavlis, T.L., 2003, Dextral-slip reactivation of an arc-forearc boundary during Late Cretaceous-Early Eocene oblique convergence in the northern Cordillera: Geology of a Transpressional Orogen Developed During Ridge–Trench Interaction Along the North Pacific Margin. Geological Society of America, Special Papers, v. 371, p. 141–169.

Sagar, M.W., Seward, D., and Norton, K.P., 2016, Thermochronology, uplift and erosion at the Australian-Pacific plate boundary Alpine Fault restraining bend, New Zealand: American Geopshysical Union, Fall General Assembly 2016, abstract id. T41B-2930.

Sakaguchi, A., 1996, High paleogeothermal gradient with ridge subduction beneath the Cretaceous Shimanto accretionary prism, southwest Japan: Geology, v. 24, p. 795–798, doi: 10.1130/0091-7613(1996)024<0795:HPGWRS>2.3.CO;2.

Sample, J.C., Reid, M.R., Sisson, V.B., Roeske, S.M. and Pavlis, T.L., 2003, Large-scale, latest Cretaceous uplift along the Northeast Pacific Rim: Evidence from sediment volume, sandstone petrography, and Nd isotope signatures of the Kodiak Formation, Kodiak Islands, Alaska: Geological Society of America Special Papers, p.51-70.

Samson, S.D., and Alexander, E.C., 1987, Calibration of the interlaboratory 40Ar39Ar dating standard, MMhb-1: Chemical Geology: Isotope Geoscience Section, v. 66, p. 27–34, doi: 10.1016/0168-9622(87)90025-X.

Scharman, M.R., Pavlis, T.L. and Ruppert, N., 2012, Crustal stabilization through the processes of ridge subduction: examples from the Chugach metamorphic complex, southern Alaska: Earth and Planetary Science Letters, v. 329, p.122-132.

Silberman, M.L., and Grantz. A., 1984, Paleogene volcanic rocks of the Matanuska Valley area and the displacement history of the Castle Mountain fault: US Geological Survey Circular 868, p. 82-86.

Sisson, V.B., Pavlis, T.L., Roeske, S.M. and Thorkelson, D.J., 2003. Introduction: An overview of ridge-trench interactions in modern and ancient settings: Geological Society of America Special Papers, v. 371, p.1-18.

Spotila, J.A., 2005, Applications of low-temperature thermochronometry to quantification of recent exhumation in mountain belts: Reviews in Mineralogy and Geochemistry, v. 58, p. 449-466.

Spotila, J.A., and Berger, A.L., 2010, Exhumation at orogenic indentor corners under long-term glacial conditions: Example of the St. Elias orogen, Southern Alaska: Tectonophysics, v. 490, p. 241–256, doi: 10.1016/j.tecto.2010.05.015.

Stamatakos, J.A., Trop, J.M., and Ridgway, K.D., 2001, Late cretaceous paleogeography of Wrangellia: Paleomagnetismof the MacColl Ridge Formation, southern Alaska, revisited: Geology, v. 29, p. 947–950, doi: 10.1130/0091-7613(2001)029<0947:LCPOWP>2.0.CO;2.

Stanley, R.G., Haeussler, P.J., Benowitz, J.A., Lewis, K.A., Shellenbaum, D.P., Saltus, R.W., Shah, A.K., Phillips, J.D., and Potter,C.J., 2014, Tectonic implications of new geological and geophysical results from the Susitna basin, south-central Alaska: Search and Discovery Article, 10608.

Stern, R.J., and Gerya, T., 2017, Subduction initiation in nature and models: A review: Tectonophysics, doi: 10.1016/j.tecto.2017.10.014.

Storti, F., Holdsworth, R.E., and Salvini, F., 2003, Intraplate strike-slip deformation belts: Geological Society, London, Special Publications, v. 210, p. 1–14, doi: 10.1144/GSL.SP.2003.210.01.01.

Sunderlin, D., Trop, J.M., Idleman, B.D., Brannick, A., White, J.G., and Grande, L., 2014, Paleoenvironment and paleoecology of a Late Paleocene high-latitude terrestrial succession, Arkose Ridge Formation at Box Canyon, southern Talkeetna Mountains, Alaska: Palaeogeography, Palaeoclimatology, Palaeoecology, v. 401, p. 57–80, doi: 10.1016/j.palaeo.2014.02.012.

Sylvester, A.G., 1988, Strike-slip faults: Geological Society of America Bulletin, p. 1–38, doi: 10.1130/0016-7606(1988)100<1666.

Tagami, T., and O'Sullivan P.B., 2005, Fundamentals of Fission-Track Thermochronology: Reviews in Mineralogy and Geochemistry, v. 58, p. 19–47, doi: 10.2138/rmg.2005.58.2.

Tempelman-Kluit, D.J., and Wanless, R.K., 1975, Potassium-argon age determinations of metamorphic and plutonic rocks in the Yukon Crystalline Terrane: Canadian Journal of Earth Sciences, v. 12, no. 11, pp. 1895-1909.

Thorkelson, D.J., 1996, Subduction of diverging plates and the principles of slab window formation: Tectonophysics, v. 255, p. 47-63.

Torsvik, T.H., Doubrovine, P. V., Steinberger, B., Gaina, C., Spakman, W., and Domeier, M., 2017, Pacific plate motion change caused the Hawaiian-Emperor Bend: Nature Communications, v. 8, doi: 10.1038/ncomms15660.

Trop, J.M., 2008, Latest Cretaceous forearc basin development along an accretionary convergent margin: South-central Alaska: GSA Bulletin, v. 120, p. 207–224, doi: 10.1130/B26215.1.

Trop, J.M., Hart, W.K., Snyder, D., and Idleman, B., 2012, Miocene basin development and volcanism along a strike-slip to flat-slab subduction transition: Stratigraphy, geochemistry, and geochronology of the central Wrangell volcanic belt, Yakutat-North America collision zone: Geosphere, v. 8, p. 805–834, doi: 10.1130/GES00762.1.

Trop, J.M., and Ridgway, K.D., 2007, Mesozoic and Cenozoic tectonic growth of southern Alaska : A sedimentary basin perspective: Tectonic growth of a collisional continental margin: Crustal evolution of south-central Alaska, v. 2431, p. 55–94, doi: 10.1130/2007.2431(04).

Trop, J.M., Ridgway, K.D., and Spell, T.L., 2003, Sedimentary record of transpressional tectonics and ridge subduction in the Tertiary Matanuska Valley-Talkeetna Mountains forearc basin, southern Alaska, in Special Paper 371: Geology of a transpressional orogen developed during ridge-trench interaction along the North Pacific margin, p. 89–118, doi: 10.1130/0-8137-2371-X.89.

Trop, J.M., Idleman, B., Ridgway, K.D., Sunderlin, D.,Cole, R.B., Donaghy, E.E., and Robertson, P.B., 2015, Sedimentary record of Paleogene basin development deformation and exhumation during spreading ridge subduction on southern Alaska: Geological Society of America Abstracts with Programs, v. 47, n. 4, p. 9.

Trop, J.M., Szuch, D.A., Rioux, M., and Blodgett, R.B., 2005, Sedimentology and provenance of the Upper Jurassic Naknek Formation, Talkeetna Mountains, Alaska: Bearings on the accretionary tectonic history of the Wrangellia composite terrane: Bulletin of the Geological Society of America, v. 117, p. 570–588, doi: 10.1130/B25575.1.

Valentino, J.D., Spotila, J.A., Owen, L.A., and Buscher, J.T., 2016, Rock uplift at the transition from flat-slab to normal subduction: The Kenai Mountains, Southeast Alaska: Tectonophysics, v. 671, p. 63–75, doi: 10.1016/j.tecto.2016.01.022.

Vogl, J.J., Min, K., Carmenate, A., Foster, D.A., and Marsellos, A., 2014, Miocene regional hotspot-related uplift, exhumation, and extension north of the Snake River Plain: Evidence from apatite (U-Th)/He thermochronology: Lithosphere, v. 6, p. 108–123, doi: 10.1130/L308.1.

Ward, D.J., 2010, The effects of lithology on glacial landscape evolution, paced using terrestrial cosmogenic nuclides: Examples from the Colorado Rocky Mountains and the Kichatna Mountains, Alaska Range, Alaska: [Ph. D. dissertation], University of Colorado, Boulder.

Williams, J.R., Carter, L.D., Hamilton, T.D., and Galloway, J.P., 1989, A working glacial chronology for the western Copper River basin, Alaska: Late Cenozoic history of the interior basins of Alaska and the Yukon, v. 1026, p. 81-85.

Willis, J.B., Haeussler, P.J., Bruhn, R.L., and Willis, G.C., 2007, Holocene slip rate for the western segment of the Castle Mountain fault, Alaska: Bulletin of the Seismological Society of America, v. 97, p. 1019–1024, doi: 10.1785/0120060109.

Wilson, F.H., Hults, C.P., Mull, C.G., and Karl, S.M., 2015, Geologic map of Alaska: US Geological Survey Scientific Investigations Map 3340, pamphlet 196, p., 2 sheets, scale 1:1,584,000, http://doi.org/10.3133/sim3340.

Worthington, L.L., Van Avendonk, H.J.A., Gulick, S.P.S., Christeson, G.L., and Pavlis, T.L., 2012, Crustal structure of the Yakutat terrane and the evolution of subduction and collision in southern Alaska: Journal of Geophysical Research: Solid Earth, v. 117, doi: 10.1029/2011JB008493.

Yin, A., Robinson, A., and Manning, C.E., 2001, Oroclinal bending and slab-break-off causing coeval east-west extension and east-west contraction in the Pamir-Nanga Parbat syntaxis in the past 10 my: American Geophysical Union Fall Meeting Abstracts, abstract id. T12F-03.

York, D., Hall, C.M., Yanase, Y., Hanes, J.A., and Kenyon, W.J., 1981, $^{40}Ar/^{39}Ar$ dating of terrestrial minerals with a continuous laser: Geosphysical Research Letters, v. 8, p. 1136-1138.

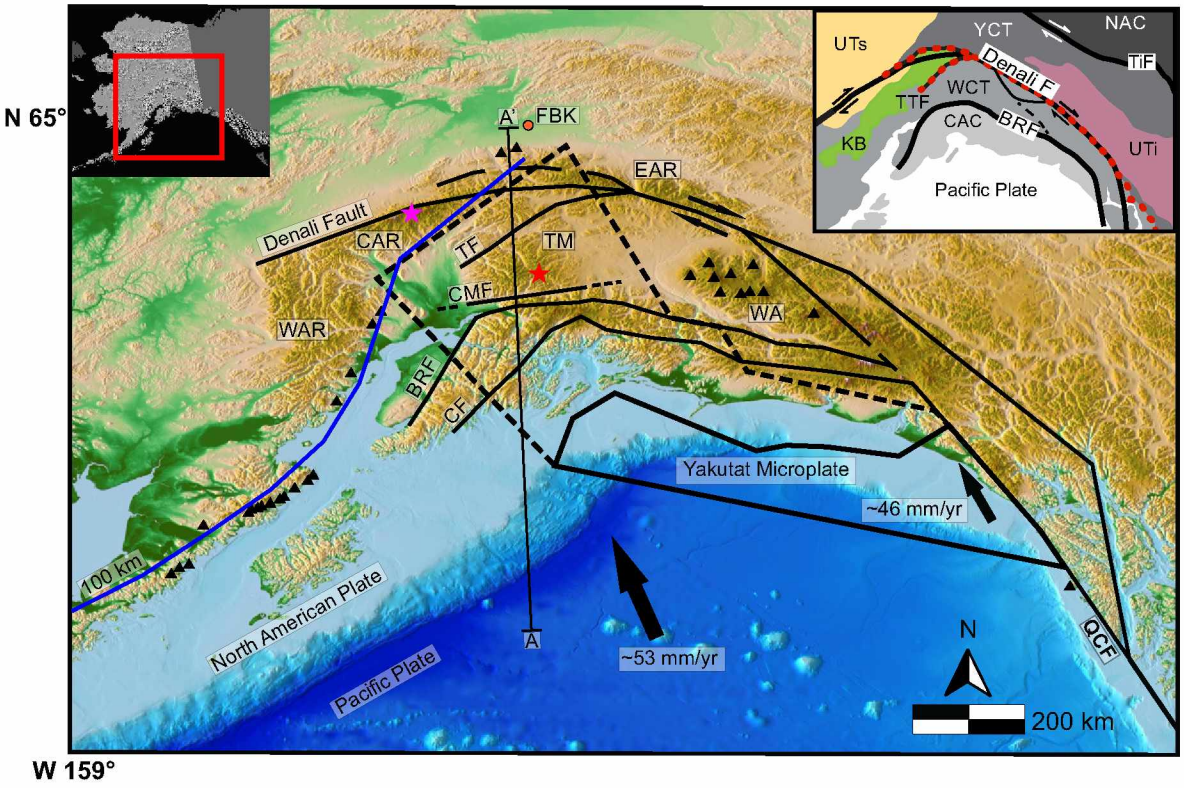

Figure 1. Simplified tectonic setting of southern Alaska. Inset map in upper left shows location in southern Alaska. Inset map in upper right shows major accreted terranes. YCT: Yukon Composite Terrane, WCT: Wrangellia Composite Terrane, CAC: Chugach Accretionery Complex, TiF: Tintina Fault, UTi: undifferentiated terranes and igneous rocks, UTs: unidentified terranes and sedimentary rocks, KB Kahiltna Basin NAC: North American Craton, and red dotted line: Mesozoic suture zone between continental (YCT) and oceanic (WCT) terranes. TF: Talkeetna Fault, BRF: Border Ranges Fault CMF: Castle Mountain Fault, CF: Contact Fault, QCF: Queen Charlotte-Fairweather Fault. TM: Talkeetna Mountains, WAR: western Alaska Range, CAR: central Alaska Range, EAR: eastern Alaska Range, WA: Wrangell Arc, FBK, Fairbanks. Pink star: Denali, red star: Mount Sovereign. Black triangles: volcanoes. Black dashed line is the subducted portion of the Yakutat Microplate from Eberhart-Phillips et al., 2006. A to A' transect: on figures 4, 21 and 23.

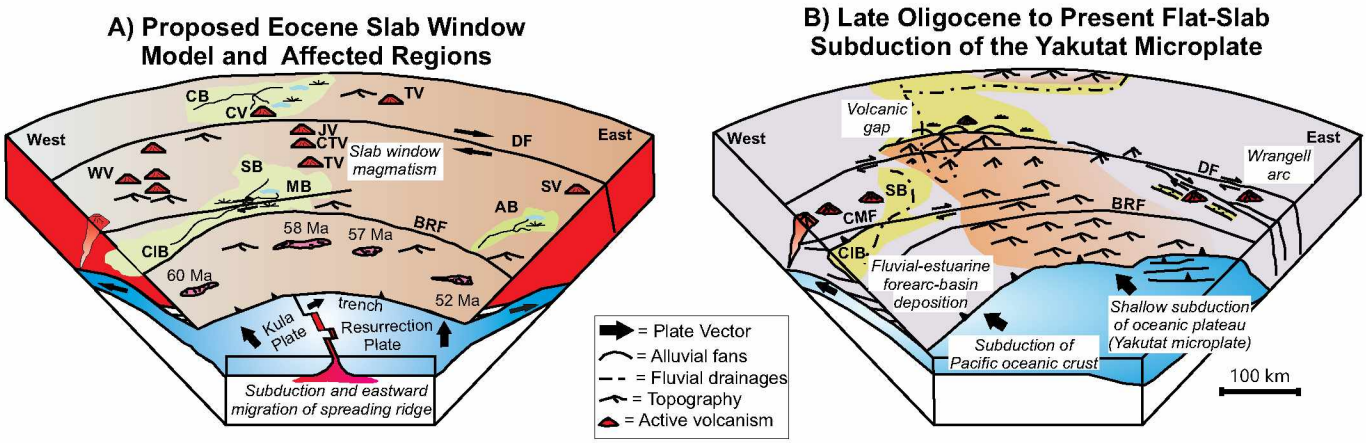

Figure 2. A) Paleocene-Eocene slab window summary figure, based on the proposed model by Haeussler et al., 2003, showing near-trench pluton emplacement ages, ages of initiation of rapid exhumation, basin formation, and regional magmatism across the region of Alaska affected by the flat-slab proposed Paleocene-Eocene ridge subduction event. B) Flat-slab subduction of the Yakutat microplate summary figure showing regions of basin subsidence, mountain building, the presence of an Aleutian Arc volcanic gap, and the initiation of the Wrangell Arc. Cook Inlet Basin: CIB; Susitna Basin: SB; Matanuska Basin: MB; Cantwell Basin: CB; Amphitheater Basin: AB. Western Alaska Range Volcanics: WV; Jack River Volcanics: JV; Central Talkeetna Volcanics: CTV; Caribou Hill Volcanics: CV; Tanana Valley Volcanics: TV; Sifton Volcanics: SV. Denali Fault: DF; Border Ranges Fault system: BRF; Castle Mountain: CMF; Talkeetna Fault: TF. Modified from Ridgway et al. (2012) and Benowitz et al. (2012).

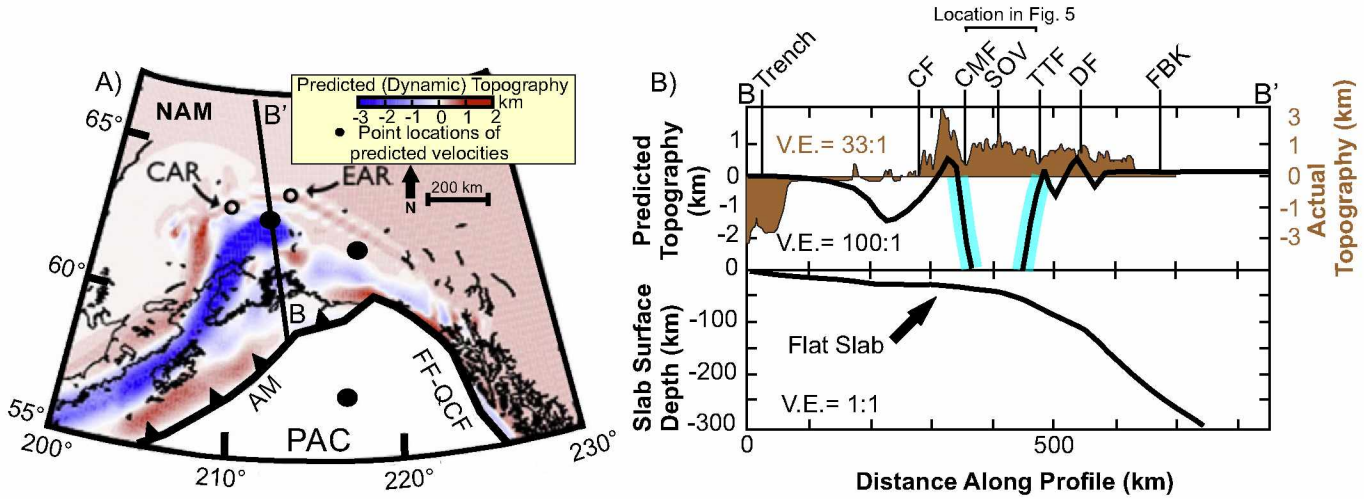

Figure 3. A) Model results from Jadamec et al. (2013) of predicted distribution of modern dynamic topography across southern Alaska based on modern plate configuration. Red corresponds to higher dynamic topography and blue corresponds to lower dynamic topography. AM-Aleutian Megathrust CAR-Central Alaska Range, EAR-Eastern Alaska Range, NAM-North American Plate, PAC-Pacific Plate, FF-QCF-Fairweather Queen Charlotte Fault B) Top: Topography predicted from model and actual topography along transect B-B'. Bottom: cross section of Yakutat flat-slab along B-B'.

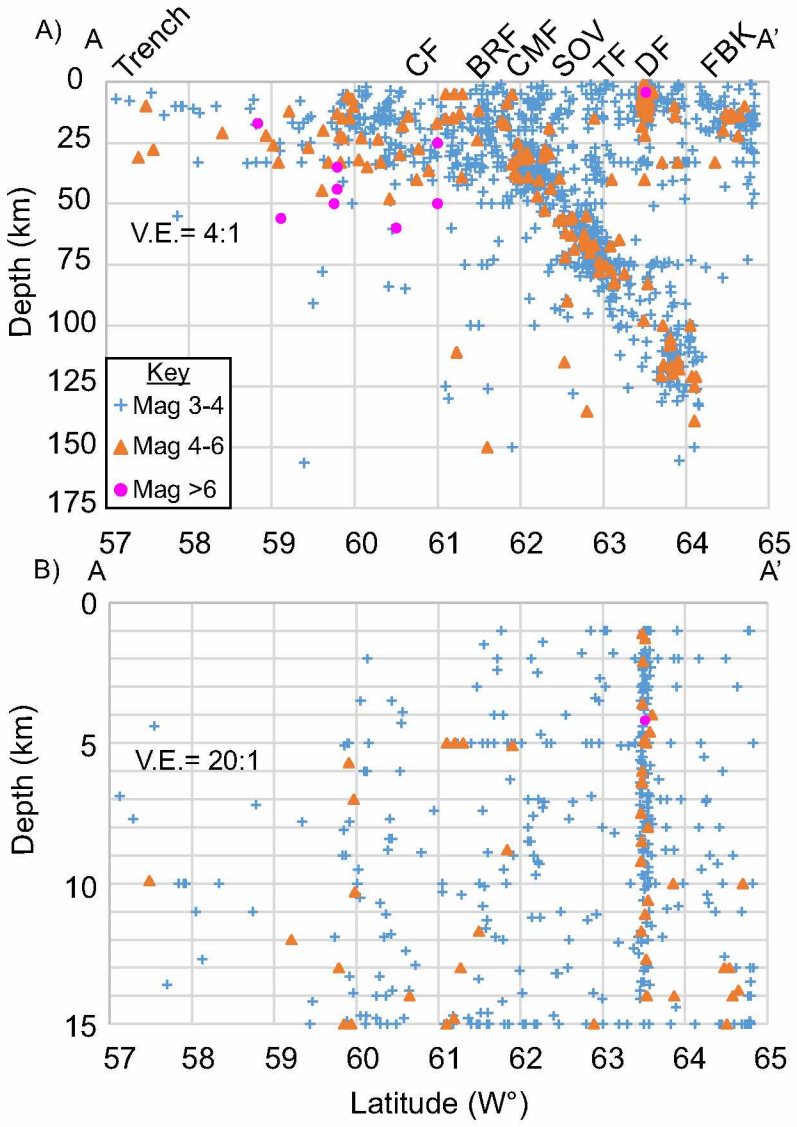

Figure 4. A) Seismicity along cross section A-A' from Figure 1 (100 km wide swath). Seismic events collected, but not relocated, from the Alaska Earthquake Information Center catalog from 1911-2015 and of magnitudes >3.0 are shown. CMF-Castle Mountain Fault, SOV-Mount Sovereign, TTF-Talkeetna Thrust Fault, DF-Denali Fault, FBK-Fairbanks. B) Same profile with depth scale enlarged to highlight the crustal scale Denali Fault.

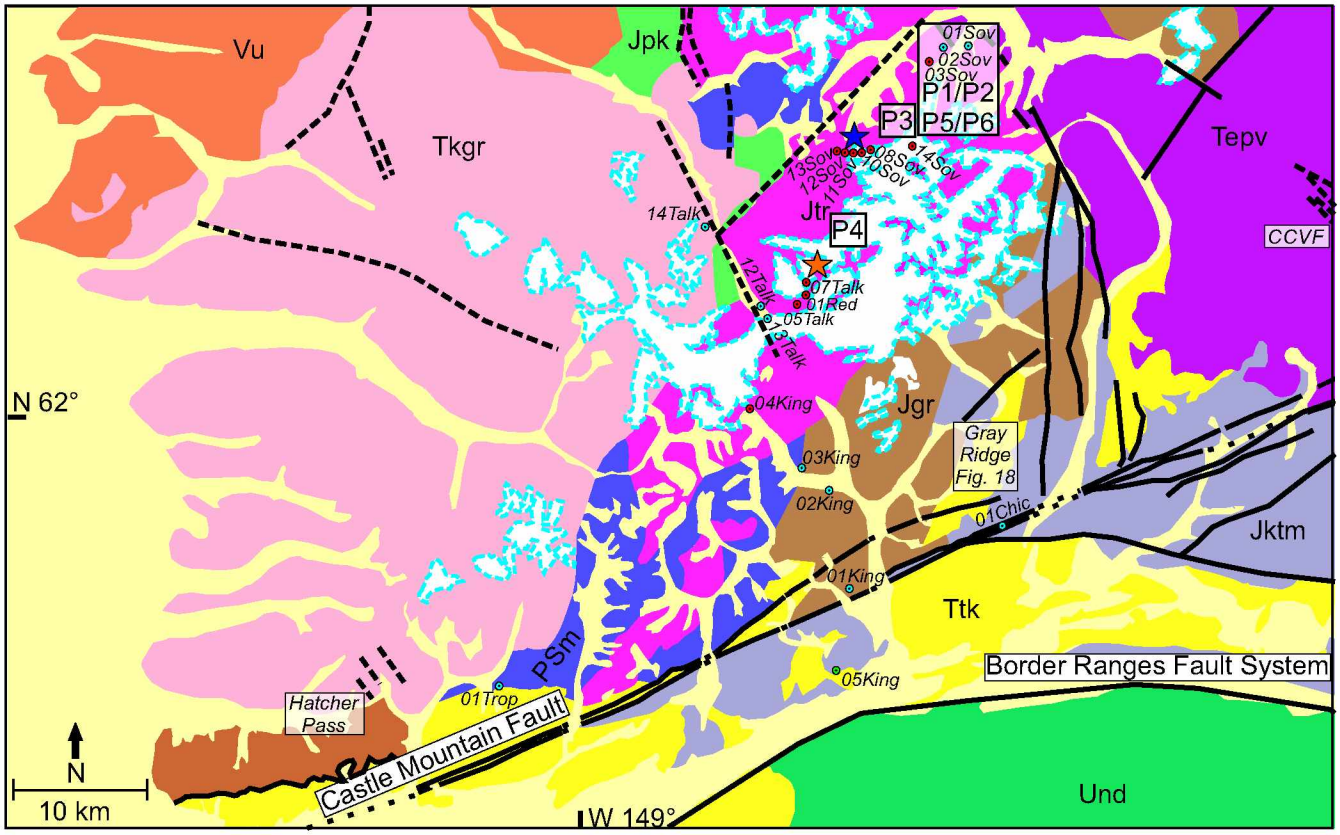

Figure 5. Simplified geologic map of the southern Talkeetna Mountains. Mu: Metamorphic rocks undifferentiated, Jgr: Jurassic granite, Jktm: Jurassic-Cretaceous Talkeetna and Matanuska Formations, Jpk: Jurassic plutonic and metamorphic rocks undifferentiated, Jtr: Jurassic trondhjemite, PSm: Permian-Jurassic metamorphic and plutonic rocks, Tepv: Tertiary, Paleocene-Eocene andesite and basalt flows, Ttk: Tertiary sedimentary rocks including Arkose Ridge and Chickaloon Formations. Und: Chugach Mountain rocks undifferentiated, Vu: Volcanic rocks undifferentiated. Heavy solid and dashed lines are mapped faults. Geology from Wilson et al. (2015). Locations of samples collected for this study are shown with sample names. Blue dots are samples collected below ~1,500 m and red are above ~1,500 m. Blue star is Mount Sovereign. Orange star is Sheep Mountain. Regional picture locations for P1, P2, P3, P4, P5 and P6 (Figure 6) denotated by large boxes and labels.

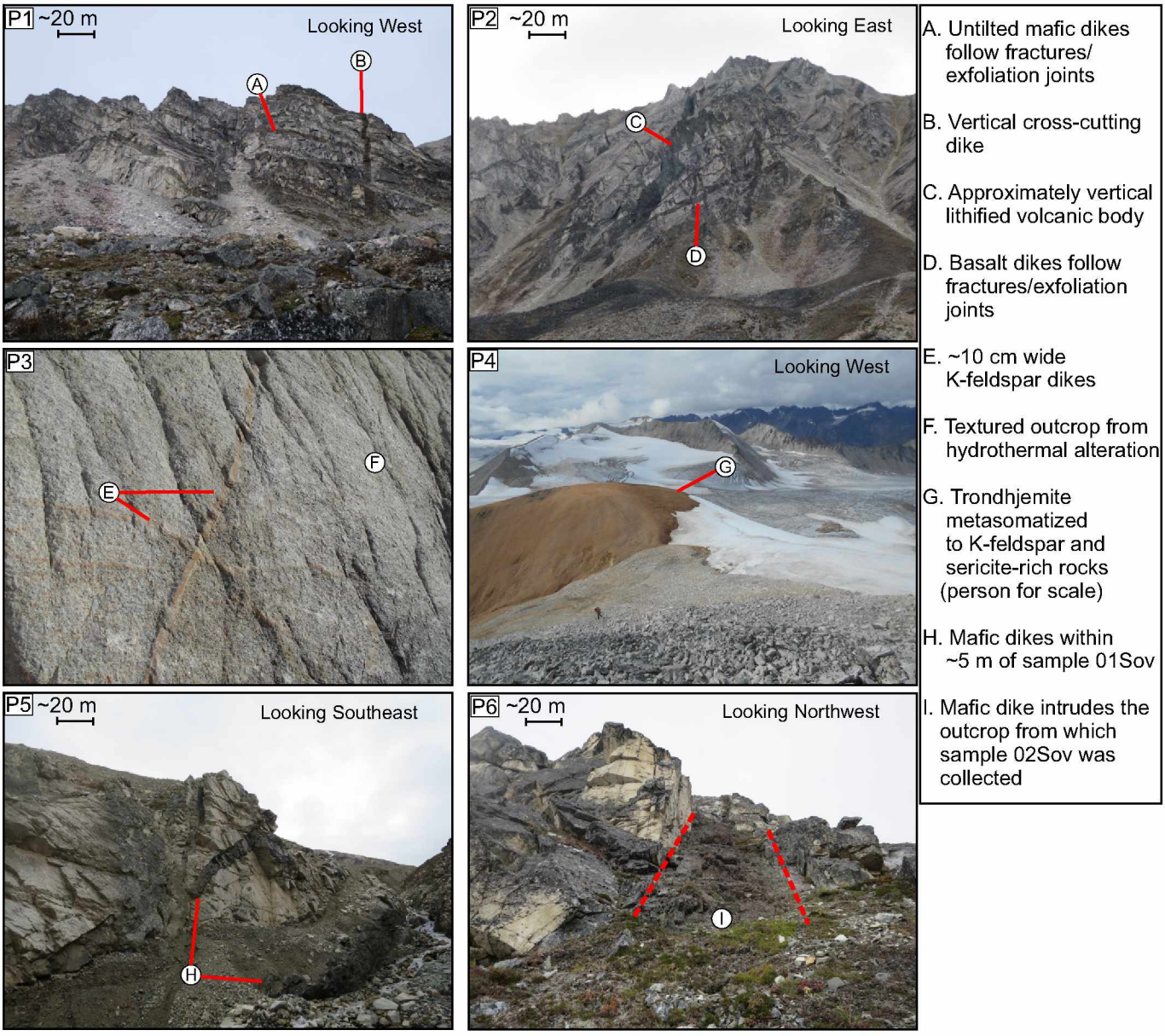

Figure 6. Photographs from our southern Talkeetna Mountains study area shown in figure 5. P1, P2) Dikes following along exfoliation joints and a cross cutting vertical dikes and lithified volcanic bodies and conduits demonstrate a lack of significant tilting in the region. P3) Many outcrops in the field area have cross-cutting K-feldspar dikes and have been altered by hydrothermal fluids. P4) Along the Sheep Mountain vertical profile trondhjemite rocks were metasomatized to K-feldspar and sericite rich rocks (person shown for scale). P5, P6) Mafic dikes at a minimum distance of ~5 m from samples 01Sov and 02Sov.

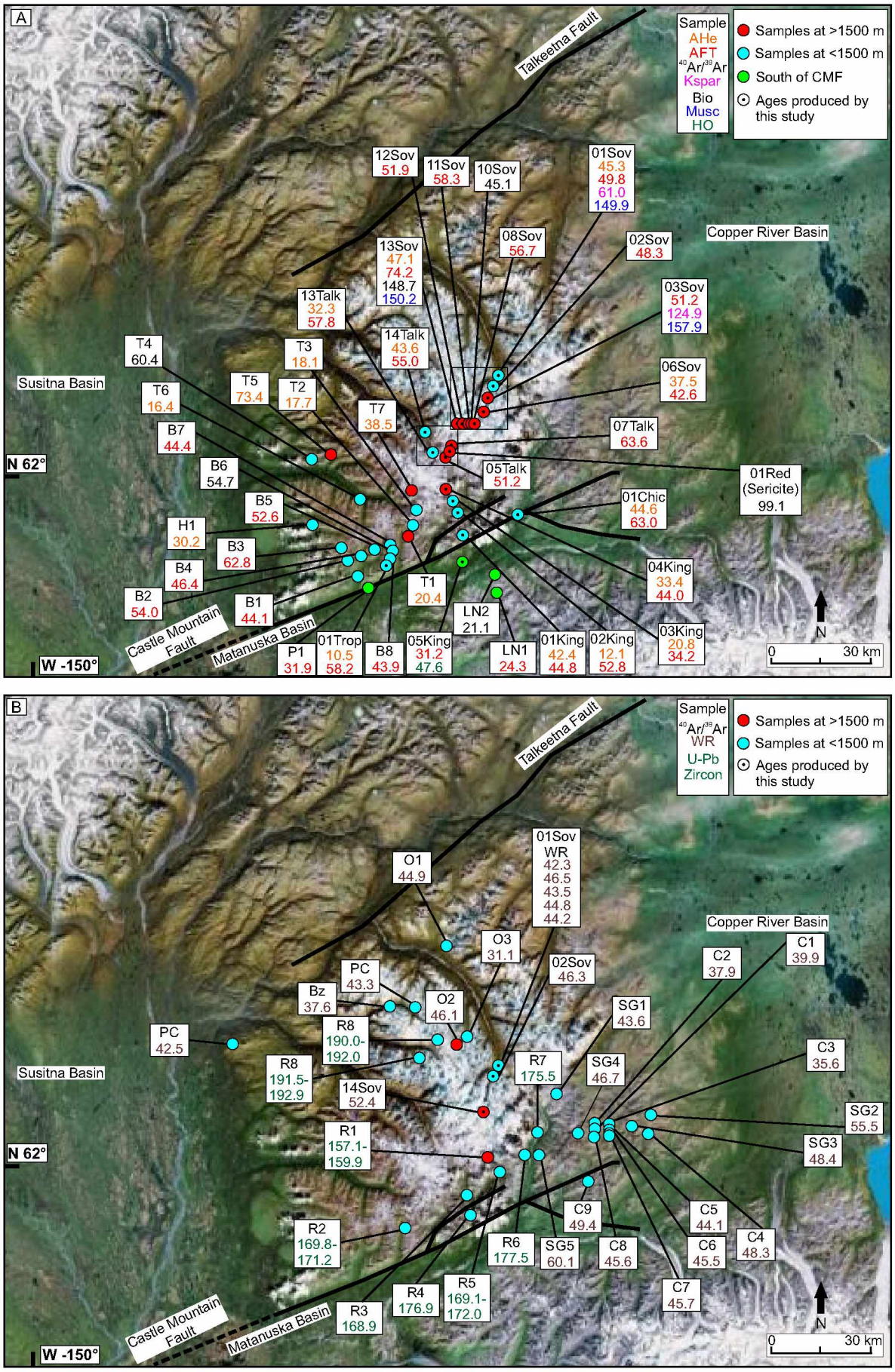

Figure 7. Satellite images of the Talkeetna Mountains and sample location maps showing cooling ages and volcanic ages from samples analyzed for this study. A) All AFT, AHe and $^{40}Ar/^{39}Ar$ K-feldspar, muscovite, biotite and hornblende cooling ages published in the region south of the Talkeetna Fault (upper map). B) All whole rock $^{40}Ar/^{39}Ar$ and zircon U-Pb ages published in the region south of the CMF (lower map). Black boxes encompass Mount Sovereign (northern box) and Sheep Mountain (southern box) vertical profiles. B-Bleick et al., 2012; Bz-Benowitz et al., 2015; C-Cole et al., 2006; H-Hacker et al., 2011; LN-Little and Naeser, 1989; O-Oswald, 2006; P-Parry et al., 2001; PC-Ron Cole personal communications; R-Rioux et al., 2007; SG-Silberman and Grantz, 1984; T-Hoffman and Armstrong., 2006.

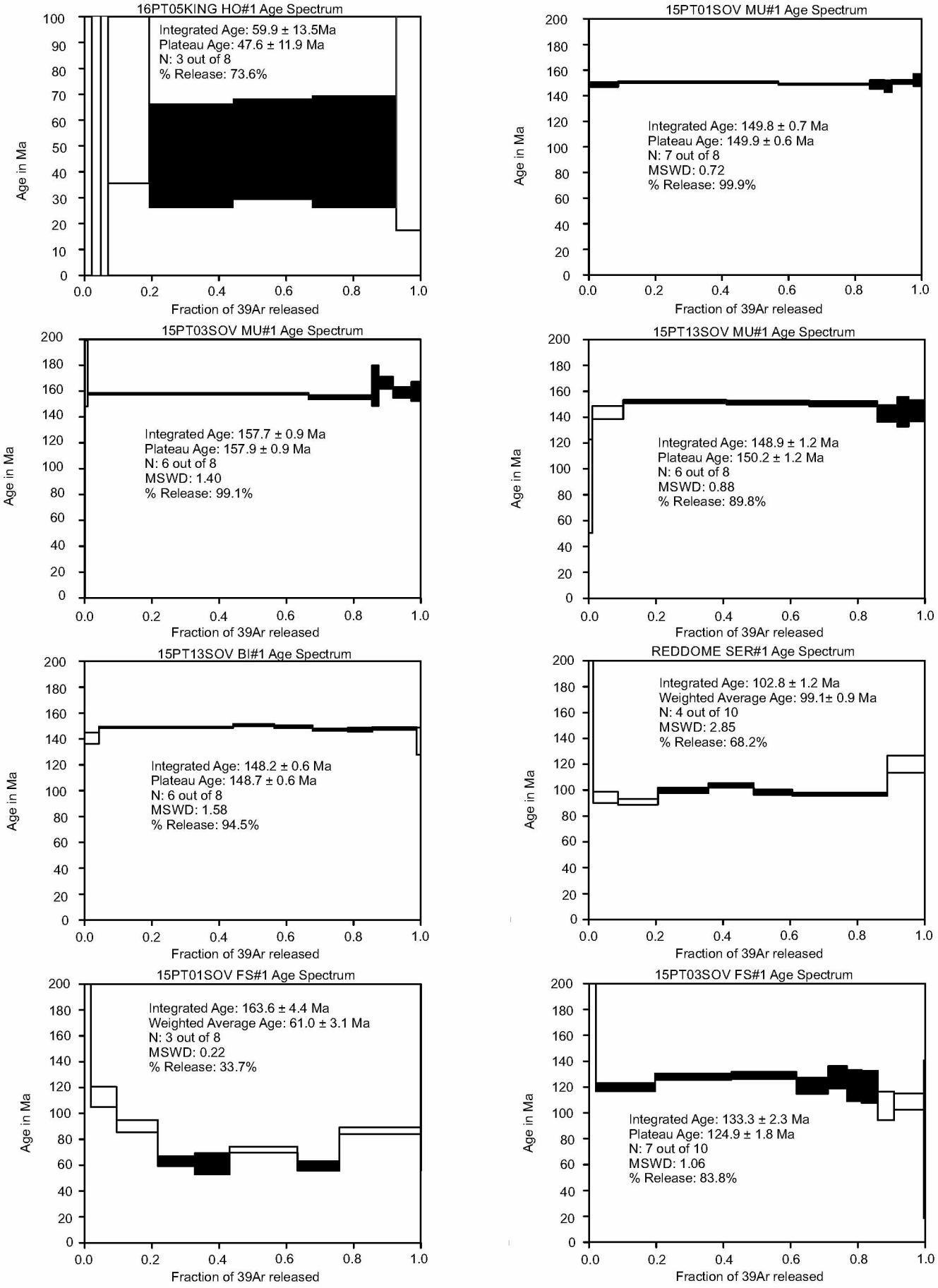

Figure 8. $^{40}Ar/^{39}Ar$ age spectra for all samples analyzed for this study. BI-biotite, FS-K-feldspar, HO-hornblende, MU-muscovite, SER-Sericite, WR-whole rock.

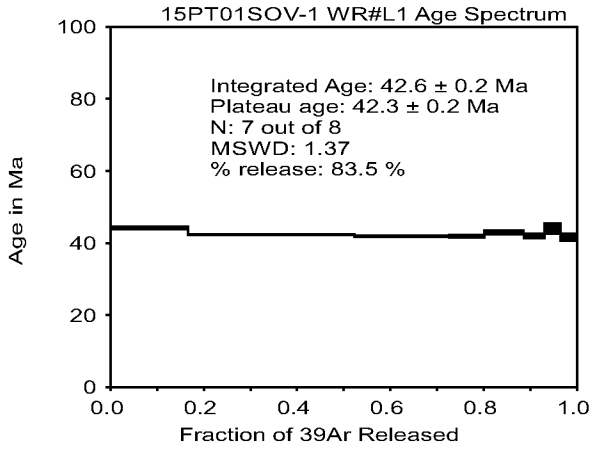

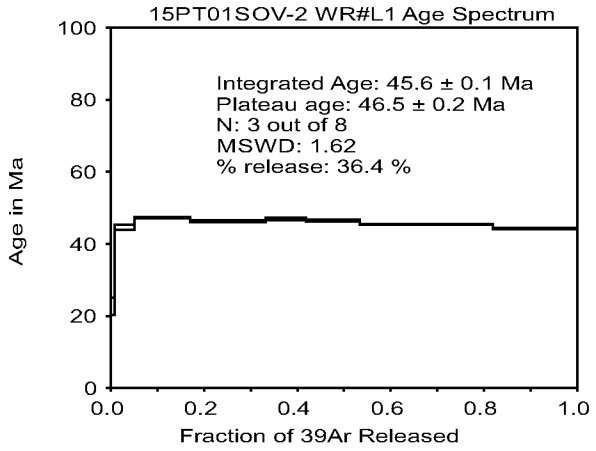

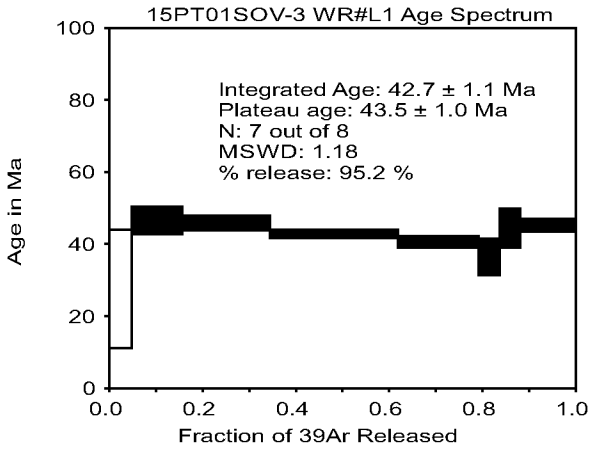

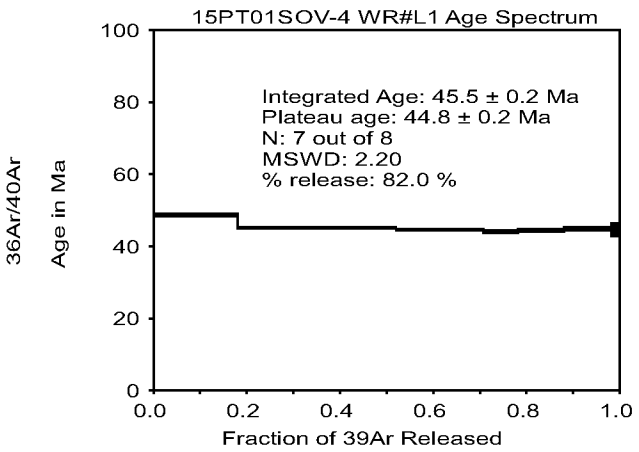

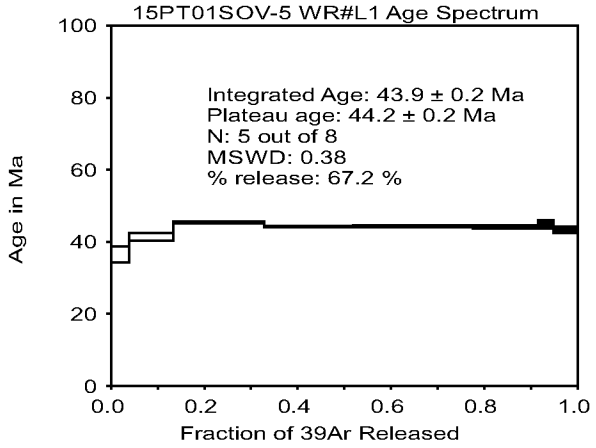

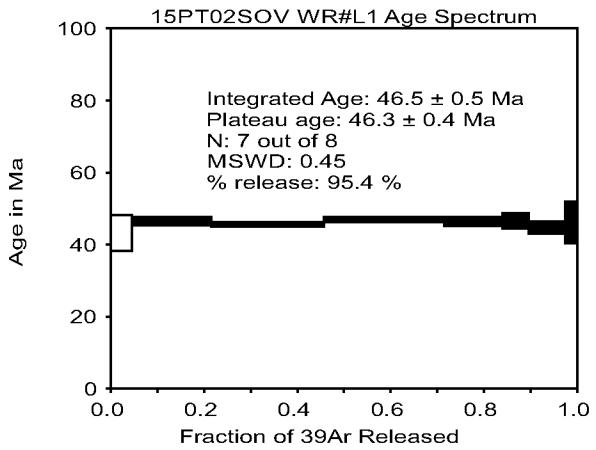

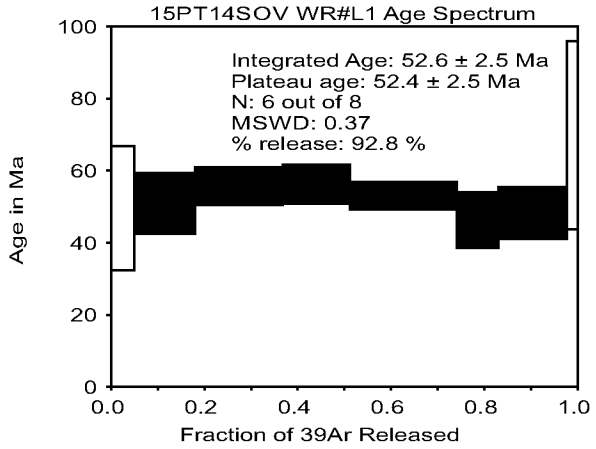

Figure 8 continued.

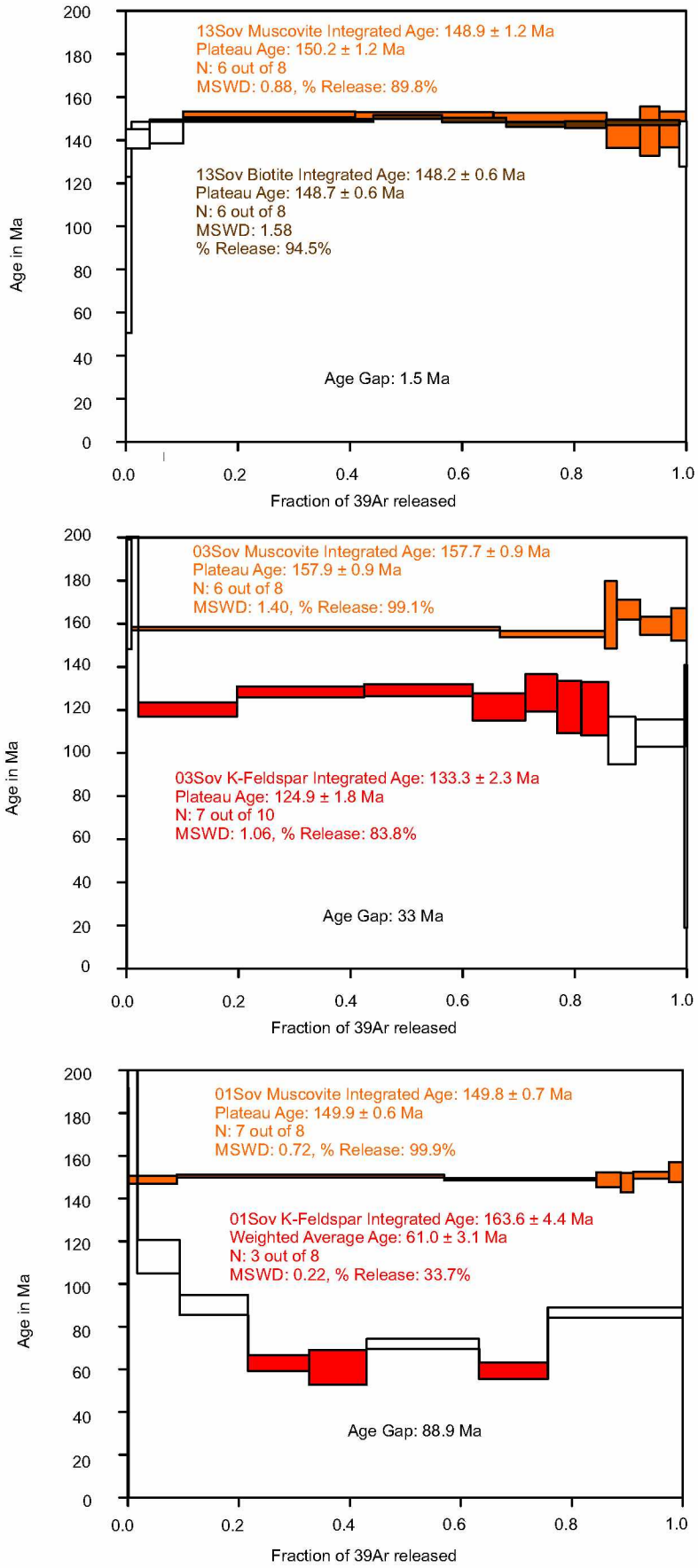

Figure 9. Muscovite/biotite and muscovite/K-feldspar $^{40}Ar/^{39}Ar$ age spectra pairs for samples 01Sov, 03Sov and 13Sov. The 'age gap' represents the closure between the two mineral phases. Filled red, brown and orange bars represent the steps used for the muscovite, biotite and K-feldspar steps respectively.

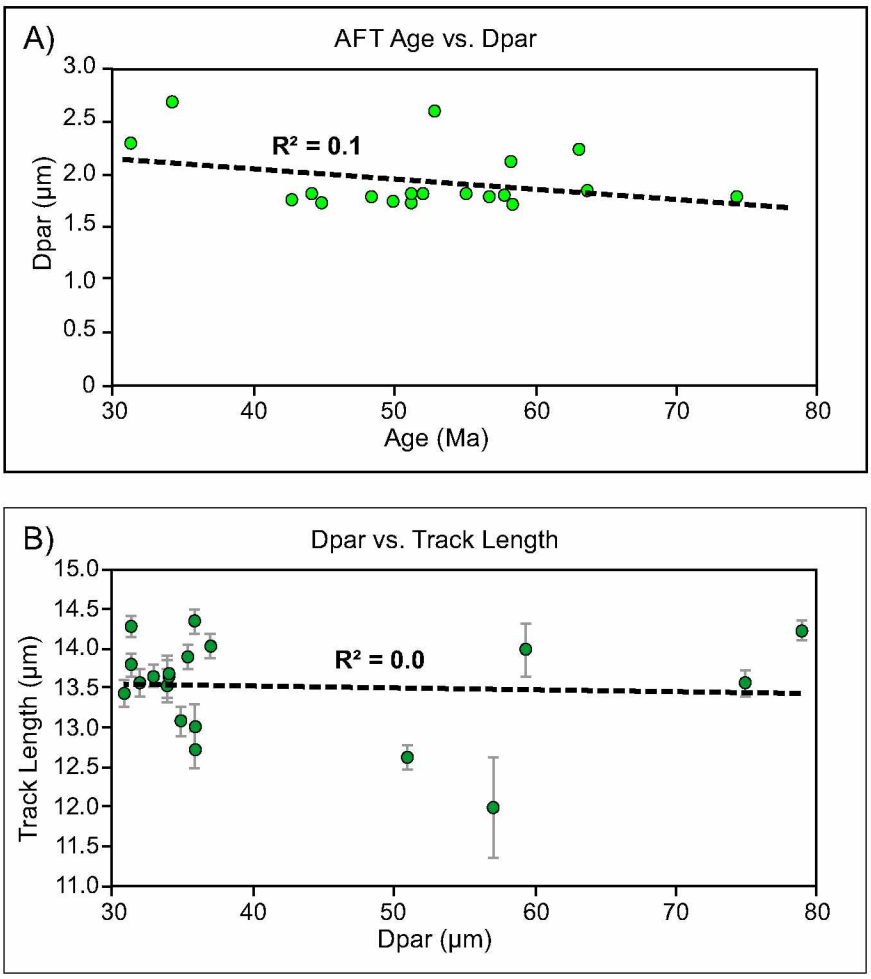

Figure 10. There is no correlation between A) Dpar values vs. age or B) Dpar values vs. track lengths, suggesting similar annealing kinetics for all samples.

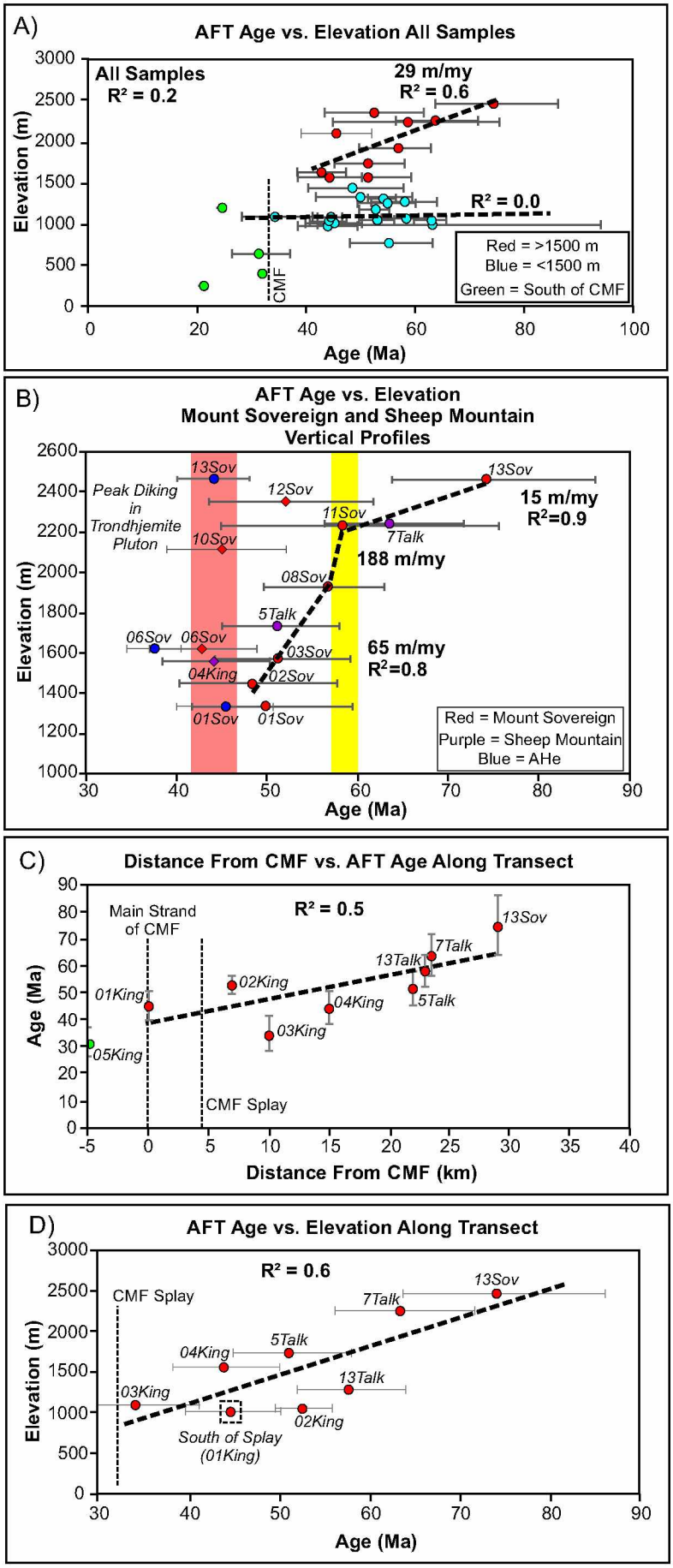

Figure 11. A) AFT age vs elevation plot including all cooling ages from this study and other published sources. B) AFT age vs elevation plot for samples (this study) from Mount Sovereign and Sheep Mountain vertical profile. Yellow bar is inflection point which we interpret reflects a change to more rapid rock cooling and inferred exhumation and width of bar is qualitative error. Exhumation rates estimated from lines qualitatively fit through sample ages are shown in bold font. Blue circles are AHe cooling ages that may have been thermally reset during peak regional volcanism (red bar). C) AFT age vs distance from CMF along N-S transect approaching CMF. D) AFT age vs. elevation along the same N-S transect approaching the CMF. There is an apparent relationship of AFT ages getting younger approaching the CMF in figure 11C. However, all AFT ages in the southern Talkeetna Mountains do not show a trend of getting younger towards the CMF (See figure 14) and the R2 relationship in figure 11D is slightly stronger, suggesting these age patterns are controlled by elevation, rather than distance from CMF.

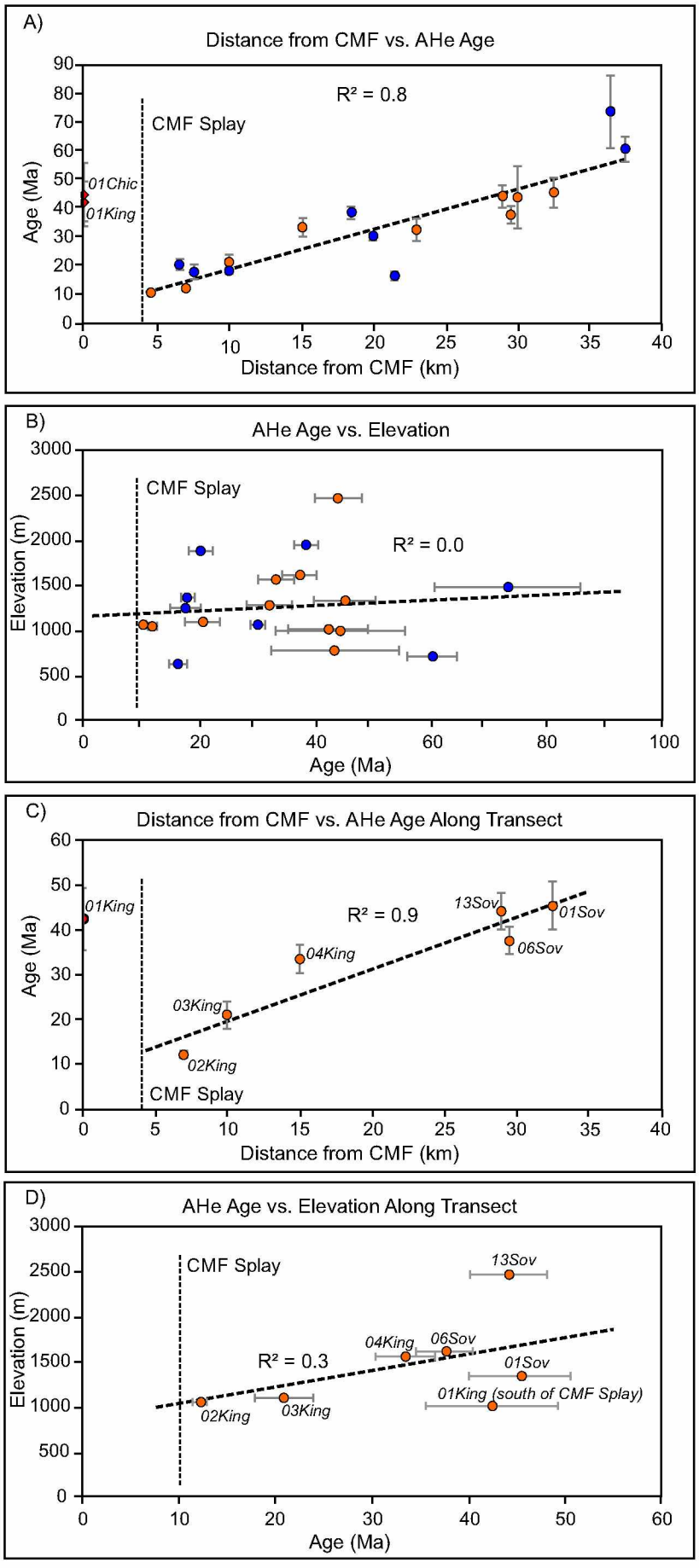

Figure 12. A) All AHe cooling ages existing in our study area vs distance from CMF. Orange circles are ages analyzed for this study and blue dots are previously published ages (Hoffman and Armstrong, 2006; Hacker et al., 2011). 01King, a distinct outlier from the data set, is north of the continuous strand of the CMF but south of the northernmost strand of the CMF, suggesting that the northernmost strand is the active strand of the CMF. B) There is no relationship between AHe age and elevation. C) AHe age vs. Distance from CMF along N-S transect approaching CMF shows a pattern of ages getting younger approaching the northernmost (and inferred active) strand of the CMF. D) AHE age vs. Elevation along the same transect shows no relationship.

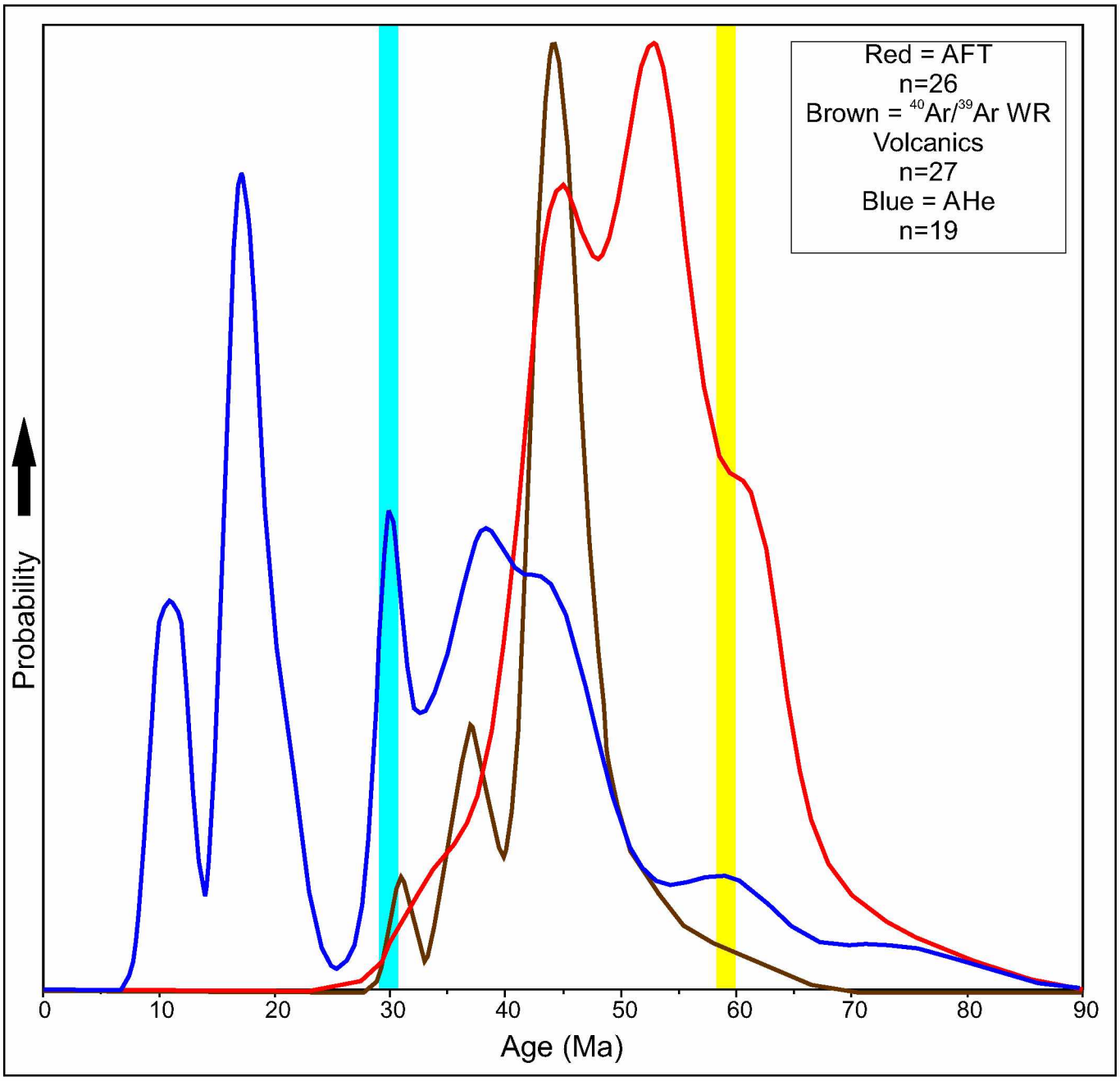

Figure 13. Normalized probability density function of all published whole rock $^{40}Ar/^{39}Ar$, AFT and AHe cooling ages for samples located north of the CMF and south of the Talkeetna Fault (Fig. 6). Yellow bar to the right represents the inflection point from our AFT age-elevation profile (Fig. 11B). Light blue bar to the left represents the approximate timing of initiation of Yakutat microplate flat-slab subduction.

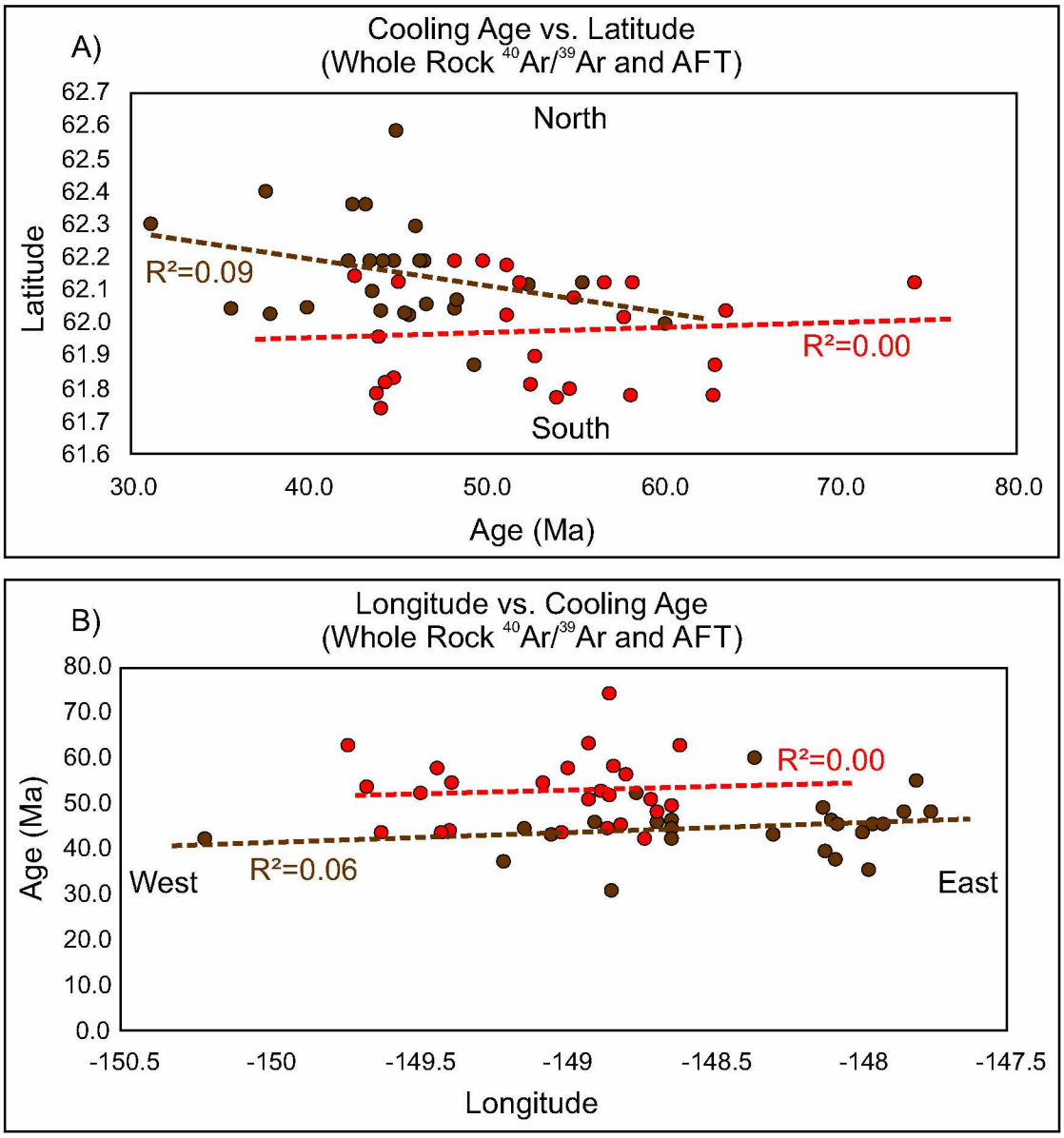

Figure 14. Spatial volcanic and cooling age patterns for all whole rock $^{40}Ar/^{39}Ar$ (brown circles) and AFT (red circles) cooling ages in the Talkeetna Mountains north of the CMF and south of the Talkeetna Fault. A) Whole rock $^{40}Ar/^{39}Ar$ and AFT age vs latitude. R^2 relationships show no N-S cooling age progressions. B) Longitude vs. whole rock $^{40}Ar/^{39}Ar$ and AFT age. R^2 relationships show no W-E cooling age progressions.

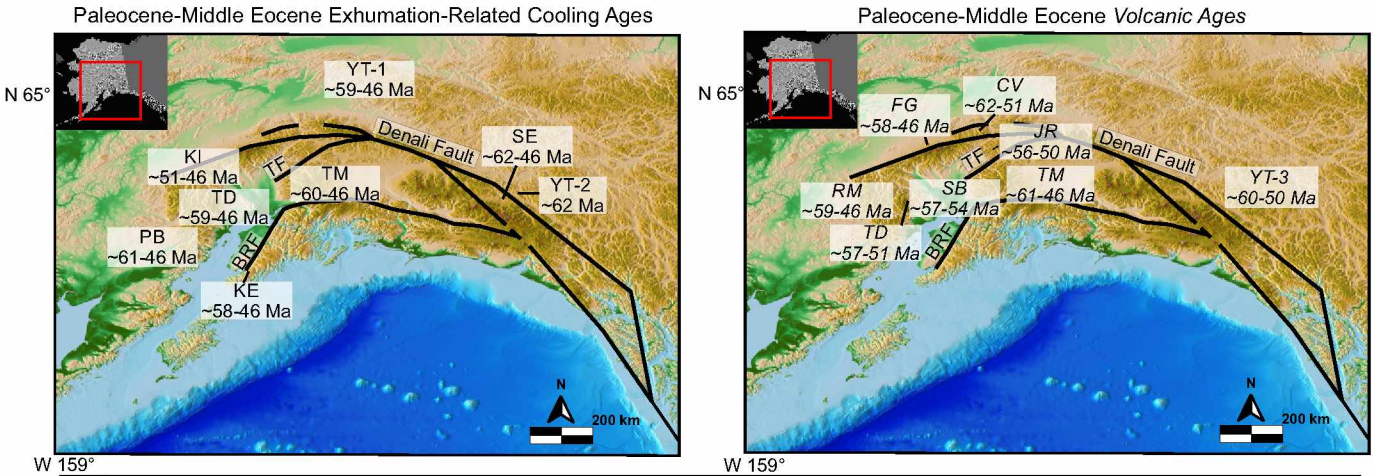

Paleocene- Middle Eocene Exhumation Related Cooling ages and *Volcanic Ages*	Pebble (PB)	Revalation Mountains (RM)	Tordrillo Mountains (TD)	Kichatna Mountains (KI)	Kenai Mountains (KE)	Foraker Glacier (FG)	Susitna Basin (SB)	Cantwell Volcanics (CV)	Jack River (JR)	Talkeetna Mountains (TM)	Saint Elias (SE)	Yukon-Tanana Terrane (YT)
					~58-46 Ma (AHe)					~60-46 Ma (AHe)		
	~61-46 Ma (AFT)		~59-46 Ma (AFT)	~51-46 Ma (AFT)						~58-46 Ma (AFT)	~50 Ma (AFT)	~59-46 Ma (AFT)
											~62-46 Ma (ZFT)	~62 Ma (ZFT)
			~57-46 Ma (KF)							*~61 Ma (KF)*		
			~57-51 Ma (WR)			*~57-46 Ma (WR)*	*~57-54 Ma (WR)*	*~62-51 Ma (WR)*	*~56-50 Ma (WR)*	*~60-46 Ma (WR)*		*~60-50 Ma (WR)*
		~59-46 Ma (BI)				*~58 Ma (BI)*						

Figure 15. Paleocene-Middle Eocene exhumation and volcanism-related cooling ages from samples across southern Alaska show no N-S or W-E age progressions. Ages younger than ~46 Ma are not reported due to this being the well constrained time of Aleutian Arc initiation (i.e. the time that normal subduction reinitiated) (Jicha et al., 20). PB-Pebble Mine (O'sullivan et al, 2010); RM- Revelation Mountains region (Reed and Lanphere, 1972); TD-Tordrillo Mountains (Haeussler et al., 2008; Benowitz et al., 2012a); KI-Kichatna Mountains (Ward, 2010); KE-Kenai Mountains (Valentino et al., 2016); FG-Foraker Glacier region (Reed and Lanphere, 1972; Cole and Layer, 1984); SB-Susitna Basin (Stanley et al., 2014); CV-Cantwell Volcanics (Cole et al., 1999); JR-Jack River Volcanics (Cole et al., 2007); TM-Talkeetna Mountains (Silberman and Grantz., 1984; Parry et al., 2001; Cole et al., 2006; Hoffman and Armstrong, 2006; Oswald, 2006; Cole et al., 2007; Bleick et al., 2012; Hacker et al., 2011; Benowitz et al.,2015); SE-St. Elias Mountains (Enkelmann et al., 2017); YT-Yukon-Tanana Terrane (Tempelman-Kluit and Wanless, 1975; Dusel-Bacon and Murphy, 2001; Enkelmann et al., 2017).

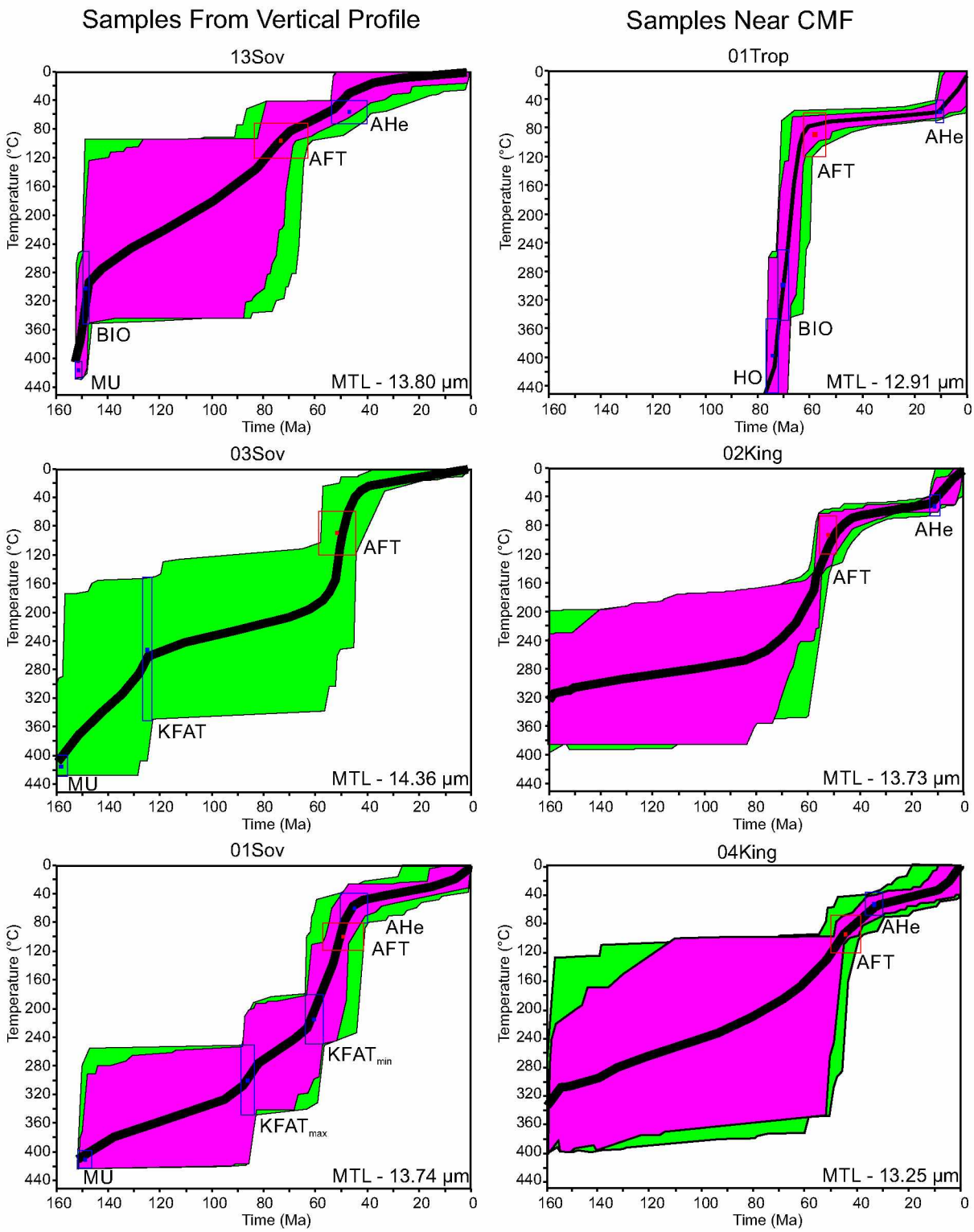

Figure 16. Inverse thermal models for samples along the Mount Sovereign vertical profile and near the CMF (Fig. 6). Models were created by generating 50,000 random cooling paths using the HeFTy thermal modelling program (Ketcham, 2007) and all cooling age constraints. Time-temperature envelopes and weighted mean cooling paths are shown. Purple envelopes are defined by all good fit cooling paths and green envelopes are constrained by acceptable fit cooling paths. Blue boxes are cooling age constraints where width of box represents age uncertainty and height of box represents nominal closure temperatures for each mineral system. Red boxes represent the approximate time-temperature window for the AFT system. AFT age and track length information for each sample was directly input into HeFTy to generate the models. Hence, red boxes are meant to demonstrate the use of the AFT system in the making of these models but are not an input box constraint as used for other systems (blue boxes). AHe: apatite (U-Th)/He; AFT: apatite fission track; BI: $^{40}Ar/^{39}Ar$ bioite; KFAT: $^{40}Ar/^{39}Ar$ K-feldspar; MU: $^{40}Ar/^{39}Ar$ muscovite. MTL is mean track length value for each sample. For HeFTy models of all samples, see Appendix 3.

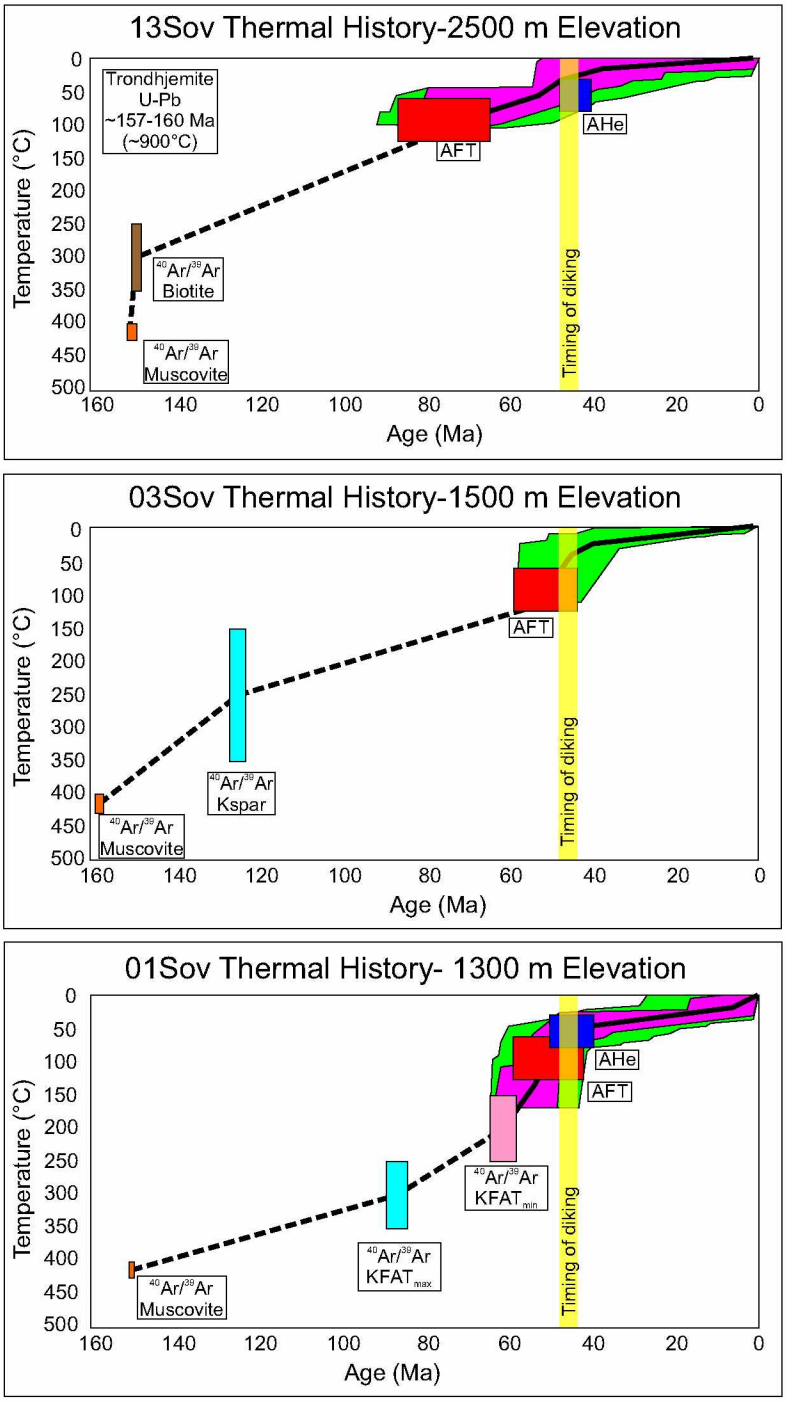

Figure 17. Thermal histories for samples 13Sov, 03Sov and 01Sov modelled using the HeFTy inverse thermal modelling program (Ketcham, 2007) and $^{40}Ar/^{39}Ar$, AFT and AHe age constraints. U-Pb zircon crystallization ages are noted (Rioux et al., 2007). Width of boxes represents age uncertainty and height of boxes represents nominal closure temperatures for each mineral system. Dashed line is the approximate cooling path between mineral phases.

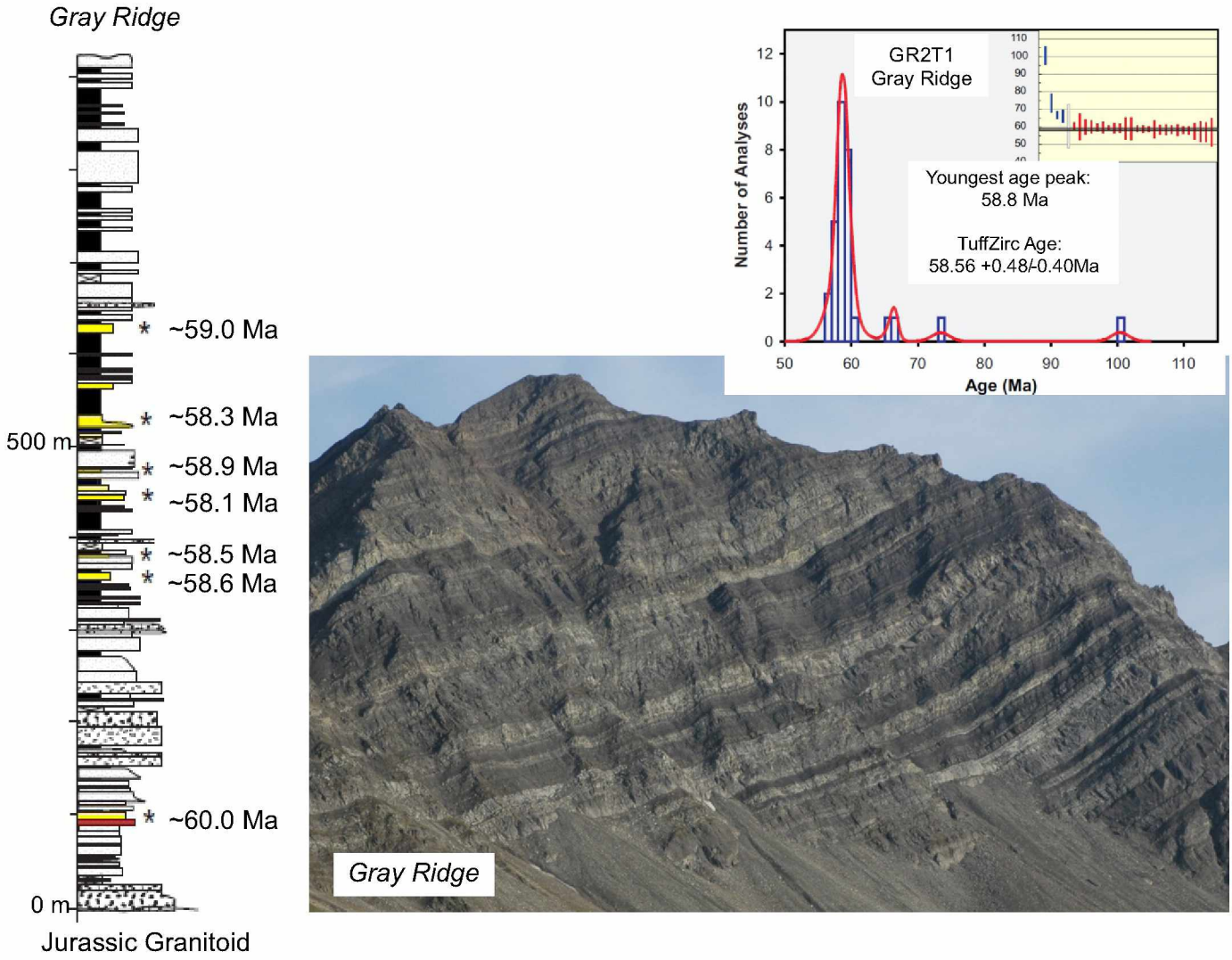

Figure 18. Zircon U-Pb tuff ages from Gray Ridge in the southern Talkeetna Mountains (location in figure 5) are Late Paleocene-Early Eocene (Sunderlin et al., 2014; Trop et al., 2015), indicating basin subsidence and significant clastic sediment deposition at the time of the inferred thermal and exhumation event initiating at ~61 Ma. This is consistent with our interpretation of initiation of rapid exhumation in the southern Talkeetna Mountains at this time. * denotes the locations of dated tuffs.

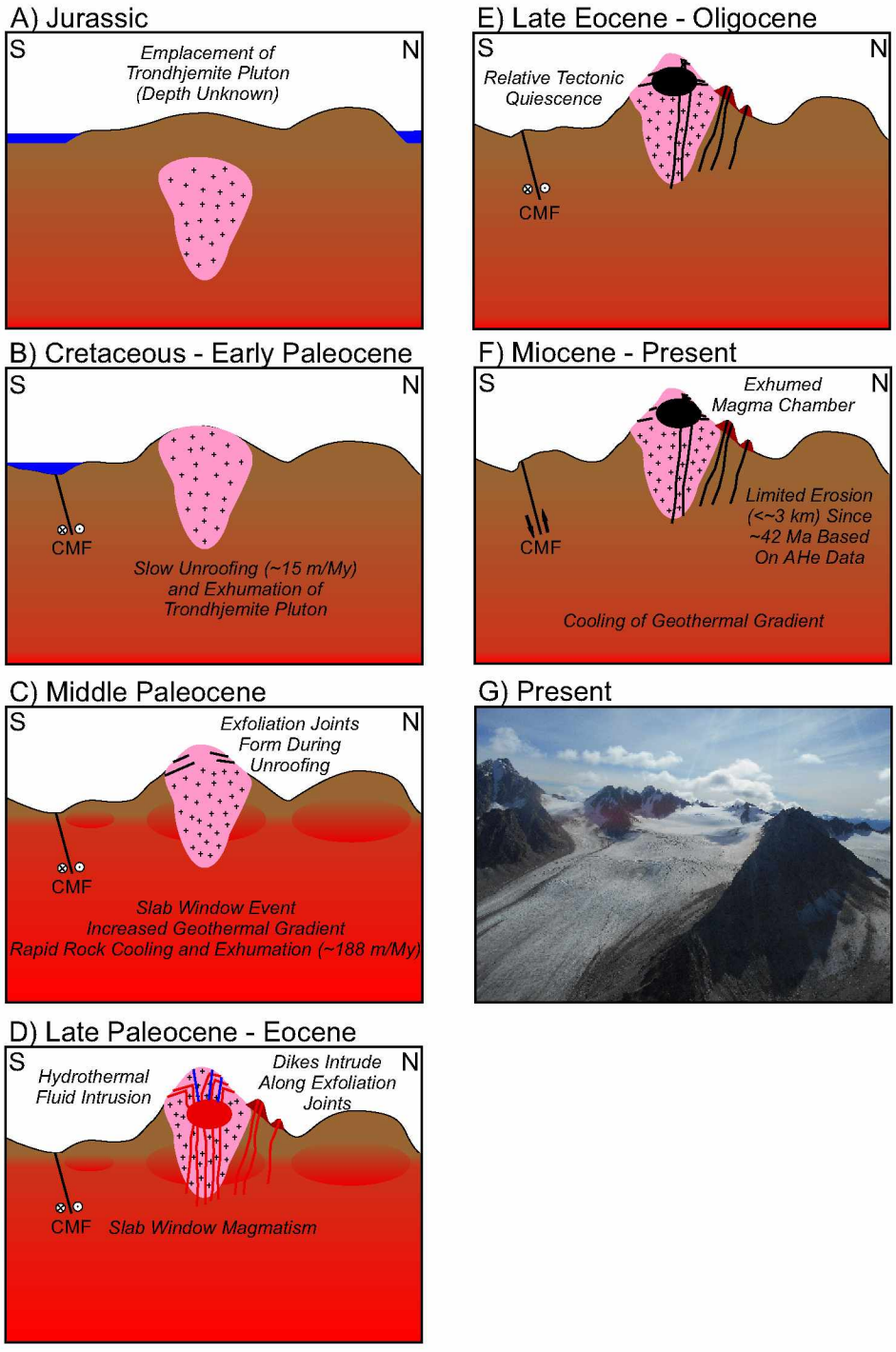

Figure 19. Simplified topographic development history of the southern Talkeetna Mountains Jurassic Trondhjemite pluton. A) Pluton is emplaced during the Jurassic at an unknown depth. B) Slow Cretaceous unroofing and exhumation. C) Inferred Paleocene-Eocene slab window event beneath southern Alaska (Cole et al., 2006) increases the geothermal gradient followed by rapid rock cooling and exhumation. Exfoliation joints form during unroofing of the trondhjemite pluton. D) Dikes intrude along exfoliation joints during slab window magmatism. Injection of hydrothermal fluids lead to spatially variable resetting. E) Period of relative tectonic quiescence. F) Vertical displacement along Castle Mountain Fault. AHe data and exhumed magma chamber indicate limited erosion (<~3 km) since the Late Eocene. G) Picture of the glaciated southern Talkeetna Mountains Jurassic Trondhjemite pluton.

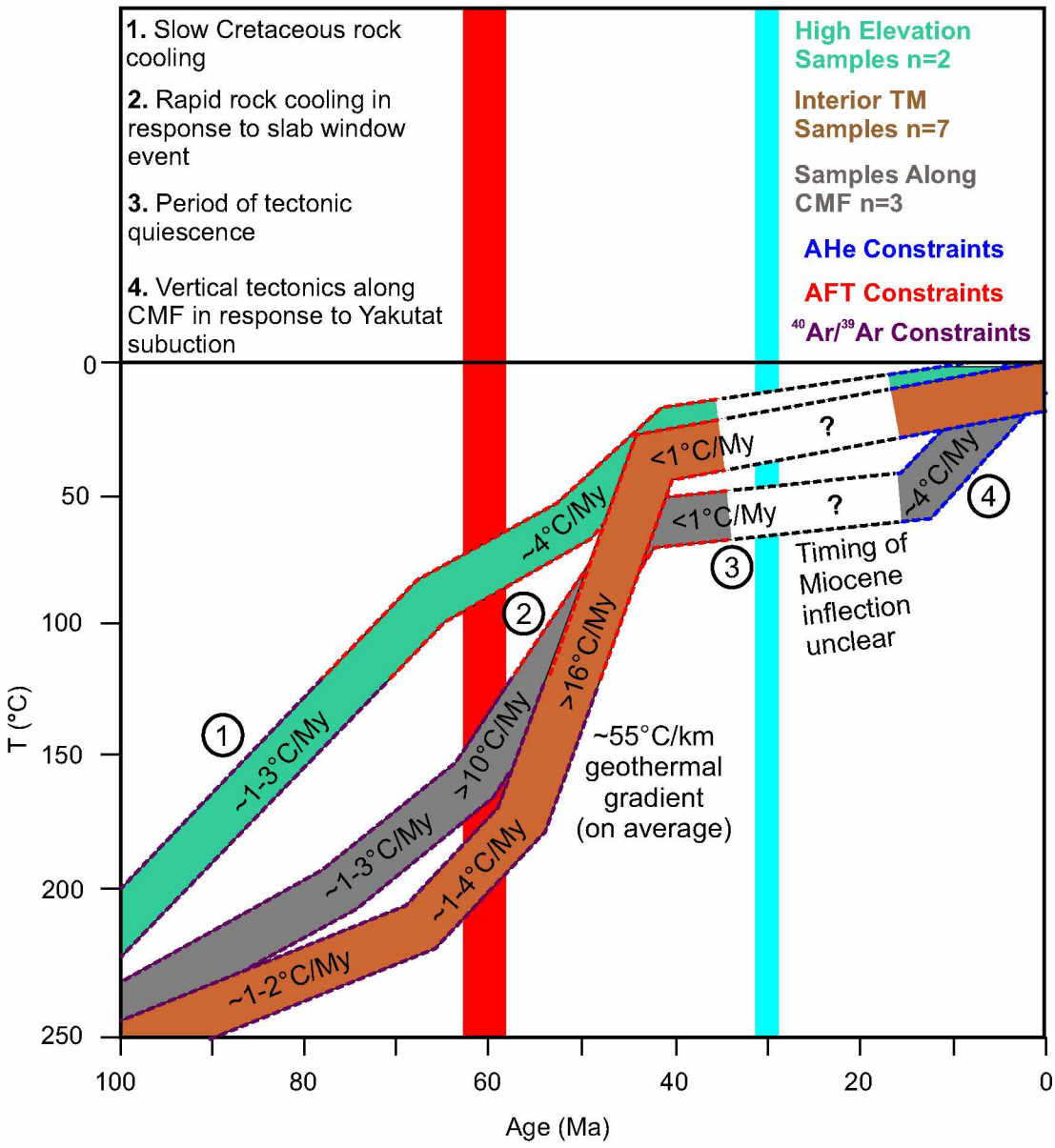

Figure 20. Time-temperature summary diagram for samples in the interior Talkeetna Mountains/along vertical profiles (brown box), at the highest elevations (teal box) and near the CMF (gray box). Cooling rates are estimated from HeFTy thermal models (Fig. 14). Red bar at ~60 Ma represents the onset of the inferred thermal event discussed in the text. Light blue bar at ~30 Ma represents approximate initiation of subduction of the Yakutat flat-slab.

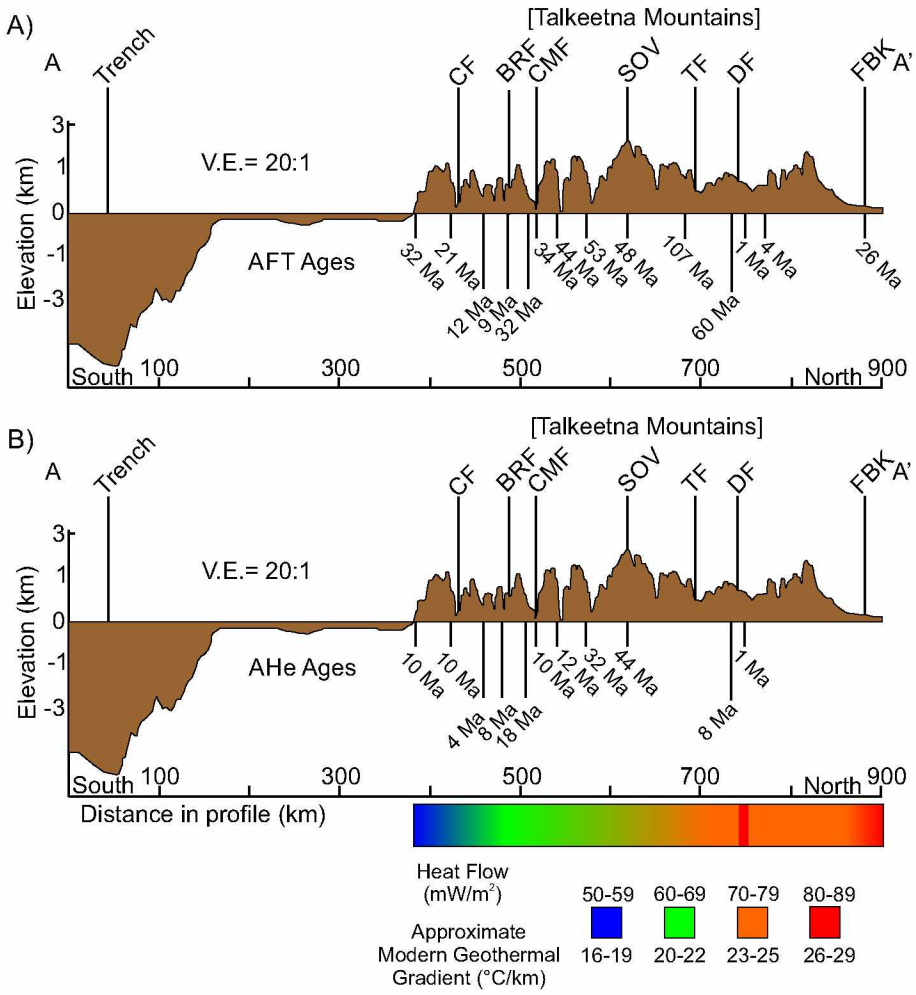

Figure 21. A) Topographic profile and youngest apatite fission track ages plotted along transect A to A' (Fig. 1). Ages show a pattern of changing across major structures, with a less pronounced change across the CMF. B) Topographic profile and youngest apatite (U-Th)/He ages plotted along A to A' (Fig. 1). Ages show a pattern of changing across major structures, including a pronounced change across the CMF. Approximate geothermal gradient and heat flow shown along profile is calculated from Batir et al. (2013).

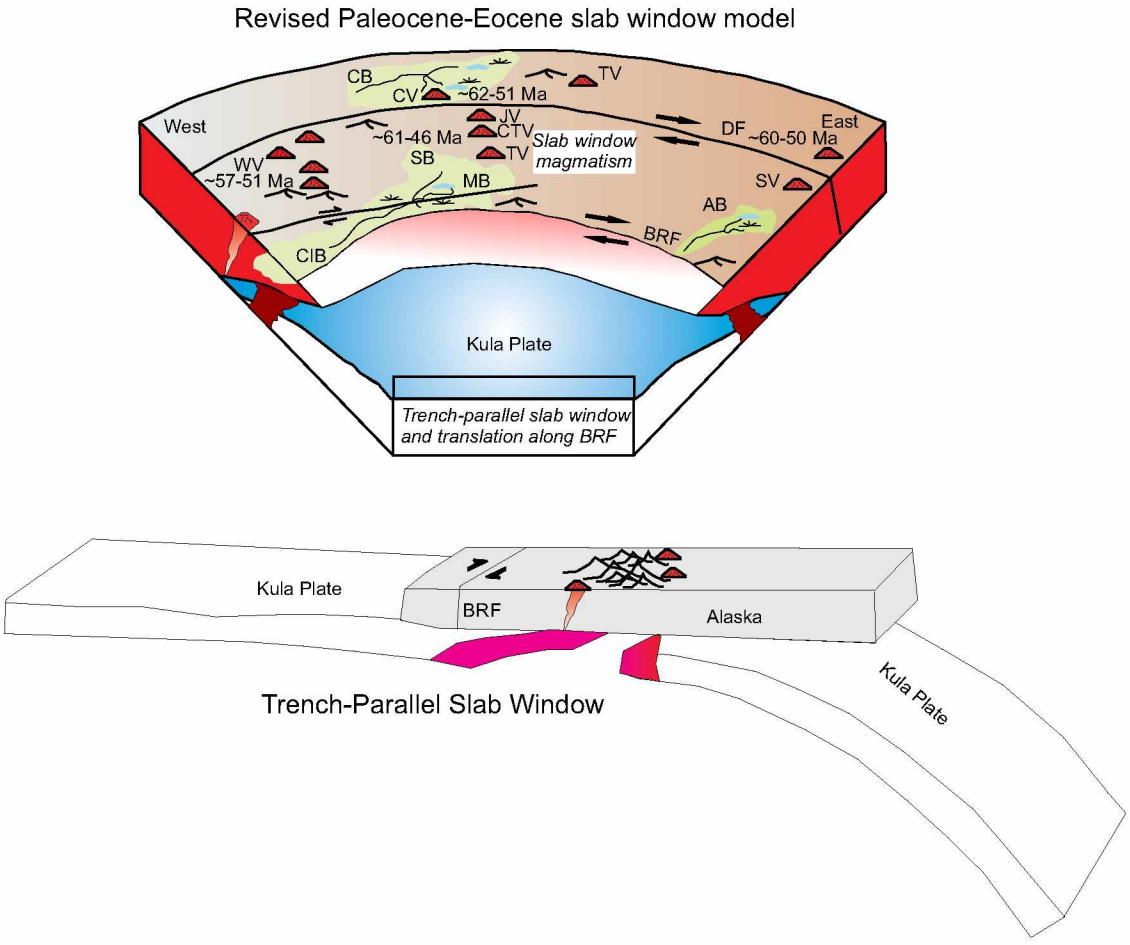

Figure 22. Paleocene-Eocene slab window model revised from figure 2 to show interpretations made in this study of a trench-parallel slab window event. Cook Inlet Basin: CIB; Susitna Basin: SB; Matanuska Basin: MB; Cantwell Basin: CB; Amphitheater Basin: AB. Western Alaska Range Volcanics: WV; Jack River Volcanics: JV; Central Talkeetna Volcanics: CTV; Caribou Hill Volcanics: CV; Tanana Valley Volcanics: TV; Sifton Volcanics: SV. Denali Fault: DF; Border Ranges Fault system: BRF; Castle Mountain: CMF; Talkeetna Fault: TF. Modified from Ridgway et al. (2012) and Benowitz et al. (2012a).

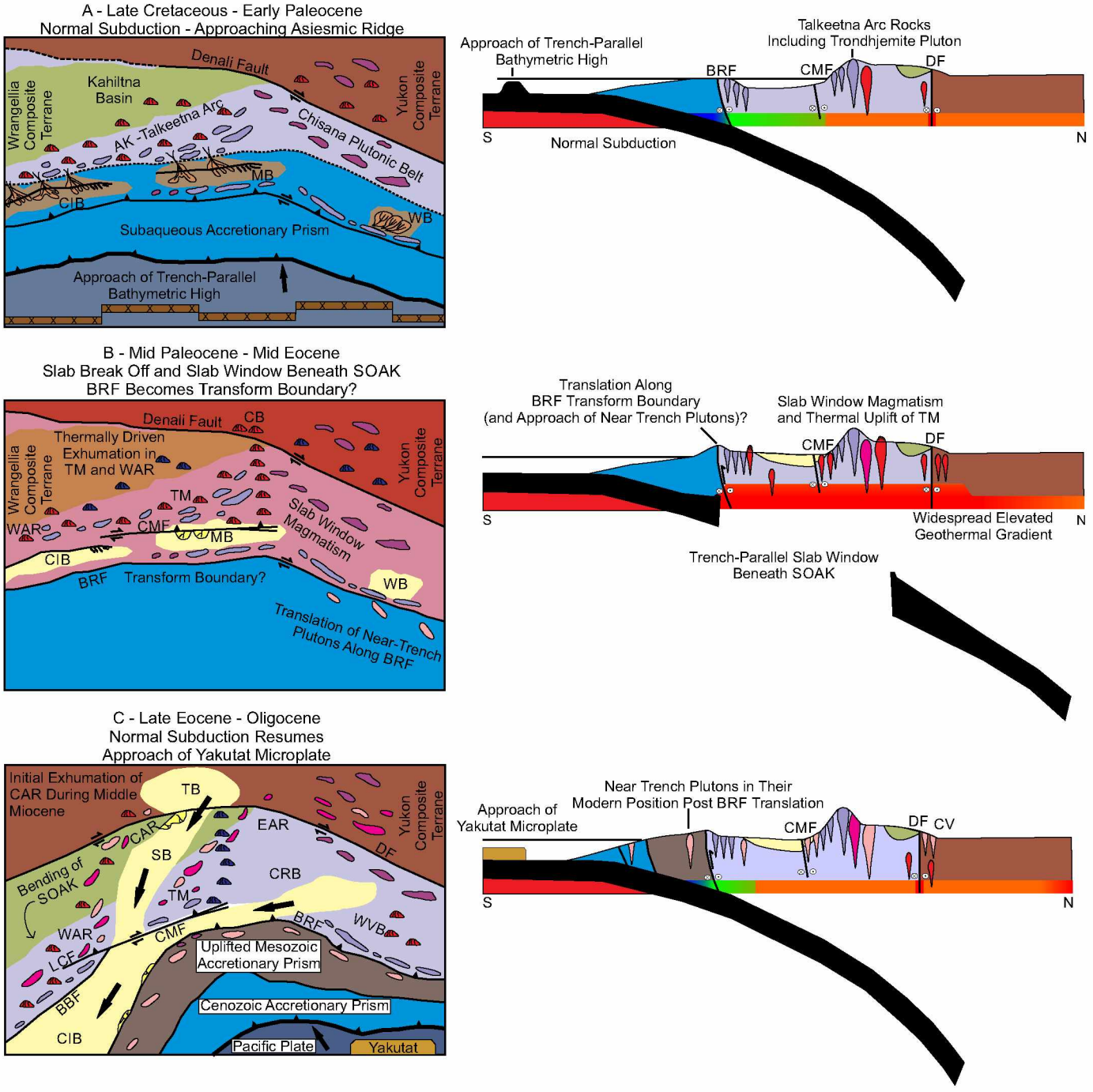

Figure 23. Paleogeographic maps and cross sections showing the inferred tectono-thermal evolution of southern Alaska from Late Cretaceous to present (Modified from Trop and Ridgway, 2007 and Trop et al., 2015). A) Late Cretaceous-Early Paleocene paleogeographic map and cross section illustrating normal subduction and approach of inferred trench-parallel aseismic ridge. CIB-Cook Inlet Basin; MB-Matanuska Basin; WB-Wrangell Basin. B) Mid Paleocene-Mid Eocene paleographic map illustrating slab window event beneath southern Alaska, heating of the thermal regime, thermally driven exhumation and topographic development, and approach of near trench plutons along inferred Border Ranges Fault transform boundary. BRF-Border Ranges Fault; CB-Cantwell Basin; CMF-Castle Mountain Fault; DF-Denali Fault; TM-Talkeetna Mountains; WAR-western Alaska Range. C) Late Eocene- Oligoene paleogeographic map and cross section illustrating resumption of normal subduction, oroclinal bending of southern Alaska, approach of Yakutat microplate and cooling of the thermal regime. BBF-Bruin Bay Fault; CAR-central Alaska Range; CRB-Copper River Basin; CV-Cantwell Volcanics; EAR-eastern Alaska Range; LCF-Lake Clark Fault; SB-Susitna Basin; TB-Tanana Basin; WVB-Wrangell Volcanic Belt.

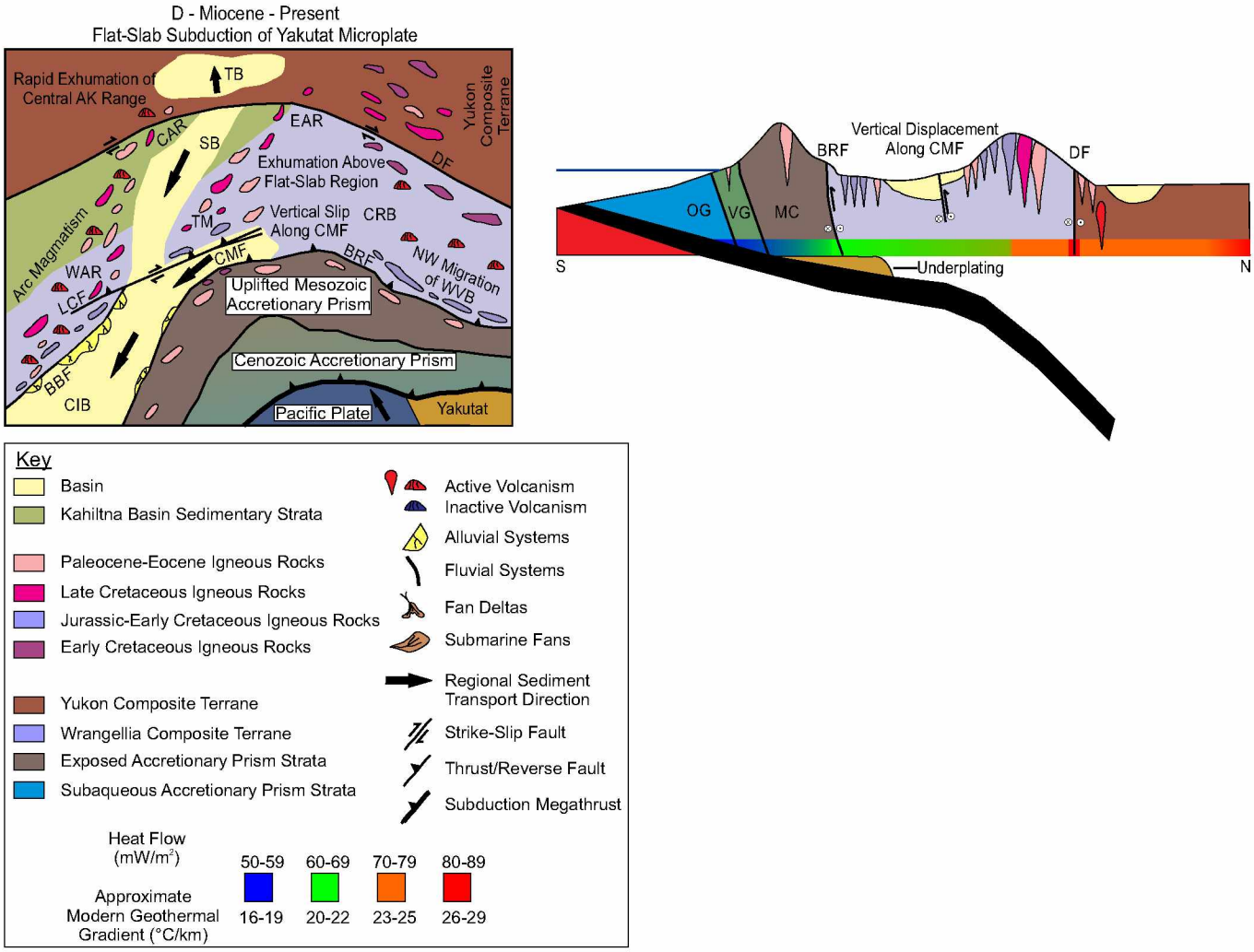

Figure 23 continued. D) Miocene to present paleographic map and cross section illustrating modern tectonic configuration of southern Alaska including flat-slab subduction of the Yakutat microplate and subsequent inboard deformation and cooling of the thermal regime due to the subduction of the mantle wedge. MC-McHugh Complex; OG-Orca Group; VG-Valdez Group.

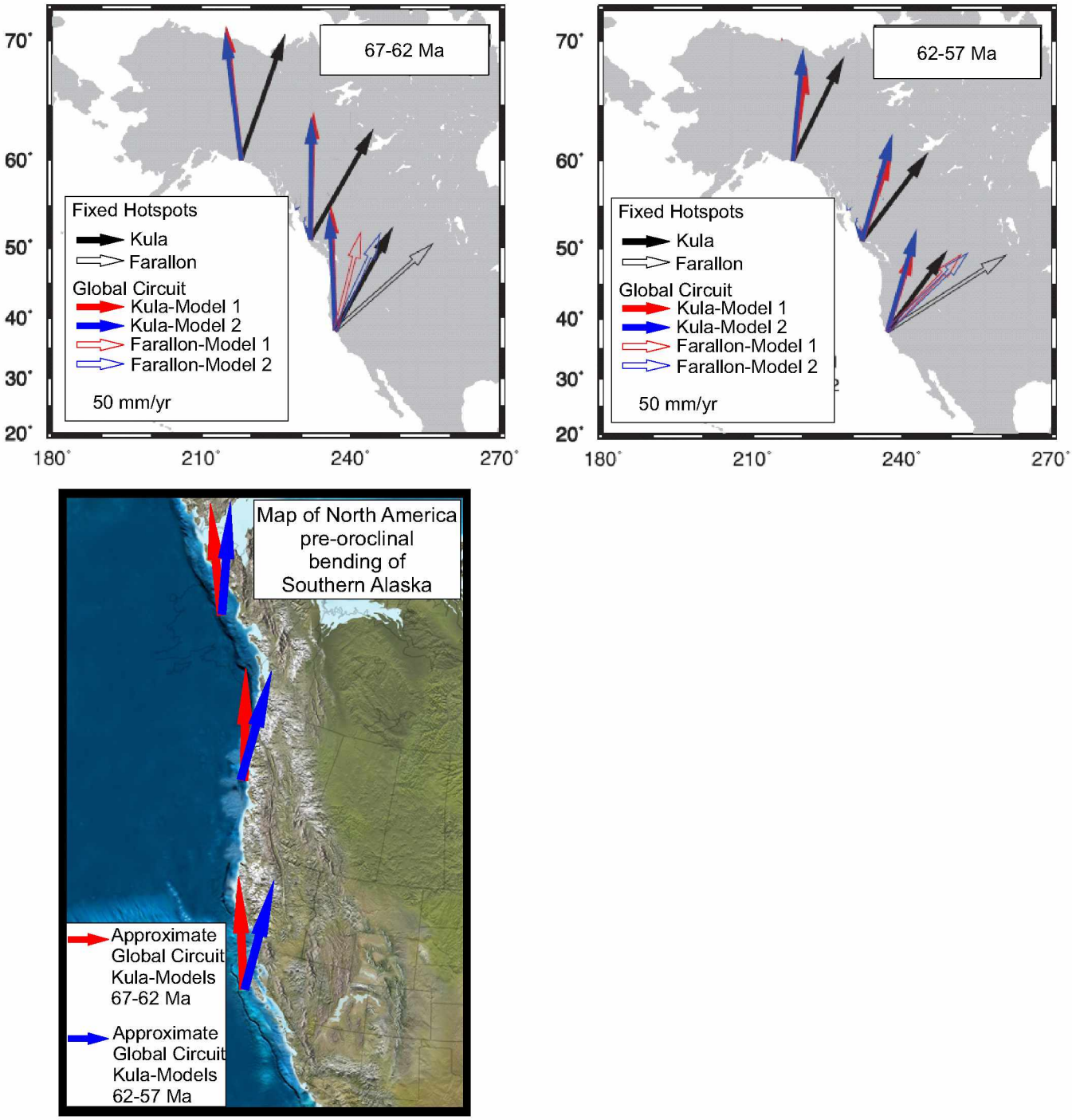

Figure 24. Paleo-vectors of Pacific Plate motion from Doubrovine and Tarduno, (2008) and map illustrating inferred paleographic configuration of North America prior to inferred oroclinal bending of Alaska. If Alaska is unbent, then paleo-vectors agree with translation of the Chugach Accretionary Complex and near trench plutons along the western margin of North America.

TABLE 1. SUMMARY OF $^{40}Ar/^{39}Ar$ RESULTS

Sample	Lat. (°N)	Long. (°W)	Elevation (m)	Mineral	Integrated age (Ma)	Plateau age (Ma)	Plateau information	Isochron age (Ma)	Isochron or other information
05King	61.77	-148.68	635	HO	59.9 ± 13.5	**47.6 ± 11.9**	3 of 8 fractions 73.6% ^{39}Ar release MSWD = 0.00	--	--
01Sov	62.19	-148.45	1333	MU	149.8 ± 0.7	**149.9 ± 0.6**	7 of 8 fractions 99.9% ^{39}Ar release MSWD = 0.72	--	--
03Sov	62.17	-148.51	1572	MU	157.7 ± 0.9	**157.9 ± 0.9**	6 of 8 fractions 99.1% ^{39}Ar release MSWD = 1.40	--	--
13Sov	62.12	-148.63	2463	MU	148.9 ± 1.2	**150.2 ± 1.2**	7 of 8 fractions 89.8% ^{39}Ar release MSWD = 0.88	--	--
13Sov	62.12	-148.63	2463	BI	148.2 ± 0.6	**148.7 ± 0.6**	6 of 8 fractions 94.5% ^{39}Ar release MSWD = 1.58	--	--
01Red	62.03	-148.69	1987	SE	102.8 ± 1.2	**99.1 ± 0.9**	4 of 10 fractions 68.2% ^{39}Ar release MSWD = 2.85	--	--
01Sov	62.19	-148.45	1333	FS	163.6 ± 4.4	**61.0 ± 3.1***	3 of 8 fractions 33.7% ^{39}Ar release MSWD = 0.22	61.1 ± 3.1	3 of 8 fractions $^{40}Ar/^{39}Ar_i$ = 295.7 ± 42.9 MSWD = 0.43
03Sov	62.17	-148.51	1572	FS	133.3 ± 2.3	**124.9 ± 1.8**	7 of 10 fractions 83.8% ^{39}Ar release MSWD = 1.06	129.1 ± 3.2	7 of 10 fractions $^{40}Ar/^{39}Ar_i$ = 269.9 ± 3.2 MSWD = 1.06
01Sov-1	62.19	-148.45	1333	WR	42.6 ± 0.2	**42.3 ± 0.2**	7 of 8 fractions 83.5% ^{39}Ar release MSWD = 1.62	42.2 ± 0.2	7 of 8 fractions $^{40}Ar/^{39}Ar_i$ = 297.7 ± 12.5 MSWD = 1.56
01Sov-2	62.19	-148.45	1333	WR	45.6 ± 0.1	**46.5 ± 0.2**	3 of 8 fractions 36.4% ^{39}Ar release MSWD = 1.62	--	--
01Sov-3	62.19	-148.45	1333	WR	42.7 ± 1.1	**43.5 ± 1.0**	7 of 8 fractions 95.2% ^{39}Ar release MSWD = 1.18	42.7 ± 1.1	7 of 8 fractions $^{40}Ar/^{39}Ar_i$ = 299.1 ± 2.5 MSWD = 1.18
01Sov-4	62.19	-148.45	1333	WR	45.5 ± 0.2	**44.8 ± 0.2**	7 of 8 fractions 82.0% ^{39}Ar release MSWD = 2.20	44.6 ± 0.6	7 of 8 fractions $^{40}Ar/^{39}Ar_i$ = 308.6 ± 25.2 MSWD = 2.34
01Sov-5	62.19	-148.45	1333	WR	43.9 ± 0.2	**44.2 ± 0.2**	5 of 8 fractions 67.2% ^{39}Ar release MSWD = 0.38	44.5 ± 0.5	5 of 8 fractions $^{40}Ar/^{39}Ar_i$ = 288.1 ± 14.0 MSWD = 0.40
02Sov	62.12	-148.49	1447	WR	46.5 ± 0.5	**46.3 ± 0.4**	7 of 8 fractions 95.4% ^{39}Ar release MSWD = 0.45	46.1 ± 0.7	7 of 8 fractions $^{40}Ar/^{39}Ar_i$ = 297.0 ± 5.8 MSWD = 0.52
14Sov	62.12	-148.55	1789	WR	52.6 ± 2.5	**52.4 ± 2.5**	6 of 8 fractions 92.8% ^{39}Ar release MSWD = 0.37	49.6 ± 5.8	6 of 8 fractions $^{40}Ar/^{39}Ar_i$ = 304.0 ± 14.1 MSWD = 0.37

Samples analyzed with standard MMHB-1 with an age of 523.5 Ma

Most robust age in **bold**.

*Does not meet all the criteria of a plateau age so weighted average age used.

Ages reported at ± 1 sigma

TABLE 2. APATITE FISSION TRACK AGE SUMMARY

Sample	Rock Type	Lat (°N)	Long (°W)	Elev (m)	Pooled Age (Ma)	- Error (Ma)	+ Error (Ma)	Mean Track Length (μm)	+/- Error (μm)
01Sov	Trondhjemite	62.19	-148.46	1332	49.82	8.09	9.65	13.74	0.15
02Sov	Trondhjemite	62.19	-148.49	1446	48.31	7.90	9.44	13.70	0.18
03Sov	Trondhjemite	62.18	-148.51	1571	51.20	6.92	7.99	14.36	0.12
06Sov	Trondhjemite	62.15	-148.53	1618	42.63	4.26	4.73	13.81	0.13
08Sov	Trondhjemite	62.12	-148.58	1928	56.73	7.09	6.31	13.83	0.16
10Sov	Trondhjemite	62.12	-148.60	2110	45.08	6.07	7.01	14.67	0.12
11Sov	Trondhjemite	62.12	-148.62	2231	58.34	13.38	17.33	13.62	0.15
12Sov	Trondhjemite	62.12	-148.63	2352	51.96	8.31	9.89	14.41	0.14
13Sov	Trondhjemite	62.12	-148.63	2463	74.23	10.39	12.06	13.80	0.23
05Talk	Trondhjemite	62.03	-148.69	1733	51.21	6.07	6.88	14.02	0.13
07Talk	Trondhjemite	62.04	-148.68	2247	63.62	7.24	8.17	14.14	0.13
13Talk	Trondhjemite	62.02	-148.74	1279	57.80	5.72	6.35	13.31	0.16
14Talk	Granodiorite	62.08	-148.82	777	55.03	7.14	8.20	12.99	0.20
01King	Granite	61.84	-148.64	1006	44.80	5.00	5.60	13.93	0.13
02King	Granite	61.90	-148.65	1046	52.79	3.06	3.25	13.73	0.14
03King	Granite	61.92	-148.70	1086	34.20	5.92	7.15	14.31	0.11
04King	Trondhjemite	61.96	-148.76	1561	44.03	5.53	6.32	13.25	0.25
05King	Tonalite	61.78	-148.68	634	31.23	4.92	5.84	14.10	0.29
01Trop	Granite	61.78	-149.11	1058	58.23	4.22	4.55	12.91	0.14
01Chic	Metabasalt	61.88	-148.43	992	63.00	20.90	31.10	12.35	0.56

AFT age errors are calculated to the +/- 95% confidence interval

Track length errors are 1 SD

TABLE 3. APATITE FISSION TRACK ANALYTICAL RESULTS

Sample	# of Grains	Mean U (ppm)	AFT Age/Error (Ma)	Mean Track Length (μm)	SD (μm)	Mean Dpar (μm)
01Sov	40	5.53	49.82 (-8.09, +9.65)	13.74 ± 0.15 (80)	1.30	1.74
02Sov	40	3.47	48.31 (-7.9, +9.44)	13.7 ± 0.18 (97)	1.77	1.78
03Sov	40	6.22	51.20 (-6.92, +7.99)	14.36 ± 0.12 (105)	1.19	1.73
06Sov	40	14.29	42.63 (-4.26, +4.73)	13.81 ± 0.13 (135)	1.56	1.76
08Sov	40	9.02	56.73 (-7.09, +6.31)	13.83 ± 0.16 (135)	1.86	1.78
10Sov	40	6.77	45.08 (-6.07, +7.01)	14.67 ± 0.12 (108)	1.28	1.68
11Sov	40	3.57	58.34 (-13.38, +17.33)	13.62 ± 0.15 (101)	1.50	1.72
12Sov	40	4.23	51.96 (-8.31, 9.89)	14.41 ± 0.14 (95)	1.33	1.82
13Sov	40	3.73	74.23 (10.39, 12.06)	13.8 ± 0.23 (65)	1.87	1.78
05Talk	40	9.18	51.21 (-6.07, +6.88)	14.02 ± 0.13 (116)	1.40	1.81
07Talk	40	10.59	63.62 (-7.24, +8.17)	14.14 ± 0.13 (94)	1.21	1.84
13Talk	40	12.91	57.80 (-5.72, +6.35)	13.31 ± 0.16 (104)	1.60	1.80
14Talk	40	7.63	55.03 (-7.14, +8.2)	12.99 ± 0.2 (66)	1.63	1.82
01King	40	14.40	44.80 (-5, +5.6)	13.93 ± 0.13 (85)	1.16	1.73
02King	41	83.45	52.79 (-3.06. +3.25)	13.73 ± 0.14 (125)	1.58	2.60
03King	40	8.39	34.20 (-5.92 +7.15)	14.31 ± 0.11 (151)	1.33	2.68
04King	40	9.59	44.03 (-5.53, +6.32)	13.25 ± 0.25 (47)	1.72	1.82
05King	40	11.47	31.23 (-4.92, +5.84)	14.1 ± 0.29 (27)	1.50	2.29
01Trop	40	41.84	58.23 (-4.22, +4.55)	12.91 ± 0.14 (125)	1.55	2.12
01Chic	38	4.89	63.00 (-20.9, +31.1)	12.35 ± 0.56 (10)	1.68	2.24

Numbers in brackets represent the number of tracks counted or measured.

TABLE 4. APATITE (U-Th)/He DATA AND AGE SUMMARY

Sample	Elev (m)	Lat (°N)	Long (°W)	Mass (mg)	4He (nmol/g)	U (ppm)	Th (ppm)	F_T	Corr. Age (Ma)	Pooled Age (Ma)	SD (Ma)
01Sov	1332	62.19	-148.45	2.75	0.63	2.47	2.04	0.73	48.82	45.31	5.34
				1.45	0.71	3.27	1.02	0.66	48.62		(11.78%)
				1.43	0.75	4.32	1.91	0.69	37.48		
				1.30	1.77	9.75	1.24	0.66	46.31		
06Sov	1618	62.15	-148.53	3.86	2.89	19.14	1.61	0.80	32.57	37.52	4.20
				9.33	2.39	14.24	0.44	0.78	38.29		(11.18%)
				3.25	3.74	24.10	1.66	0.75	36.54		
				1.66	1.17	6.59	0.69	0.69	42.70		
13Sov	2463	62.12	-148.63	2.88	1.53	7.79	4.36	0.75	40.40	44.10	3.33
				3.08	1.01	4.52	2.26	0.75	45.07		(7.54%)
				2.49	0.99	3.90	3.22	0.73	46.83		
05Talk	1733	62.03	-148.69	4.46	2.868	16.33	0.69	0.75	40.11	Does not meet parameters	
				1.41	0.681	0.79	0.95	0.67	164.12	for age determination	
				1.19	3.994	17.55	1.64	0.66	60.09		
				1.03	2.750	12.49	2.71	0.6247	59.71		
				1.32	20.825	26.43	2.93	0.64	213.55		
13Talk	1279	62.02	-148.74	0.65	2.36	20.22	0.00	0.57	36.44	32.33	3.81
				0.90	4.05	32.09	8.81	0.64	33.46		(11.78%)
				15.95	3.29	21.71	0.77	0.86	32.11		
				3.19	1.66	14.17	0.71	0.76	27.30		
14Talk	777	62.08	-148.82	1.70	3.14	14.66	0.13	0.69	56.34	43.61	11.03
				1.16	2.02	15.03	0.00	0.66	37.37		(25.29%)
				1.24	1.25	9.03	1.17	0.66	37.12		
01King	1006	61.84	-148.64	1.15	2.99	17.10	0.77	0.65	47.48	42.38	6.86
				0.49	4.98	33.31	2.09	0.57	46.48		(16.19%)
				0.50	1.84	16.26	3.10	0.55	35.15		
				0.65	4.44	27.60	3.36	0.58	48.14		
				0.48	1.87	17.62	1.42	0.54	34.63		
02King	1046	61.90	-148.65	1.29	6.26	109.13	174.32	0.63	12.31	12.13	0.76
				0.76	5.02	91.02	160.77	0.57	12.59		(6.29%)
				0.76	3.12	63.03	112.81	0.59	10.87		
				0.76	6.62	112.89	204.88	0.59	12.84		
				1.02	5.20	90.71	163.37	0.62	12.06		
03King	1086	61.92	-148.70	1.11	0.38	5.64	0.54	0.65	18.04	20.85	3.01
				0.76	9.06	90.18	141.7	0.57	23.48		(14.43%)
				0.71	3.55	42.67	8.63	0.62	23.42		
				0.49	0.47	8.80	0.20	0.52	18.47		

TABLE 4 Continued.

Sample	Elev (m)	Lat (°N)	Long (°W)	Mass (mg)	4He (nmol/g)	U (ppm)	Th (ppm)	F_T	Corr. Age (Ma)	Pooled Age (Ma)	SD (Ma)
04King	1561	61.96	-148.76	7.33	1.69	9.68	2.59	0.81	36.85	33.37	3.13
				2.69	1.57	11.02	3.44	0.74	32.62		(9.39%)
				1.33	1.30	10.99	4.05	0.66	30.01		
				1.20	0.36	3.16	0.81	0.63	30.93		
				0.67	1.74	14.23	3.32	0.58	36.44		
01Trop	1058	61.78	-149.11	1.41	1.71	33.56	47.04	0.63	11.18	10.54	0.41
				0.86	2.89	64.16	92.40	0.61	10.10		(3.90%)
				3.09	3.11	55.88	77.20	0.74	10.50		
				1.30	3.54	70.41	94.54	0.66	10.63		
				1.92	2.66	50.59	80.35	0.69	10.27		
01Chic	992	61.88	-148.43	1.39	0.99	4.94	10.73	0.66	35.80	44.62	11.18
				0.91	1.87	7.24	12.26	0.61	54.50		(25.05%)
				1.41	1.36	5.51	5.14	0.67	54.06		
				0.69	0.95	5.63	13.36	0.57	34.12		

Appendix A - $^{40}Ar/^{39}Ar$ Spectra for Samples from the Southern Talkeetna Mountains

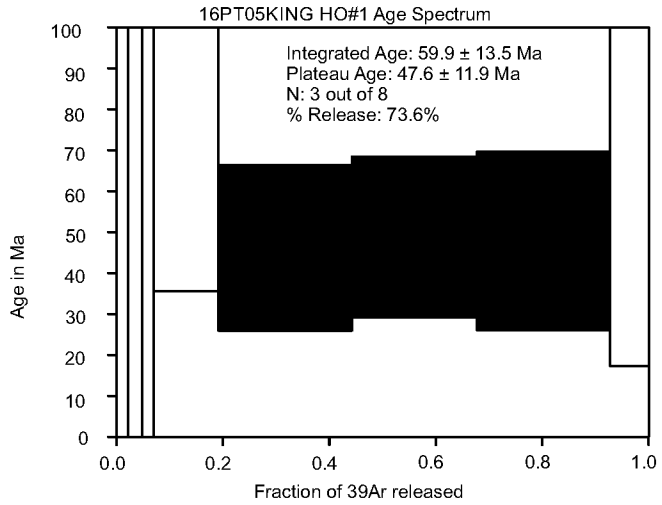

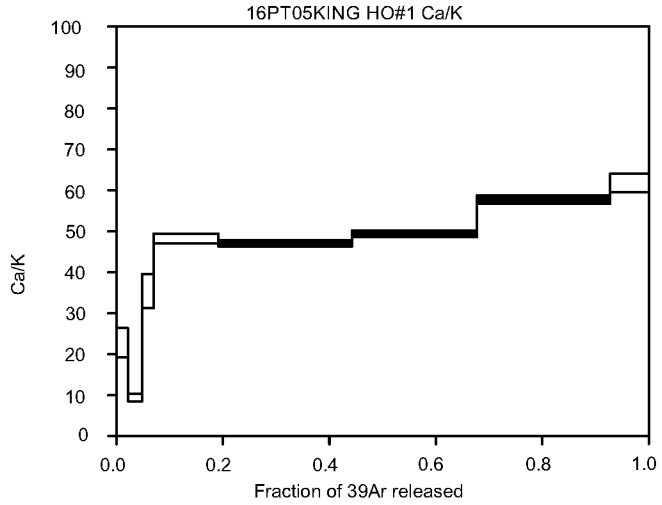

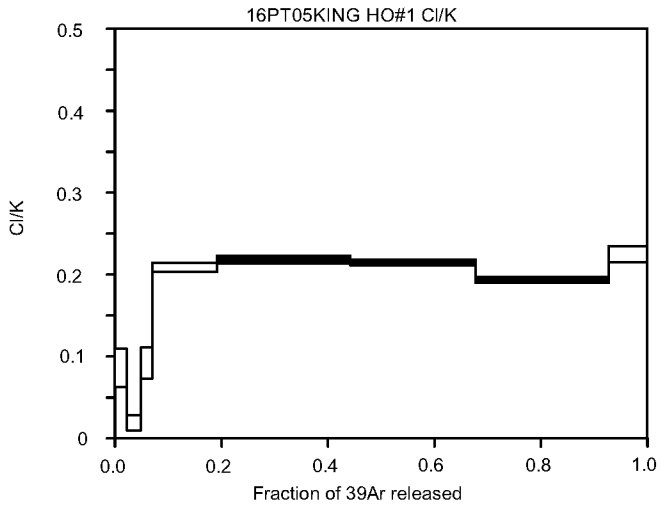

A1. $^{40}Ar/^{39}Ar$ age spectra for hornblende from Talkeetna Mountains sample 05King.

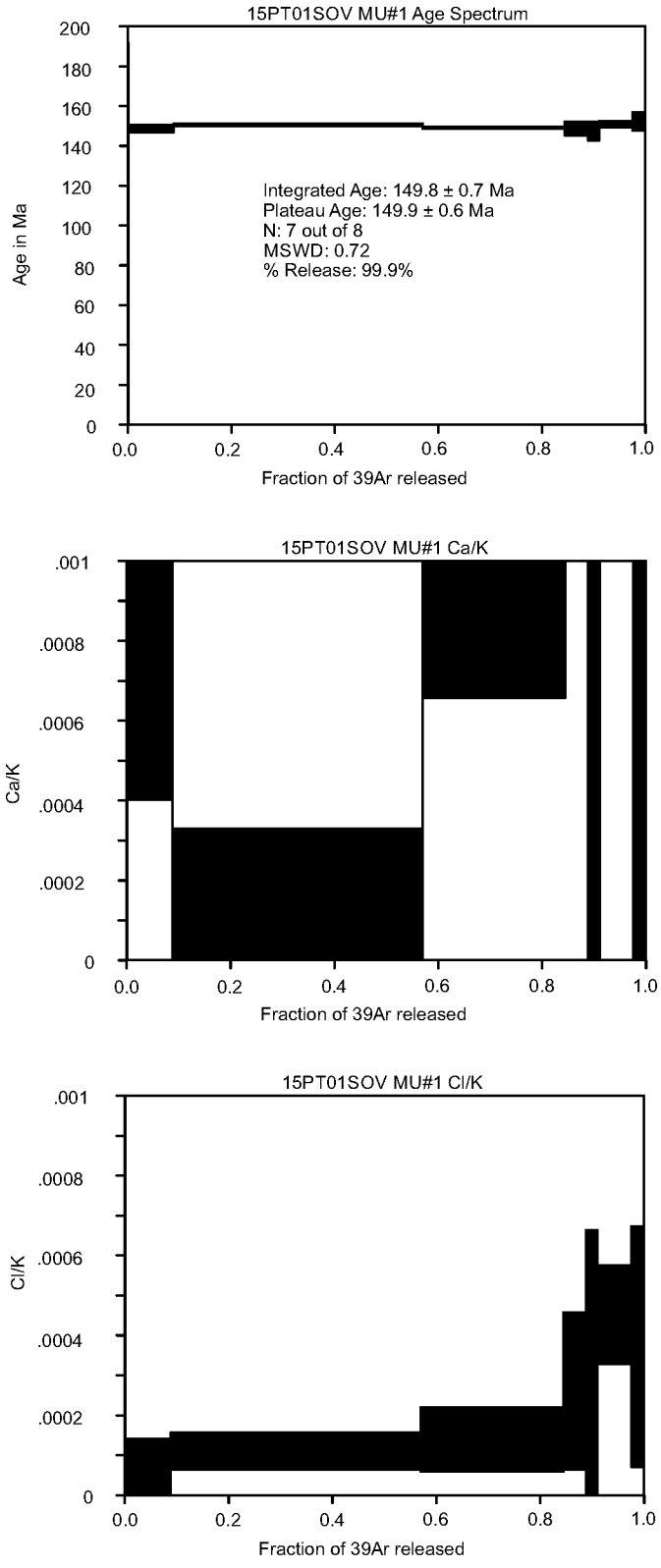

A2. $^{40}Ar/^{39}Ar$ age spectra for muscovite from Talkeetna Mountains sample 01Sov.

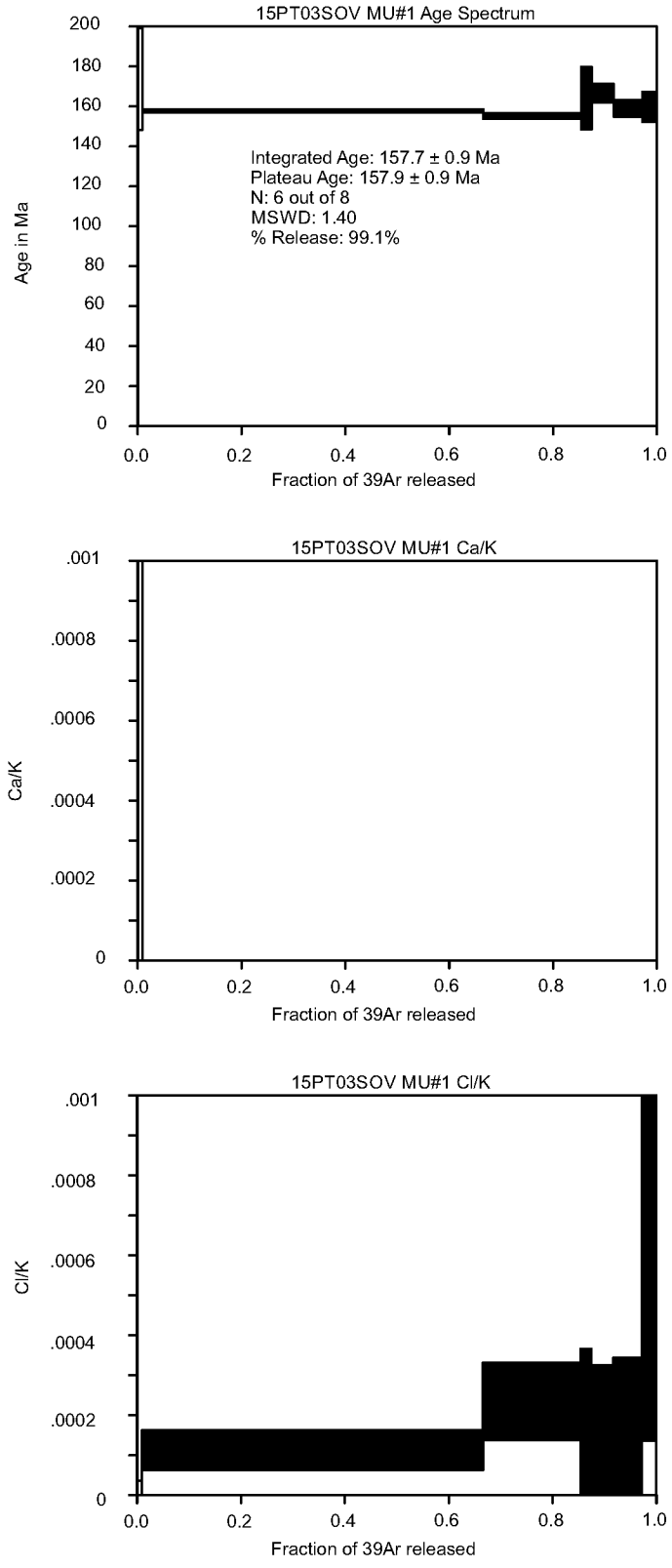

A3. $^{40}Ar/^{39}Ar$ age spectra for muscovite from Talkeetna Mountains sample 03Sov.

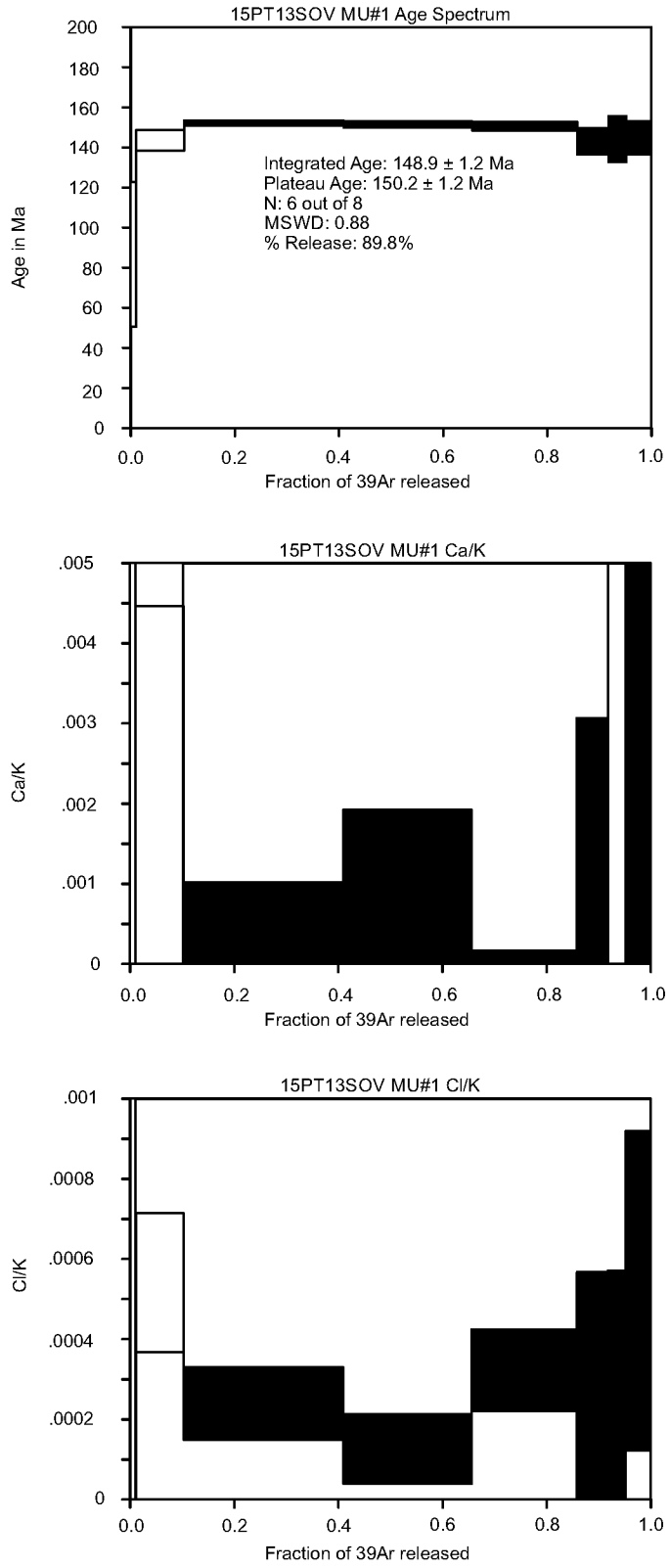

A4. $^{40}Ar/^{39}Ar$ age spectra for muscovite from Talkeetna Mountains sample 13Sov.

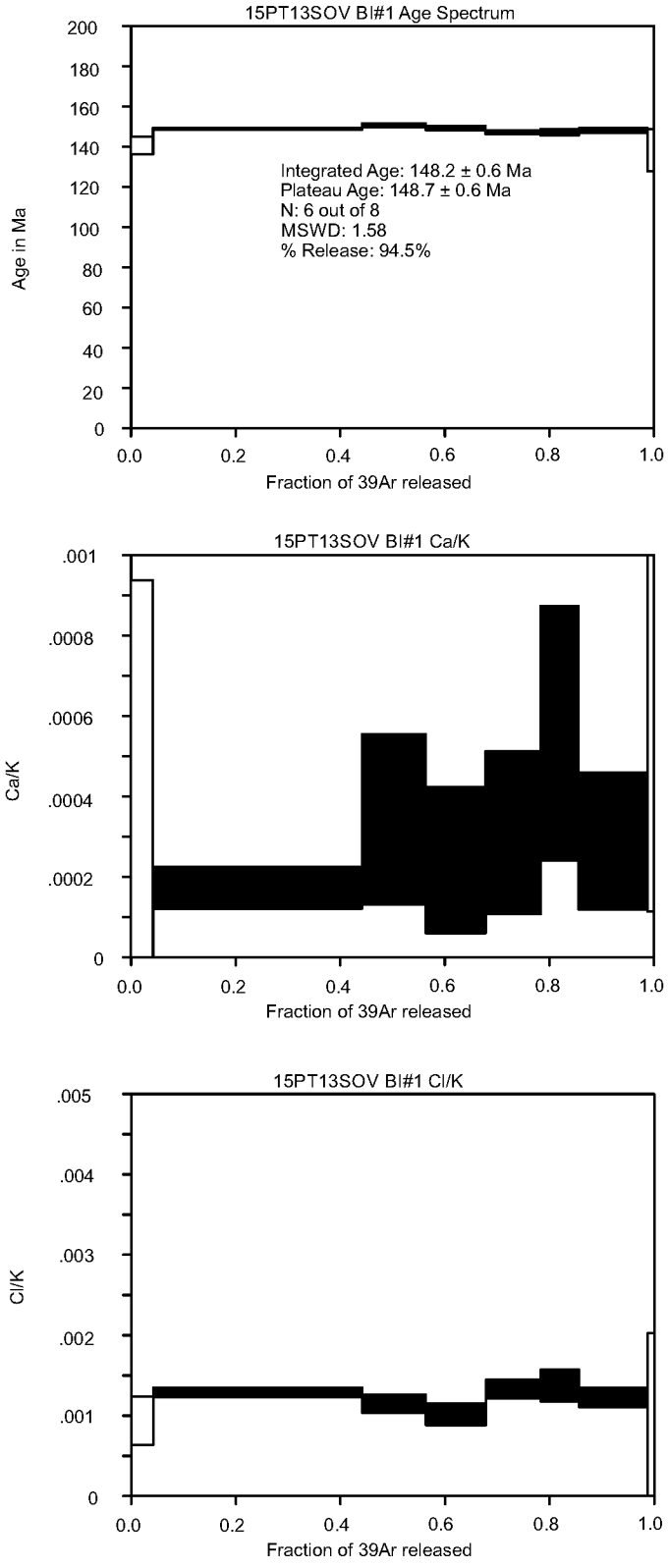

A5. $^{40}Ar/^{39}Ar$ age spectra for biotite from Talkeetna Mountains sample 13Sov.

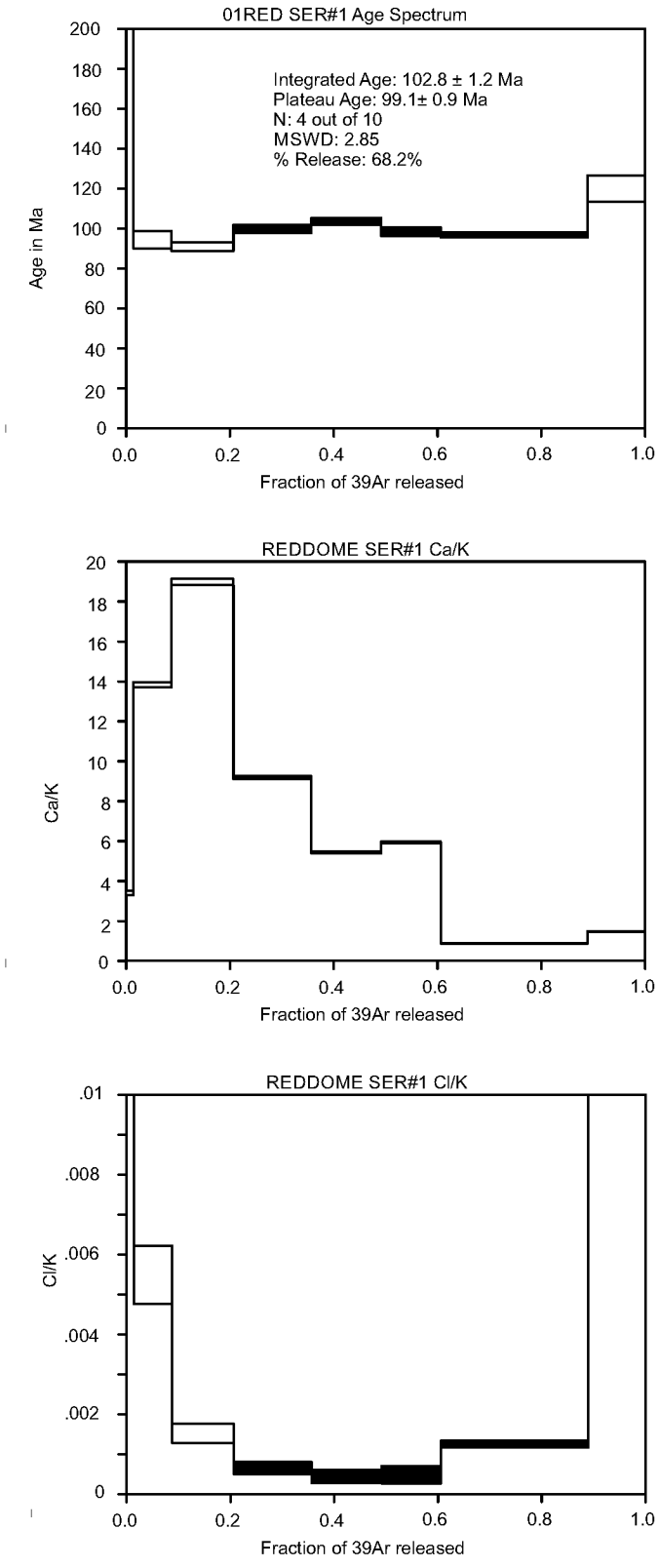

A6. $^{40}Ar/^{39}Ar$ age spectra for sericite from Talkeetna Mountains sample 01Red.

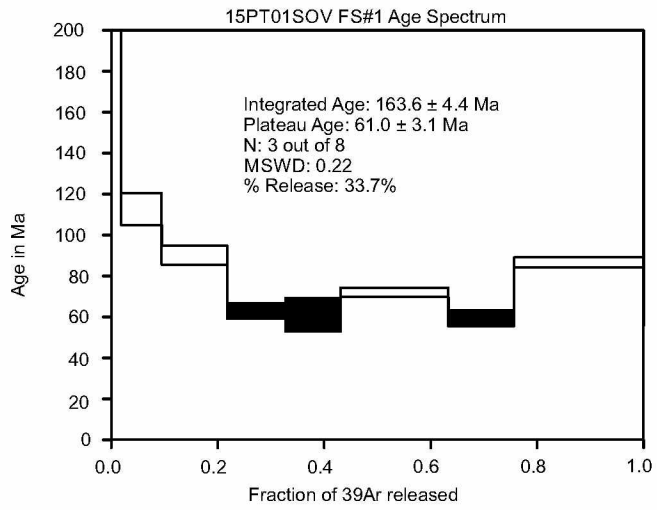

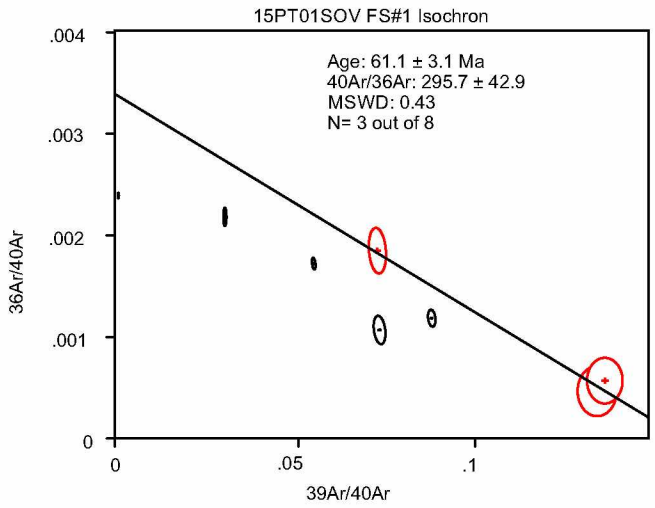

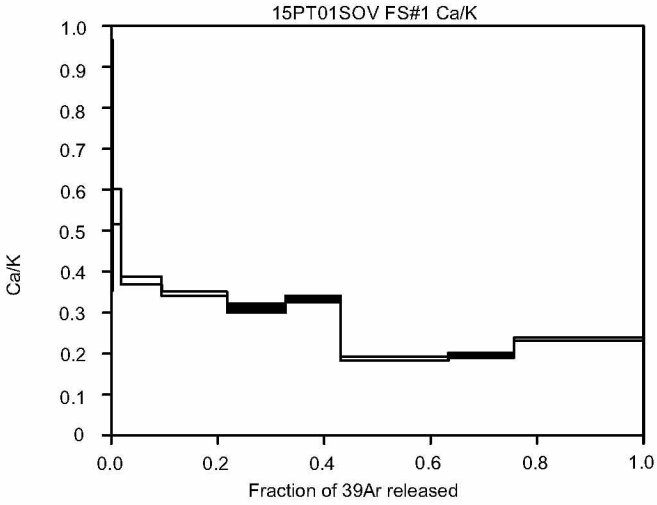

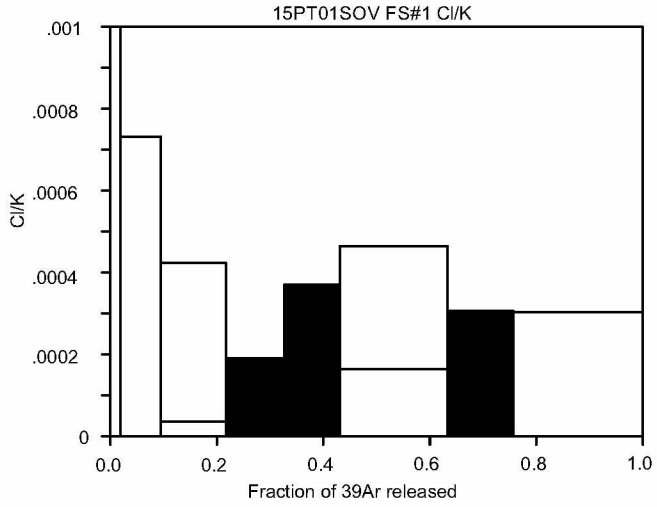

A7. $^{40}Ar/^{39}Ar$ age spectra for K-feldspar from Talkeetna Mountains sample 01Sov.

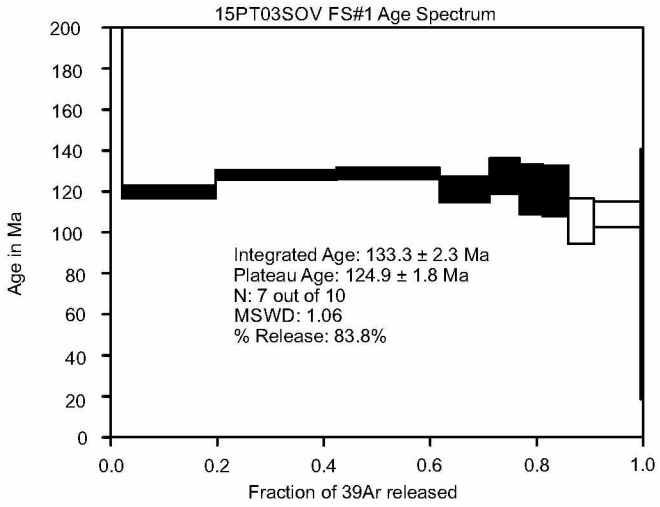

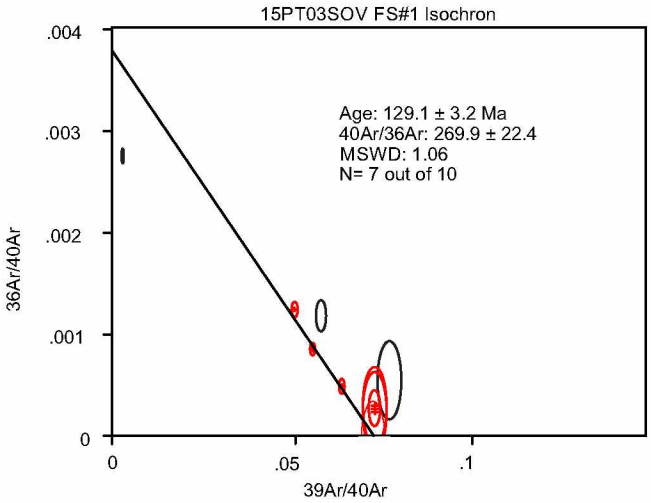

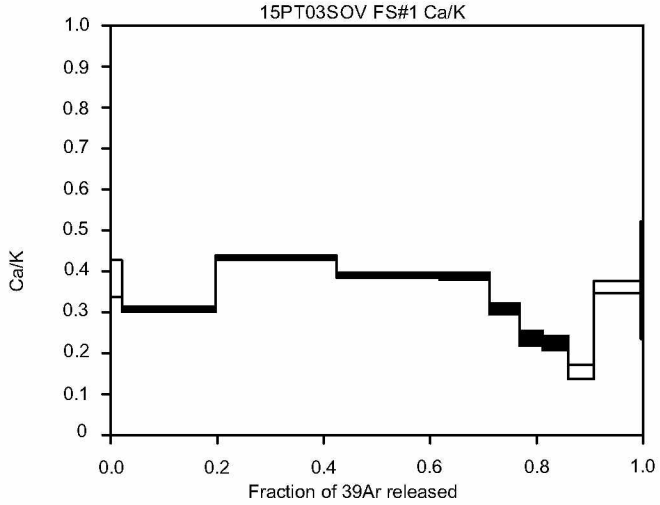

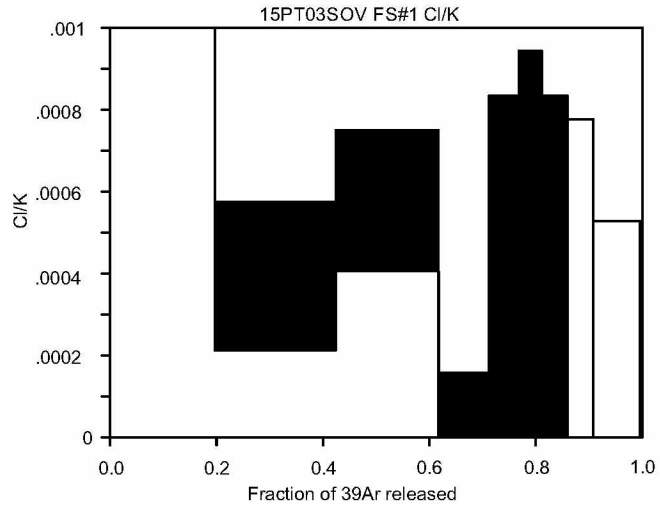

A8. $^{40}Ar/^{39}Ar$ age spectra for K-feldspar from Talkeetna Mountains sample 03Sov.

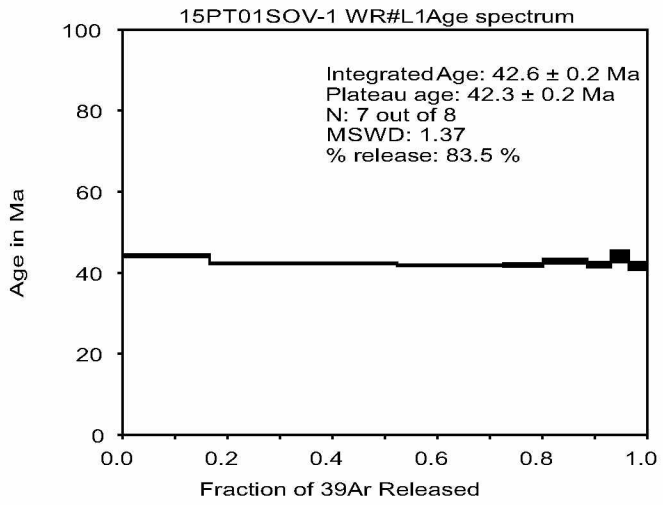

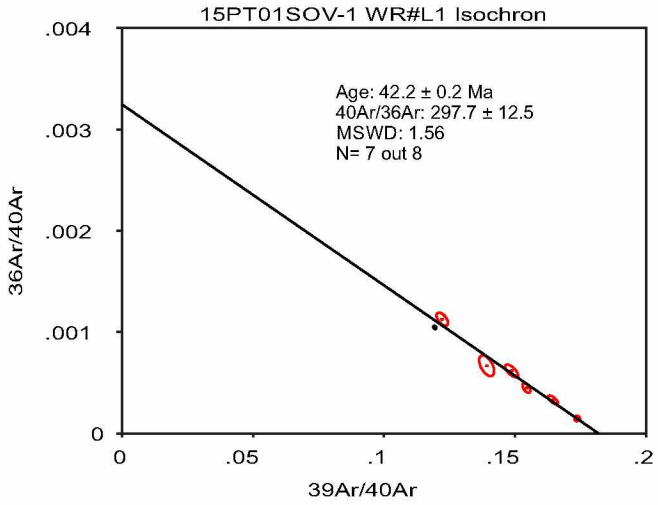

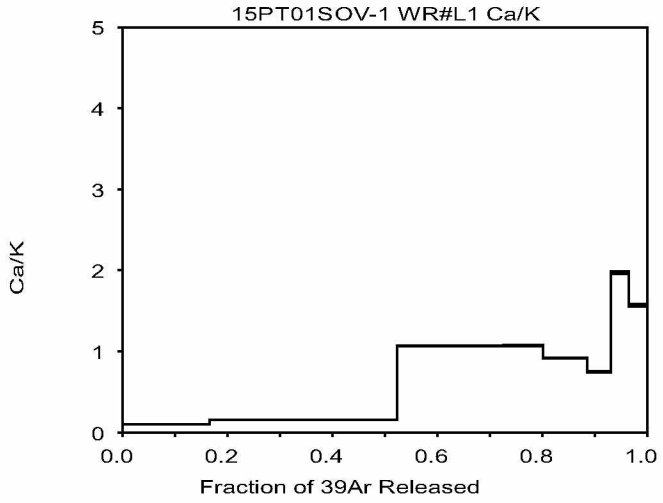

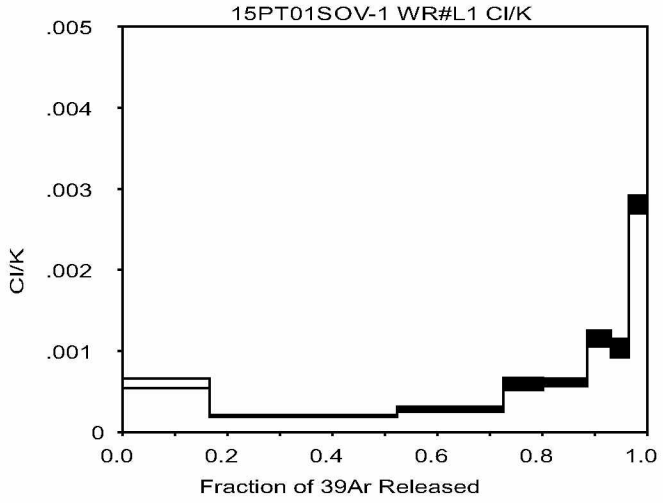

A9. $^{40}Ar/^{39}Ar$ age spectra for whole rock volcanics from Talkeetna Mountains sample 01Sov-1.

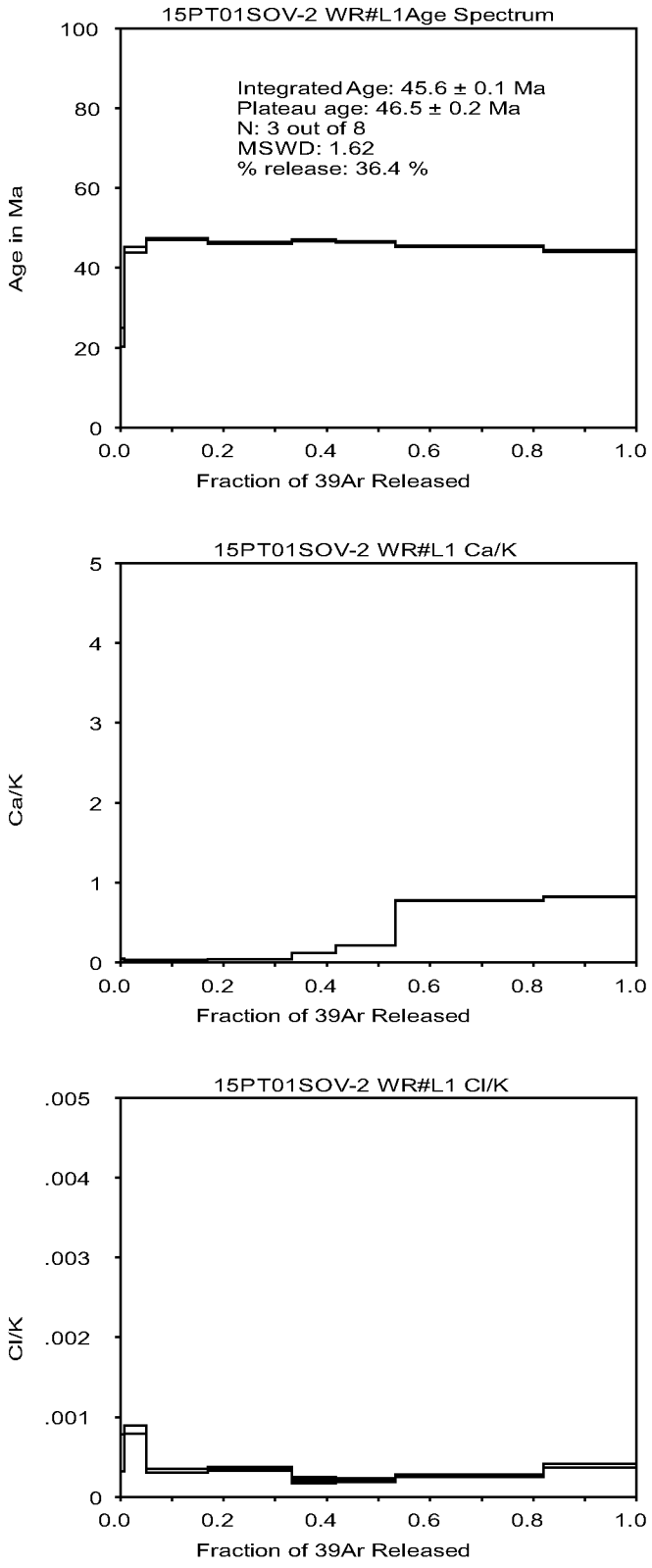

A10. $^{40}Ar/^{39}Ar$ age spectra for whole rock volcanics from Talkeetna Mountains sample 01Sov-2.

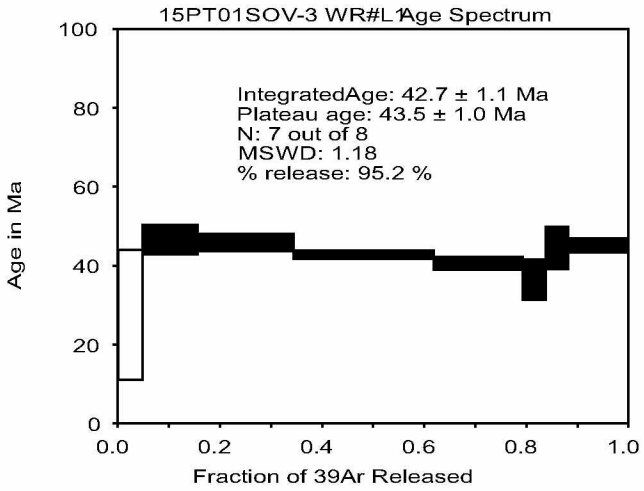

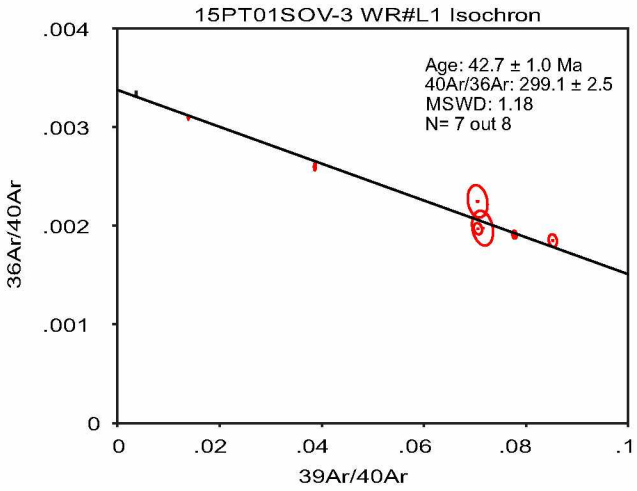

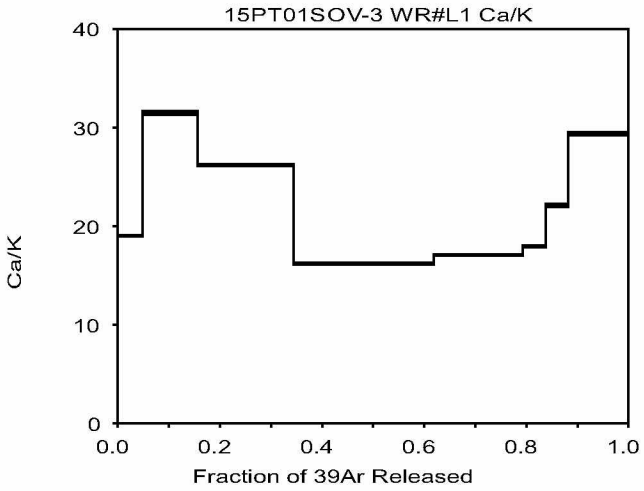

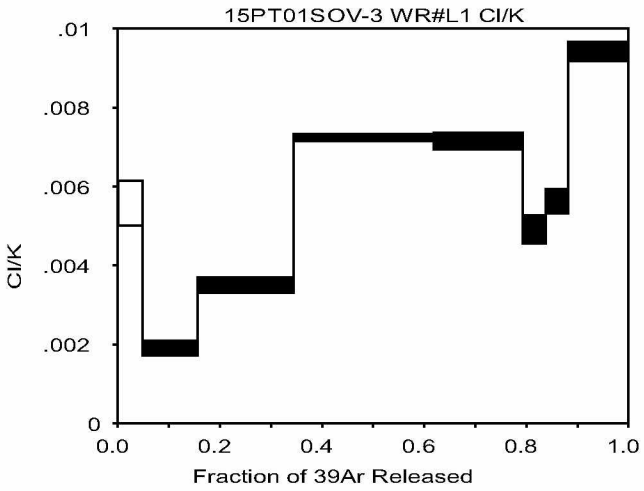

A11. $^{40}Ar/^{39}Ar$ age spectra for whole rock volcanics from Talkeetna Mountains sample 01Sov-3.

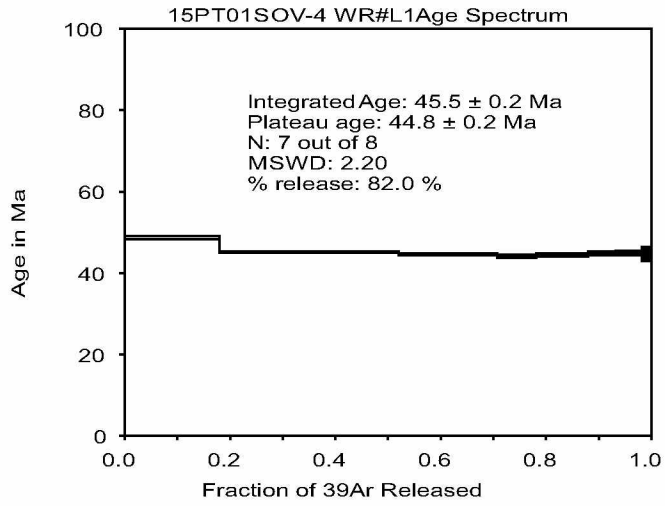

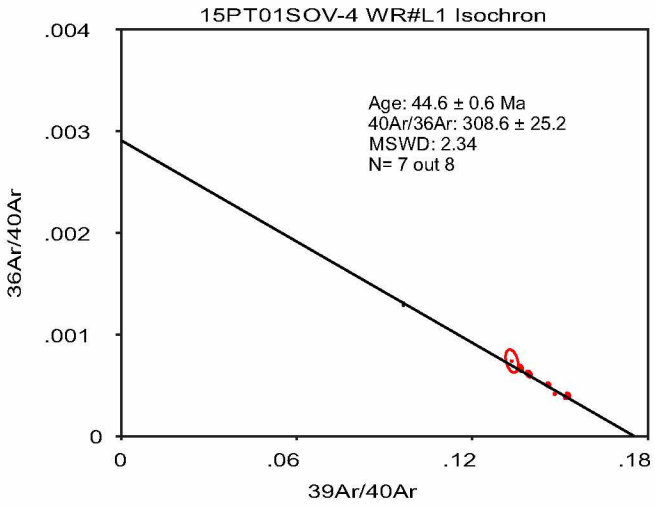

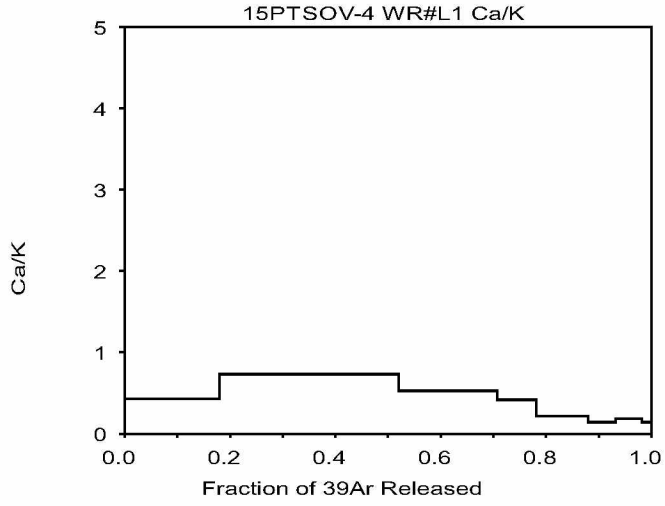

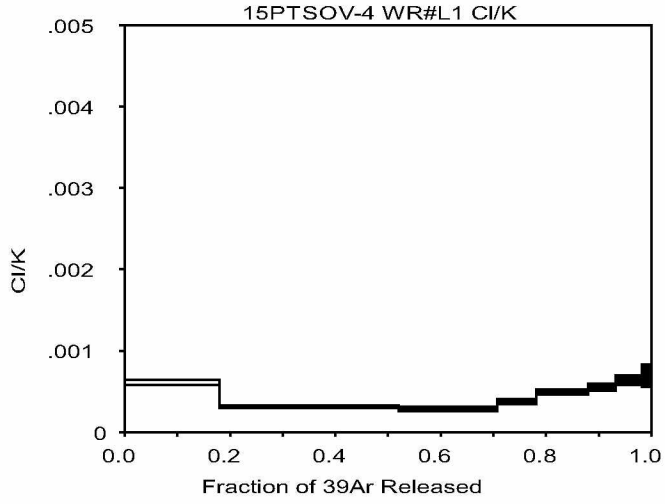

A12. $^{40}Ar/^{39}Ar$ age spectra for whole rock volcanics from Talkeetna Mountains sample 01Sov-4.

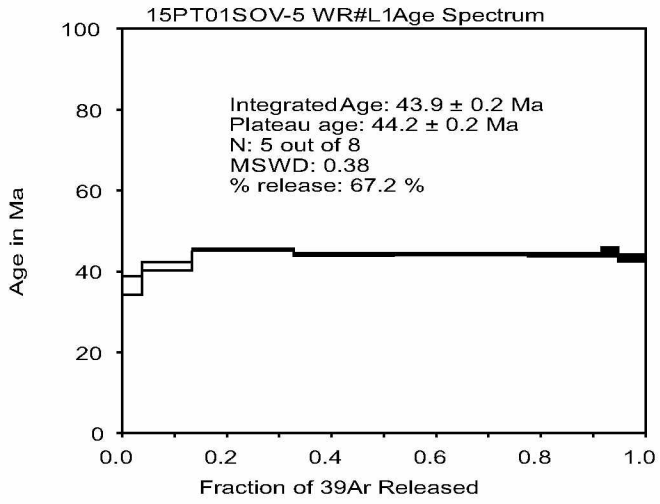

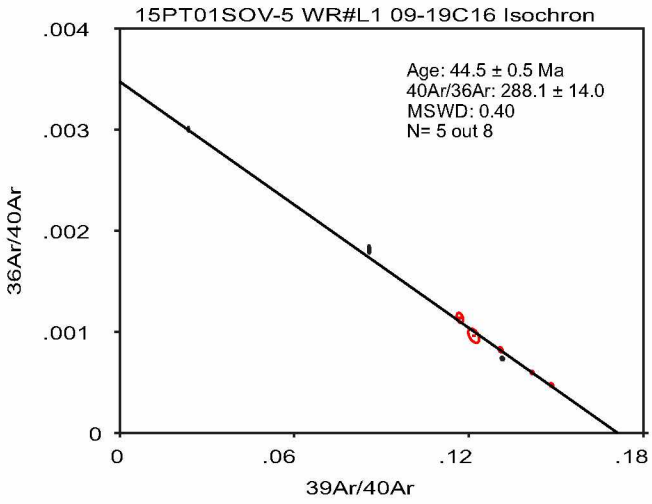

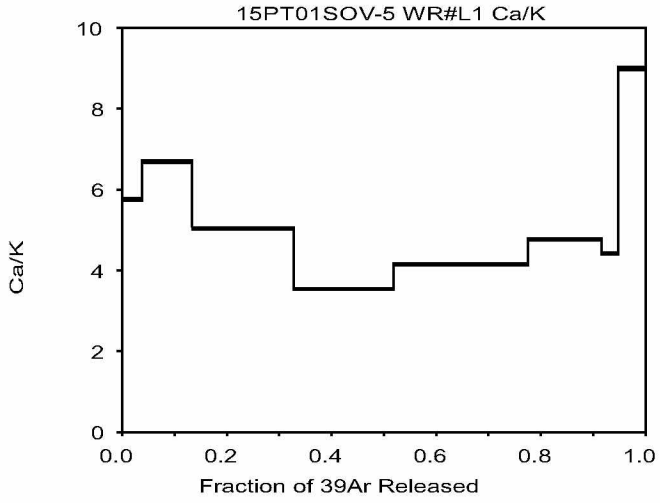

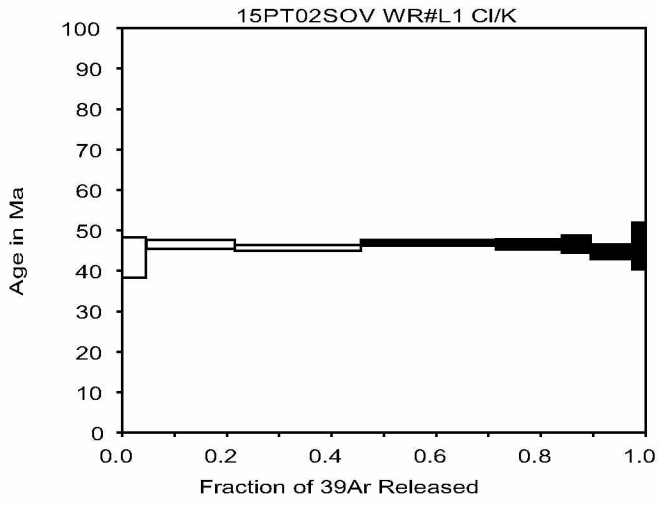

A13. $^{40}Ar/^{39}Ar$ age spectra for whole rock volcanics from Talkeetna Mountains sample 01Sov-5.

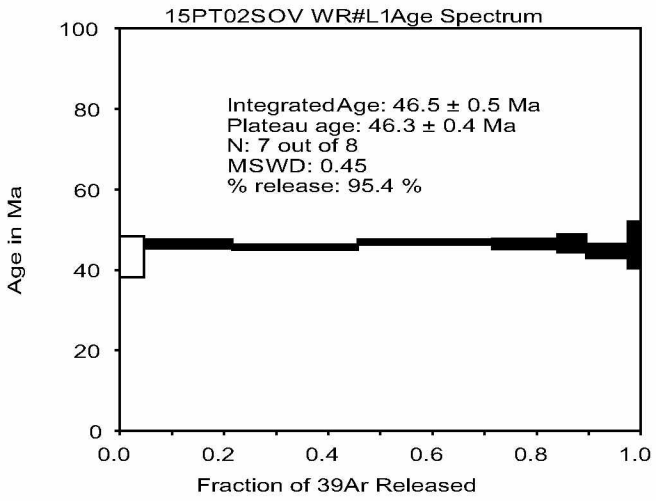

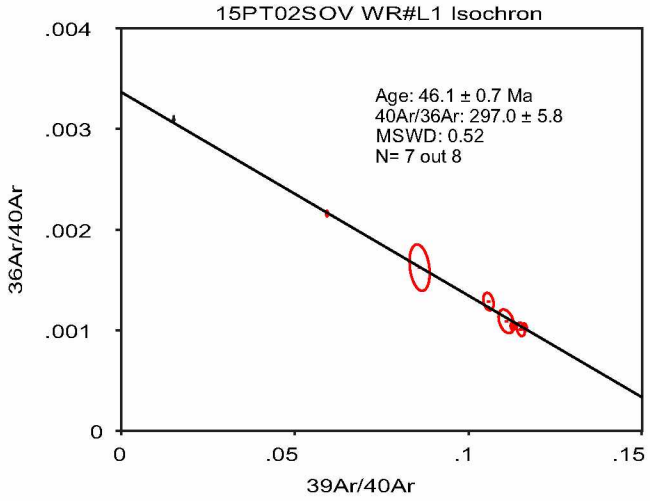

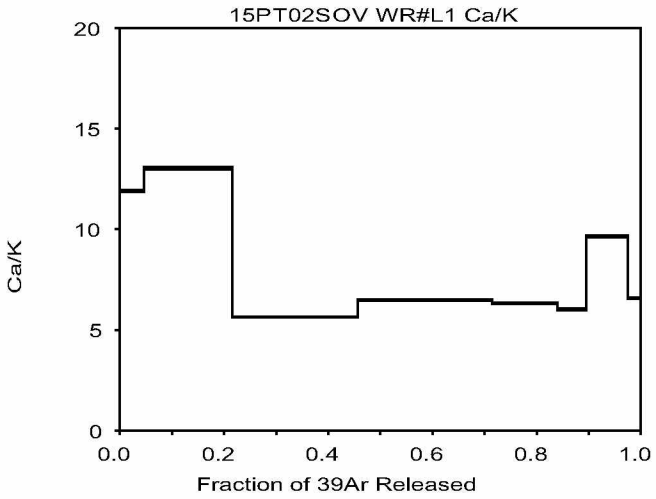

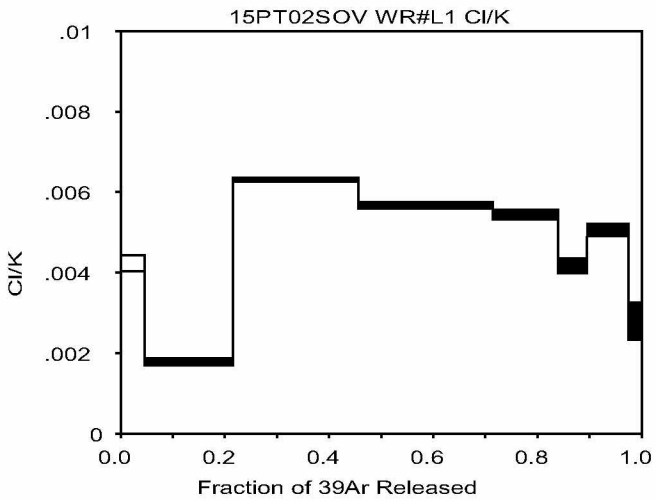

A14. $^{40}Ar/^{39}Ar$ age spectra for whole rock volcanics from Talkeetna Mountains sample 02Sov.

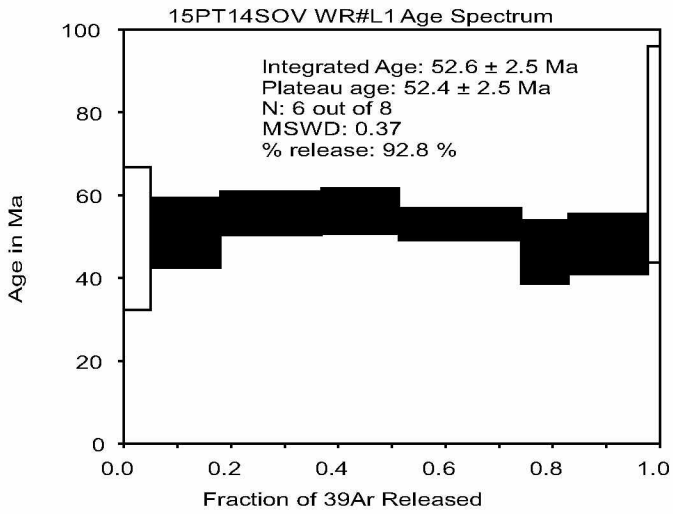

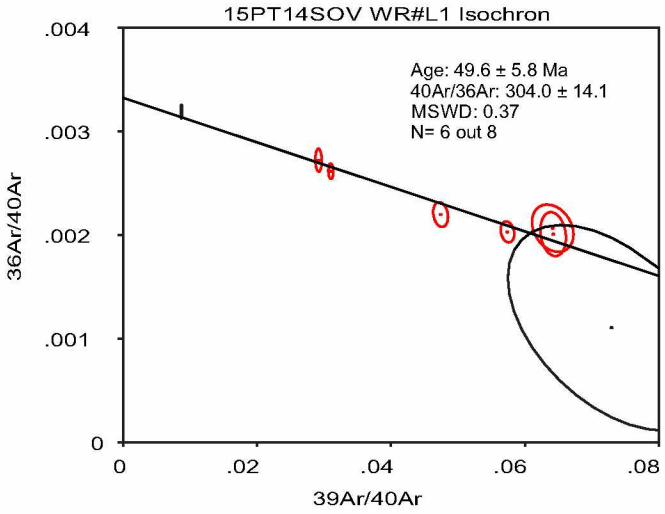

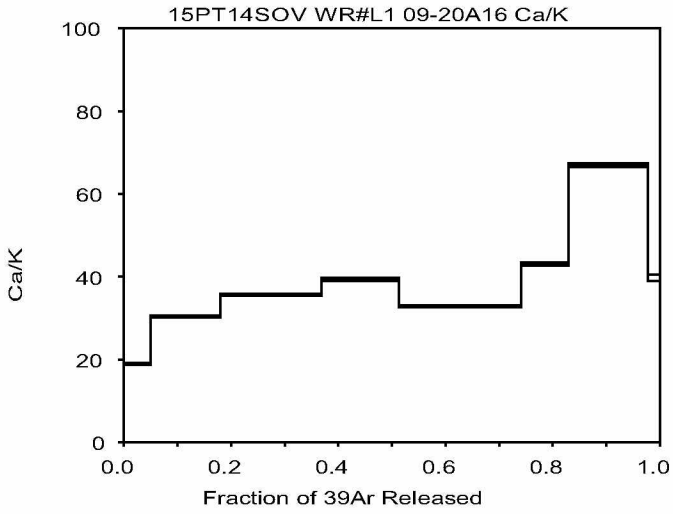

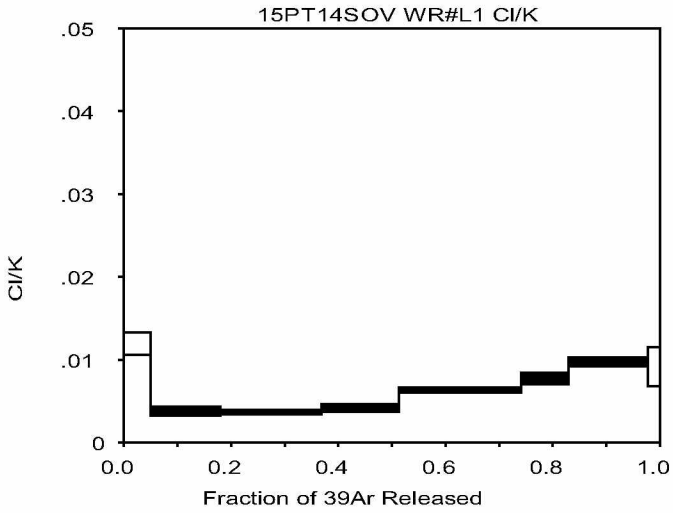

A15. $^{40}Ar/^{39}Ar$ age spectra for whole rock volcanics from Talkeetna Mountains sample 14Sov.

Appendix B. $^{40}Ar/^{39}Ar$ Data For Samples From The Southern Talkeetna Mountains

L=laser

05King HO#1 Weighted average of J from standards = 5.570e-03 1.672e-05

Laser Power (mW)	Cumulative 39Ar	40Ar/39Ar meas.	+/-	37Ar/39Ar meas.	+/-	36Ar/39Ar meas.	+/-	% Atm. 40Ar	+/-	Ca/K	+/-	Cl/K	+/-	40*/39K	+/-	Age (Ma)	+/- (Ma)
500	0.022	339.75173	51.84288	12.32584	1.88727	1.09486	0.1838	94.9345	6.67554	22.81482	3.52397	0.08589	0.02342	17.35975	23.03524	166.34	210.84
1000	0.0484	59.56567	5.53678	5.10782	0.49078	0.17342	0.0612	85.36899	29.32064	9.40608	0.90704	0.01915	0.00931	8.74226	17.54041	85.69	167.9
1500	0.0704	33.52787	3.90693	19.04461	2.21377	0.04748	0.0759	37.19336	66.77993	35.42064	4.17347	0.09197	0.0189	21.32616	22.8172	202.29	204.72
2000	0.1919	9.60396	0.22654	25.83471	0.61465	0.01485	0.01297	23.59911	40.02859	48.28408	1.1701	0.20875	0.00577	7.45118	3.90825	73.29	37.67
2500	0.4422	8.33093	0.14055	25.17005	0.41908	0.01964	0.00685	44.91895	24.37212	47.01937	0.79703	0.21851	0.0046	4.65545	2.06186	46.14	20.17
3000	0.6771	9.56367	0.14434	26.40699	0.39484	0.02328	0.00667	49.32458	20.63771	49.37397	0.75227	0.21483	0.00362	4.92348	2.00692	48.76	19.61
5000	0.9273	9.8004	0.1573	30.77286	0.49459	0.02567	0.00736	51.65787	22.23617	57.71831	0.94827	0.19371	0.00362	4.82861	2.22282	47.83	21.73
9000	1	13.65613	0.50079	32.88802	1.18219	0.03023	0.01964	45.66046	42.5212	61.77989	2.27355	0.22513	0.00972	7.58099	5.93981	74.54	57.21
Integrated		18.63542	0.16869	26.57672	0.24493	0.05023	0.00463	67.99789	7.31351	49.69738	0.46677	0.19978	0.00222	6.0683	1.38816	59.91	13.48

01Sov MU#1 Weighted average of J from standards = 5.570e-03 1.672e-05

Laser Power (mW)	Cumulative 39Ar	40Ar/39Ar meas.	+/-	37Ar/39Ar meas.	+/-	36Ar/39Ar meas.	+/-	% Atm. 40Ar	+/-	Ca/K	+/-	Cl/K	+/-	40*/39K	+/-	Age (Ma)	+/- (Ma)
500	0.0014	26.63036	1.485	-0.0057	0.06269	0.058	0.03526	64.42867	39.03067	-0.01046	0.11503	-0.00213	0.00821	9.46217	10.39944	92.56	99.17
1000	0.0883	16.29403	0.06122	0.00137	0.00115	0.00277	0.00068	5.02322	1.23066	0.00252	0.00212	0.00001	0.00013	15.44735	0.20857	148.75	1.93
1500	0.5697	15.71504	0.06494	0.00003	0.00015	0.00017	0.00014	0.32619	0.26927	0.00006	0.00027	0.00011	0.00005	15.63418	0.0773	150.48	0.71
2000	0.8441	15.66148	0.03769	0.00072	0.00036	0.00051	0.00015	0.96287	0.28166	0.00132	0.00067	0.00014	0.00008	15.48127	0.05775	149.07	0.53
2500	0.8883	15.94177	0.07997	0.00388	0.00277	0.00159	0.00126	2.95884	2.33934	0.00712	0.00509	0.00026	0.0002	15.4413	0.38028	148.7	3.52
3000	0.9103	16.03604	0.15617	-0.00046	0.00397	0.00239	0.00162	4.41515	2.98368	-0.00084	0.00728	0.00023	0.00044	15.29963	0.50042	147.39	4.63
5000	0.9748	15.92285	0.03571	0.0072	0.00161	0.00075	0.00059	1.3935	1.09584	0.01322	0.00296	0.00045	0.00012	15.67176	0.17772	150.82	1.64
9000	1	16.20457	0.11403	0.00319	0.00474	0.00116	0.00169	2.12501	3.0787	0.00585	0.0087	0.00037	0.0003	15.83119	0.51038	152.3	4.71
Integrated		15.80925	0.0341	0.00103	0.00028	0.00075	0.00014	1.4005	0.26522	0.00189	0.00052	0.00014	0.00004	15.55857	0.0537	149.78	0.66

Appendix B continued

03Sov MU#1 Weighted average of J from standards = 5.570e-03 1.672e-05

Laser Power (mW)	Cumulative 39Ar	40Ar/39Ar meas.	+/-	37Ar/39Ar meas.	+/-	36Ar/39Ar meas.	+/-	% Atm. 40Ar	+/-	Ca/K	+/-	Cl/K	+/-	40*/39K	+/-	Age (Ma)	+/- (Ma)
500	0.0012	46.30248	5.28053	-0.04554	0.13551	0.18643	0.08955	119.06388	55.57825	-0.08356	0.24862	-0.02451	0.01224	-8.8211	25.73423	-90.8	271.68
1000	0.0094	24.04745	0.47844	-0.00825	0.0276	0.01983	0.00937	24.40474	11.51763	-0.01513	0.05064	-0.00182	0.00186	18.15618	2.79031	173.62	25.44
1500	0.6659	16.85493	0.04751	-0.00116	0.00035	0.00137	0.00021	2.39916	0.36498	-0.00212	0.00064	0.00011	0.00005	16.42155	0.077	157.73	0.71
2000	0.8539	16.3564	0.07151	-0.00191	0.00086	0.00061	0.0005	1.1122	0.89898	-0.0035	0.00158	0.00023	0.0001	16.14509	0.16295	155.19	1.5
2500	0.8744	16.51472	0.11168	-0.01139	0.00689	-0.00216	0.00574	-3.86823	10.28903	-0.0209	0.01265	-0.00058	0.00094	17.12256	1.70004	164.17	15.58
3000	0.9169	16.57306	0.12557	-0.00716	0.00285	-0.00283	0.00166	-5.04306	2.96579	-0.01314	0.00524	-0.00008	0.0004	17.37756	0.50797	166.51	4.65
5000	0.972	16.10216	0.11217	-0.00489	0.00254	-0.00164	0.00147	-3.01126	2.69768	-0.00897	0.00465	0.00003	0.00032	16.55639	0.44867	158.97	4.12
9000	1	16.4174	0.17064	-0.00909	0.00462	-0.00085	0.0027	-1.53492	4.86098	-0.01668	0.00848	0.00073	0.0006	16.63914	0.81519	159.73	7.49
Integrated		16.7817	0.0356	-0.0023	0.00048	0.00111	0.00027	1.96242	0.48117	-0.00422	0.00087	0.00008	0.00006	16.42323	0.08786	157.75	0.93

13Sov MU#1 Weighted average of J from standards = 5.570e-03 1.672e-05

Laser Power (mW)	Cumulative 39Ar	40Ar/39Ar meas.	+/-	37Ar/39Ar meas.	+/-	36Ar/39Ar meas.	+/-	% Atm. 40Ar	+/-	Ca/K	+/-	Cl/K	+/-	40*/39K	+/-	Age (Ma)	+/- (Ma)
500	0.0107	20.17711	0.30652	0.01106	0.01497	0.03826	0.0128	56.10617	18.76342	0.0203	0.02747	0.00089	0.00158	8.84354	3.78312	86.66	36.19
1000	0.1023	19.36072	0.0968	0.00392	0.00149	0.01505	0.00184	23.00866	2.80536	0.00719	0.00273	0.00054	0.00017	14.88325	0.54792	143.53	5.08
1500	0.4094	16.12708	0.04921	0.00017	0.00039	0.001	0.00045	1.83962	0.82819	0.0003	0.00072	0.00024	0.00009	15.80125	0.14182	152.02	1.31
2000	0.6556	16.1885	0.04167	0.00033	0.00072	0.00144	0.00055	2.64154	1.01332	0.0006	0.00132	0.00013	0.00009	15.73197	0.16873	151.38	1.56
2500	0.8581	16.07761	0.06471	-0.00049	0.00058	0.00139	0.00074	2.55604	1.35883	-0.0009	0.00107	0.00032	0.0001	15.63771	0.22702	150.51	2.1
3000	0.9178	16.17744	0.07401	-0.00077	0.00244	0.00451	0.00238	8.2579	4.36218	-0.00141	0.00448	0.00013	0.00044	14.81427	0.70774	142.89	6.56
5000	0.9517	16.42786	0.08409	0.01109	0.00456	0.0049	0.00418	8.82721	7.53441	0.02034	0.00837	0.00008	0.0005	14.95077	1.23794	144.16	11.47
9000	1	16.35496	0.08204	0.00225	0.00304	0.0044	0.00302	7.9672	5.46097	0.00413	0.00559	0.00052	0.0004	15.02462	0.89479	144.84	8.29
Integrated		16.49584	0.02529	0.00095	0.00041	0.00338	0.00041	6.06793	0.73741	0.00174	0.00076	0.00026	0.00006	15.46699	0.12375	148.93	1.22

Appendix B continued

01Red SE#1 Weighted average of J from standards = 5.570e-03 1.672e-05

Laser Power (mW)	Cumulative 39Ar	40Ar/39Ar meas.	+/-	37Ar/39Ar meas.	+/-	36Ar/39Ar meas.	+/-	% Atm. 40Ar	+/-	Ca/K	+/-	Cl/K	+/-	40*/39K	+/-	Age (Ma)	+/- (Ma)
500	0.0141	364.47562	4.36073	1.84936	0.05559	1.13299	0.01875	91.82289	1.05378	3.39776	0.10226	0.02683	0.00203	29.84012	3.86312	277.1	33.25
1000	0.0876	26.60061	0.19811	7.49784	0.07375	0.0595	0.00159	63.83977	1.70933	13.83074	0.13677	0.00549	0.00073	9.65931	0.46316	94.44	4.41
1500	0.2067	13.61165	0.07982	10.2662	0.08325	0.01758	0.00076	32.02281	1.63145	18.97463	0.15499	0.00152	0.00024	9.3002	0.23024	91.02	2.2
2000	0.3567	13.15467	0.06167	4.98761	0.03545	0.01132	0.00076	22.36457	1.69989	9.18393	0.06551	0.00065	0.00015	10.22573	0.2294	99.83	2.18
2500	0.4916	12.73042	0.04159	2.95252	0.02197	0.00792	0.00058	16.50124	1.34808	5.42878	0.04049	0.00044	0.00016	10.62716	0.17568	103.64	1.66
3000	0.606	11.99554	0.0492	3.22238	0.02368	0.00735	0.00075	15.93446	1.85487	5.92611	0.04364	0.00049	0.00022	10.08215	0.22655	98.47	2.15
5000	0.889	14.47488	0.04101	0.478	0.00338	0.01547	0.00046	31.37006	0.93453	0.87736	0.0062	0.00125	0.00009	9.91707	0.13839	96.9	1.32
9000	1	40.33932	0.17352	0.79427	0.01015	0.09481	0.0024	69.34248	1.74068	1.45819	0.01865	0.01105	0.00049	12.36487	0.70475	120.03	6.62
Integrated		22.34723	0.03507	3.54566	0.01116	0.04094	0.00041	52.89723	0.54052	6.52213	0.02058	0.00276	0.0001	10.5386	0.12228	102.8	1.2

01Sov FS#1 Weighted average of J from standards = 5.570e-03 1.672e-05

Laser Power (mW)	Cumulative 39Ar	40Ar/39Ar meas.	+/-	37Ar/39Ar meas.	+/-	36Ar/39Ar meas.	+/-	% Atm. 40Ar	+/-	Ca/K	+/-	Cl/K	+/-	40*/39K	+/-	Age (Ma)	+/- (Ma)
300	0.0001	80619.10202	114594.2674	-5.45848	8.15269	261.87984	372.25786	95.98962	1.21513	-9.9771	14.8444	0.12189	0.44758	3220.71333	4663.80764	5300.43	2471.73
600	0.0029	13452.44676	1194.71336	0.3593	0.16665	40.52267	3.63265	89.01314	1.09115	0.65943	0.30594	0.09533	0.03095	1478.37377	197.04717	4006.01	214.18
1000	0.0185	1051.86673	34.36346	0.30456	0.02324	2.50492	0.08778	70.36996	0.89452	0.55894	0.04267	0.0046	0.00221	311.72673	13.87648	1814.06	50.9
1500	0.0949	32.3809	0.22596	0.20605	0.00523	0.07034	0.00283	64.19247	2.54851	0.37813	0.00959	0.00036	0.00037	11.58585	0.82884	112.7	7.82
2000	0.2177	13.47011	0.08739	0.18837	0.00297	0.01436	0.00166	31.44961	3.65403	0.34568	0.00545	0.00023	0.00019	9.21468	0.49511	90.2	4.73
2500	0.3273	7.41366	0.0514	0.16965	0.00629	0.00345	0.00132	13.59996	5.28346	0.31132	0.01154	-0.00009	0.00028	6.38051	0.3929	62.94	3.81
3000	0.4308	13.57862	0.12865	0.18175	0.00419	0.02499	0.00286	54.3841	6.22476	0.33354	0.0077	0.00014	0.00023	6.18126	0.84576	61	8.21
4000	0.6333	11.25676	0.06578	0.10189	0.00256	0.01326	0.00079	34.83841	2.05869	0.18696	0.00469	0.00031	0.00015	7.31626	0.23551	71.99	2.27
5000	0.7572	7.27922	0.03939	0.10677	0.00319	0.00421	0.00132	17.04335	5.39823	0.19592	0.00585	0.00013	0.00018	6.01441	0.3929	59.38	3.82
9000	0.9997	17.9201	0.07152	0.12837	0.00225	0.0307	0.00088	50.65293	1.43883	0.23557	0.00412	0.00014	0.00017	8.82919	0.2602	86.52	2.49
9000	1	-314.03046	178.9693	1.35819	1.46851	-1.48828	0.96214	140.06814	43.03028	2.49448	2.69968	0.08254	0.12682	125.95887	152.94542	957.97	902.25
Integrated		76.6757	0.17558	0.14672	0.00148	0.2017	0.00166	77.74616	0.61657	0.26924	0.00271	0.00054	0.00013	17.05845	0.4747	163.58	4.38

Appendix B continued

03Sov FS#1 Weighted average of J from standards = 5.570e-03 1.672e-05

Laser Power (mW)	Cumulative 39Ar	40Ar/39Ar meas.	+/-	37Ar/39Ar meas.	+/-	36Ar/39Ar meas.	+/-	% Atm. 40Ar	+/-	Ca/K	+/-	Cl/K	+/-	40*/39K	+/-	Age (Ma)	+/- (Ma)
300	0.0211	362.40419	8.29317	0.20822	0.02473	0.99592	0.03447	81.20783	2.10949	0.38212	0.0454	0.03282	0.00233	68.10806	7.8038	579.62	56.79
600	0.1968	19.51895	0.09403	0.16754	0.00327	0.02423	0.00115	36.66872	1.73031	0.30744	0.006	0.00155	0.00022	12.34425	0.34303	119.84	3.22
1000	0.424	17.68455	0.04938	0.23595	0.00303	0.01508	0.00087	25.13655	1.45711	0.433	0.00555	0.00039	0.00018	13.21924	0.26055	128.04	2.44
1500	0.6173	15.50807	0.05209	0.21315	0.00345	0.0074	0.001	14.01615	1.90943	0.39116	0.00634	0.00058	0.00017	13.31091	0.29914	128.9	2.8
2000	0.7118	13.95551	0.09726	0.21141	0.00494	0.00498	0.00223	10.43956	4.73433	0.38796	0.00907	-0.00012	0.00028	12.47389	0.66527	121.06	6.24
2500	0.768	13.81184	0.08128	0.16797	0.00766	0.00213	0.00312	4.47571	6.68587	0.30823	0.01405	0.00037	0.00046	13.16686	0.92488	127.55	8.65
3000	0.8112	13.81533	0.11839	0.12893	0.00997	0.00448	0.00436	9.52833	9.35287	0.23659	0.01831	0.00043	0.00051	12.47323	1.29407	121.05	12.15
4000	0.8591	13.91926	0.17932	0.12246	0.00946	0.00514	0.00444	10.8687	9.43464	0.22472	0.01736	0.00024	0.00059	12.38102	1.32033	120.19	12.4
5000	0.9076	12.92438	0.06913	0.08404	0.0095	0.00705	0.00394	16.11235	9.03904	0.15422	0.01744	0.00026	0.00052	10.81769	1.16724	105.44	11.05
9000	0.9955	17.18529	0.09846	0.19695	0.00786	0.02028	0.00222	34.84339	3.82606	0.36142	0.01442	0.00022	0.00031	11.17956	0.65991	108.87	6.24
9000	1	4.90318	0.29847	0.20631	0.07828	-0.01088	0.02149	-66.29057	130.31075	0.37861	0.14368	-0.00322	0.00325	8.10533	6.35862	79.58	61.07

01SOV-1 WR#L1 Weighted average of J from standards = 4.286e-03 9.931e-06

Laser Power (mW)	Cumulative 39Ar	40Ar/39Ar meas.	+/-	37Ar/39Ar meas.	+/-	36Ar/39Ar meas.	+/-	% Atm. 40Ar	+/-	Ca/K	+/-	Cl/K	+/-	40*/39K	+/-	Age (Ma)	+/- (Ma)
500	0.1654	8.4074	0.02626	0.05525	0.00044	0.00878	0.00012	30.89899	0.4188	0.10138	0.00081	0.0006	0.00006	5.7893	0.04049	44.17	0.31
1000	0.523	5.80265	0.01372	0.0841	0.00056	0.00078	0.00005	3.86991	0.24164	0.15432	0.00103	0.0002	0.00001	5.54987	0.01939	42.36	0.15
1500	0.7257	5.77803	0.01402	0.58178	0.00307	0.00106	0.00008	4.61459	0.41794	1.06792	0.00564	0.00028	0.00003	5.48533	0.02763	41.88	0.21
2000	0.8009	6.10746	0.01828	0.5842	0.00359	0.00216	0.00018	9.72897	0.88335	1.07237	0.00659	0.0006	0.00008	5.48873	0.05653	41.9	0.43
2500	0.8859	6.50811	0.02576	0.50026	0.00316	0.00304	0.00024	13.22874	1.10584	0.91823	0.0058	0.00061	0.00005	5.62339	0.07542	42.92	0.57
3000	0.9312	6.75632	0.02548	0.40785	0.00279	0.00427	0.0003	18.24019	1.30214	0.74856	0.00513	0.00116	0.0001	5.50126	0.09035	42	0.68
4000	0.965	7.212	0.02662	1.0744	0.00769	0.00509	0.00062	19.72324	2.53626	1.97288	0.01413	0.00104	0.00011	5.77011	0.18381	44.02	1.39
9000	1	8.20876	0.04197	0.85478	0.00736	0.00946	0.00043	33.30028	1.54045	1.56934	0.01352	0.00281	0.00011	5.45872	0.12975	41.67	0.98
Integrated		6.48646	0.00773	0.32839	0.00084	0.00306	0.00005	13.59757	0.22373	0.60269	0.00154	0.00051	0.00002	5.5801	0.0161	42.59	0.16

Appendix B continued

01SOV-2 WR#L1 Weighted average of J from standards = 4.286e-03 9.931e-06

Laser Power (mW)	Cumulative 39Ar	40Ar/39Ar meas.	+/-	37Ar/39Ar meas.	+/-	36Ar/39Ar meas.	+/-	% Atm. 40Ar	+/-	Ca/K	+/-	Cl/K	+/-	40*/39K	+/-	Age (Ma)	+/- (Ma)
500	0.008	7.88682	0.03852	0.0217	0.00232	0.01661	0.00106	62.44559	3.99676	0.03982	0.00426	0.00055	0.00023	2.95074	0.31462	22.65	2.4
1000	0.0504	7.84707	0.0255	0.01748	0.00042	0.0067	0.00031	25.31349	1.17425	0.03208	0.00076	0.00085	0.00005	5.8386	0.09454	44.54	0.71
1500	0.1697	6.80758	0.01634	0.0152	0.00022	0.00195	0.00008	8.47832	0.36714	0.02788	0.00041	0.00033	0.00002	6.20329	0.02949	47.29	0.22
2000	0.3324	6.56178	0.01423	0.02124	0.00026	0.00156	0.00008	7.03695	0.34675	0.03898	0.00048	0.00035	0.00002	6.07252	0.02647	46.3	0.2
2500	0.4178	6.55349	0.02234	0.06261	0.00042	0.00126	0.00011	5.62295	0.49823	0.11488	0.00077	0.00021	0.00004	6.15724	0.0391	46.94	0.29
3000	0.5333	6.44433	0.01962	0.1171	0.00059	0.00111	0.00007	4.94106	0.32822	0.21488	0.00108	0.00021	0.00002	6.09818	0.02848	46.49	0.21
4000	0.8195	6.39666	0.01373	0.42279	0.00177	0.00151	0.00003	6.44124	0.14565	0.776	0.00325	0.00026	0.00002	5.95863	0.01609	45.44	0.12
9000	1	6.42938	0.01291	0.44573	0.00217	0.00214	0.00009	9.32244	0.39287	0.81811	0.00398	0.00039	0.00002	5.80491	0.02795	44.29	0.21
Integrated		6.57075	0.00637	0.22655	0.00062	0.00196	0.00003	8.55187	0.141	0.41575	0.00114	0.00033	0.00001	5.98263	0.01104	45.62	0.13

01SOV-3 WR#L1 Weighted average of J from standards = 4.286e-03 9.931e-06

Laser Power (mW)	Cumulative 39Ar	40Ar/39Ar meas.	+/-	37Ar/39Ar meas.	+/-	36Ar/39Ar meas.	+/-	% Atm. 40Ar	+/-	Ca/K	+/-	Cl/K	+/-	40*/39K	+/-	Age (Ma)	+/- (Ma)
500	0.0482	272.34709	1.22349	10.29764	0.05153	0.91234	0.00817	98.68895	0.78959	19.03317	0.09595	0.00558	0.00057	3.59637	2.16681	27.56	16.48
1000	0.1562	71.19239	0.20409	16.96751	0.09991	0.22514	0.00173	91.52072	0.69288	31.51063	0.18779	0.00191	0.00019	6.1073	0.50106	46.56	3.77
1500	0.3439	25.65381	0.05813	14.1344	0.05721	0.07051	0.00093	76.76766	1.08353	26.19617	0.10711	0.0035	0.0002	6.01317	0.28259	45.85	2.13
2000	0.6189	12.81558	0.03188	8.78168	0.04399	0.02687	0.0005	56.43744	1.15174	16.21374	0.08173	0.00724	0.0001	5.60469	0.14984	42.78	1.13
2500	0.7921	11.68519	0.04823	9.25493	0.04437	0.02415	0.00073	54.67676	1.83583	17.09324	0.08248	0.00715	0.00021	5.31749	0.21748	40.61	1.64
3000	0.8375	14.11602	0.07405	9.72271	0.06796	0.03437	0.00228	66.40558	4.76819	17.96318	0.12644	0.00491	0.00036	4.765	0.67713	36.43	5.13
4000	0.8812	13.90216	0.07264	11.95664	0.07725	0.03074	0.00239	58.37655	5.08538	22.12561	0.14416	0.00563	0.00031	5.82347	0.71251	44.43	5.37
9000	1	14.04256	0.07715	15.83258	0.10106	0.03202	0.00078	58.20953	1.61834	29.3791	0.18966	0.00942	0.00025	5.9224	0.23329	45.17	1.76
Integrated		34.10967	0.04361	11.85158	0.0244	0.09985	0.00051	83.71067	0.43372	21.92956	0.04553	0.00595	0.00008	5.5983	0.14982	42.73	1.13

Appendix B continued

01SOV-4 WR#L1 Weighted average of J from standards = 4.286e-03 9.931e-06

Laser Power (mW)	Cumulative 39Ar	40Ar/39Ar meas.	+/-	37Ar/39Ar meas.	+/-	36Ar/39Ar meas.	+/-	% Atm. 40Ar	+/-	Ca/K	+/-	Cl/K	+/-	40*/39K	+/-	Age (Ma)	+/- (Ma)
500	0.1803	10.39321	0.01959	0.23352	0.0007	0.0135	0.00018	38.30723	0.51551	0.42855	0.00128	0.00061	0.00003	6.3946	0.05569	48.72	0.42
1000	0.5201	6.77734	0.01336	0.39881	0.00188	0.00291	0.00004	12.23807	0.17246	0.73198	0.00346	0.00031	0.00002	5.92353	0.0171	45.18	0.13
1500	0.7076	6.61143	0.01805	0.2879	0.00157	0.00257	0.00008	11.19967	0.36935	0.52836	0.00288	0.00028	0.00003	5.84579	0.02961	44.59	0.22
2000	0.7813	6.57627	0.01638	0.22884	0.0015	0.00266	0.00017	11.70044	0.78825	0.41997	0.00275	0.00038	0.00003	5.78153	0.05384	44.11	0.41
2500	0.8798	6.87818	0.01836	0.11819	0.0006	0.00349	0.00014	14.91533	0.62149	0.21688	0.0011	0.00049	0.00003	5.82749	0.04576	44.46	0.34
3000	0.9321	7.20491	0.02453	0.0776	0.00058	0.00439	0.0002	18.00938	0.82367	0.14239	0.00106	0.00055	0.00004	5.88333	0.06334	44.88	0.48
4000	0.9822	7.35785	0.0186	0.10029	0.00099	0.00492	0.00022	19.71391	0.87678	0.18403	0.00181	0.00064	0.00006	5.8839	0.06664	44.88	0.5
9000	1	7.51736	0.0299	0.07874	0.00162	0.00555	0.00079	21.79719	3.12808	0.14448	0.00298	0.00069	0.00014	5.85589	0.23555	44.67	1.77
Integrated		7.45788	0.00734	0.27061	0.00072	0.00502	0.00005	19.66368	0.18954	0.49662	0.00132	0.00042	0.00001	5.96867	0.01554	45.52	0.16

01SOV-5 WR#L1 Weighted average of J from standards = 4.286e-03 9.931e-06

Laser Power (mW)	Cumulative 39Ar	40Ar/39Ar meas.	+/-	37Ar/39Ar meas.	+/-	36Ar/39Ar meas.	+/-	% Atm. 40Ar	+/-	Ca/K	+/-	Cl/K	+/-	40*/39K	+/-	Age (Ma)	+/- (Ma)
500	0.0381	42.39858	0.19809	3.12938	0.01647	0.12813	0.00112	88.75174	0.69512	5.75471	0.03036	0.00884	0.00019	4.77633	0.29793	36.52	2.25
1000	0.1338	11.66321	0.02994	3.63827	0.01613	0.02211	0.00046	53.58814	1.16711	6.69293	0.02974	0.00243	0.00005	5.41328	0.13736	41.33	1.04
1500	0.3278	7.61577	0.02203	2.74105	0.01267	0.00634	0.00011	21.71638	0.44329	5.03921	0.02334	0.00101	0.00004	5.95021	0.03894	45.38	0.29
2000	0.5186	6.75738	0.0165	1.92536	0.00819	0.00372	0.0001	13.97313	0.45436	3.53758	0.01507	0.00279	0.00003	5.79553	0.03428	44.21	0.26
2500	0.7753	7.07068	0.01607	2.25621	0.00997	0.00483	0.0001	17.63873	0.43616	4.14645	0.01835	0.00354	0.00003	5.80834	0.03403	44.31	0.26
3000	0.9161	7.65088	0.02452	2.59293	0.01195	0.00699	0.00017	24.29171	0.66583	4.7664	0.02201	0.0045	0.00007	5.78049	0.05485	44.1	0.41
4000	0.9479	8.23077	0.03378	2.40531	0.01375	0.00855	0.0005	28.39845	1.78848	4.42093	0.02532	0.0039	0.00012	5.88212	0.1494	44.87	1.13
9000	1	8.54855	0.02265	4.88588	0.02155	0.01104	0.0004	33.56703	1.39868	8.99595	0.03981	0.0039	0.00008	5.67899	0.12118	43.34	0.91
Integrated		9.09825	0.00966	2.64206	0.00472	0.01201	0.00008	36.73488	0.25671	4.85688	0.00869	0.00317	0.00002	5.74799	0.02449	43.86	0.21

Appendix B continued

02SOV WR#L1 Weighted average of J from standards = 4.286e-03 9.931e-06

Laser Power (mW)	Cumulative 39Ar	40Ar/39Ar meas.	+/-	37Ar/39Ar meas.	+/-	36Ar/39Ar meas.	+/-	% Atm. 40Ar	+/-	Ca/K	+/-	Cl/K	+/-	40*/39K	+/-	Age (Ma)	+/- (Ma)
500	0.0458	65.94839	0.22736	6.45127	0.02956	0.20577	0.00229	91.43687	1.00323	11.89136	0.05473	0.00423	0.0002	5.67055	0.66637	43.27	5.02
1000	0.2153	16.82871	0.0513	7.0599	0.0346	0.03827	0.00049	63.85484	0.86069	13.01886	0.06412	0.00179	0.00009	6.10251	0.14799	46.53	1.11
1500	0.4563	8.62299	0.02349	3.06689	0.01453	0.00972	0.00029	30.48625	0.99657	5.63954	0.02678	0.00631	0.00005	5.98653	0.08821	45.65	0.66
2000	0.7145	8.88443	0.02005	3.5292	0.01625	0.01017	0.0003	30.65402	0.99146	6.49177	0.02997	0.00567	0.00008	6.15579	0.08928	46.93	0.67
2500	0.8401	8.70028	0.03803	3.43382	0.0173	0.00972	0.00056	29.84513	1.89863	6.31591	0.0319	0.00544	0.00012	6.09767	0.16769	46.49	1.26
3000	0.8955	9.02996	0.03854	3.27112	0.02322	0.01072	0.00098	32.19571	3.2253	6.01596	0.04281	0.00417	0.00019	6.11674	0.29257	46.63	2.2
4000	0.9748	9.45323	0.04927	5.23996	0.02832	0.01358	0.00078	37.98473	2.45058	9.65032	0.05235	0.00506	0.00016	5.8658	0.23442	44.74	1.77
9000	1	11.64166	0.05532	3.56838	0.02011	0.01985	0.0026	47.96856	6.60886	6.56402	0.03708	0.0028	0.00046	6.05717	0.77004	46.19	5.8
Integrated		12.88963	0.01629	4.26216	0.00869	0.0243	0.00021	53.10585	0.48213	7.84408	0.01604	0.00487	0.00004	6.0488	0.06304	46.12	0.49

14SOV WR#L1 Weighted average of J from standards = 4.286e-03 9.931e-06

Laser Power (mW)	Cumulative 39Ar	40Ar/39Ar meas.	+/-	37Ar/39Ar meas.	+/-	36Ar/39Ar meas.	+/-	% Atm. 40Ar	+/-	Ca/K	+/-	Cl/K	+/-	40*/39K	+/-	Age (Ma)	+/- (Ma)
500	0.0493	113.64291	1.10436	10.28376	0.10598	0.36549	0.00842	94.31612	2.00397	19.00732	0.19731	0.01195	0.00139	6.50489	2.29562	49.55	17.25
1000	0.1803	33.88527	0.23166	16.35545	0.12265	0.09675	0.00378	80.46308	3.25947	30.36069	0.23034	0.00378	0.00053	6.69169	1.11858	50.96	8.4
1500	0.3684	31.82871	0.15051	19.18104	0.11055	0.08851	0.00237	77.2792	2.18301	35.67786	0.20846	0.00368	0.00028	7.3243	0.70586	55.7	5.29
2000	0.5125	20.80541	0.16969	21.12181	0.20814	0.05156	0.00244	64.95369	3.43469	39.34247	0.39355	0.00421	0.00046	7.39153	0.72801	56.2	5.45
2500	0.7406	17.2347	0.09648	17.72084	0.12912	0.03988	0.00172	60.00226	2.93708	32.92737	0.24296	0.00635	0.0003	6.96898	0.51407	53.04	3.86
3000	0.8301	15.36329	0.12599	23.07557	0.19576	0.03811	0.00338	61.041	6.50421	43.04192	0.3712	0.00776	0.0007	6.07297	1.01597	46.3	7.65
4000	0.9771	15.21159	0.09877	35.57221	0.23363	0.04043	0.00317	59.36952	6.16474	66.95205	0.45106	0.00973	0.00053	6.32774	0.96197	48.22	7.23
9000	1	13.52758	0.27137	21.33051	0.39781	0.02087	0.0117	32.66269	25.5933	39.73715	0.75243	0.00918	0.00235	9.22843	3.51397	69.9	26.11
Integrated		26.83001	0.06712	21.15751	0.06296	0.07355	0.00112	74.58467	1.22358	39.40998	0.11905	0.00617	0.00019	6.91482	0.33379	52.63	2.51

Appendix C. HeFTy Inverse Thermal Models and AFT Track Length Distributions for Samples from the Southern Talkeetna Mountains.

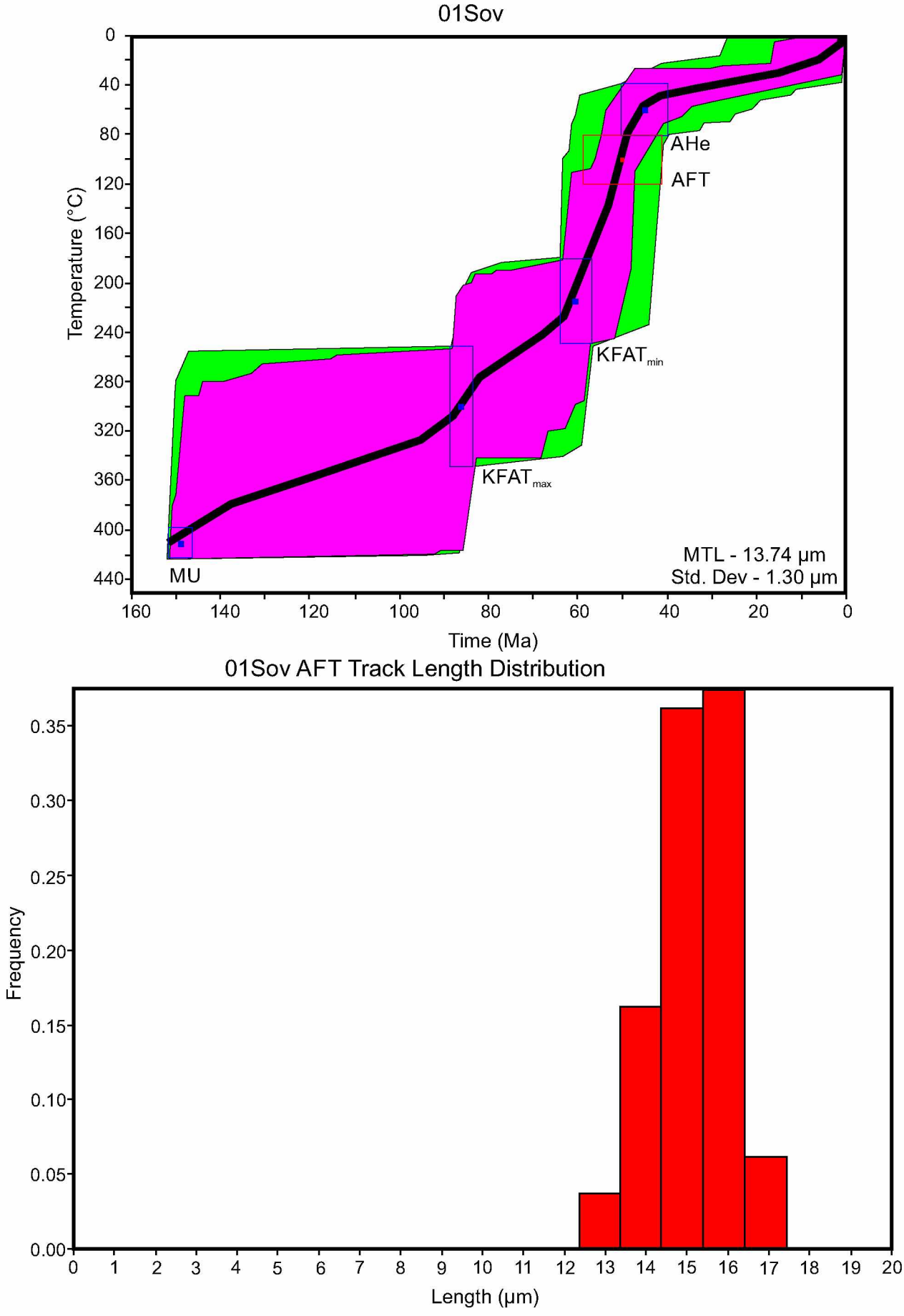

C1. HeFTy inverse thermal model and track length distribution for sample 01Sov.

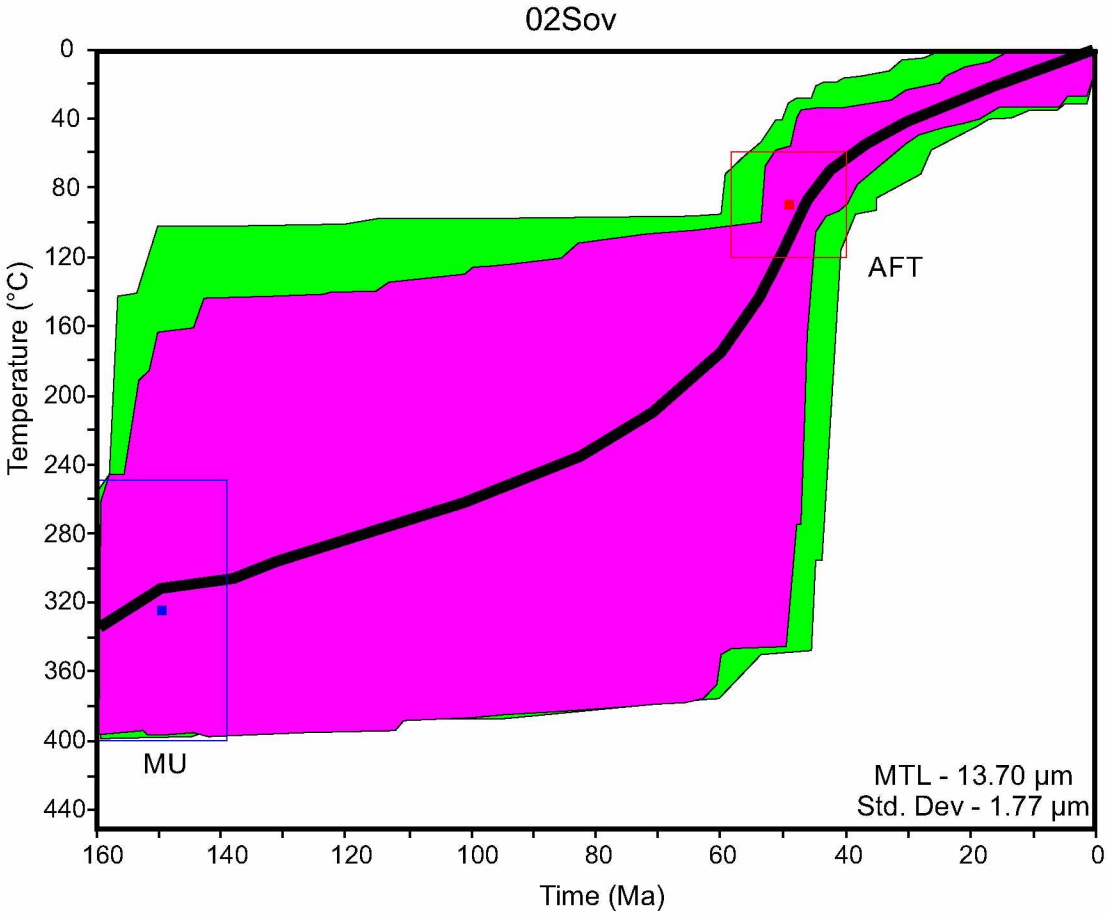

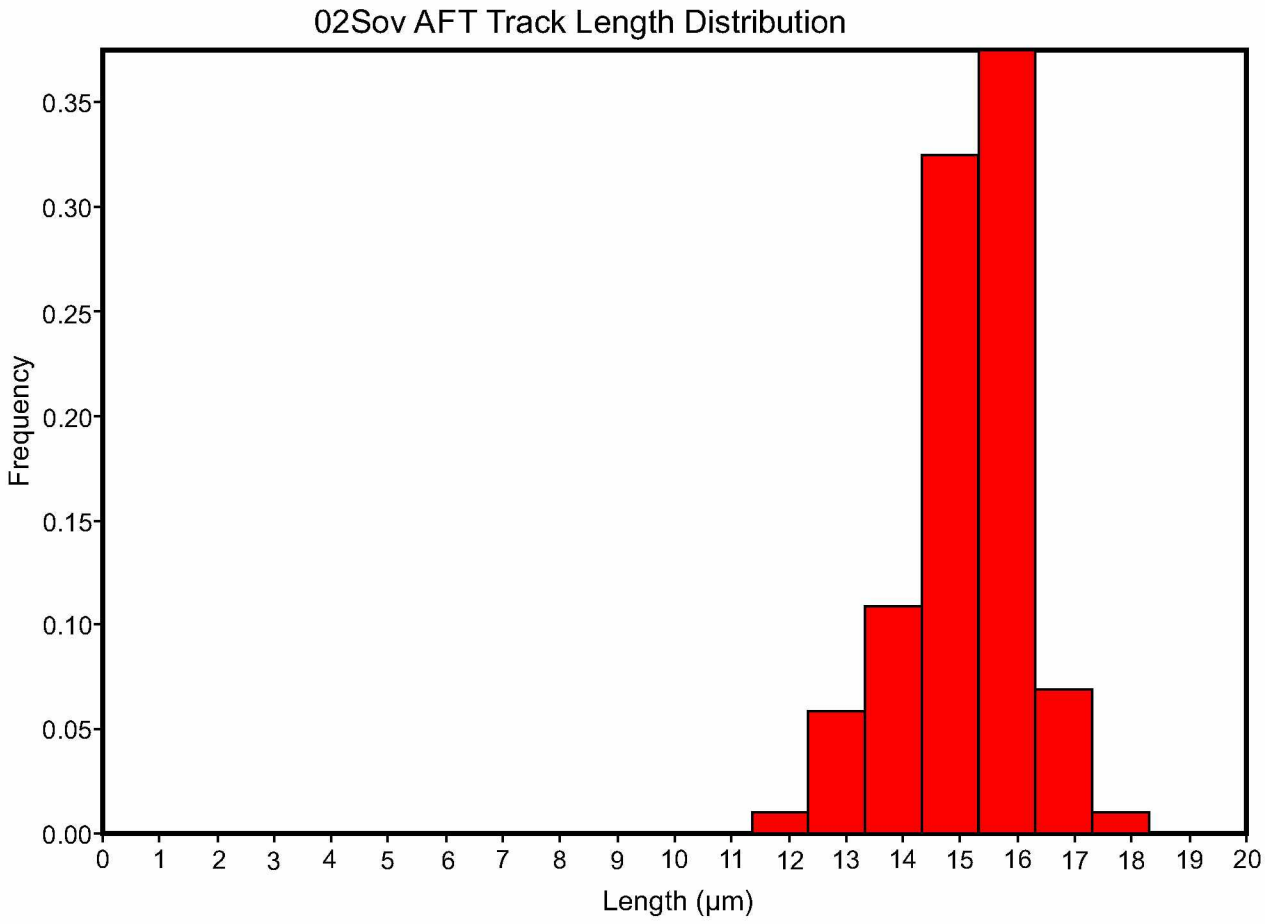

C2. HeFTy inverse thermal model and track length distribution for sample 02Sov.

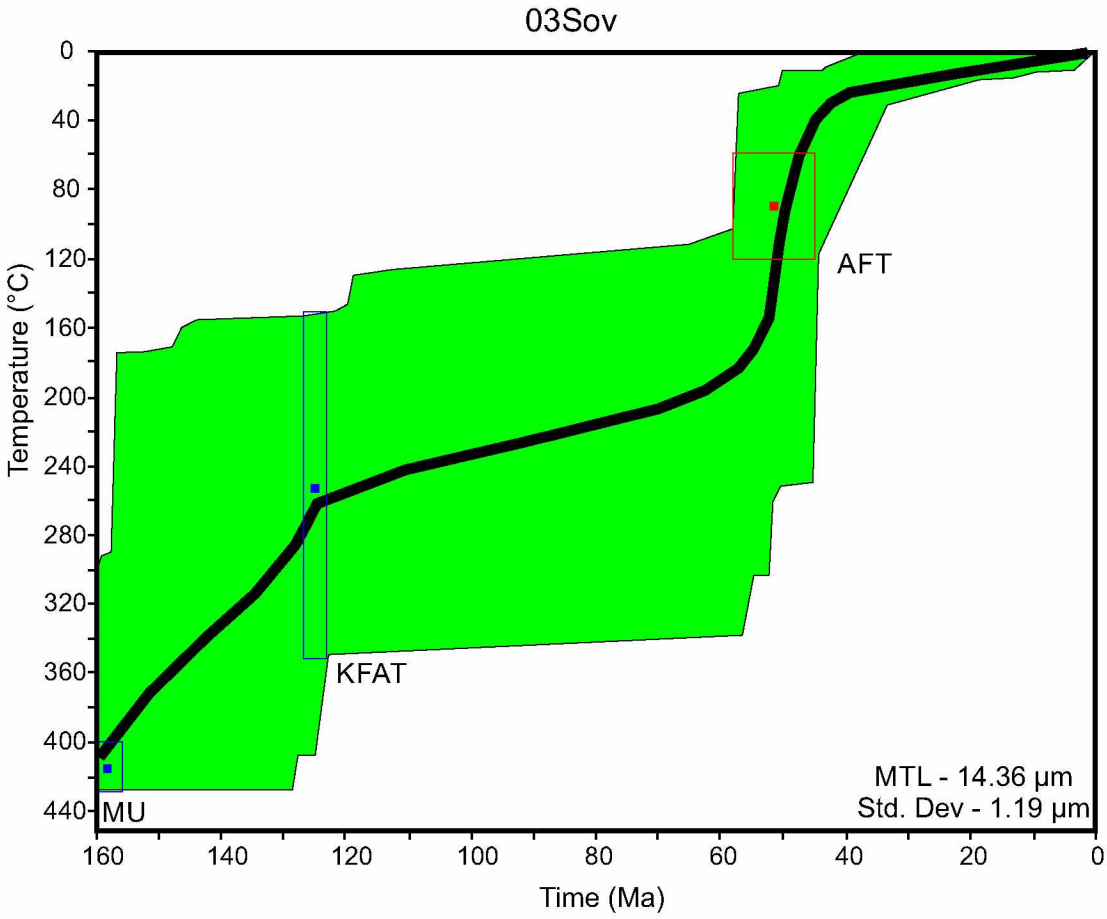

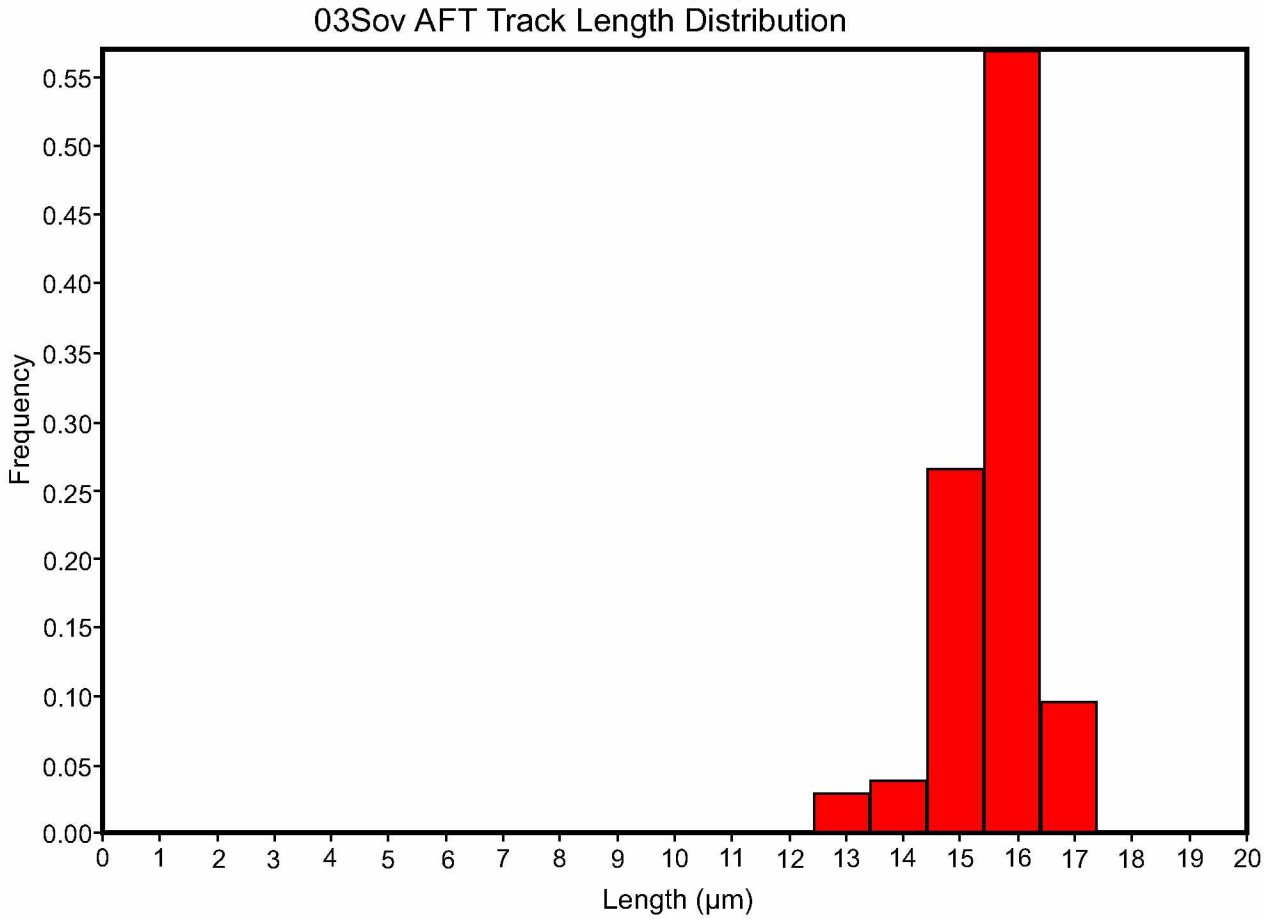

C3. HeFTy inverse thermal model and track length distribution for sample 03Sov.

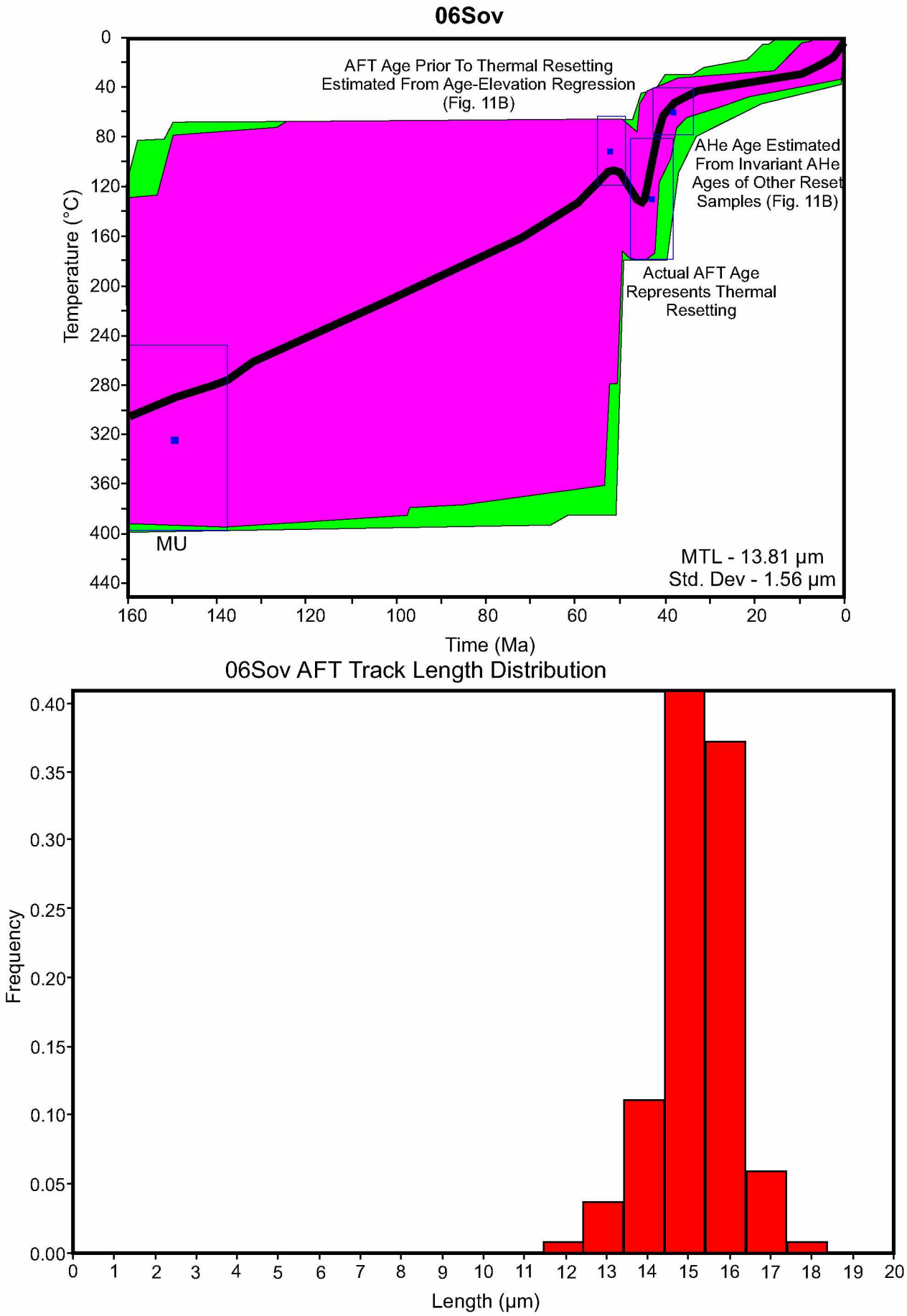

C4. HeFTy inverse thermal model and track length distribution for sample 06Sov.

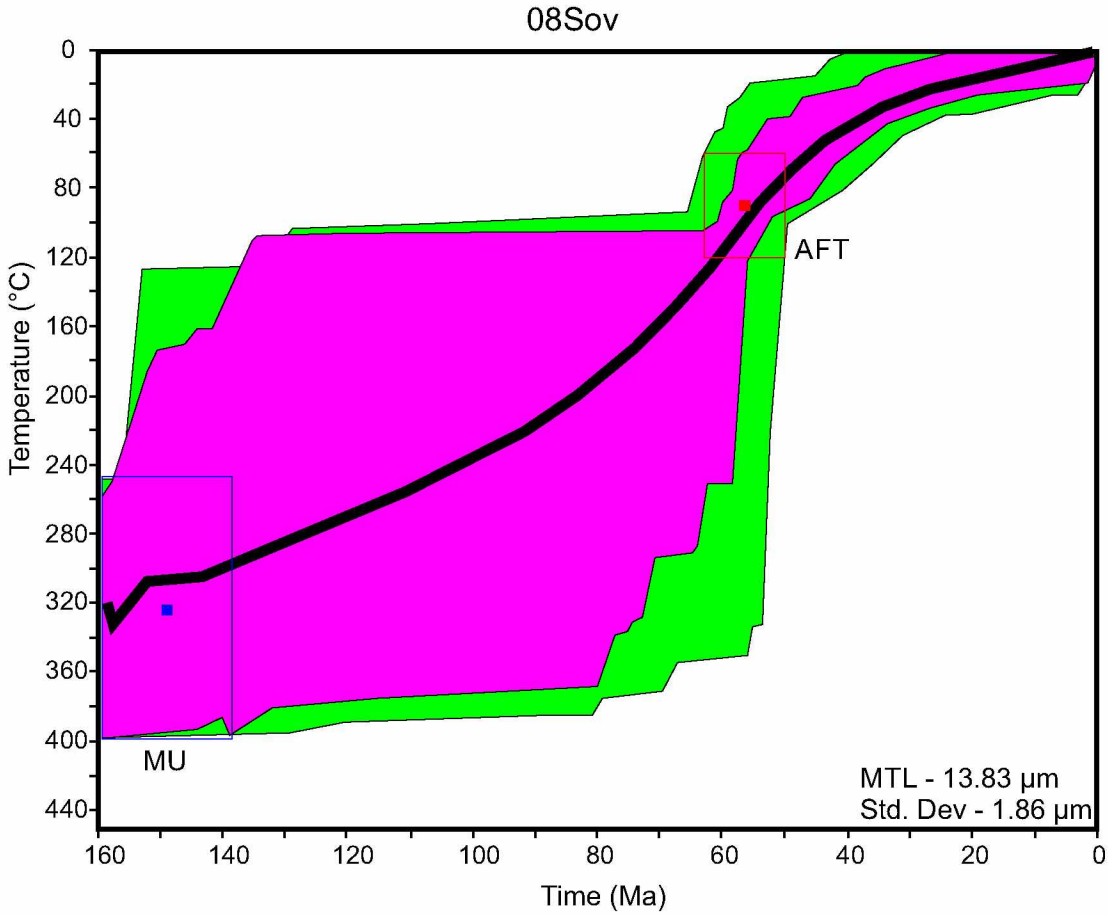

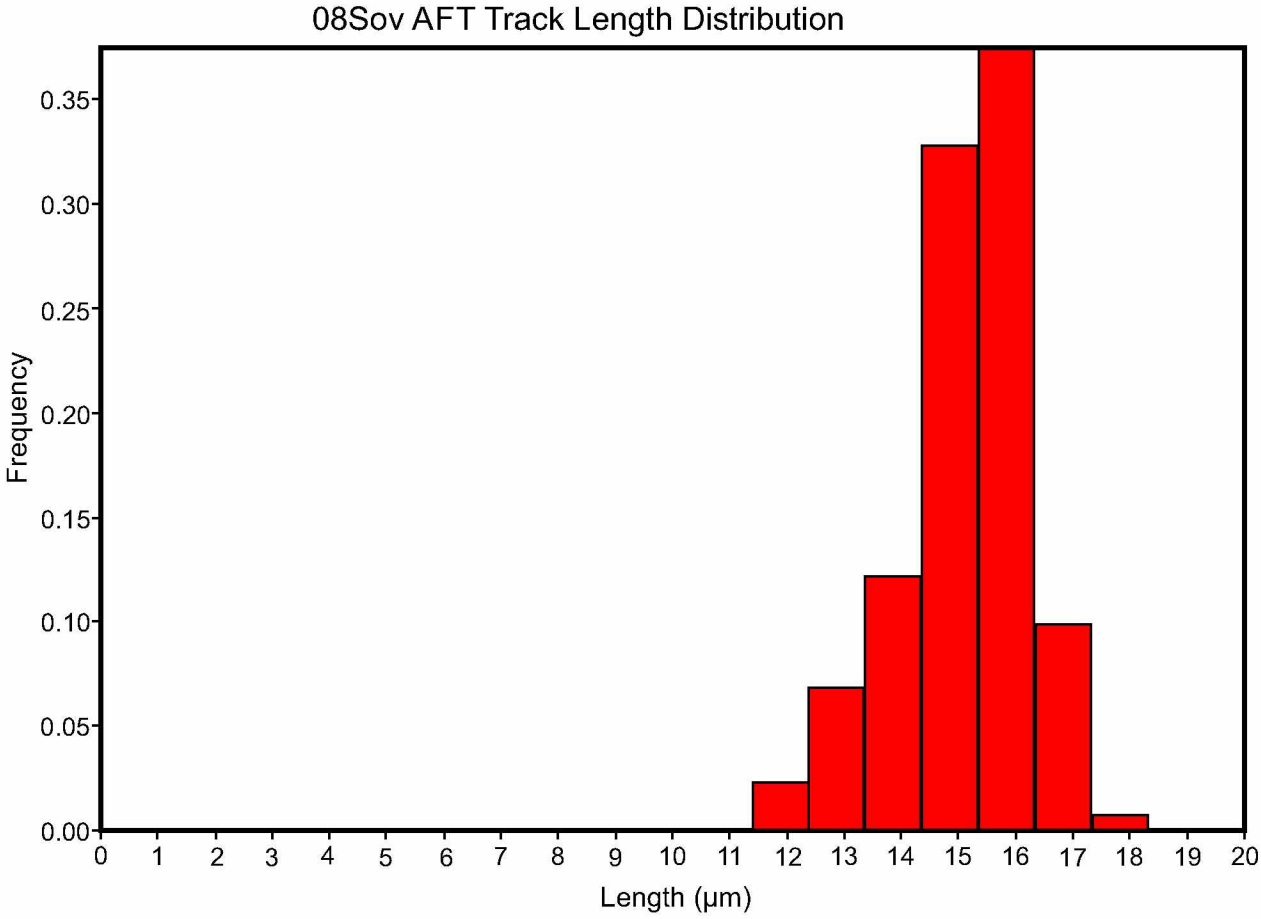

C5. HeFTy inverse thermal model and track length distribution for sample 08Sov.

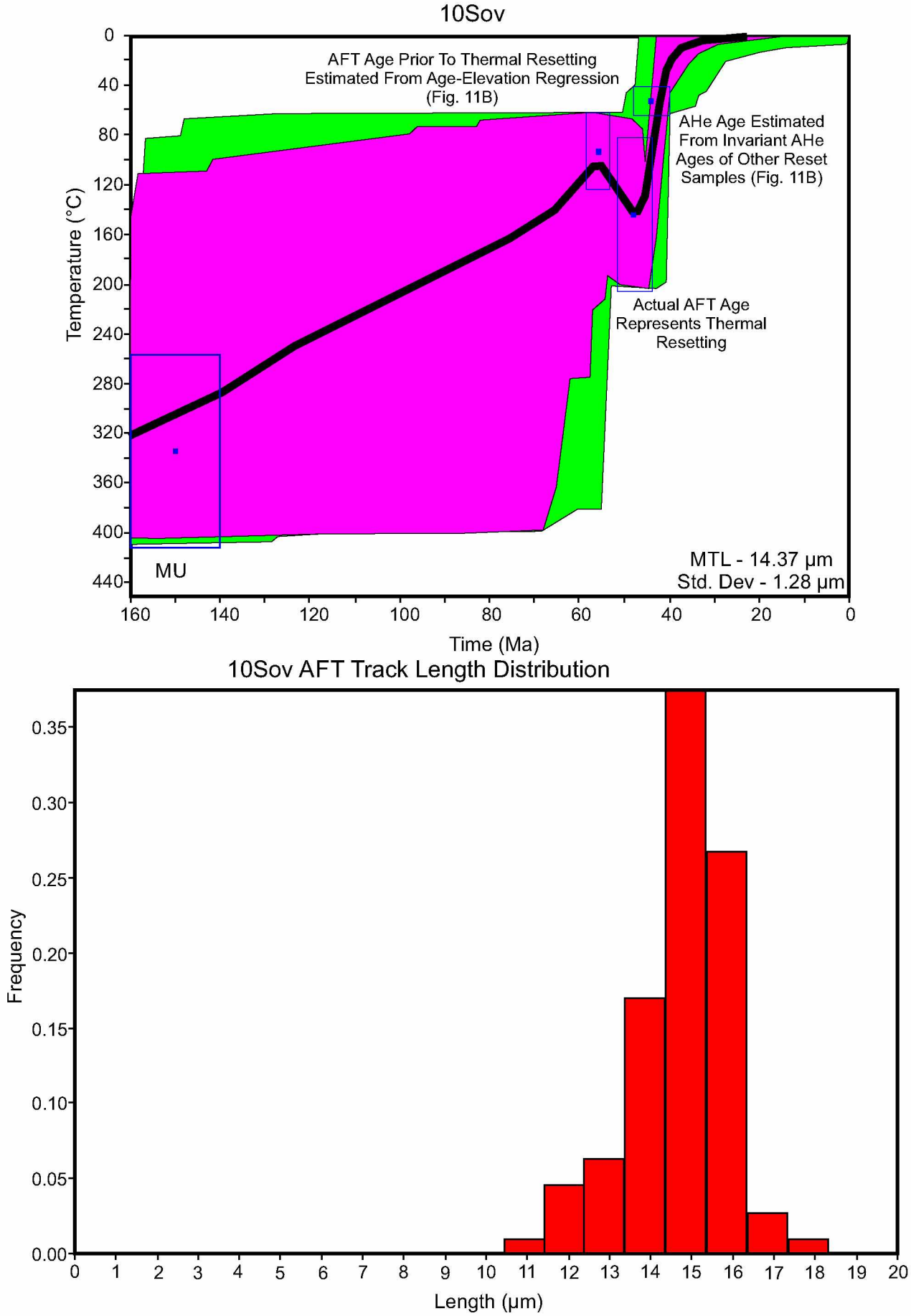

C6. HeFTy inverse thermal model and track length distribution for sample 10Sov.

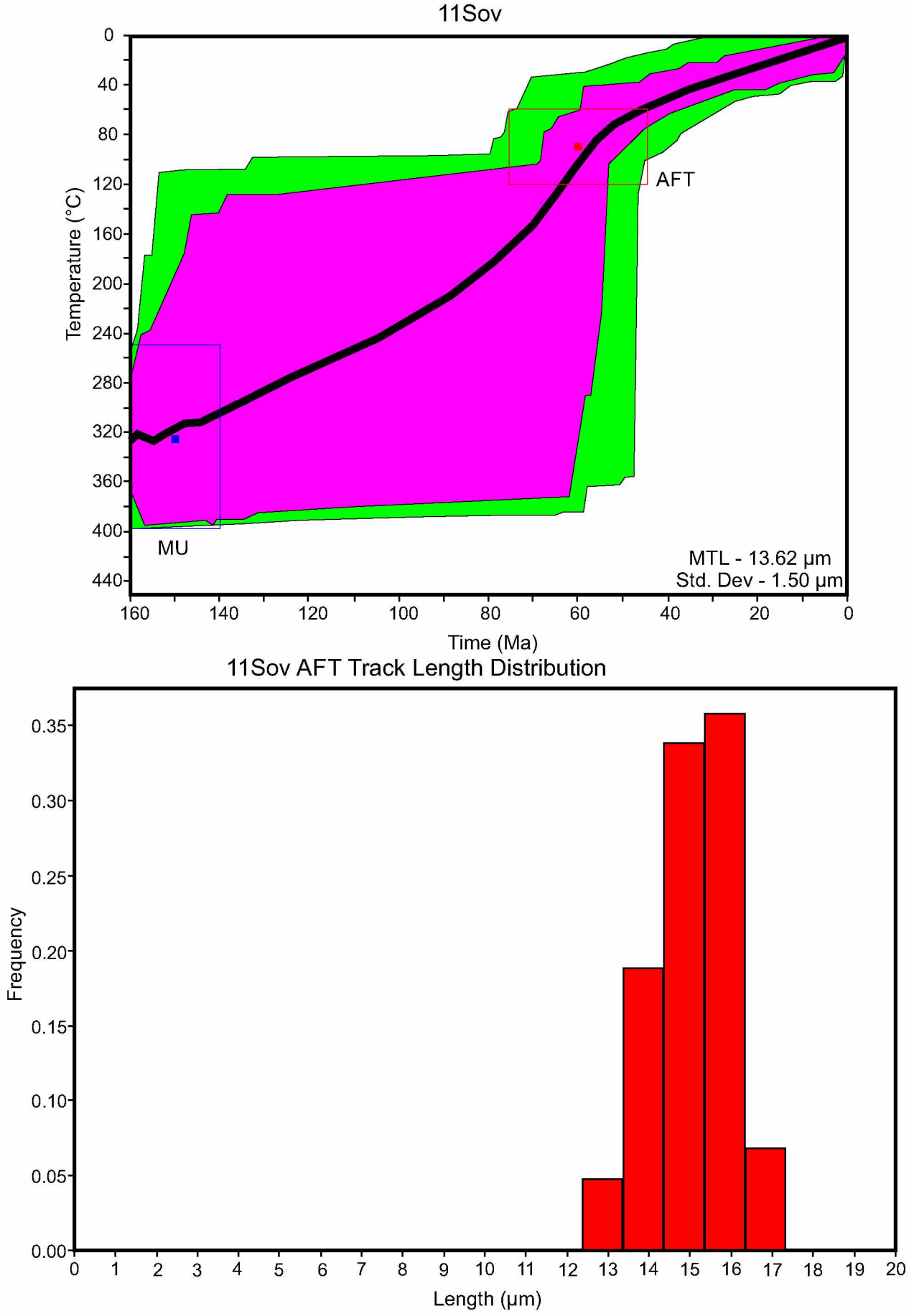

C7. HeFTy inverse thermal model and track length distribution for sample 11Sov.

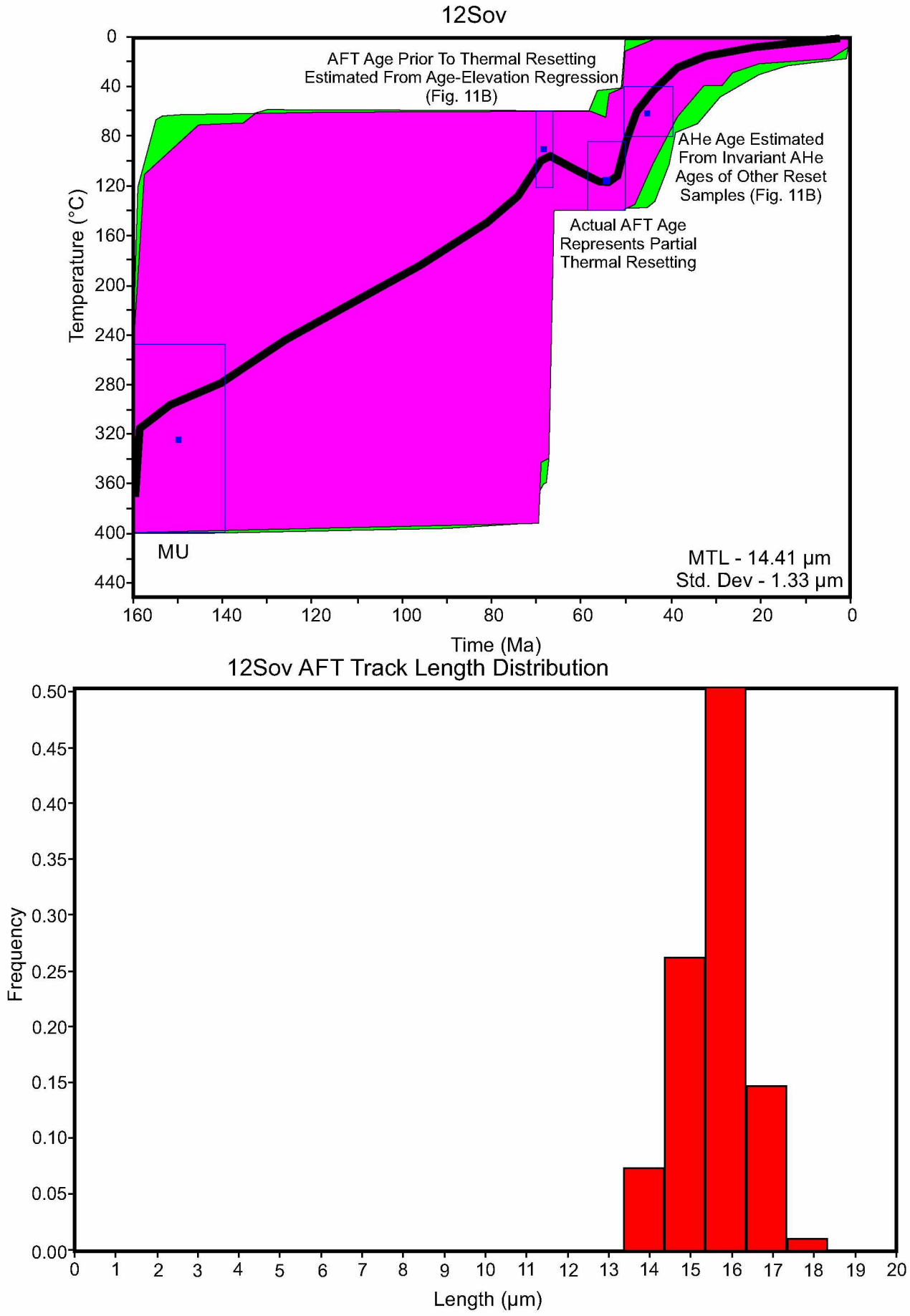

C8. HeFTy inverse thermal model and track length distribution for sample 12Sov.

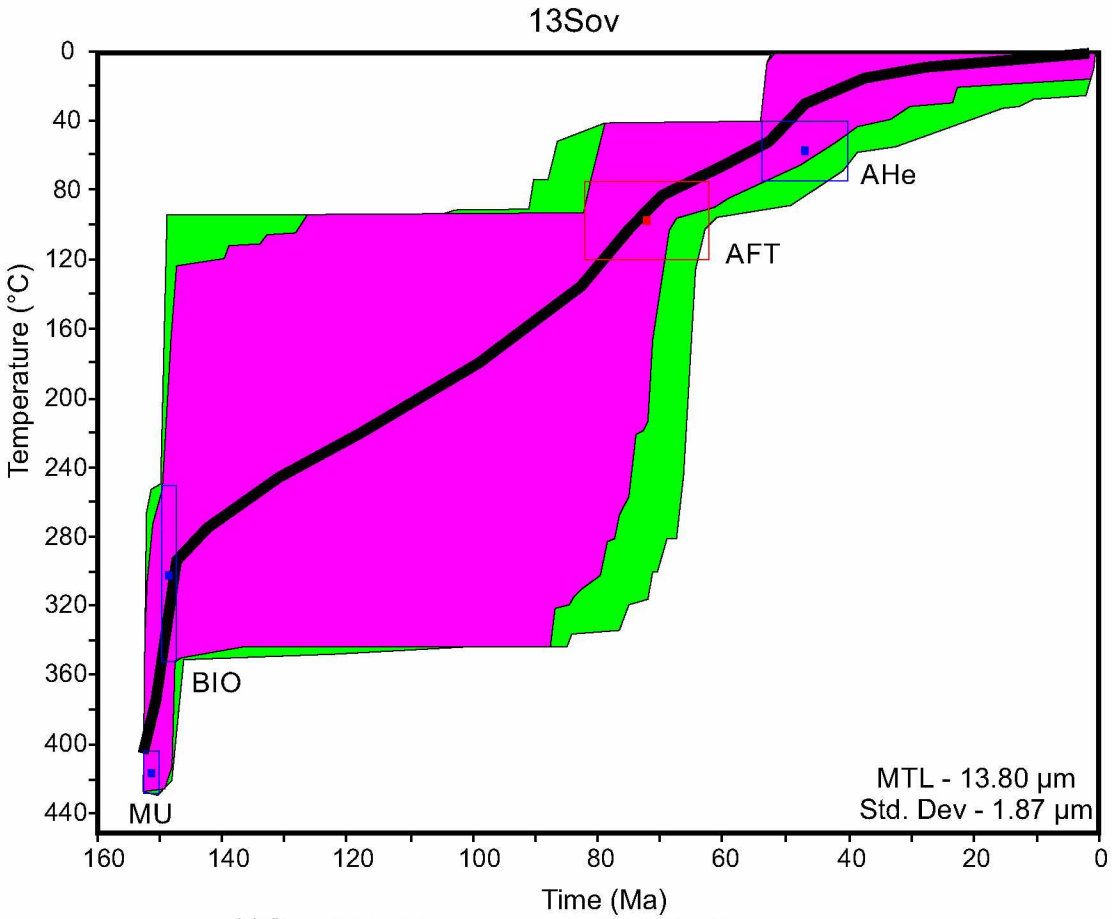

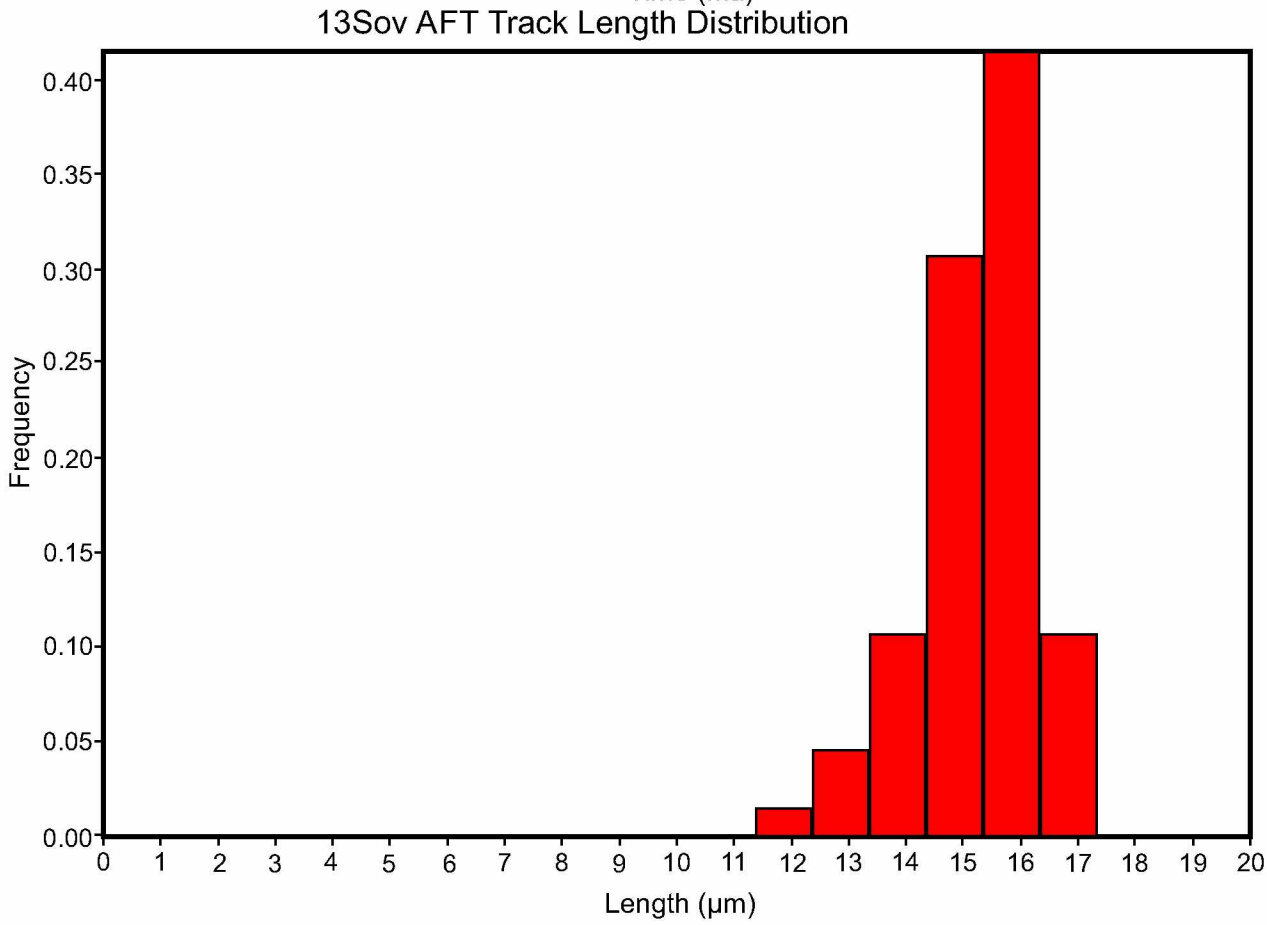

C9. HeFTy inverse thermal model and track length distribution for sample 13Sov.

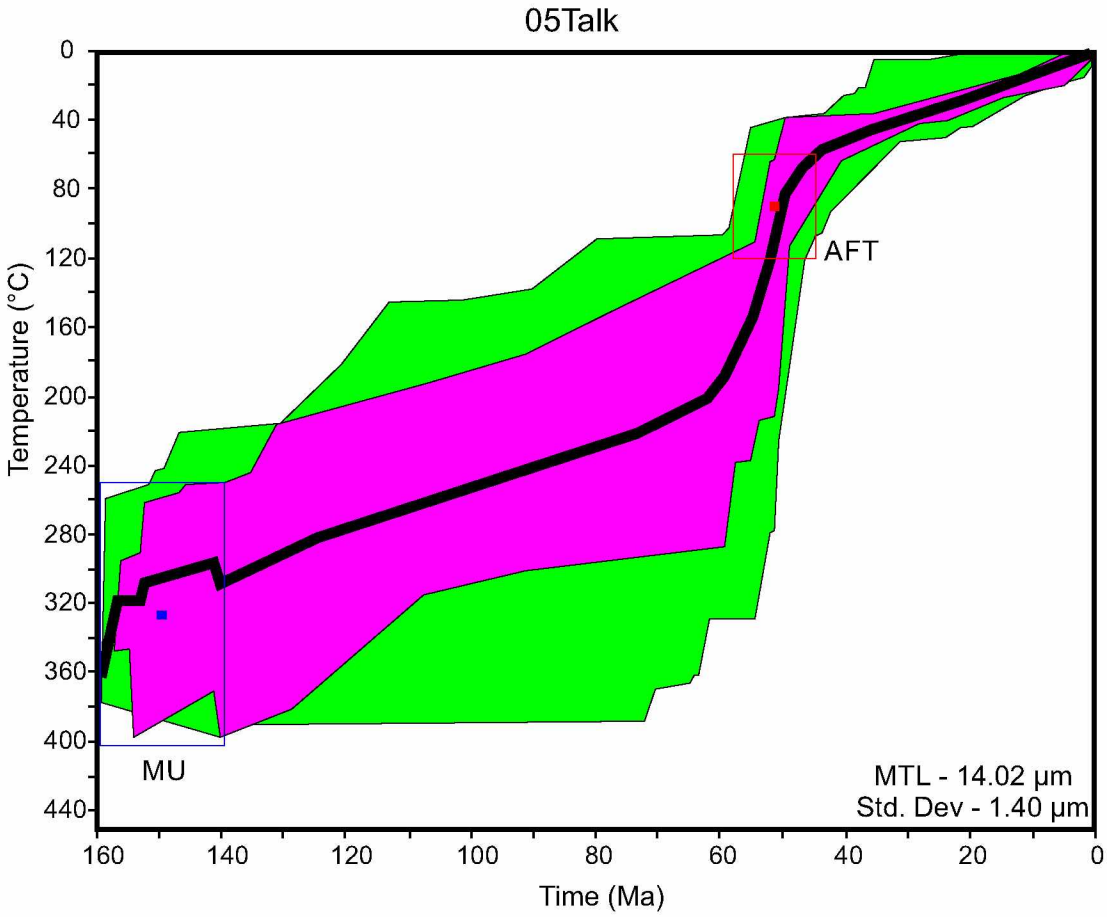

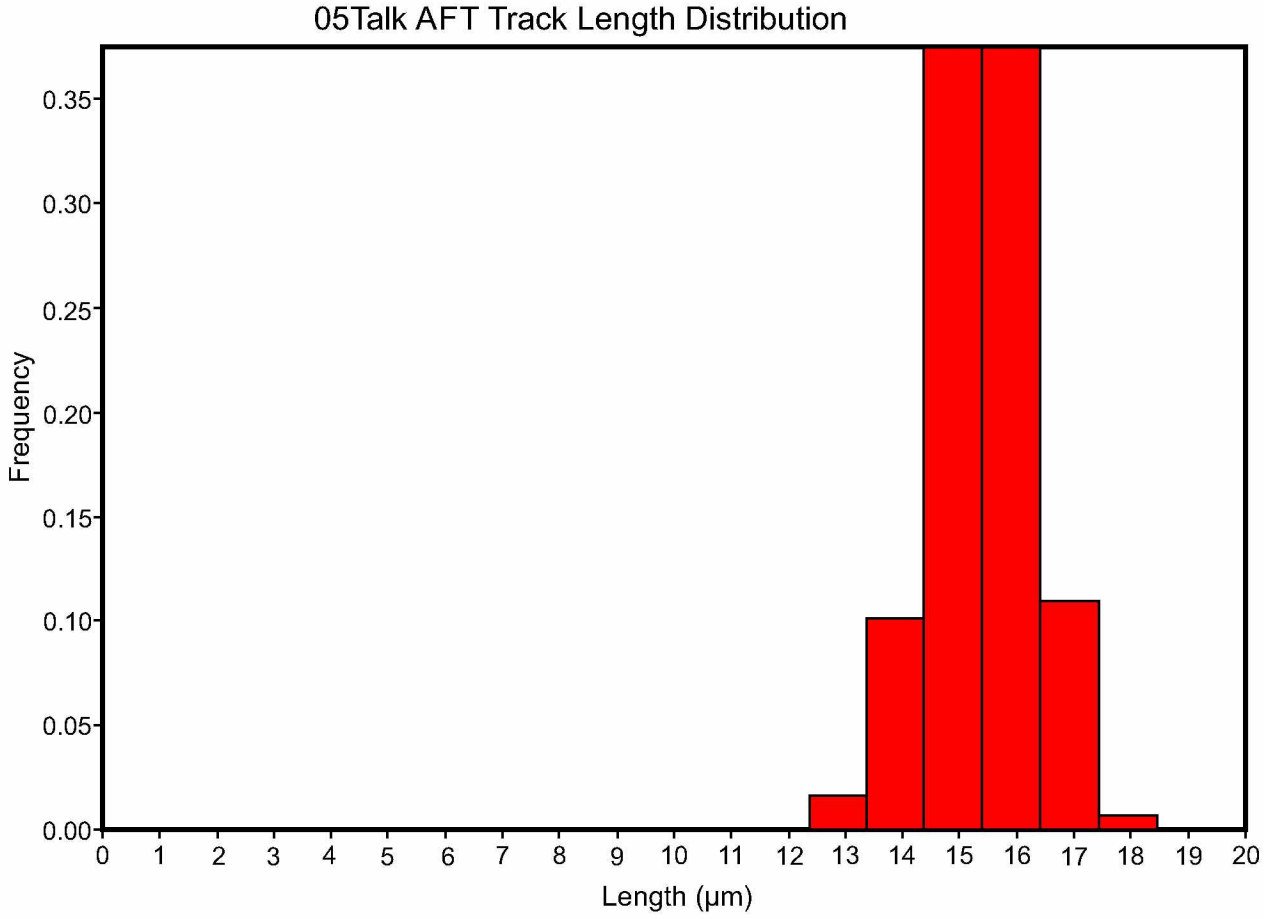

C10. HeFTy inverse thermal model and track length distribution for sample 05Talk.

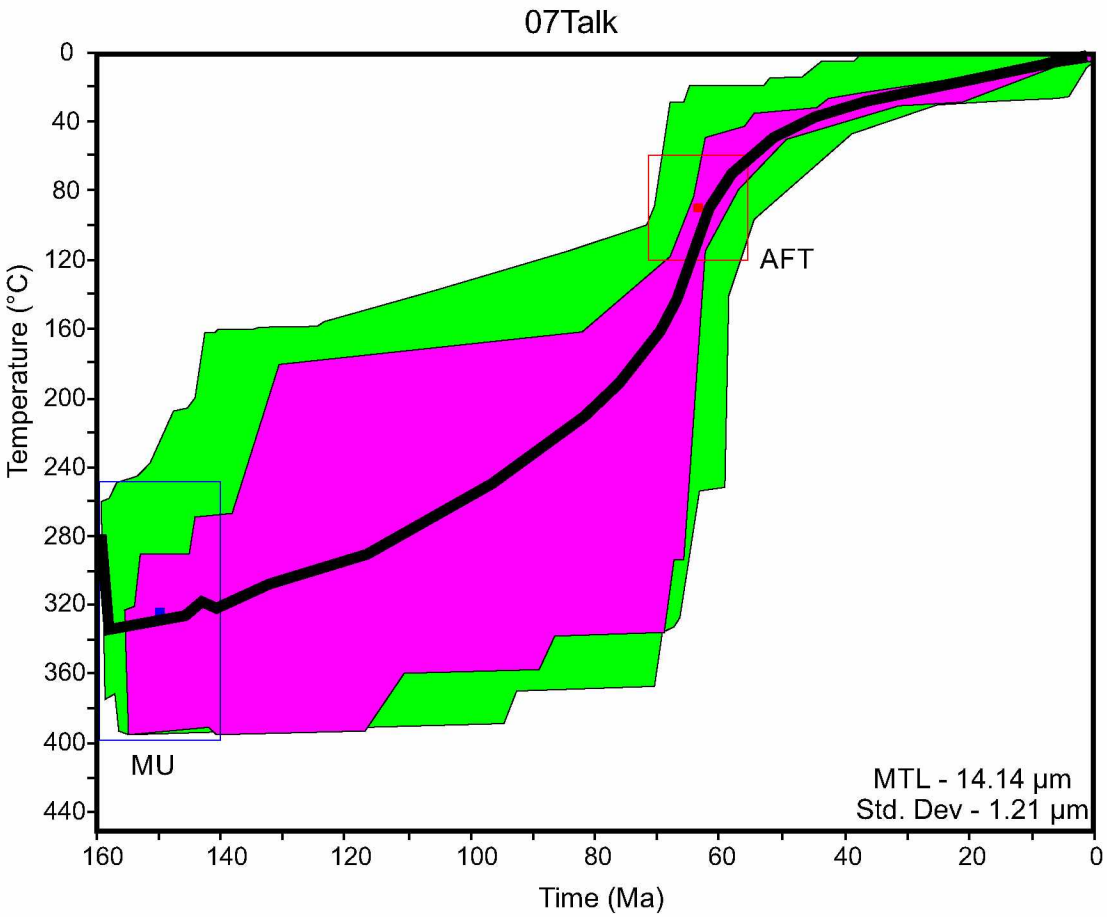

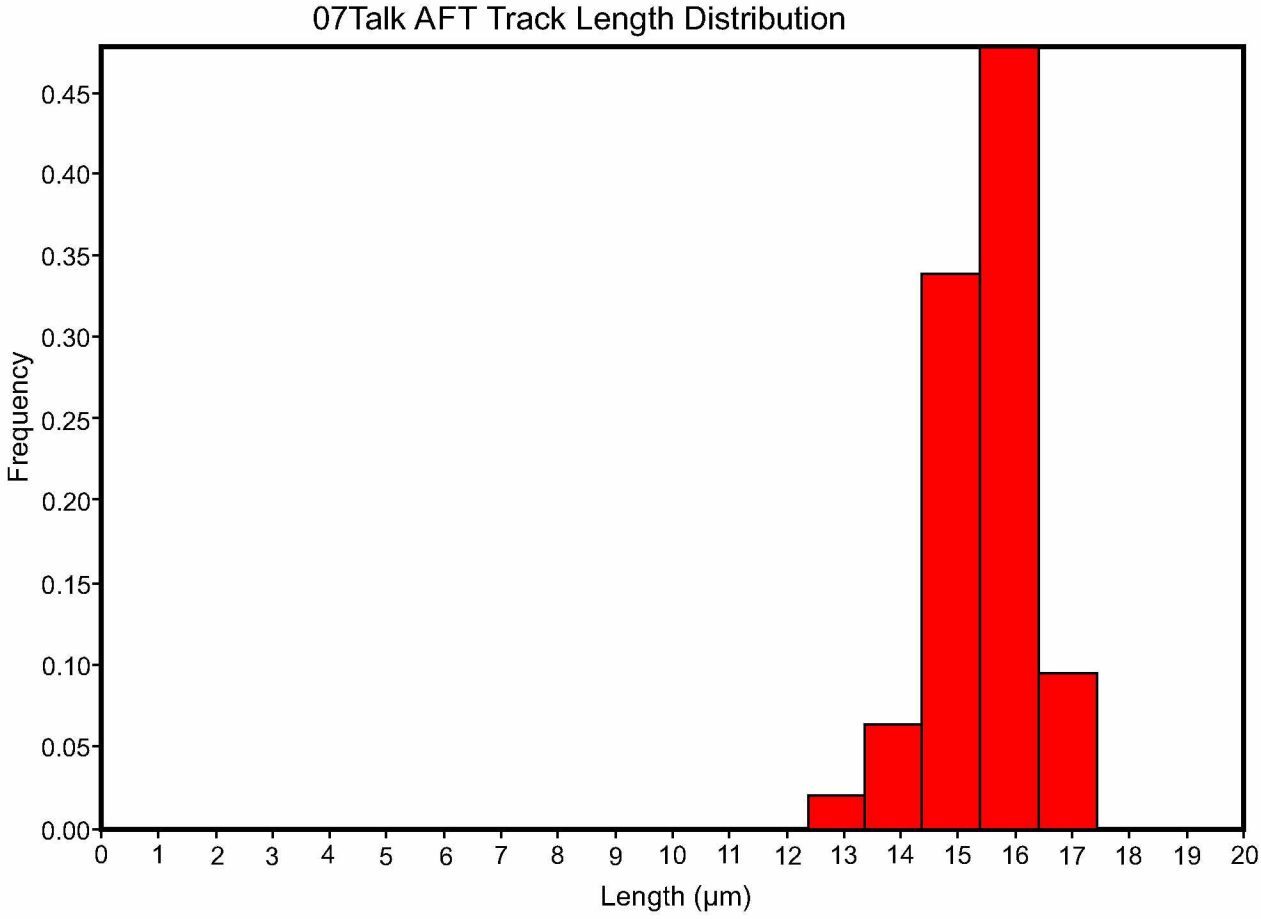

C11. HeFTy inverse thermal model and track length distribution for sample 07Talk.

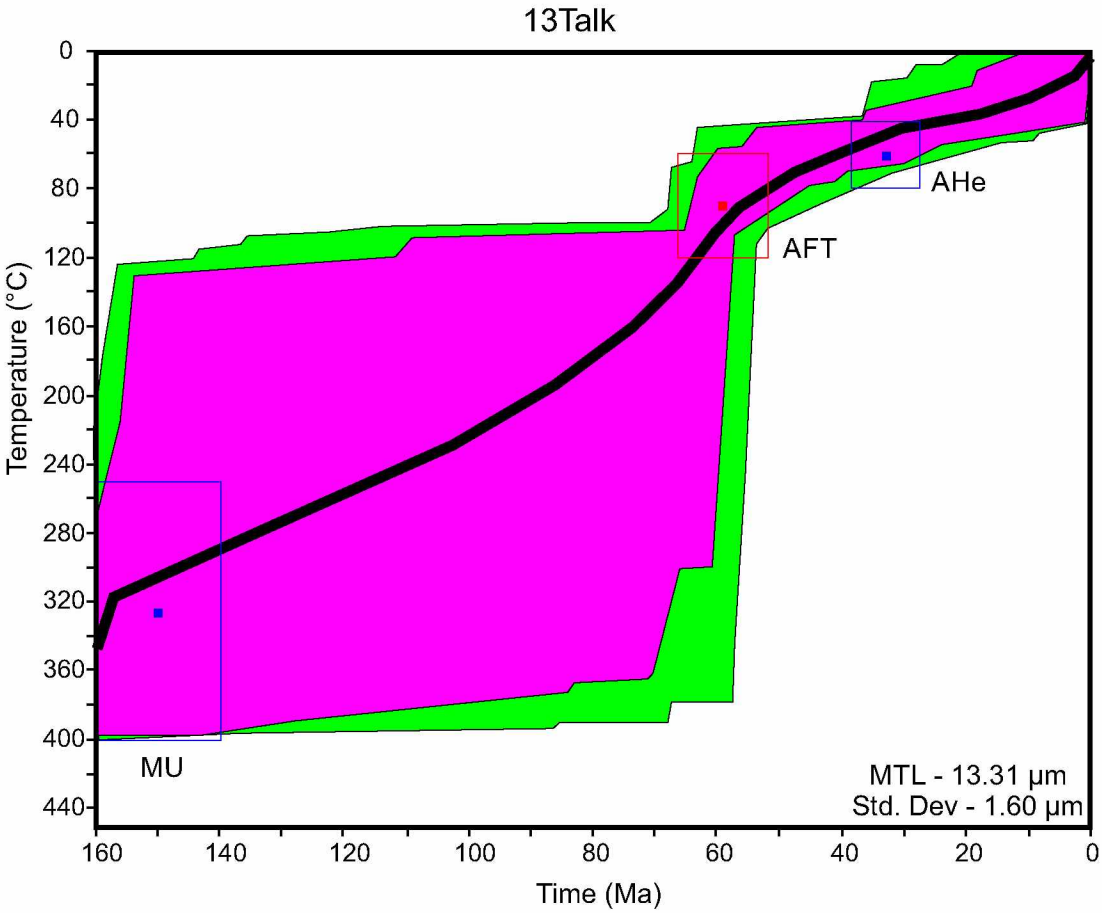

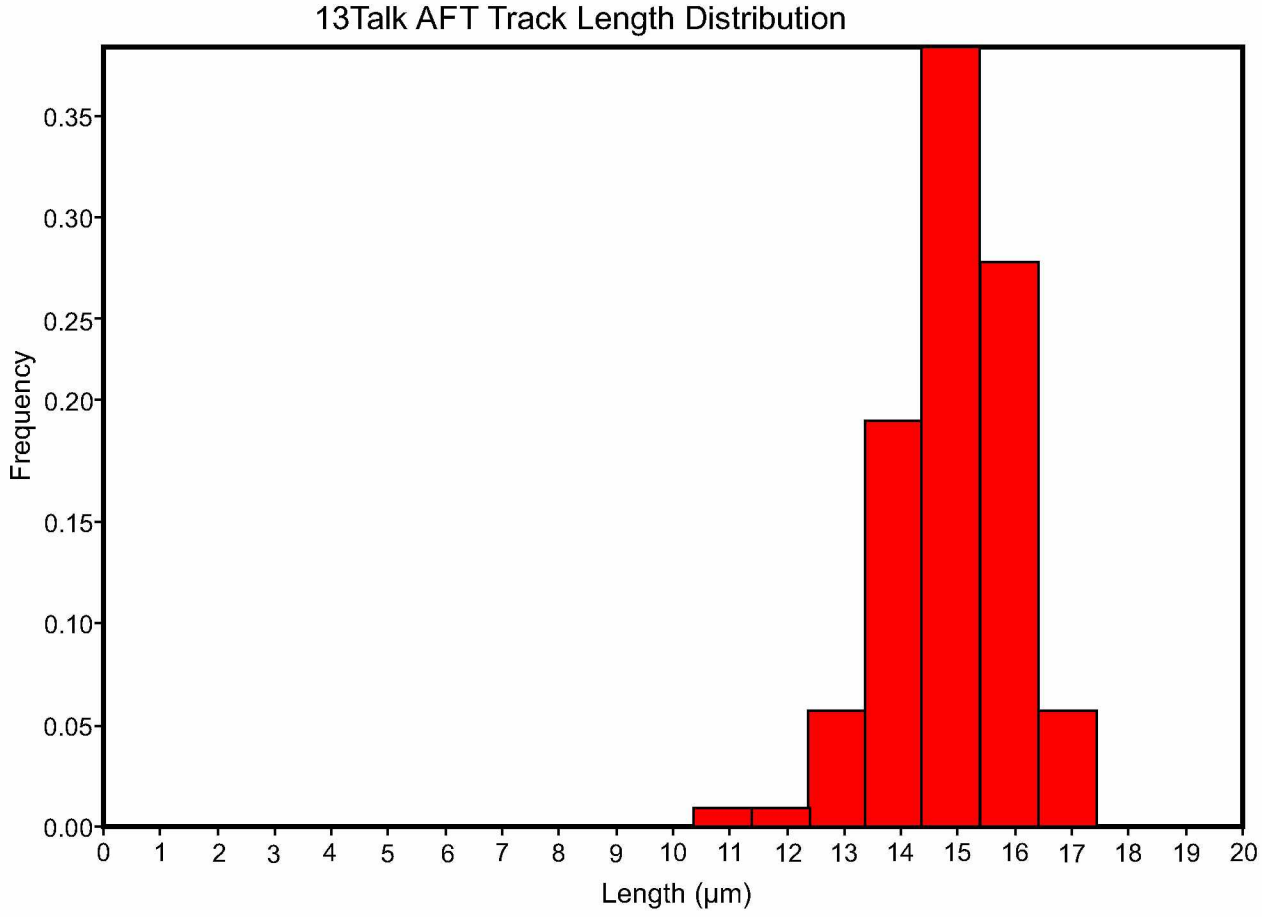

C12. HeFTy inverse thermal model and track length distribution for sample 13Talk.

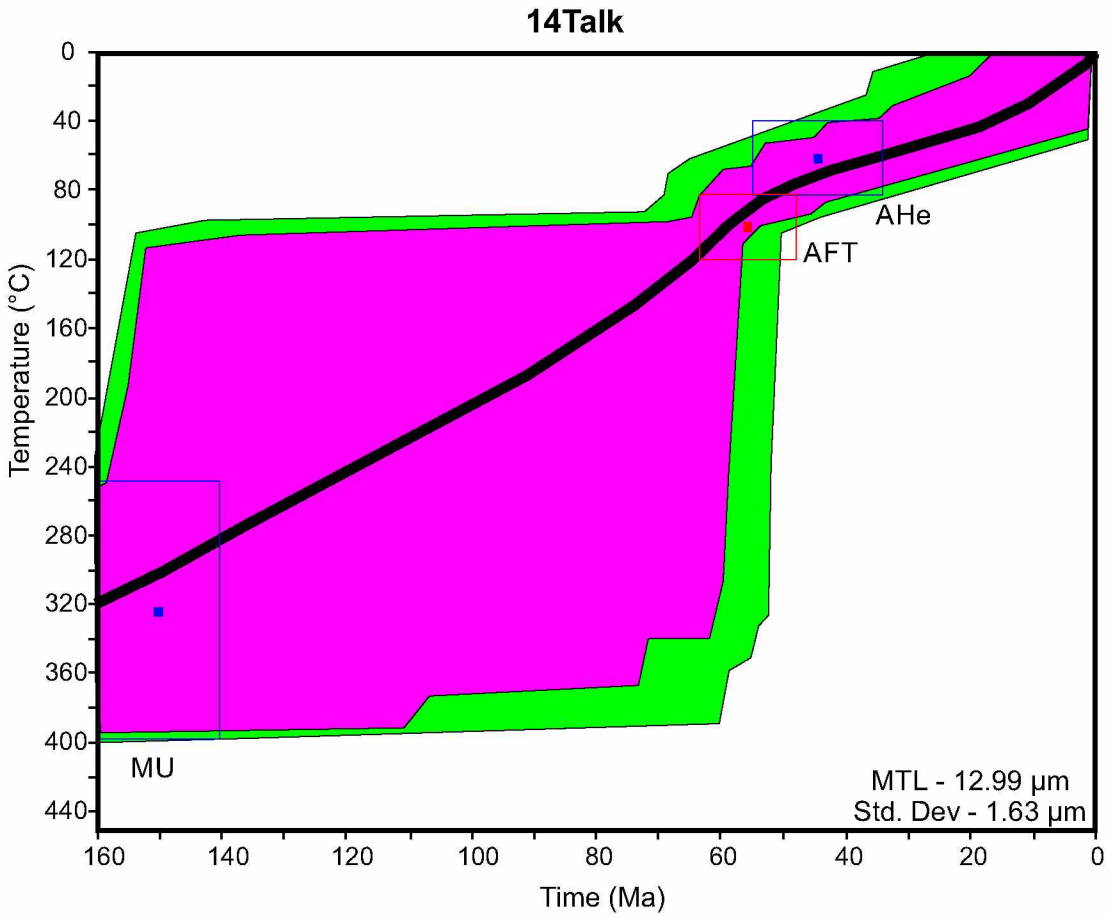

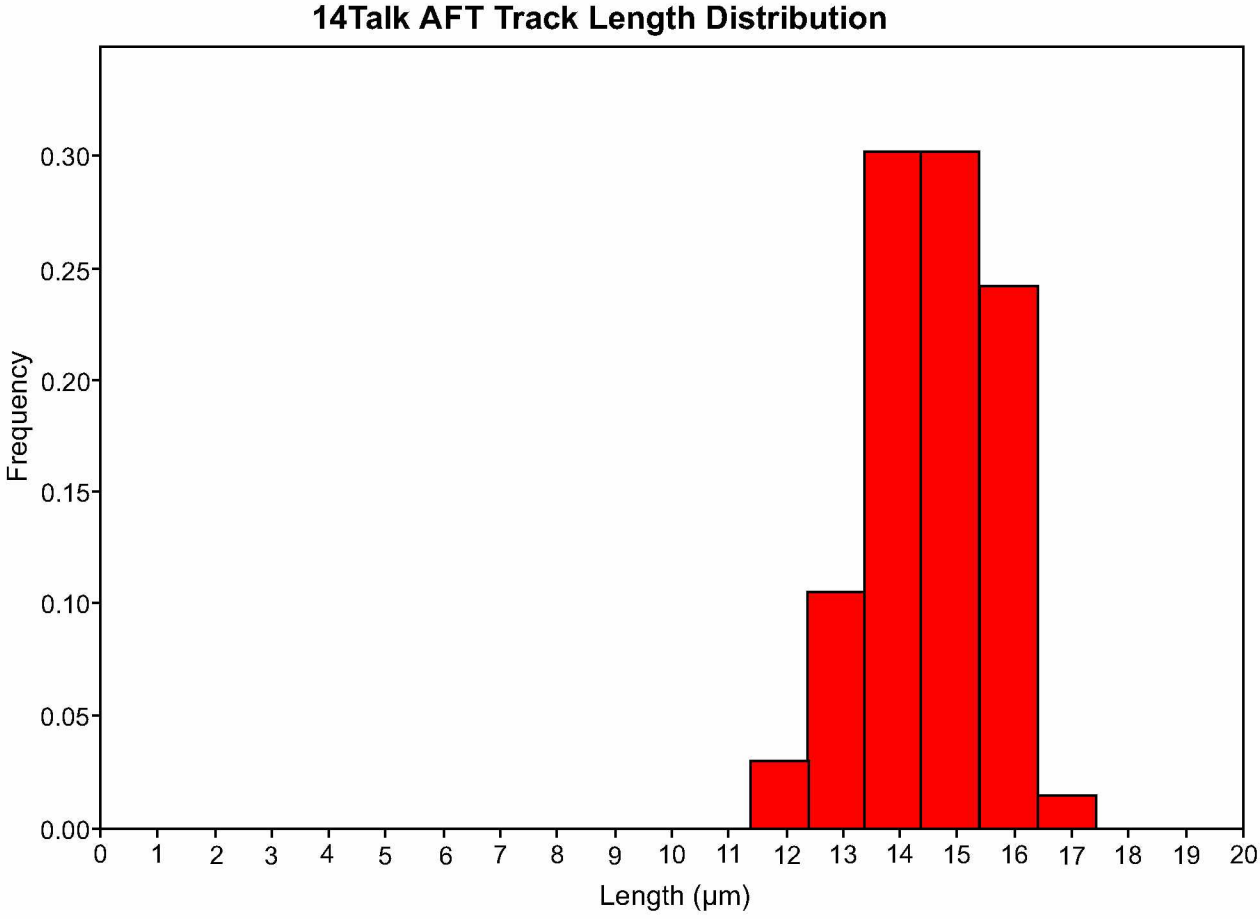

C13. HeFTy inverse thermal model and track length distribution for sample 14Talk.

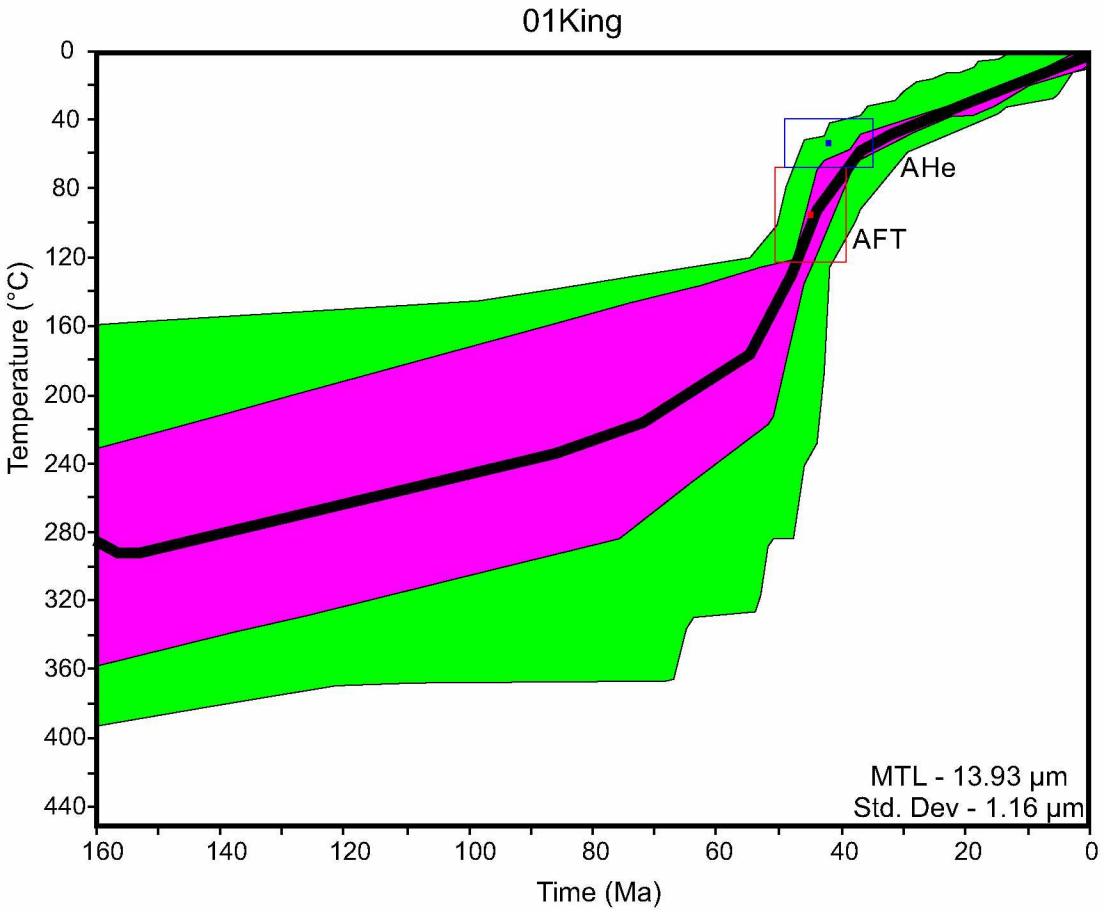

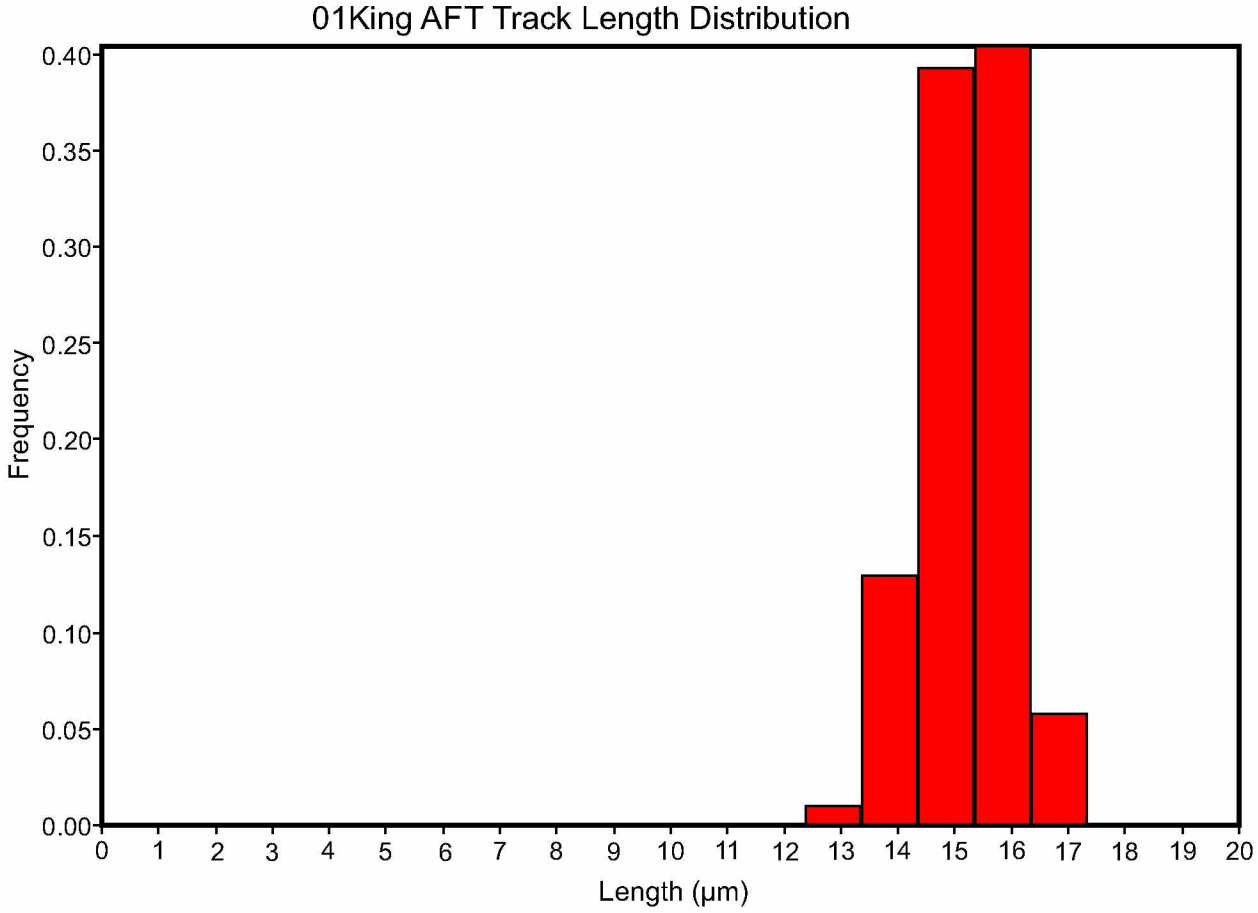

C14. HeFTy inverse thermal model and track length distribution for sample 01King.

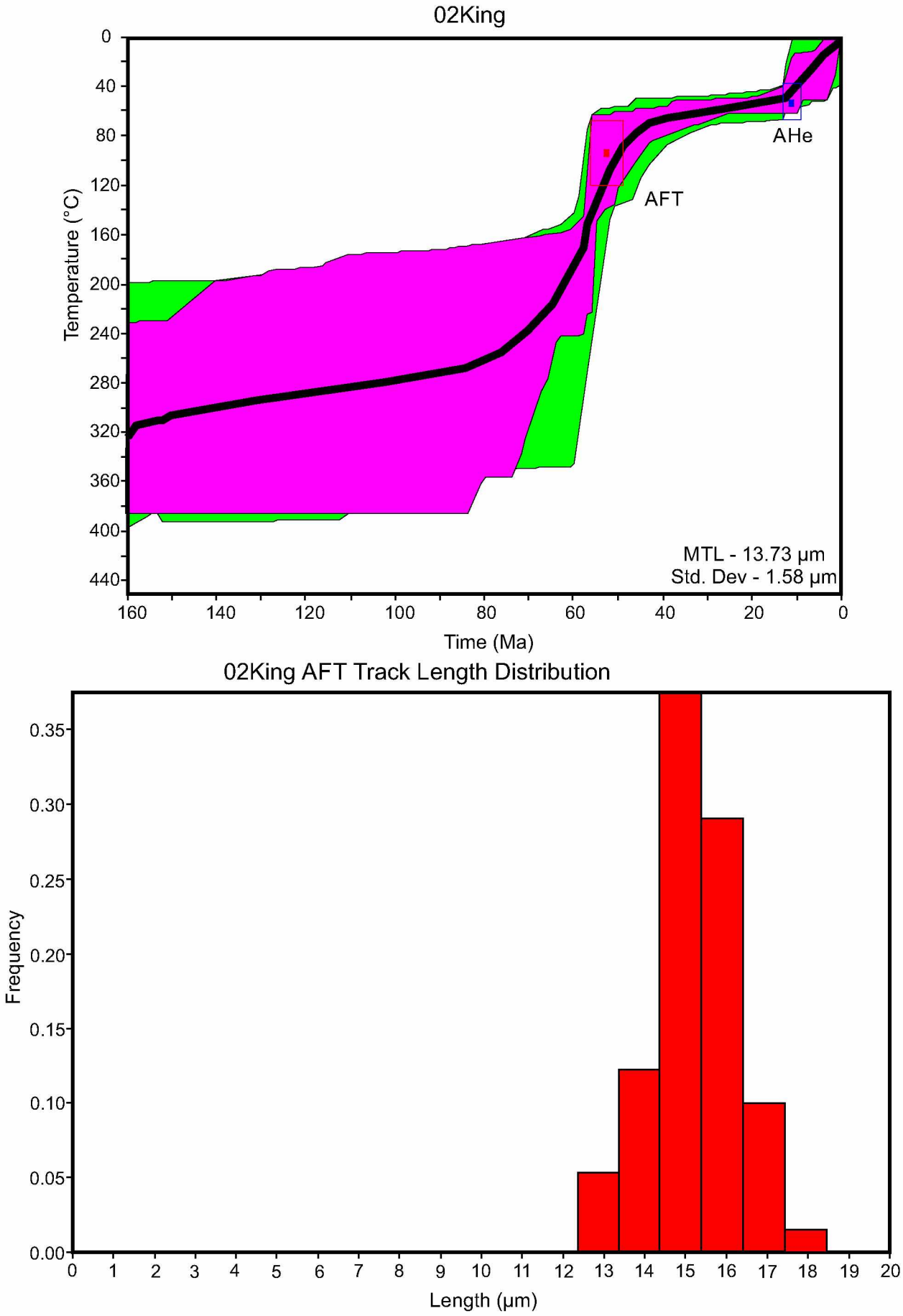

C15. HeFTy inverse thermal model and track length distribution for sample 02King.

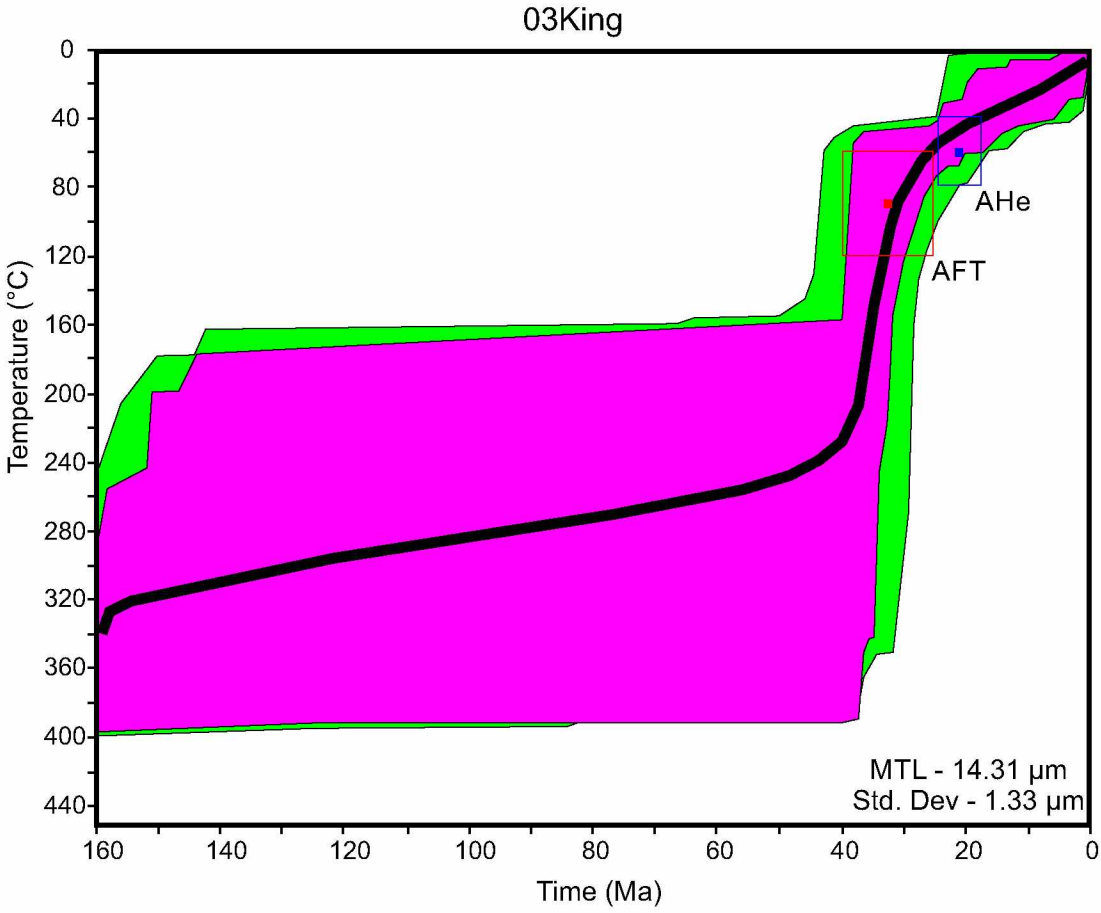

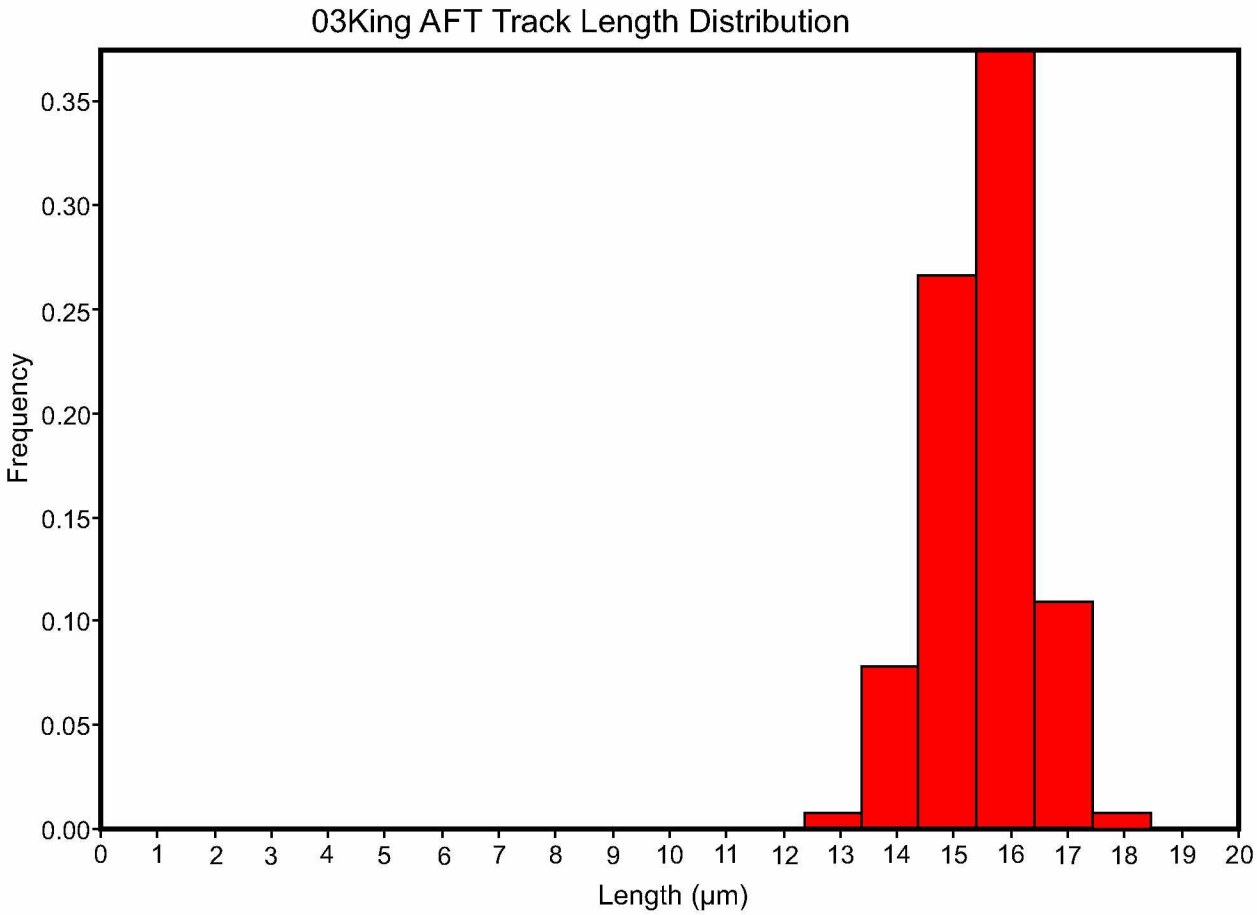

C16. HeFTy inverse thermal model and track length distribution for sample 03King.

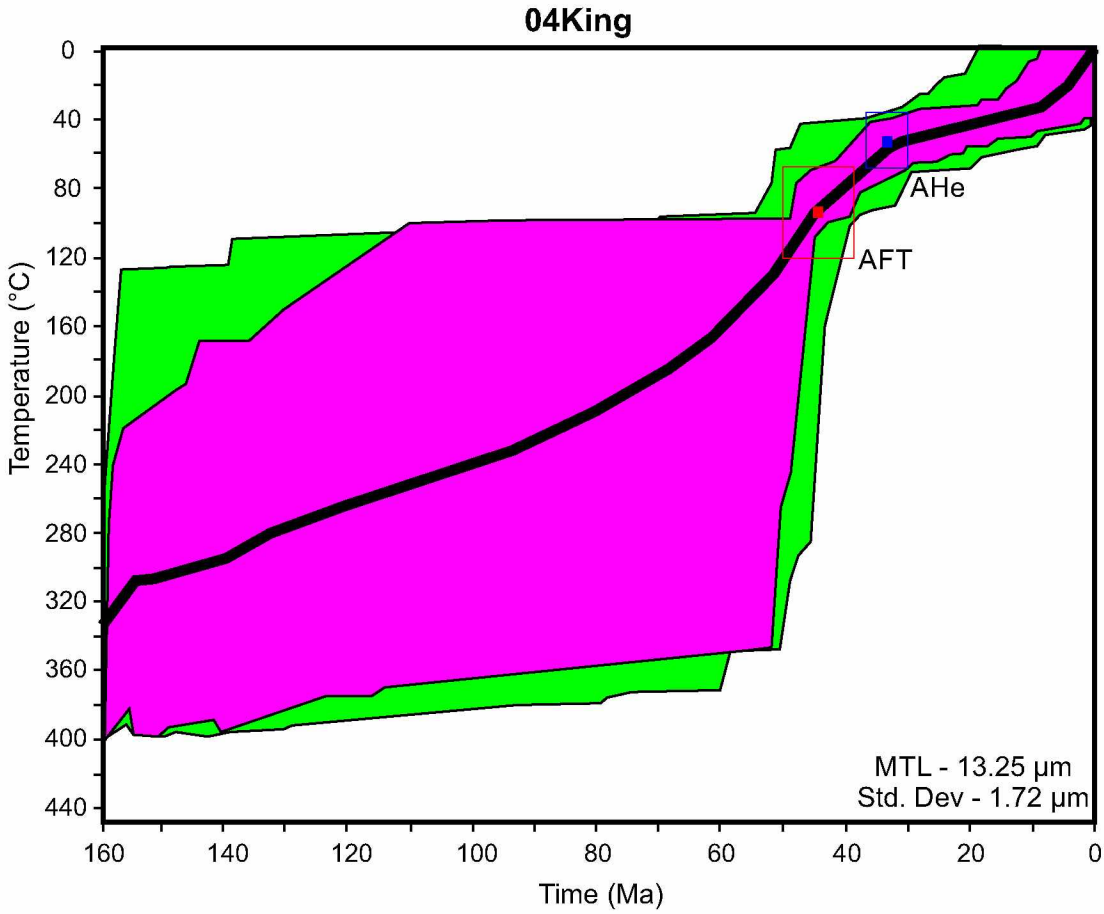

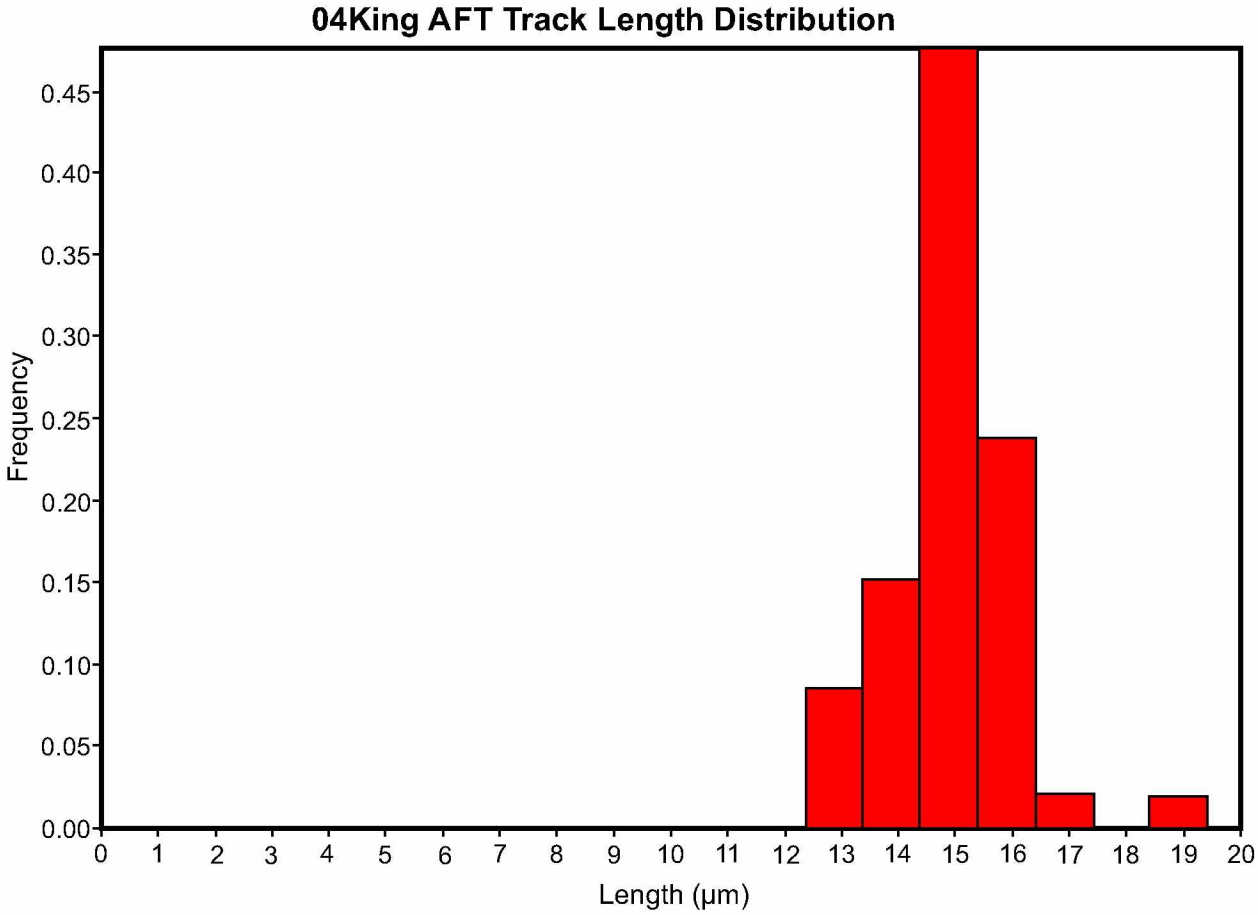

C17. HeFTy inverse thermal model and track length distribution for sample 04King.

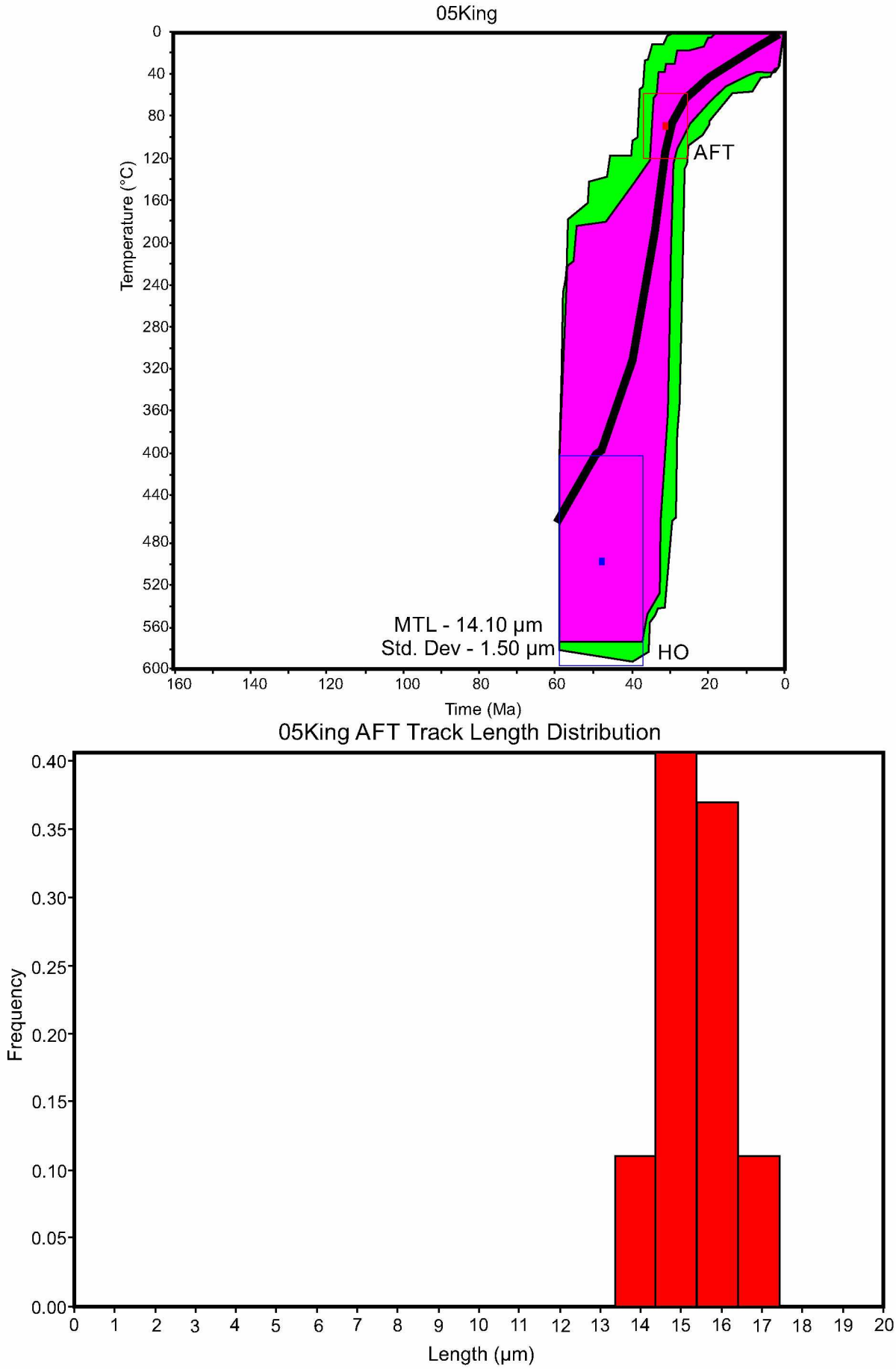

C18. HeFTy inverse thermal model and track length distribution for sample 05King.

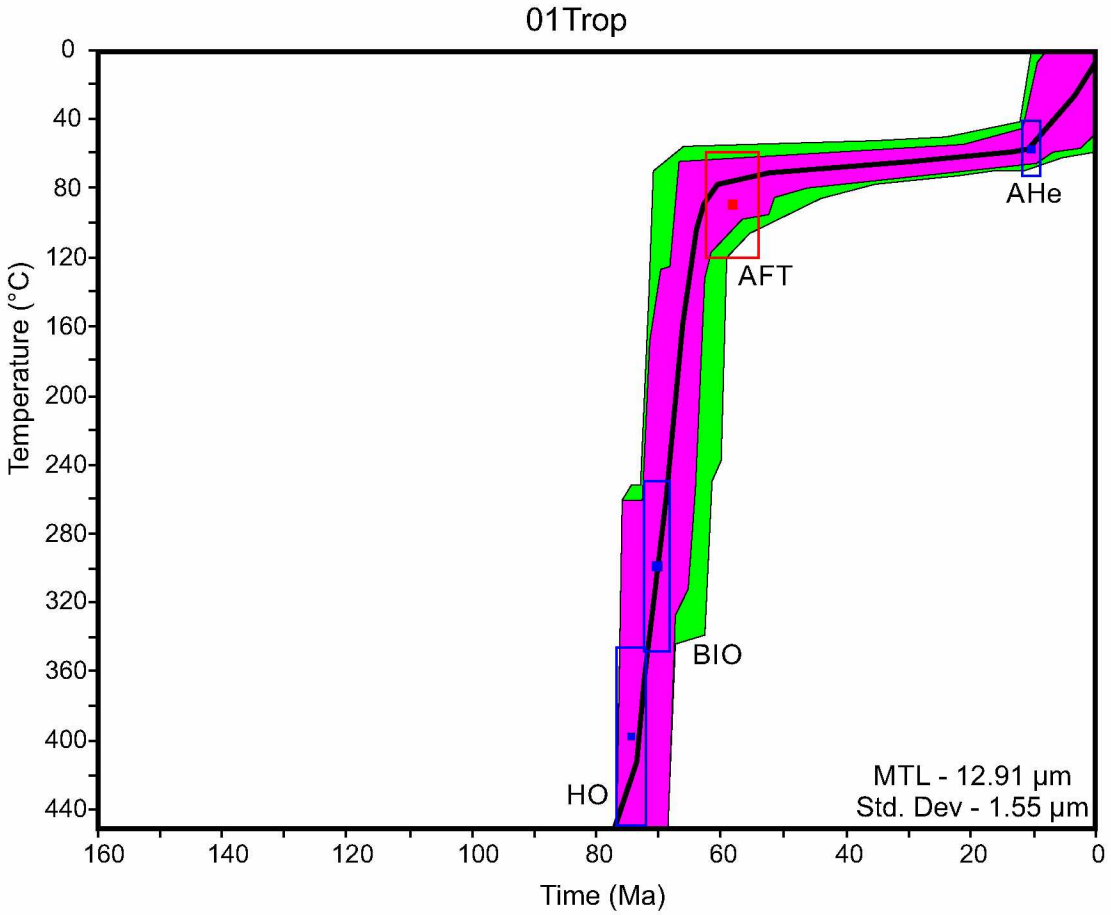

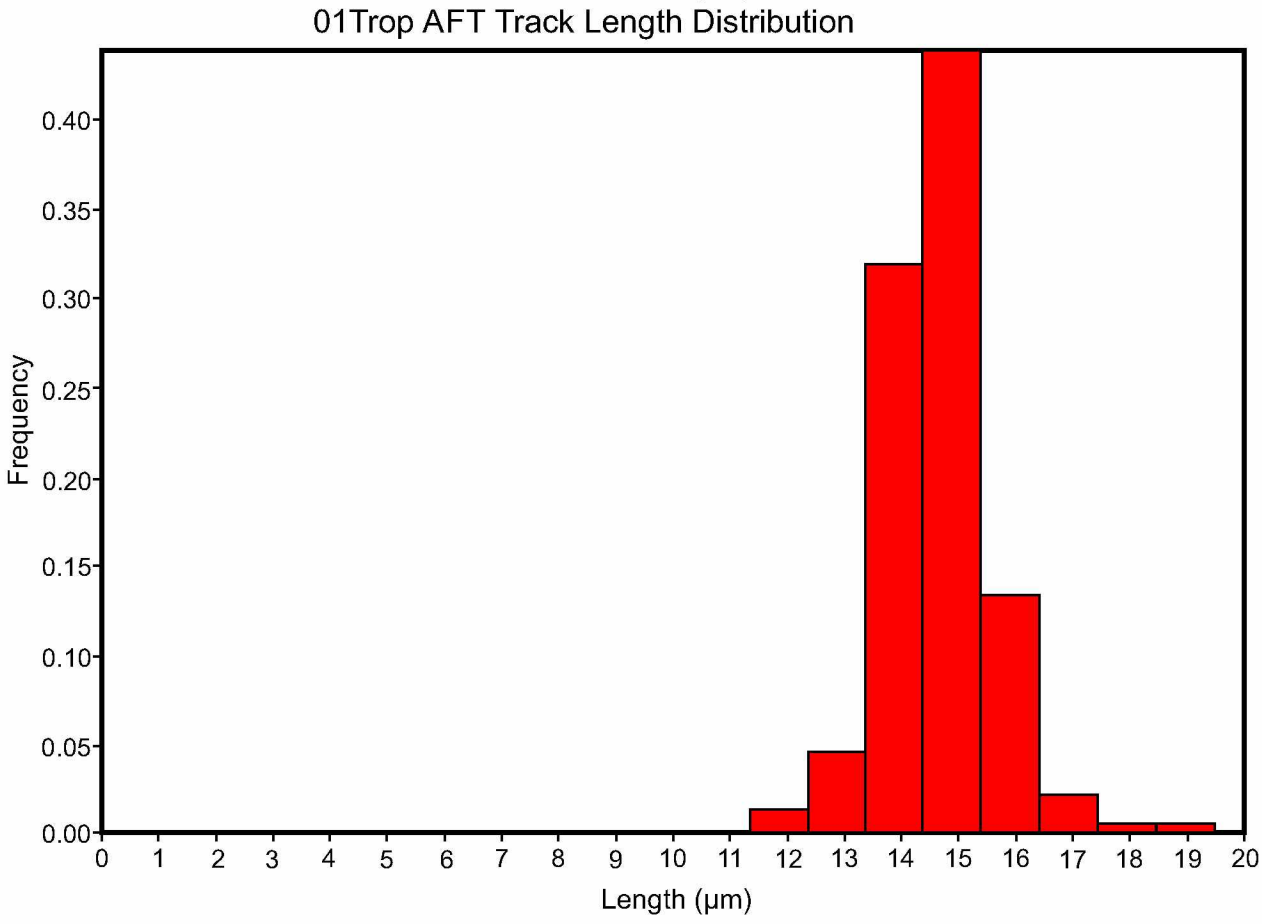

C19. HeFTy inverse thermal model and track length distribution for sample 01Trop.

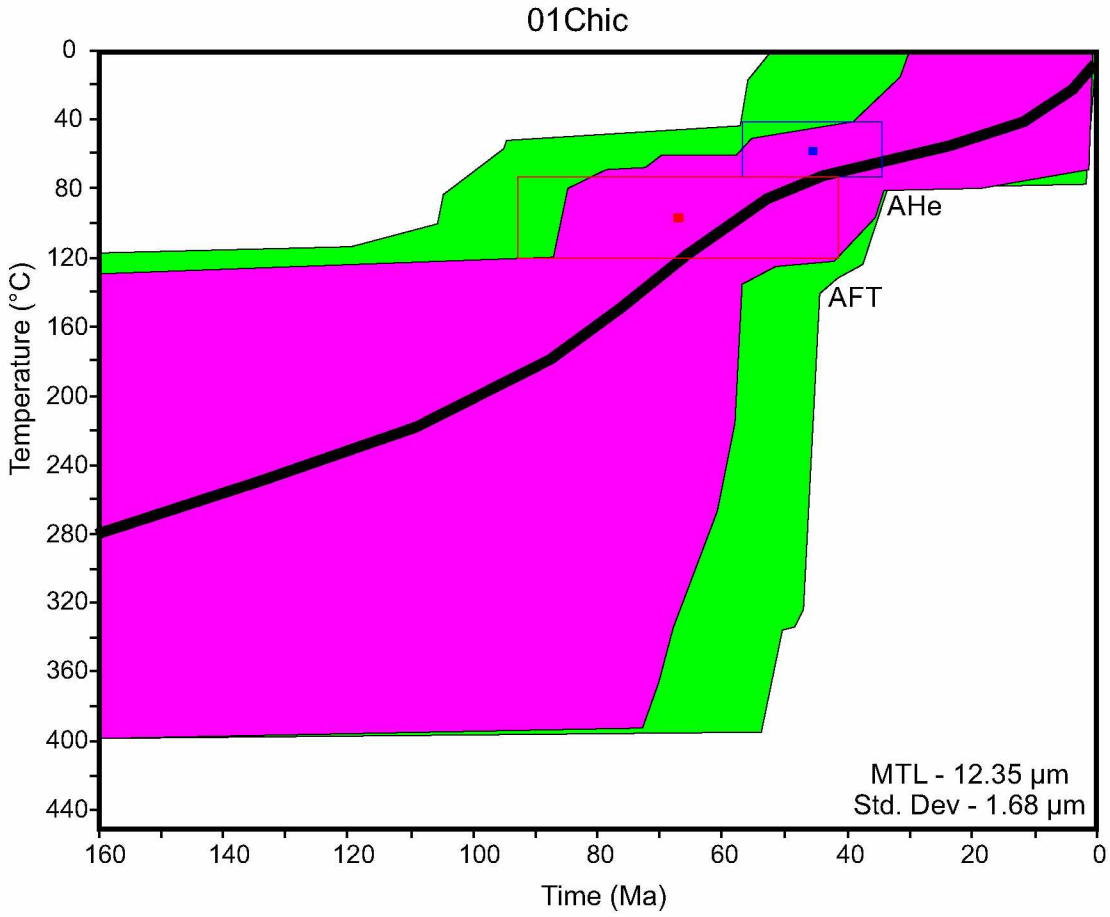

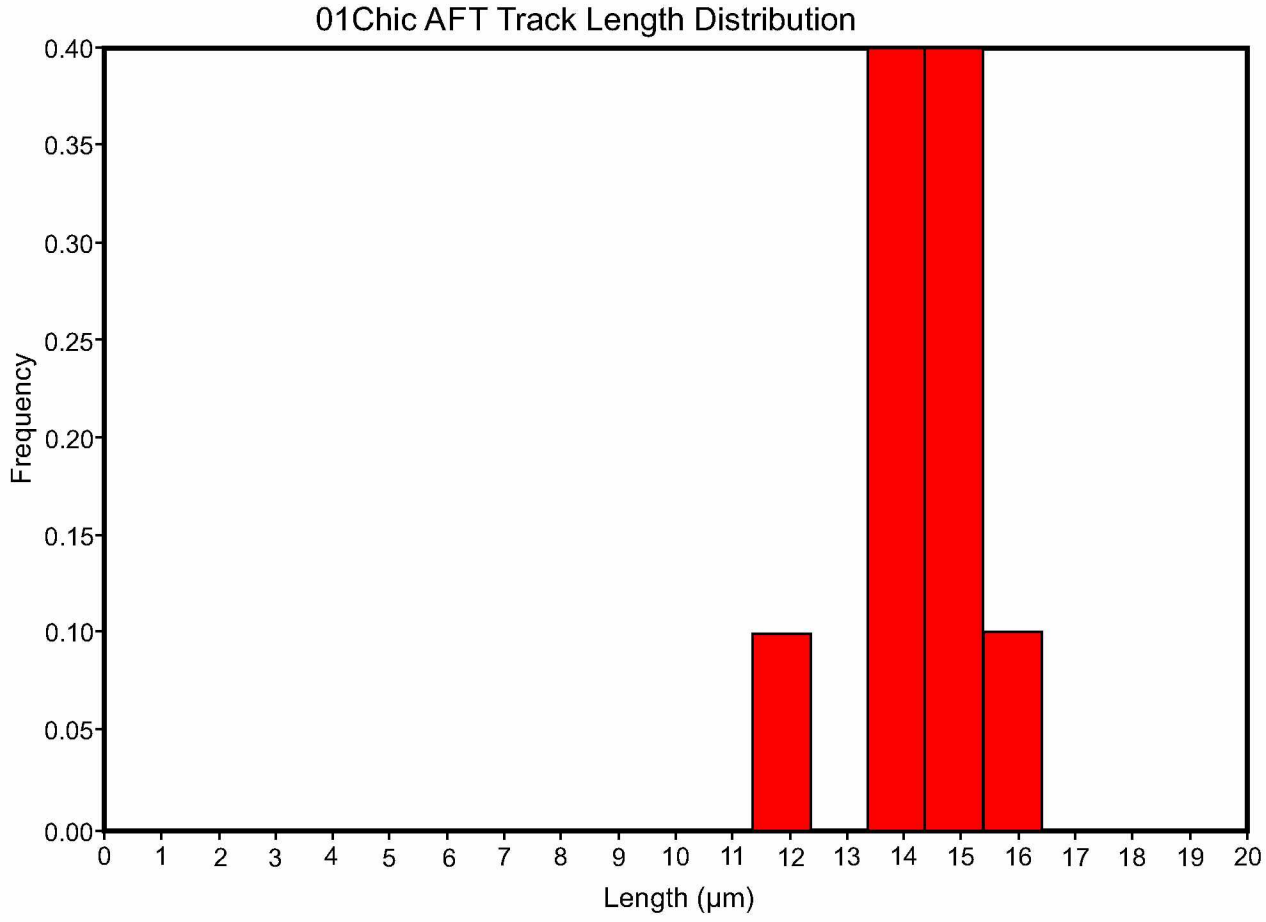

C20. HeFTy inverse thermal model and track length distribution for sample 01Chic.